Bulk and Surface Properties of Electrolytes at Eutectic Compositions

A thesis presented for the degree of

Doctor of Philosophy



Hannah Jane Hayler

New College

Physical & Theoretical Chemistry

University of Oxford

22nd June 2022

Abstract

The ubiquity of electrolytes is exemplified by the variety of fields in which they are encountered including technology, biology, and geology. Our understanding of dilute electrolytes is well established by Debye-Hückel theory, but in concentrated systems where continuum theories fail, the behaviour is not yet fully understood.

Deep eutectic solvents (DESs) are concentrated electrolytes commonly formed from eutectic mixtures of a quaternary ammonium salt and some molecular component. Recognised as an ionic liquid sub-category, they find use in synthesis, metal processing, and as lubricants. The immense range of potential components means 'green' DESs can be manufactured that are biodegradable, non-toxic, and inexpensive.

This thesis explores the interfacial structure and frictional response across electrolyte films. Using the surface force balance and white light interferometry, the film thickness can be controlled with sub-nanometre precision and the surface forces measured with sub-micronewton resolution. Bulk phase behaviour is also studied using differential scanning calorimetry.

Measurements across two DESs, choline chloride:ethylene glycol (ChCl:EG) and ChCl:glycerol, and the corresponding pure molecular fluids show time- and water-dependent interfacial structures. In ChCl:EG, a long-ranged exponentially decaying force is observed that decays faster with added water, suggesting an

underscreening-like behaviour previously observed in ionic liquids. The frictional response across the DESs highlights the molecular fluid-controlled nature of the lubrication mechanism. Varying the composition of ChCl:EG reveals that optimal lubrication properties do not coincide with the eutectic composition. The bulk phase behaviour of ChCl:EG mixtures shows a drastically different eutectic point compared with the literature, emphasising the importance of distinguishing thermodynamic and kinetic thermal events.

Studies across concentrated aqueous monovalent nitrate solutions, and ionic liquids under different confinement geometries demonstrate the prevalence of underscreening. It is also shown that the proposed underscreening scaling exponent does not depend on the mean ion diameter definition, but the transition point to underscreening does.

Declaration

This thesis is submitted for the degree of Doctor of Philosophy in Physical and Theoretical Chemistry at the University of Oxford. I confirm that the work presented here is my own. Where information has been derived from other sources, I confirm that this has been indicated in the thesis.

The measurements, analyses and interpretations reported in Chapter 5, Section 5.1 were completed in partnership with Dr James Hallett, and relates to the published article by Hallett, Hayler, and Perkin.[1] Karl Fischer titration measurements were completed by Andrew Wang (DPhil student in the group of Charles Monroe, Oxford).

Acknowledgements

First and foremost, I would like to thank my supervisor, Prof. Susan Perkin, for your support and guidance throughout my DPhil. It has been an absolute pleasure working with such an enthusiastic, patient, and knowledgable scientist. You have inspired me throughout my DPhil and will continue to do so going forward.

I must also thank Dr Carla Perez-Martinez, Dr James Hallett, and Dr Romain Lhermerout. Carla, without your help I would have been pretty incompetent. I am hugely grateful for the time you spent teaching me everything in and out of the lab. It was a privilege to work alongside you, and I am so glad our paths crossed. James, my fellow deep eutectic solvent enthusiast, thank you for looking after me on Carla's departure. I will always be in awe of your calm and relaxed approach to science. I am also incredibly grateful for your guidance when things were not going to plan. Romain, although we only worked together for a year, you have continued to help me via email and I am very grateful for that. Hydrodynamics would have got the better of me without you!

Tim and Astrid - the only two remaining from the beginning of my DPhil. Thank you both for a memorable time. There has definitely been a lot of ups and downs but you guys have kept me sane and laughing the whole 4 years. I would like to thank the current group: Aurora, Catherine, Ilaria, Josh, Kieran, and Lauriane. The group this year has been particularly awesome especially after

2 COVID-filled years. I also extend my thanks to previous group members: Ellie, Weichao, Xiaoyue, Luis, Daniel, and Alex.

I am grateful to those in the PTCL that have dealt with my incessant questions and queries, namely Paul and the building management team - thank you. Also to Leigh, who has always been chatty and accommodating of my solvent requests.

My time at Oxford would have been very different without the outreach team. Thank you to Saskia for allowing me play a role in the team, and trusting me to lead primary school days. I have learnt a lot through this experience and will always recommend it to fellow chemists.

I am also thankful to the Oxford careers service, namely Juliet who has helped me immensely in pursuing a career that I did not think was possible with my background.

I am indebted to my parents for their support throughout my university career and in pursuing this route. I can now conclude that I no longer want to attend culinary school!

Finally, I thank my fiancé, Mark Wellen, for being by my side for 10 years. You have been my absolute rock and so supportive throughout my career choices, even if it meant living away from you for 8 years. I am so looking forward to moving back and am excited for the rest of our adventures together.

Contents

Abstract **i**

Declaration **iii**

Acknowledgements **v**

1 Introduction **1**

1.1 Intermolecular and Surface Forces 2

1.2 Direct Force Measuring Techniques 4

1.2.1 Surface Forces Apparatus (SFA) 4

1.2.2 Atomic Force Microscopy (AFM) 6

1.3 Interfacial Forces 6

1.3.1 DLVO Theory 7

1.3.2 Non-DLVO Forces 8

1.4 Electrolytes 10

1.5 Deep Eutectic Solvents 12

1.6 Overview 13

2 Experimental **15**

2.1 Surface Force Balance 15

2.1.1 Minimising Contamination 16

2.1.2 Mica and Lens Preparation 17

2.1.3 Surface Force Balance Setup 19
2.1.4 Liquid Preparation and Injection 21
2.2 SFB Measurements and Analysis 23
2.2.1 Multiple Beam Interferometry 23
2.2.2 Normal Forces 26
2.2.3 Hydrodynamic Forces: A Note 28
2.2.4 Screening Lengths 30
2.2.5 Shear Forces 33
2.3 Refractive Indices 35
2.4 Differential Scanning Calorimetry 37
2.4.1 DSC Principles 37
2.4.2 Sample Preparation 40
2.4.3 Experimental Setup 41

3 Control Systems: Ethylene Glycol 43
3.1 Normal Forces 45
3.1.1 Structural Forces across Confined Ethylene Glycol 45
3.1.2 DLVO Forces 48
3.1.3 Oscillatory Forces 50
3.2 Lateral Forces 52
3.2.1 Quantised Friction across Ethylene Glycol Nanofilms . . . 52
3.2.2 The Role of Adsorbed Water 55
3.3 Summary 57

4 Control Systems: Glycerol 59
4.1 Normal Forces 61
4.1.1 Viscous Forces 61
4.1.2 Structural Forces across Confined Glycerol 64
4.2 Lateral Forces 66

4.2.1 Quantised Friction across Glycerol Nanofilms 66
4.2.2 The Role of Adsorbed Water 69
4.3 Summary 70

5 Nanostructure of Deep Eutectic Solvents (I) 73
5.1 1:2 Choline Chloride:Ethylene Glycol 76
5.1.1 Normal Forces 77
5.1.2 Lateral Forces 83
5.2 1:3 Choline Chloride:Ethylene Glycol 87
5.2.1 Normal Forces 87
5.2.2 Lateral Forces 90
5.3 1:10 Choline Chloride:Ethylene Glycol 92
5.3.1 Normal Forces 92
5.3.2 Lateral Forces 92
5.4 On- and Off-Eutectic ChCl:EG 94
5.4.1 Normal Forces 95
5.4.2 Lateral Forces 96

6 Nanostructure of Deep Eutectic Solvents (II) 101
6.1 Normal Forces 102
6.1.1 Viscous Forces 103
6.1.2 Structural Forces 105
6.2 Lateral Forces 107
6.3 The Influence of Added Water 111
6.4 Summary 114

7 Differential Scanning Calorimetry 117
7.1 Background and Motivation 117
7.1.1 Ideal Solution Theory 117
7.1.2 Regular Solutions 121

7.1.3 Depression of Freezing Point 124
7.1.4 Kinetic Considerations 127
7.1.5 Literature Measurements 127
7.2 DSC Observations 129
7.2.1 Featureless Thermograms 130
7.2.2 The Influence of Water 131
7.2.3 Thermal History 133
7.3 Choline Chloride:Ethylene Glycol 135
7.4 Summary 139

8 Underscreening in Concentrated Electrolytes 143
8.1 Theory of Electrolytes 144
8.1.1 Dilute Electrolytes: Debye-Hückel Theory 144
8.1.2 Recent Observations in Concentrated Electrolytes 147
8.1.3 Theory of Concentrated Electrolytes 149
8.1.4 Perspective 153
8.2 Measurements with Concentrated Aqueous Monovalent Salts . . . 155
8.3 Ion Diameter Considerations 157
8.4 Confinement Geometry 163
8.4.1 Hydrodynamic Forces 163
8.4.2 Comparison Factors 165
8.4.3 Using C_{reg} values 166
8.4.4 C_2C_1Im TFSI 167
8.5 Summary 170

9 Conclusions and Outlook 173

References 179

Chapter 1

Introduction

Liquids are incredibly important: without water, life on Earth would not exist. Liquids can be organised into numerous categories from organic solvents to emulsions, inorganic liquids to colloidal suspensions, aqueous solutions to liquid crystals. They are used in a number of everyday applications including lubricants for engines, coolants for nuclear reactors, and surfactants for soaps and detergents (see examples in Figure 1.1).



Figure 1.1 Liquids are ubiquitous. They are found in a multitude of fields and applications. Three examples are given here: water photo by Silas Baisch; battery photo by Roberto Sorin; oil photo by Fulvio Ciccolo. All images from Unsplash.[2]

Liquids excite interest across a range of length-scales, from the thousands of

kilometres of an ocean basin to the nanometric interactions between single atoms in liquid argon. This work aims to aid in the understanding of liquids, viewing interactions both in the bulk and at surfaces.

1.1 Intermolecular and Surface Forces

The term 'intermolecular forces' encompasses a variety of different force types including electrostatic, induction, and dispersion interactions. The wide variety of forces leads to a diverse range of condensed matter phases. Intermolecular forces can help us understand a whole host of everyday phenomena (Figure 1.2) including differences in the surface wettabilities of liquids, why polymers change their conformation in 'good' and 'poor' solvents, and the existence of melting and boiling points.

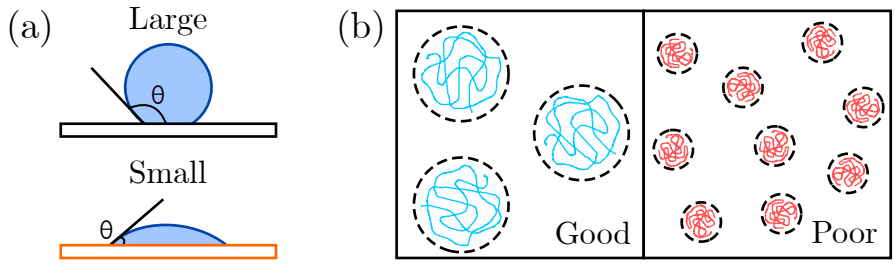


Figure 1.2 Intermolecular forces influence the (a) contact angles, θ, of liquid droplets on different surfaces, and (b) the swelling and contraction of polymers in 'good' and 'poor' solvents, respectively.

Intermolecular forces, F, and potential energies, W, are related by,

$$\vec{F} = -\nabla W. \tag{1.1}$$

For two atoms or small molecules, the interaction potential is termed the *pair potential*, w. If, for example, the two atoms are in a vacuum and interacting via a van der Waals (vdW) interaction, $w(r) \propto -r^{-6}$, where r is the separation between the atoms and the negative sign denotes an attractive interaction (see Figure 1.3). The r^{-6}-dependence makes the vdW interaction very short-ranged, and therefore

difficult to probe experimentally.[3] Extracting intermolecular potential energies experimentally is also complicated by the influence of averaging. We can study bulk properties such as viscosity or thermal conductivity, which depend on molecular collisions and hence the pair potential. However, the properties are not directly related to the pair potential and are highly averaged over separation, relative kinetic energy, and orientation.

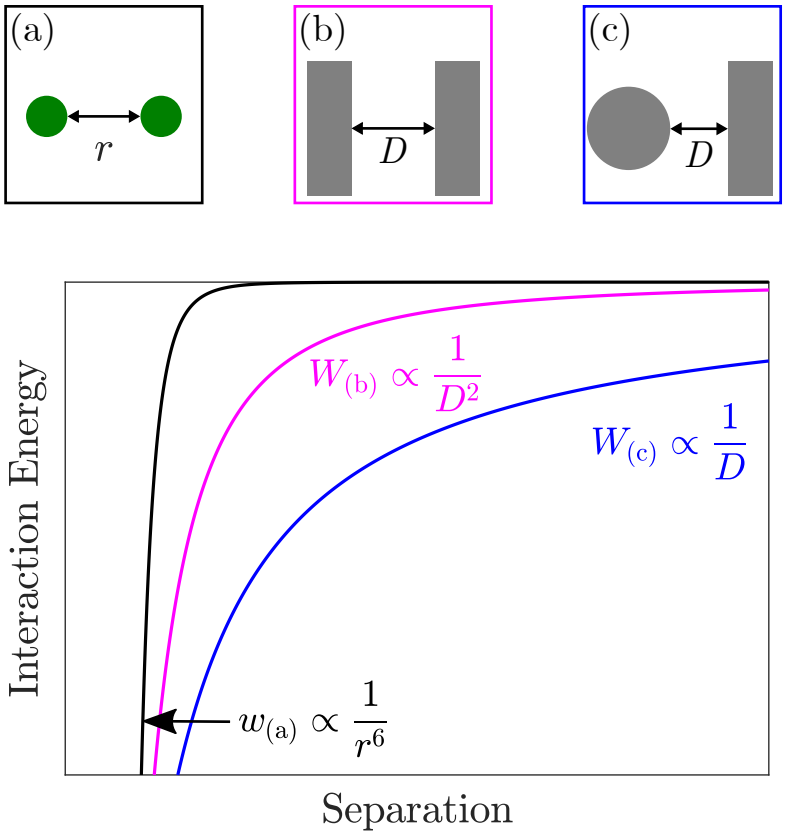


Figure 1.3 Van der Waals interaction energy. The pair potential of (a) two atoms in a vacuum separated by a distance, r, scales as $w_{(a)} \propto r^{-6}$ shown by the black line. The interaction energy between (b) two macroscopic planar surfaces separated by a distance, D, scales as $W_{(b)} \propto D^{-2}$ as shown by the pink line. The interaction energy between (c) two macroscopic bodies: a sphere and a planar surface, separated by a distance, D, scales as $W_{(c)} \propto D^{-1}$ as shown by the blue line.

As we scale up the system and consider forces between larger particles, colloids, and surfaces, the observed interactions can manifest in different ways compared to the molecular scale. When a large body composed of atoms/molecules is present, we must consider the pair potentials between all atoms and molecules

cumulatively. One implication of studying interactions, like the vdW interaction, between two large bodies is the stronger and longer ranged forces that are observed (see Figure 1.3). For example, the vdW interaction between two planar surfaces depends on the separation distance, D, as $W(D) \propto D^{-2}$. Below we will discuss the surface forces apparatus which has the same geometry as a sphere approaching a planar surface. In this instance, the vdW interaction energy, $W(D) \propto D^{-1}$, and the force, $F(D) \propto D^{-2}$. The vdW interaction between macroscopic bodies can also be attractive or repulsive, depending on the nature of the bodies and any intervening medium.[3] Unfortunately, the forces and energies between macroscopic bodies cannot be easily related to the pair potentials as we study a collective interaction of many molecules, and entropic effects may be present at the macroscale *e.g.* osmotic pressure. Nonetheless, by studying the forces between macroscopic bodies, and relating the force to the interaction energy, we can gain insight into the implication of intermolecular forces.

1.2 Direct Force Measuring Techniques

1.2.1 Surface Forces Apparatus (SFA)

One of the most sensitive ways of measuring the interactions between macroscopic surfaces is through surface force measurements. A liquid film is confined between two macroscopic surfaces and the forces observed are equivalent to the interactions in the bulk liquid.[4]

The surface forces apparatus (SFA) was first developed and used to study van der Waals forces between two macroscopic muscovite mica surfaces at small separations (5-30 nm) by Tabor and Winterton.[5] Shortly after, Israelachvili and Tabor[6] extended the original method so forces between mica surfaces could be studied between 1.5 and 130 nm. Israelachvili and Adams[7] then modified the

apparatus so forces between two surfaces immersed in a liquid could be studied.

Since its creation, the original SFA has been improved and modifications have been made allowing for a wider range of interfacial phenomena and condensed matter systems to be studied.[8–10] Surfaces other than mica have been explored including silica,[11] gold,[12,13] graphene,[14,15] and modifications made to render the mica surface hydrophobic.[16] Forces have been measured across water,[17,18] both dilute[7,19–24] and concentrated[25–27] aqueous electrolytes, ionic liquids,[28–37] polymers,[38] liquid crystals,[39–42] surfactants,[43] non-polar liquids,[44–46] polar liquids,[47,48] biological materials,[49] water-in-salt electrolytes,[50] and deep eutectic solvents.[1] The instrument has also been coupled with X-ray techniques[39,51] and adapted to measure opaque surfaces and liquids.[52]

Derjaguin Approximation

Experimentally, it is easier to measure the *forces* across two macroscopic surfaces that are *curved*. Whereas, the interaction *energy* between *planar* parallel plates is easier to determine theoretically. To compare these quantities one can use the *Derjaguin approximation*,

$$F(D)_{\text{sphere}} = 2\pi\left(\frac{R_1 R_2}{R_1 + R_2}\right) W(D)_{\text{planes}}, \tag{1.2}$$

where $F(D)_{\text{sphere}}$ is the force, as a function of surface separation, D, between two spheres with radii R_1 and R_2, and $W(D)_{\text{planes}}$ is the interaction energy between two planar surfaces.[3,53] The Derjaguin approximation is valid so long as $D << R_1, R_2$, and holds for repulsive, attractive and oscillatory force laws.

The R-dependence of the Derjaguin approximation allows experimental setups with different surface curvatures to be compared by accounting for the radii of the interacting surfaces. In the SFA (see Chapter 2), the two surfaces are

hemicylindrical and orthogonally oriented to one another, with respect to their axis of curvature. The Derjaguin approximation then becomes

$$F(D)_{\mathrm{xc}} = 2\pi R W(D)_{\mathrm{planes}}, \tag{1.3}$$

for crossed cylinders (xc) with equal radii, R. This is equivalent to a sphere of radius, R, approaching a flat surface.

1.2.2 Atomic Force Microscopy (AFM)

Atomic force microscopy (AFM) can also be used to measured the forces across confined liquid films in a similar manner to SFA. However, instead of two macroscopic surfaces, a sharp tip and a surface are used.[3]

The size of the tip can be varied from the atomic to micron scale, allowing different interactions to be probed. At the atomic scale, AFM can measure forces between individual particles as well as between a particle and a surface. The topography of a surface can also be explored.[54] Larger tips can measure longer-ranged colloidal forces. This is typically achieved by using a colloid sphere (*e.g.* silica) as the tip, and measuring the forces between the colloid probe and a surface.[55].

AFM has also been used to measure forces across numerous systems including aqueous dilute and concentrated salt solutions,[56–59] ionic liquids,[60–64] and deep eutectic solvents.[65–67]

1.3 Interfacial Forces

Measuring interfacial forces is not only useful for determining the bulk liquid force law, they also provide information regarding the liquid-surface interactions and the behaviour of the liquid under confinement. Interfacial forces are important

in everyday phenomena including the efficiency of lubricants, waterproof surface coatings, and the stability of colloidal systems. By measuring and understanding these forces, one can understand these phenomena on the molecular scale. Similarly, knowledge of the forces in confined environments is essential in fields such as engineering, biology and geology. It is also important to investigate whether physical properties change with film thickness. For example, a lubricant may have excellent lubricity in the bulk, but under strong confinement the viscosity may increase which may cause any moving parts to stick.

1.3.1 DLVO Theory

The interaction between two surfaces can be described using DLVO theory, developed by Derjaguin and Landau,[68] and Verwey and Overbeek[69] (DLVO). DLVO theory recognises that both repulsive double-layer and attractive van der Waals forces act between two surfaces and contribute to the total interaction energy.

Figure 1.4 shows an example of how the total interaction energy between two surfaces, W, may vary with surface separation, D, and the corresponding force contributions. As D tends to 0, the total interaction energy (solid line) must be dominated by the van der Waals attraction (dashed line) due to its inverse power law dependence ($W(D) \propto -1/D^n$) compared with the double-layer repulsion (dotted line) which decays exponentially with D. The van der Waals attraction results in the surfaces coming into adhesive contact.

As the surface separation approaches a few nanometres, deviations from DLVO theory can occur. One reason for these deviations is the failure of the Poisson-Boltzmann equation and Liftshitz theory used to describe the double-layer and van der Waals forces, respectively.[3] These continuum theories breakdown as molecular effects become important at small separations, so treating the surfaces and intervening medium as structureless is incorrect. Also, bulk properties of the

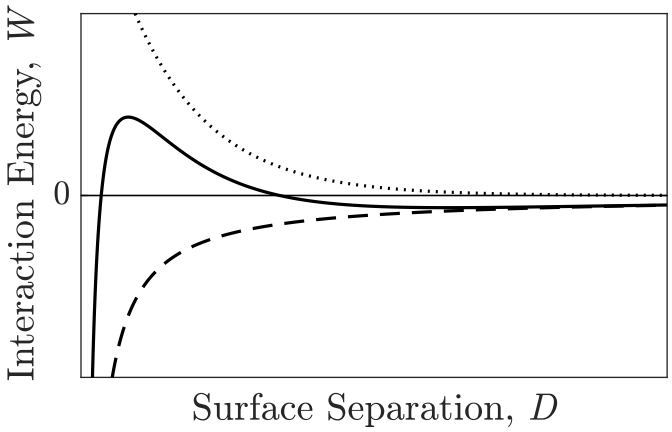


Figure 1.4 Interaction energy, W, between two surfaces as a function of surface separation, D. Both the van der Waals attraction (dashed line) and double-layer repulsion (dotted line) contribute to the DLVO interaction (solid line).

intervening medium, like refractive index and viscosity, may not necessarily be appropriate to describe the forces. Deviations can also occur due to the presence of other non-DLVO forces.

1.3.2 Non-DLVO Forces

Non-DLVO forces usually occur at small surface separations and can be monotonically repulsive or attractive, or oscillatory.

Structural (or solvation) forces occur across confined liquid films due to the geometric constraints.[3] To remain in the gap, the liquid molecules order themselves into layers between the two surfaces. As the surface separation decreases, this ordering (and the liquid density) will change giving rise to a structural force.

The nature of the structural force depends on both the surface properties and the intervening medium.[3] An exponentially decaying oscillatory structural force, as in Figure 1.5, can only occur if there is a high degree of order *i.e.* symmetric liquid molecules confined between two smooth and hard surfaces. With the period of the oscillations, ξ, corresponding to the molecular diameter of the confined molecules. The oscillatory force can also be superimposed on a monotonic repulsive

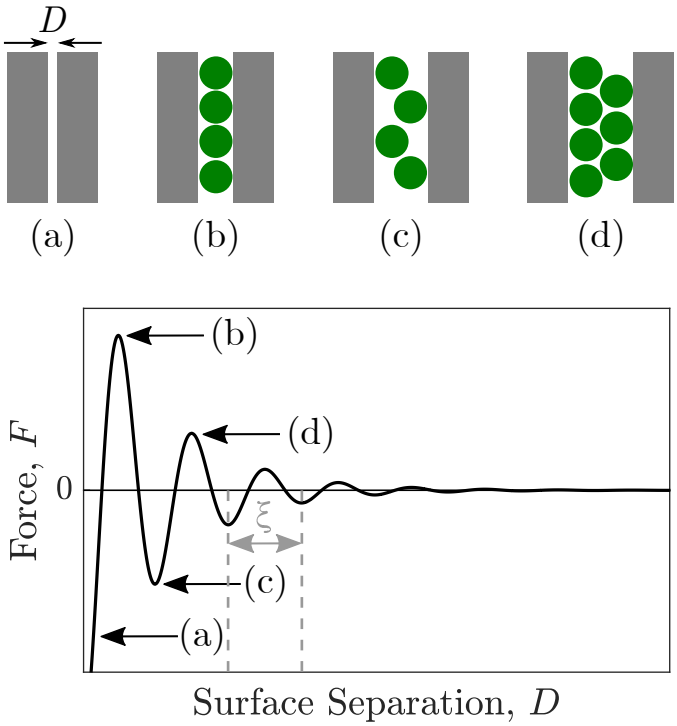


Figure 1.5 Force, F, as a function of surface separation, D, schematic. The sketches above the plot show how the molecules order with changing surface separation, and correspond to the labelled points on the plot.[3] The oscillation period, ξ, is shown by the grey dashed lines and arrow.

or attractive force. If the surface is rough or the molecules are asymmetric, a monotonic structural force is more likely.

The oscillation period depends on the confined liquid structure (see Figure 1.6). In a single-component molecular fluid (Figure 1.6(a)), the structural force typically has an oscillation period corresponding to the molecular diameter of the confined molecules.[45] When an electrolyte is present, the repeat unit must remain charge neutral. Figures 1.6(b) and (c) show two example structures that have been observed previously: a 'checkerboard-like' structure and an alternating structure.[29,34,70–73] In the checkerboard structure, the repeat unit contains a single layer of cations, anions, and solvent. The period of oscillation is approximately the molecular diameter of the largest constituent (in Figure 1.6(b), the anion is largest). As the surface charge, σ, increases, it is favourable for the interfacial layers to charge separate into alternating cation and anion layers (Figure 1.6(c)).[73]

In the alternating structure, the oscillation period is approximately the ion-pair dimension. It should be noted that the checkerboard and alternating structures can be observed in the presence and absence of solvent.

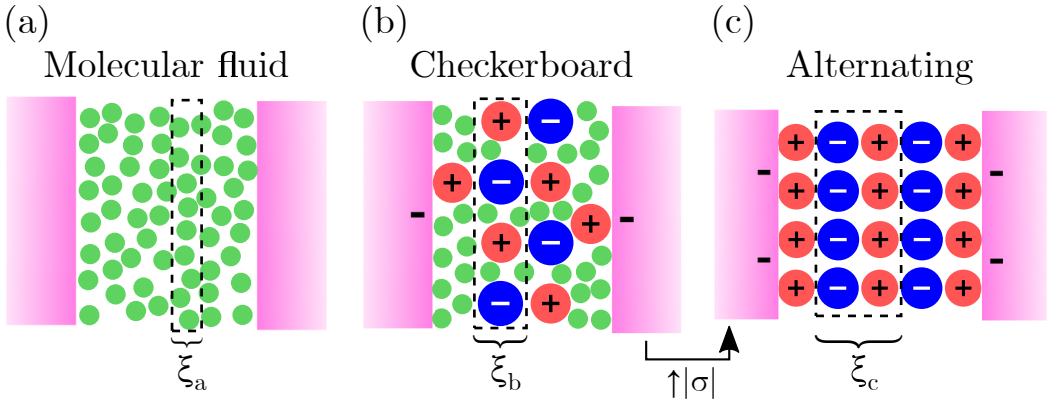


Figure 1.6 Schematics of confined (a) molecular fluid, (b) checkerboard and (c) alternating structures. The charge-neutral repeat units are indicated using dashed black boxes and the oscillation period by ξ. In (a) the repeat unit contains predominantly molecular fluid molecules, and the period of oscillation, ξ_a, is approximately the molecular diameter. When ions are present in the confined region *e.g.* in an electrolyte, the structure can resemble schematics (b) and/or (c). In (b) the checkerboard repeat unit comprises a single layer containing cations (red), anions (blue), and solvent (green). The period of oscillation, ξ_b, is approximately the molecular diameter of the largest constituent (here, the anion). As the surface charge, σ, increases the interfacial layers are more likely to charge separate into (c) the alternating structure. In (c) the repeat unit contains a layer of cations and a layer of anions, and the period of oscillation, ξ_c, is approximately the ion-pair dimension. The (negatively charged) surfaces are shown in pink.

1.4 Electrolytes

The main liquids of interest throughout this work are electrolytes - condensed media containing mobile charge carriers that allow the passage of current.[3] From battery technology in smartphones and laptops, to their presence in natural and biological systems like the dead sea and human blood plasma, electrolytes are ubiquitous. By gaining a deeper insight into the behaviour of electrolytes, both at the interfacial and bulk levels, we can understand how their force laws and physical properties vary with concentration, extent of confinement, and the species present.

The theory and behaviour of dilute electrolytes is well established by Debye-Hückel (DH) theory,[74] and will be discussed further in Chapter 8. Briefly, if we have a positive test charge at a distance, r, from a positive point charge, the potential, $\psi(r)$, arising from the point charge decays as,

$$\psi(r) = \frac{e}{4\pi\epsilon_r\epsilon_0 r} e^{-\kappa r}, \tag{1.4}$$

where,

$$\frac{1}{\kappa} = \lambda_{\mathrm{D}} = \sqrt{\frac{\epsilon_r\epsilon_0 k_{\mathrm{B}} T}{2e^2 n}}, \tag{1.5}$$

λ_{D} is the Debye (screening) length, ϵ_r is the dielectric constant of the medium, ϵ_0 is the vacuum permittivity, k_{B} is the Boltzmann constant, T is the temperature, e is the elementary charge, and n is the number density of ions. Compared with a purely Coulombic decay, as would be expected in a vacuum, the potential in a dilute electrolyte decays much faster due to the screening of the potential by the electrolyte (see Figure 1.7).

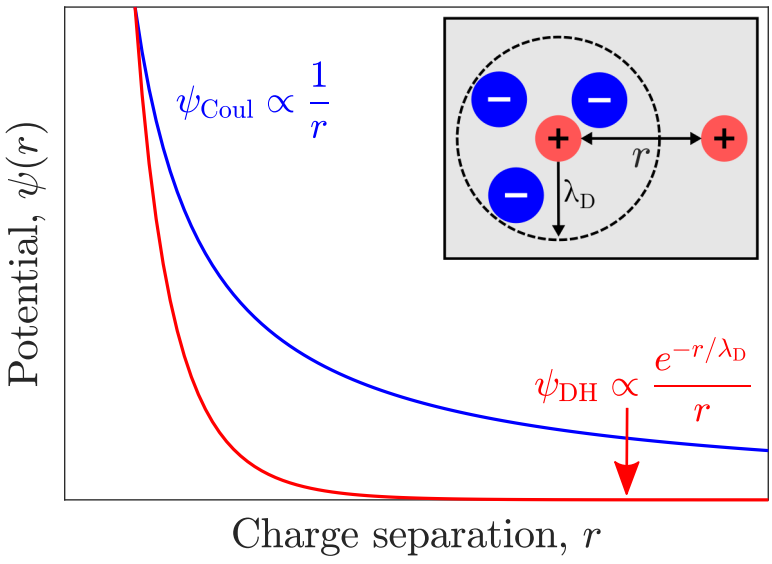


Figure 1.7 Potential, $\psi(r)$, arising from a positive point charge as a function of separation, r, in a vacuum or dielectric medium (blue line) and in a dilute electrolyte (red line). In the former, the potential is purely Coulombic (ψ_{Coul}) and scales as r^{-1}. In a dilute electrolyte, pictured in the inset, the potential, ψ_{DH}, decays according to DH theory (Equation 1.4).

Equations 1.4 and 1.5 are valid in the limit of high dilution. At concentrations greater than ≈ 1 mM, the (linearised) DH theory begins to breakdown[75] and the Debye length approaches molecular dimensions. Using the DH theory exactly allows concentrations up to 1 M to be described,[3,74,76] but beyond this point the assumptions on which DH theory is derived, fail *e.g.* point charges and negligible correlation effects.

To date, a universal theory for the behaviour of concentrated electrolytes, akin to DH theory, has not been established. Unfortunately, everyday systems rely on concentrated electrolytes including potassium ion channels in the body and supercapacitor energy storage, so understanding the behaviour of concentrated electrolytes is crucial.

We will revisit and consider the theory of dilute and concentrated electrolytes more extensively in Chapter 8.

1.5 Deep Eutectic Solvents

Numerous chemical industries depend on organic solvents that can be harmful and/or environmentally damaging. The large-scale consumption of these solvents, and corresponding waste production can be addressed by considering more green and sustainable chemistry practices.[77] Alternative solvents have been proposed such as ionic liquids (ILs), which have been studied extensively and have promise in areas such as catalysis, electrochemistry, and drug delivery.[78] More recently, deep eutectic solvents (DESs) have been suggested as an alternative solvent.

DESs are commonly recognised as a sub-category of ILs, and were first reported by Abbott *et al.*[79] in 2001. ILs and DESs are chemically similar as both contain constituent cations and anions. They can therefore be classed as electrolytes, and actually have high intrinsic concentrations. DESs differ from ILs

in chemical composition by the presence of a third molecular solvent constituent. ILs and DESs have similar physical properties including tunability, high thermal stability, and low vapour pressures.[80] Depending on the components used, DESs can have advantages over ILs including biodegradability, non-toxicity, and ease of manufacture from inexpensive starting materials.[81] In fact, DESs have been classed as more 'green', and hence the interest in DESs as a solvent alternative.[82,83]

In Chapters 5, 6, and 7, we will discuss the nature of DESs in more detail.

1.6 Overview

In this thesis, we explore the interfacial forces across electrolyte films. The work carried out uses the SFA developed by Klein and Kumacheva,[84] known as the surface force balance (SFB). This apparatus and the experimental procedure are discussed thoroughly in Chapter 2.

We are interested in the behaviour of concentrated electrolytes, namely DESs, aqueous monovalent salts, and ILs. As the name eludes to, DESs are formed at a eutectic composition, and we will explore different eutectic compositions. Firstly, we will study the interfacial and shear forces across the molecular fluids ethylene glycol (Chapter 3) and glycerol (Chapter 4). The pure liquids have a number of applications and are commonly used to prepare DESs. By studying the pure fluids we can determine their contribution to the interfacial forces observed in the corresponding DESs.

Chapters 5 and 6 will focus on the interfacial and shear forces across DESs formed by mixing the quaternary ammonium salt, choline chloride (ChCl), with ethylene glycol and glycerol, respectively. In both systems, the on-eutectic compositions will be studied and the influence of added water explored. We will also investigate the differences between on- and off-eutectic mixtures of choline chloride

and ethylene glycol. Using a differential scanning calorimeter (DSC), Chapter 7 will explore the bulk phase behaviour of the ChCl:ethylene glycol DES.

The final chapter will focus on concentrated electrolytes more generally. We will present a perspective on the theory and experimental observations made in concentrated electrolytes. Chapter 8 then goes on to explore the interfacial forces across highly concentrated nitrate salts, how the ion diameter should be defined in concentrated electrolytes, and finally considers the influence of confinement geometry on the observed behaviour.

Chapter 2

Experimental

2.1 Surface Force Balance

The surface force balance (SFB) has been used throughout this work to measure force laws across confined liquid films. In this section, the technique and experimental procedures are discussed.

Figure 2.1 summarises the SFB. The liquid is confined between two hemicylindrical lenses that are mounted in a crossed-cylindrical fashion. On top of the lenses, we adhere a single muscovite mica piece that has a thin silver layer evaporated onto the backside. The arrangement of the silver-mica-medium-mica-silver forms an interferometric cavity that we pass white light through. Only those wavelengths that interfere constructively between the silver mirrors will pass through the cavity to the spectrometer, yielding fringes of equal chromatic order (FECO) as pictured in Figure 2.1. By monitoring the positions of the FECO with respect to a calibration image, we can deduce the distance, D, between the surfaces as we move the lenses towards or apart from one another. We can then determine the surface forces by simply measuring the deflection of a Hookean

spring upon which one lens is mounted. This method allows the distances to be measured with sub-nanometre precision, and the forces with sub-micronewton resolution.

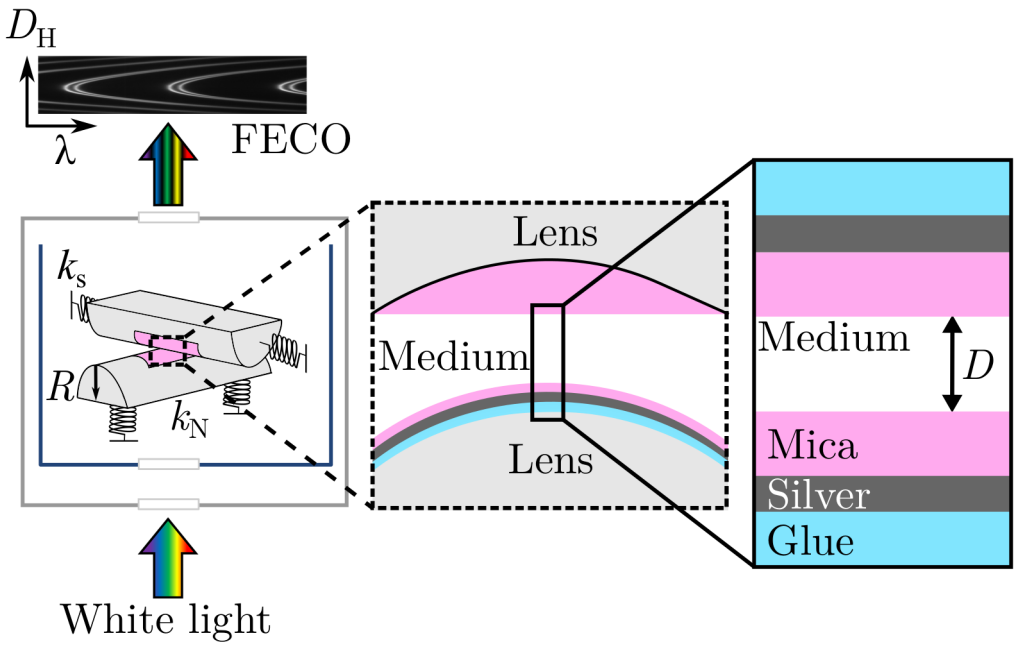


Figure 2.1 Summary of the SFB. White light passes into the chamber and through the bottom lens into the interferometric cavity created by the silver-mica-medium-mica-silver stack. Wavelengths that constructively interfere pass through the top lens to the spectrometer and then the camera, yielding fringes of equal chromatic order (FECO). The FECO are used to determine surface separation, D, and radius of curvature of the lenses, R, using the apical position of the fringes in wavelengths, λ, and the in-plane (horizontal) distance, D_H. Normal and shear springs with spring constants k_N and k_s are used to determine the normal and frictional forces, respectively.

2.1.1 Minimising Contamination

Surface forces measurements are sensitive to any contaminants that may sit on the surfaces.[85] To minimise contamination, all equipment is cleaned in toluene, chloroform and ethanol. After rinsing in ultrapure water (total organic content (TOC) $<$ 3 ppb, resistivity 18.2 MΩcm), glassware and Teflon™ pieces are cleaned in piranha solution (1:3 hydrogen peroxide:sulfuric acid) and all stainless steel tools are passivated in 33% nitric acid in water. All the equipment is again rinsed in ultrapure water and, if necessary, stored in ethanol.

Experiment preparation and setup is carried out in a laminar flow hood (LFH) which filters out all particles less than 5 μm from the laboratory air thus creating a dust and particle-free working environment.

2.1.2 Mica and Lens Preparation

Muscovite mica surfaces are commonly used for surface forces measurements. This naturally occurring mineral can be cleaved along its natural cleavage plane exposing a surface that is atomically smooth with facets of uniform thickness. Thin mica sheets are also transparent to visible light which makes them ideal for interferometric measurements.[86]

Preparation of the surfaces begins with a large, thick sheet of mica. The tip of a needle is inserted into the edge of the sheet to initiate the separation. The two sheets are then gently separated by peeling them apart by hand. This process is repeated with the ever-thinner mica sheet until interference colours are observed, as in Figure 2.2. Facets of uniform thickness are indicated by areas of the same colour, with abrupt colour changes corresponding to steps in the crystal plane.

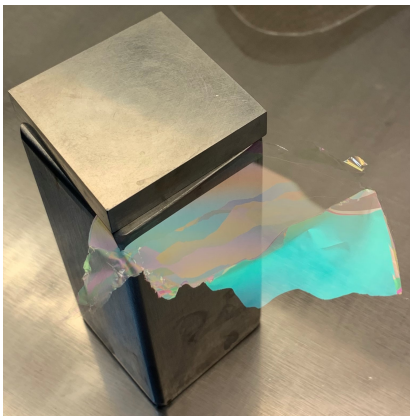


Figure 2.2 Multi-coloured facets are observed on freshly cleaved mica. The colour and brightness depends on the mica thickness.

If a large single-facet mica piece is cleaved, with an appropriate thickness ($<$ 5 μm), it is cut away with a hot platinum wire. To minimise surface contami-

nation by platinum nanoparticles, the cleaved piece remains between the source of the laminar air flow (at the back of the LFH) and the platinum wire (at the front). Once cut away, the piece is placed on a freshly cleaved, thick mica sheet (the base sheet) and allowed to adhere. Mica pieces are cleaved until the base sheet is full or until the base sheet has been exposed to air for 1-2 hours, after which a new base sheet is started.

The exposed mica surfaces on the base sheet are then coated in a thin film of silver using a thermal evaporator under vacuum (pressure $\approx 10^{-6}$ mbar). A silver film of 40-50 nm thick, measured using a quartz crystal microbalance, is deposited at a rate of 1 Å s^{-1}. The rate can be controlled by adjusting the heater current and the position of the mechanical shutter. To limit silver oxidation, the silvered base sheet(s) (Figure 2.3) are stored under vacuum in a desiccator until they are needed.

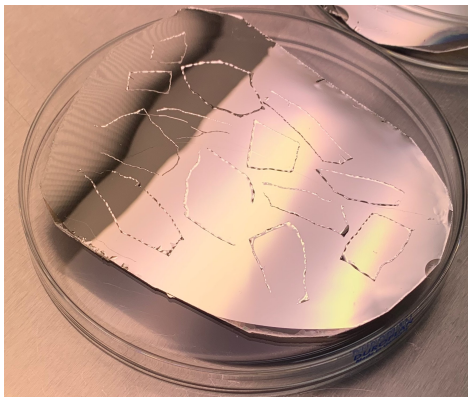


Figure 2.3 Silvered mica pieces on a base sheet.

On the day of an experiment, the mica pieces are cut into small rectangular pieces using a scalpel. Using a pair of tweezers, a small piece is peeled off of the base sheet and glued, silver-side down, to a fused silica lens. EPON epoxy resin is applied to the lens and smoothed out before the mica piece is placed down. This is repeated with another small mica piece from the same facet (*i.e.* of identical thickness) to create two back-silvered mica substrates mounted in an appropriate geometry for the experiment, as in Figure 2.4.



Figure 2.4 Back-silvered mica adhered to hemicylindrical lenses using EPON epoxy resin.

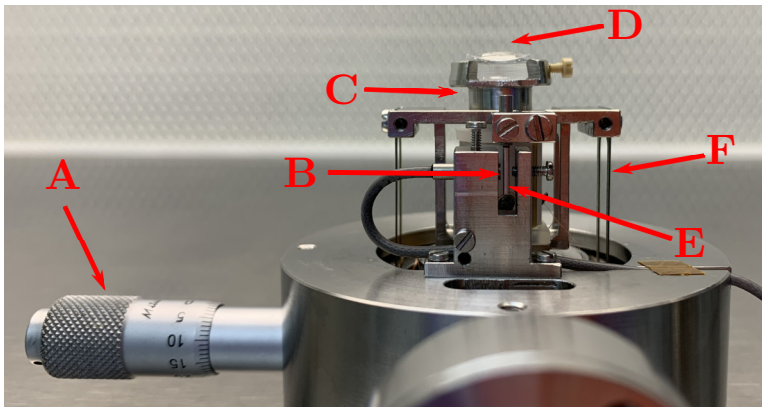
2.1.3 Surface Force Balance Setup

In the LFH, the section of the SFB that contains the piezoelectric tube and upper lens, known as the 'top part' (shown in Figure 2.5), is removed from the SFB and the small steel plate, known as the 'flag', is aligned with respect to the capacitance probe using a series of screws. One lens is then placed in the lower lens holder in the 'boat' as in Figure 2.6. The other is placed in the upper lens holder which attaches to the top part. The lenses are mounted in the SFB such that their axes are perpendicular as shown in Figure 2.7. This crossed-cylinder configuration is equivalent to a sphere approaching a flat surface.

If the system to be studied needs to remain dry during the experiment, a small cup of phosphorus pentoxide can be added to the chamber before closing. The chamber can also be purged under nitrogen *in situ*.

In the measurement room (see Figure 2.8), the SFB sits on an isolation table atop a series of materials (rubber-marble-rubber-concrete) that damp mechanical vibrations. The position of the SFB on the isolation table is such that the reflected white light passes through the bottom window with maximum intensity. A microscope is placed in the path of the light emerging from the SFB and a prism reflects the light onto the spectrometer slit. Multiple connections to the SFB are made to control lens movement and measure the air-gap capacitance. A

a)



b)

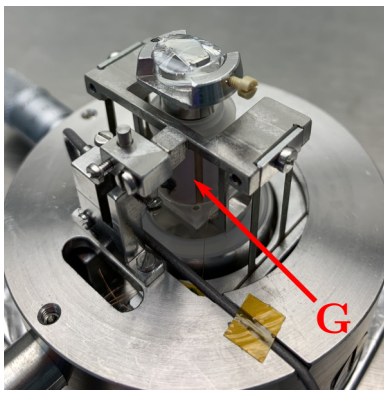


Figure 2.5 The 'top part' viewed from (a) the front and (b) the side. Labels correspond to A - micrometer, B - capacitance probe, C - stainless steel lens holder, D - lens, E - 'flag', F - vertical leaf spring, G - sectored piezoelectric tube (PZT).

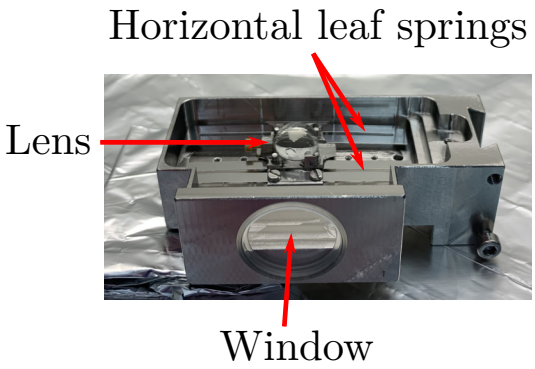


Figure 2.6 The 'boat', in which the lower lens sits atop horizontal leaf springs.

polystyrene box is also placed around the SFB to minimise air vibrations. Thermal drift is minimised by keeping the room at a constant temperature.

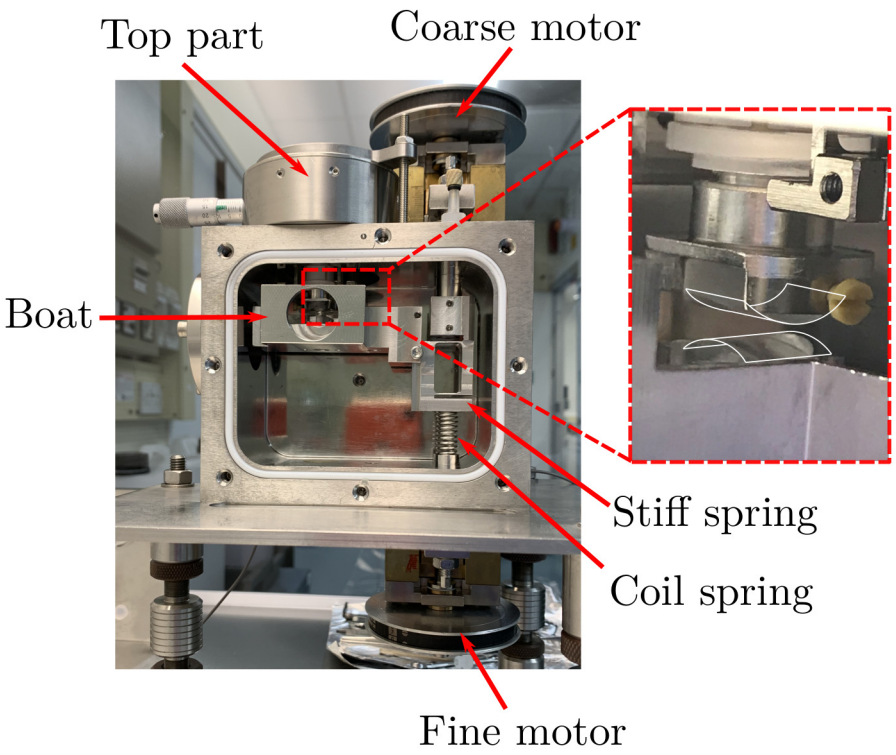


Figure 2.7 The setup in the SFB chamber, viewed from the front, before securing the door. The lenses are mounted in a crossed-cylinder configuration (zoomed image) with their axes mutually perpendicular by fixing the boat and the top part in position. The differential spring mechanism (coil and stiff springs) sits on the right of the chamber and allows the lenses to be positioned with 1 nm precision.

2.1.4 Liquid Preparation and Injection

The liquid to be studied is injected between the two lenses with a syringe. Liquids were either used as received or prepared before injection.

Molecular Fluids

Ethylene glycol (Acros, anhydrous, 99.8%) and glycerol (Sigma-Aldrich, anhydrous, $\geq$ 99.5%) were used as received.

Ionic Liquids

1-Ethyl-3-methylimidazolium bis(trifluoromethylsulfonyl)imide, C_2C_1Im TFSI, (Iolitec, 99%) was dried on a Schlenk line at 65 ^{o}C and $< 1 \times 10^{-2}$ mbar, overnight.

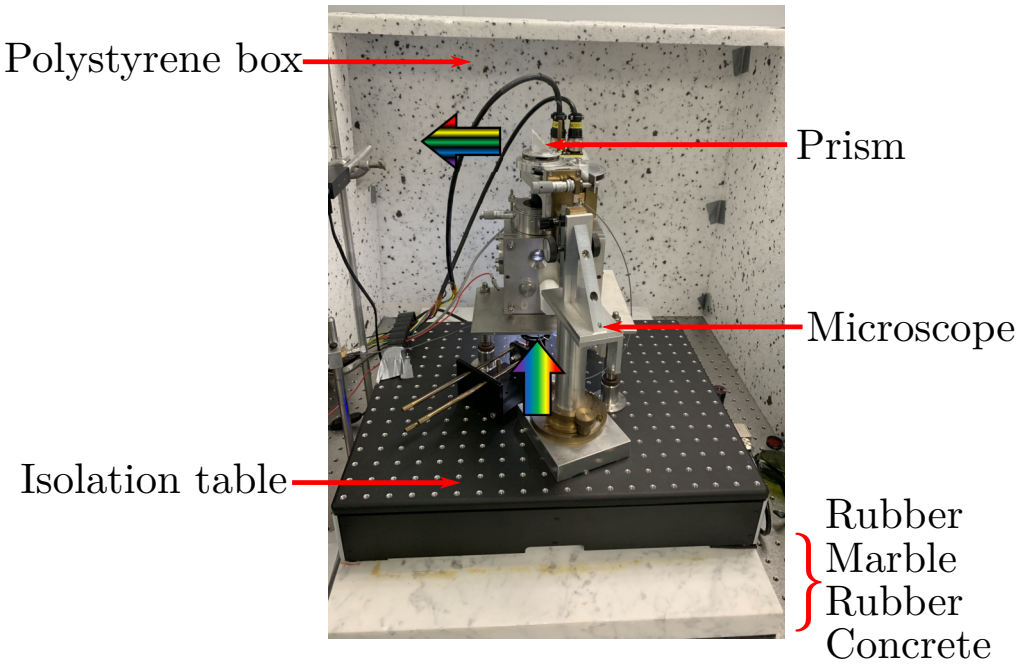


Figure 2.8 The SFB in the measurement room. The path of the light before entering the SFB and on leaving the prism is shown via the multicoloured arrows.

Concentrated Salt Solutions

Concentrated salt solutions were prepared on the day of use. Pure salts ($>$ 99.9%) were used as received. Ultrapure water (Sartorius, TOC $<$ 3 ppb, resistivity 18.2 MΩcm) was used to prepare all the solutions. A homogenous solution was produced by mixing the mixture with a vortexer, avoiding any unnecessary contamination from using a stirrer bar.

Deep Eutectic Solvents

Fresh deep eutectic solvents (DESs) were prepared the day before use. Anhydrous ethylene glycol (Acros, 99.8%), choline chloride (Sigma-Aldrich, $\geq$ 99%), glycerol (Sigma-Aldrich, anhydrous, $\geq$ 99.5%) were used as received.

Eutectic mixtures were prepared by mixing 1 molar equivalent choline chloride (ChCl) with 2 molar equivalents ethylene glycol (EG) or glycerol (Gly), respectively. The resulting mixture was stirred overnight at 60 ^{o}C under a nitrogen atmosphere and the homogenous liquid formed was subsequently stored under nitrogen until

required. 'Ambient' samples were generally produced by allowing the liquid to equilibrate with the humid lab air at room temperature and pressure for approximately 12 hours *in situ* in the SFB. The exact equilibration process is given in the relevant chapters. 1:2 ChCl:EG-water and 1:2 ChCl:Gly-water mixtures were prepared by adding ultrapure water (Millipore, TOC < 3 ppb, resistivity 18.2 MΩcm) at different weight percentages to the DES samples and stirring until a homogenous liquid was formed.

Off-eutectic ethaline samples (ChCl:EG molar ratios 1:3 and 1:10) were prepared at room temperature and pressure, and stirred overnight at 60 ^{o}C at atmospheric pressure.

2.2 SFB Measurements and Analysis

All analysis is carried out in MATLAB®, Python™ and/or `C++`.

2.2.1 Multiple Beam Interferometry

As the silvered mica surfaces are semi-transparent, the silver-mica-medium-mica-silver stack in the SFB forms an interferometric cavity (Figure 2.9). When white light is passed through the interferometer, only certain wavelengths will interfere constructively between the two mirrors and pass through the cavity to the spectrometer. The emerging wavelengths yield observable multiple beam interference fringes, known as fringes of equal chromatic order (FECO) that are curved as a result of the contact geometry. FECO can be used to determine the surface separation, D, the radius of curvature of the lenses, R, and the mica thickness. During an experiment, the fringes are recorded using a CCD camera and monitored using a LabVIEW™ interface.

Israelachvili[86] derived the following formula to determine the surface separa-

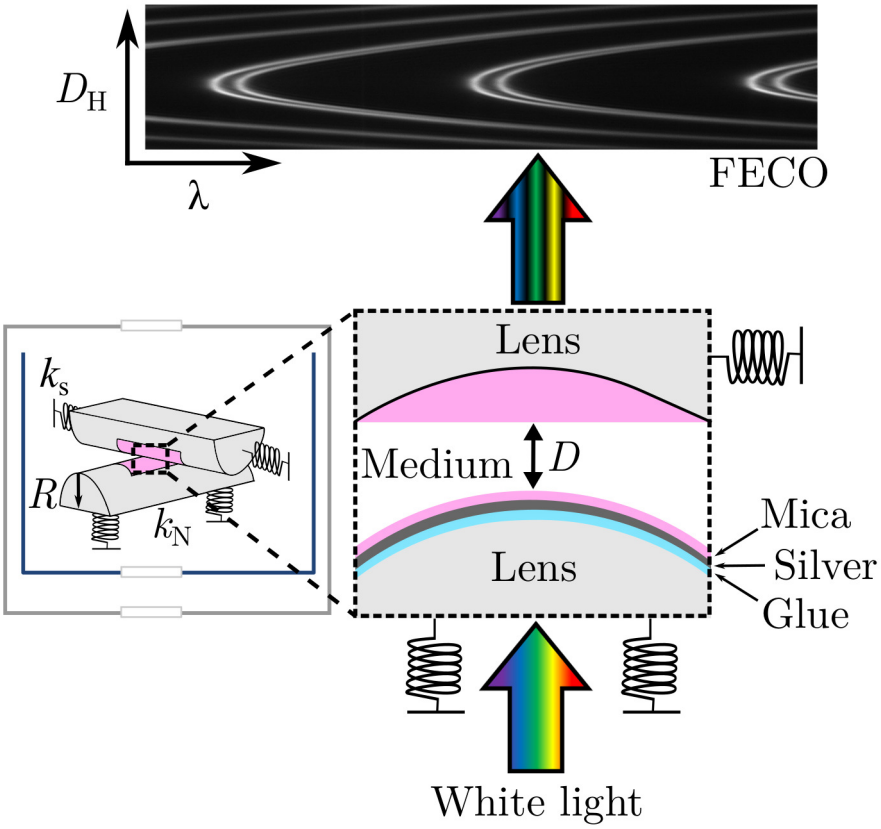


Figure 2.9 Schematic of the SFB. White light is passed through the bottom lens into the interferometric cavity. Wavelengths that constructively interfere pass through the top lens to the spectrometer and then the camera, yielding fringes of equal chromatic order (FECO). The FECO are used to determine surface separation, D and radius of curvature of the lenses, R, using the position of the fringes in wavelengths, λ, and the in-plane (horizontal) distance, D_H. Normal and shear springs with spring constants k_N and k_s are used to determine the normal and frictional forces, respectively.

tion, D, in a symmetrical three-layer interferometer,

$$\tan(k\mu_{\text{medium}}D) = \frac{2\bar{\mu}\sin\theta}{(1+\bar{\mu}^2)\cos\theta \pm (\bar{\mu}^2-1)}, \tag{2.1}$$

where $k = 2\pi/\lambda$, $\pm$ refers to the odd and even order fringes, respectively,

$$\bar{\mu} = \frac{\mu_{\text{mica}}}{\mu_{\text{medium}}}, \theta = \frac{n\pi\Delta\lambda_n}{\lambda'_n}, n = \frac{\lambda_{n-1}}{\lambda_{n-1}-\lambda_n},$$

μ_i is the refractive index of layer i, n is the fringe order, λ_n and λ_{n-1} are the wavelengths of the fringes n and $n-1$ at $D = 0$ nm, respectively. If $D \neq 0$ nm, the

wavelength of the n-fringe shifts to λ_n' by $\Delta\lambda_n = \lambda_n' - \lambda_n$. FECO can be divided into odd and even order fringes. Odd fringes do not depend on the refractive index of the medium, whereas even fringes do.[86] By tracking the shift in an odd fringe, D can be determined directly.

Surface separation is measured relative to mica-mica direct contact ($D = 0$ nm) as calibrated at the start of each experiment. The calibration is made by recording the wavelengths of two adjacent fringes *e.g.* p and $p-1$ with wavelengths λ_p and λ_{p-1} in Figure 2.10(a). When a medium sits between the lenses, as in Figure 2.10(b), the position of the p-fringe shifts to λ_p' by $\Delta\lambda_p = \lambda_p' - \lambda_p$. By tracking λ_p' as the lenses approach/retract, the surface separation can be determined.

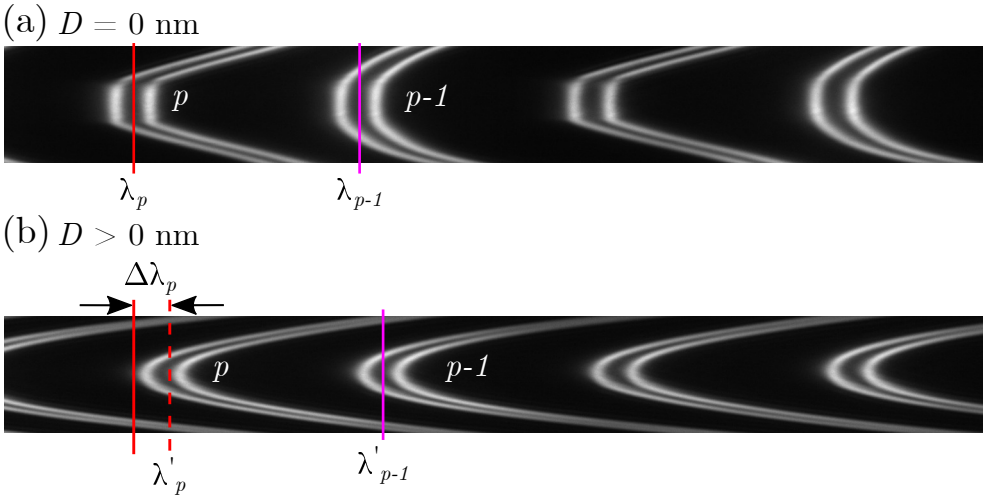


Figure 2.10 FECO fringe pattern example in (a) air and in (b) liquid. The fringes appear as doublets due to the birefringence of mica. The left-most odd fringe is termed the 'p-fringe'. In air, the flattening of the fringes indicates clean mica-mica contact. In liquid, the p-fringe is shifted by $\Delta\lambda_p$ relative to the p-fringe in air, with the shift corresponding to the surface separation.

Using multiple beam interferometry, the surface separation relative to the calibration can be measured with a precision of 0.1 nm, provided the fringes are of good enough quality. This will be determined by factors such as the light alignment, condition of the mica surface and the silver quality.[86]

2.2.2 Normal Forces

The bottom lens sits on a pair of parallel leaf springs, as in Figure 2.6, with spring constant, k_{N}. When the lenses are at infinite separation, no forces act between the lenses. The two surfaces are brought together using a three-stage mechanism (see Figures 2.5 and 2.7): the coarse motor positions the lenses within about 1 μm, the fine motor via a differential spring mechanism positions to 1 nm, and a piezoelectric tube (PZT) allows positioning to 0.1 nm. Generally, measurements are conducted with the fine motor or PZT. The fine motor allows for a larger range of linear motion, however can introduce mechanical vibrations, while the PZT minimises vibrations but has a smaller range of motion.

As the lenses approach one another at constant velocity, v, from a surface separation, D_0, (at time, $t = 0$ s) the surface separation changes by $\Delta x = vt$ during approach time, t. The imposed motion is linear and given by

$$D = D_0 - \Delta x = D_0 - vt. \tag{2.2}$$

This baseline is shown in Figure 2.11. Any interactions that occur between the surfaces will result in spring deflection, $\delta(t)$, that can be determined by measuring the difference between the observed $D(t)$ profile and the expected baseline (subtract the red plot from the black plot in Figure 2.11),

$$\delta(t) = D(t) - [D_0 - vt]. \tag{2.3}$$

The normal surface force, F_{N}, is then given by,

$$F_{\mathrm{N}}(t) = k_{\mathrm{N}}\delta(t) = k_{\mathrm{N}}[D(t) - D_0 + vt]. \tag{2.4}$$

An experimental surface separation versus time profile is shown in Fig-

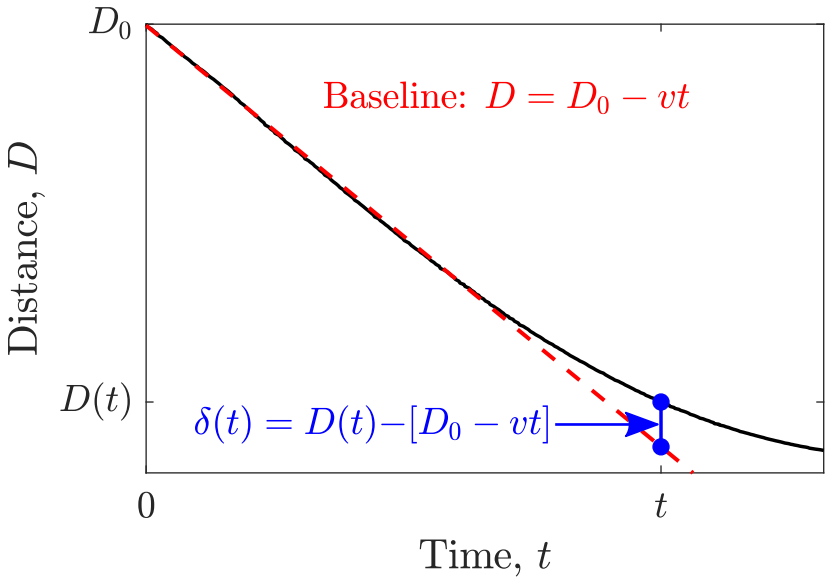


Figure 2.11 Distance, D, versus time, t, schematic. The black line shows the experimental $D(t)$ profile. When the lenses approach one another, the imposed motion is described by a linear baseline: $D = D_0 - vt$, that depends on the starting distance, D_0, approach velocity, v, and time. This baseline is shown in red. The deflection, $\delta(t)$, in blue is given by the difference between $D(t)$ and the linear baseline: $\delta(t) = D(t) - [D_0 - vt]$.

ure 2.12(a), for an ionic liquid. The linear approach is fitted when $D > 40$ nm (in red). Below approximately 20 nm, $D(t)$ deviates from the linear baseline indicating the presence of surface interactions. The normal force is then determined and plotted against surface separation yielding the normal force-surface separation profile in Figure 2.12(b). A more detailed description of the linear baseline fitting procedure is given in the following section.

If an oscillatory structural force is present, the force-distance profile will exhibit a series of repulsive steps during the approach, as in the inset in Figure 2.12(b). These steps occur because the normal springs introduce a mechanical instability into the system. A schematic force-distance profile is shown in Figure 2.13 to highlight this instability. As the surfaces approach one another (blue curve), the interaction (normal) force will be balanced by the restoring force of the spring so long as $\partial F_{\mathrm{N}}(D)/\partial D < k_{\mathrm{N}}$. If $\partial F_{\mathrm{N}}(D)/\partial D \geq k_{\mathrm{N}}$ (black dashed regions) the region is unstable and no forces can be measured, resulting in a

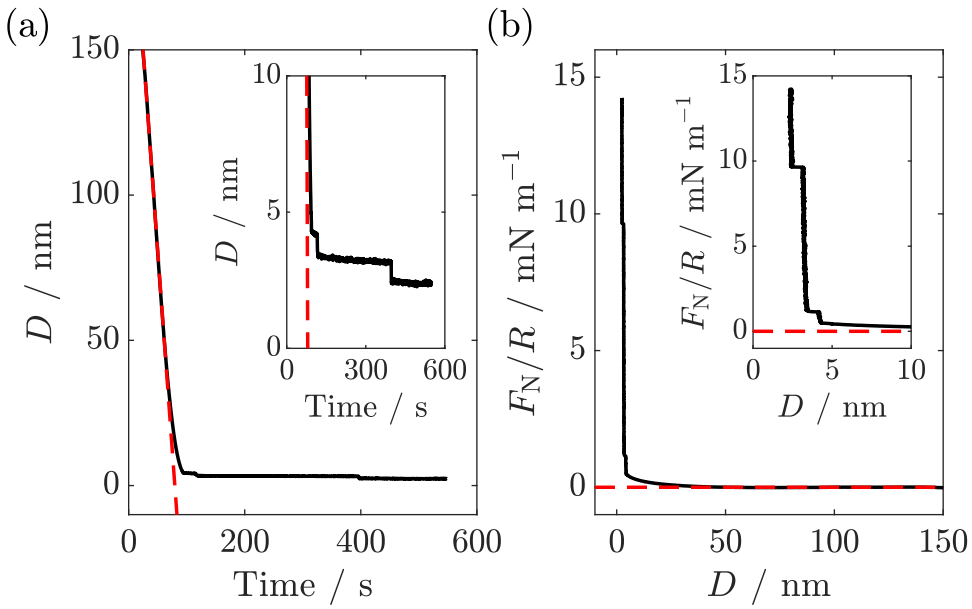


Figure 2.12 Exemplar (a) distance-time and (b) force-distance profiles for an ionic liquid. (a) Surface separation, D, versus time plot in black. When $D > 40$ nm the surface separation can be fitted linearly with time (red dashed line). A series of steps are observed when $D < 10$ nm, shown in the inset. The difference between the black and red plots in (a) gives the deflection needed to calculate the force, F_N. This is normalised by the radius of curvature of the lenses, R, and plotted as a function of D as in (b). The red dashed line in (b) shows the linear fit from (a) corresponds to $F_N = 0$ mN. The forces at $D < 10$ nm are shown in the inset.

'jump in' to a more stable region at smaller D. On retracting the surfaces (in pink), the surfaces will remain in the nearest adhesive minimum before 'jumping out' to large separations where $F_N/R = 0$. By approaching and retracting from different surface separations, different adhesive minima can be explored and the corresponding pull-off force can be obtained.[19,45]

Using the SFB, normal forces can be measured with a resolution of 10^{-7} N.[87]

2.2.3 Hydrodynamic Forces: A Note

The influence of hydrodynamic (or viscous) forces on the observed normal force profiles will be discussed throughout this work, namely in Chapters 4 and 8. Chapter 8 will discuss the work by Lhermerout and Perkin[88] in detail, however it is important to briefly introduce the concept of comparison factors.

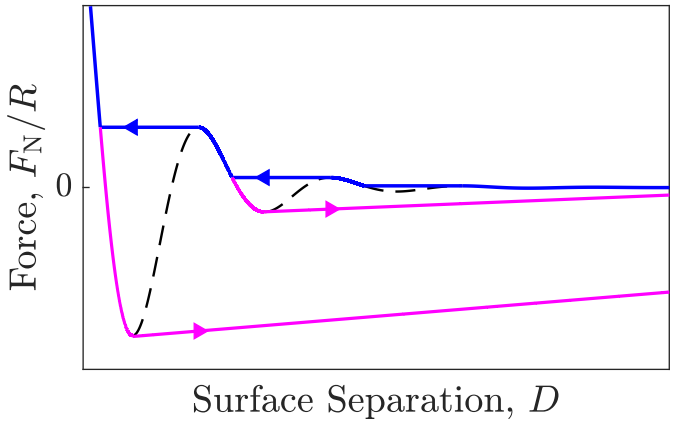


Figure 2.13 Schematic force-distance profile showing the Euler spring instability. On the approach (blue curve), the surfaces 'jump in' when they reach an unstable region (black dashed lines), at the point where $\partial F_N(D)/\partial D \geq k_N$. These jump-in points are shown by the blue left-facing arrowheads. When the surfaces are separated (pink curve) they will remain in the nearest adhesive minimum before 'jumping out' to large separations (pink right-facing arrowheads). Only one adhesive minimum can be measured during a retraction, so a series of approaches and retractions are required to explore all adhesive minima.

Three velocity regimes were studied in the work of Lhermerout and Perkin:[88]

- High - hydrodynamic forces dominate,
- Intermediate - combination of hydrodynamic and electrostatic forces,
- Low - electrostatic forces dominate.

These regimes can be compared with other systems. By using the velocity, v, radius of curvature (R = 0.885 cm), and viscosity (η = 37 mPa s at 25 ^{o}C) values from Lhermerout and Perkin,[88] a regime comparison factor, C_{reg}, can be calculated that is proportional to the hydrodynamic force, F_{hydro},

$$C_{reg} = \eta v R^2 \propto F_{hydro}. \tag{2.5}$$

Using the values in Table 2.1, a velocity for each regime can be estimated for

any system,

$$v = \frac{C_{\text{reg}}}{\eta R^2}, \tag{2.6}$$

so long as the viscosity and radius of curvature are known.

Table 2.1 Comparison factors for high, low and intermediate velocity regimes for C_2C_1Im TFSI ($\eta = 37$ mPa s at 25 ^{o}C) and $R = 0.885$ cm.

Regime	Velocity / nm s^{-1}	$C_{\text{reg}} \times 10^6$ / Pa nm m^2
High	95	275
Intermediate	1.1	3.27
Low	0.24	0.696

2.2.4 Screening Lengths

Normal force profiles can be plotted on a logarithmic-linear scale to observe how the long-range forces decay with surface separation, as per Figure 2.14. If the forces decay linearly on this scale (exponentially on a linear-linear scale), we can obtain a decay length, λ_{exp}, from the inverse of the absolute gradient of the linear region.

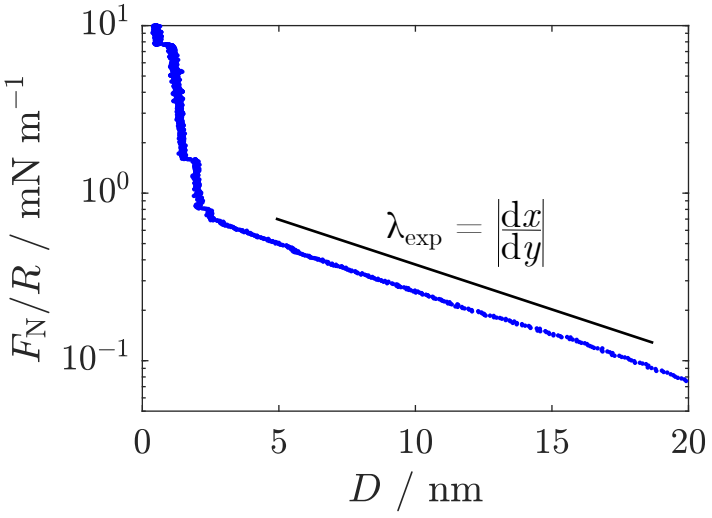


Figure 2.14 Log-linear representation of the normal force, F_N, normalised by the radius of curvature, R, as a function of surface separation, D, profile across dry ethylene glycol. The solid black line indicates the gradient of the long-range exponential decay where the experimental decay length, $\lambda_{\text{exp}} = |dx/dy|$.

The experimental decay length should not be influenced by the fitted approach

baseline discussed in Section 2.2.2. Typically, approach baselines are fitted manually using the distance-time plot and by looking for the region where the approach is most linear. Using this method means the distance range over which the baseline is fitted can change for each force profile (flexible baseline). Another method involves fitting between a set range of distance values *e.g.* 60 to 100 nm, for all force profiles (fixed baseline). However, this can result in erroneous baselines if the set range is particularly non-linear. Figure 2.15 shows the influence on λ_{exp} when fitting with flexible and fixed baselines. It is apparent from this plot that the use of a fixed baseline will produce more precise values.

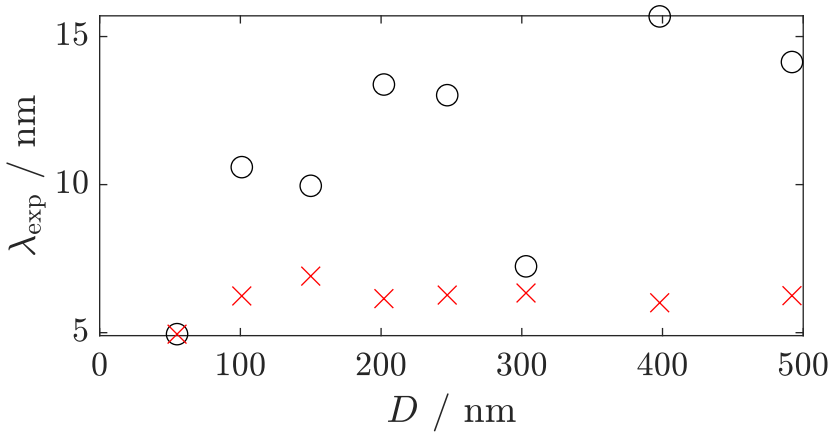


Figure 2.15 Experimental decay length, λ_{exp}, as a function of start distance for the ionic liquid 1-butyl-1-methylpyrrolidinium bis(trifluoromethylsulfonyl)imide ($R \approx 1$ cm) using a flexible baseline (black open circles) and a fixed baseline between 27 and 45 nm (red crosses).

When using a fixed baseline, a procedure is required for choosing the upper and lower surface separations. If the same or a similar system has been studied previously, a decay length could be estimated and the lower limit set as $3\lambda_{exp}$. This is a reasonable assumption as the force decays exponentially, therefore at $3\lambda_{exp}$ the force would have reduced by 95% and can be treated as negligible. For an unknown system, the process could be done iteratively whereby a flexible baseline is fitted and yields a decay length, and then the baseline bounds can be altered as necessary. The upper limit is determined predominantly by the linearity. If the fitting region is too wide, any approach non-linearity will contribute and

skew the fit. However, if the fitting region is too small, the baseline will not be representative of the actual approach.

The quality of approach linearity will also vary with the starting surface separation. Typically, screening lengths are acquired using the PZT as slower approach velocities can be used and vibrations are minimised. At larger separations a larger voltage range is needed to reach zero surface separation. The PZT that controls this motion imposes a non-linear approach over its full voltage range. Therefore, by starting at larger distances, it is more likely that some deviation from linearity, due to the PZT, will be observed. At smaller surface separations the risk of PZT non-linearity influencing the approach baseline is reduced. However, the system must have enough time to reach a constant approach velocity before forces cause deflections from the imposed motion.

Fitting Procedure

This method can be implemented as follows. When analysing a data set, firstly process all of the runs and produce all distance-time plots. Beginning with the slowest and closest start distance plot, determine λ_{exp} (literature or iterative method) and set $\approx 3\lambda_{\text{exp}}$ as the lower limit. Determine the region over which the approach is linear, starting from the lower limit, and set the upper limit to the maximum distance where this is possible. By basing this window on the slowest and closest profile, there will be no need to alter the fitting window. Once the window is fixed, all of the other approach baselines can be altered to fit over the specified window. Once all of the force profiles have been produced relative to the fixed baseline, λ_{exp} can be fitted. After fitting each approach, the quality of the baseline should be determined by the user. If the fitted baseline is not representative of the experimental approach *i.e.* the experimental approach is very wobbly and does not fit a straight line, the run should not be considered when determining the average λ_{exp}.

2.2.5 Shear Forces

The top lens is mounted on the PZT in the top part as in Figure 2.5. The sectored PZT is used for both normal and lateral motion. By applying the same ramp voltage to the outer sectors and an equal but opposite ramp voltage to the inner sector the PZT expands/contracts normally. Lateral motion is achieved by applying equal and opposite potentials to two opposing outer sectors so that one contracts whilst the other expands. However, this corresponds to a 'swaying' motion so an additional voltage is applied to the inner sector to correct the motion.

Shear forces can be measured using two approaches. The first involves repeatedly moving the motor by a fixed number of steps, then applying a lateral motion when the surface separation is constant. Alternatively, both lateral and normal motion can be applied simultaneously using the PZT. Provided the normal approach velocity is much smaller than the shearing velocity, the surface separation can be assumed constant during one shearing cycle.[89]

Vertical leaf springs with spring constant, k_s, deform if any shear forces are present between the two surfaces. The deformation is detected by measuring the change in capacitance across an air capacitor formed between the fixed capacitance probe and the flag, which is outputted as a voltage.

PZT Friction Processing

When the PZT has been used to apply both normal and lateral motion, the voltage of two PZT sectors are recorded as well as the change in capacitance signal. One sector should correspond to the normal motion of the PZT and the other a convolution of the imposed shearing motion (lateral) and the normal motion.

To produce a shear force-time profile a number of steps are required to correct the capacitance signal, V_{sig}. Firstly, the normal motion must be removed from the

convoluted voltage signal. In Figure 2.16(a), the voltage, V, is plotted with time, t, for sectors A (normal motion) and B (convoluted) of the PZT. By removing V_{A} from V_{B}, the normal motion is removed leaving only the applied shearing voltage as in Figure 2.16(b). When the lenses are out of contact the applied shearing voltage will influence V_{sig} so this contribution must also be removed. Figure 2.16(c) highlights this contribution as V_{sig} has a triangular-like shape due to the imposed triangular wave (see the shearing voltage in Figure 2.16(b)). The shearing motion is started before the normal motion and from the first shearing cycle out of contact, the imposed shearing motion can be fitted and removed. This will produce a corrected signal, V_{corr}, which is solely due to the liquid in confinement (Figure 2.16(d)). The corrected signal is then shifted and centred around 0 V using the peak (y_1) and trough (y_2) voltages in Figure 2.16(d) yielding the shifted signal, V_{shift}, in Figure 2.16(e). Finally, V_{shift} is multiplied by k_{s} and a conversion factor due to the capacitance amplifier, K_{cap}, to give the lateral force, F_{L}, as a function of time, in Figure 2.16(f).

The kinetic friction or shear force, F_{S}, is obtained by taking the mean value of the absolute lateral force across the individual maxima. By plotting these forces as a function of the normal force, the influence of increasing load on the frictional behaviour of the confined liquid can be observed, and a friction coefficient determined by taking the gradient of each linear regime (Figure 2.17). It should be noted that small changes in composition, mica alignment, temperature and contact geometry can influence the calculated friction coefficients by up to a factor of 2.[1]

Motor Friction Processing

The same set of steps (as in Section 2.2.5) are required when the motor imposes the normal motion except from the need to deconvolute the normal and lateral motion of the PZT as it is only providing lateral motion.

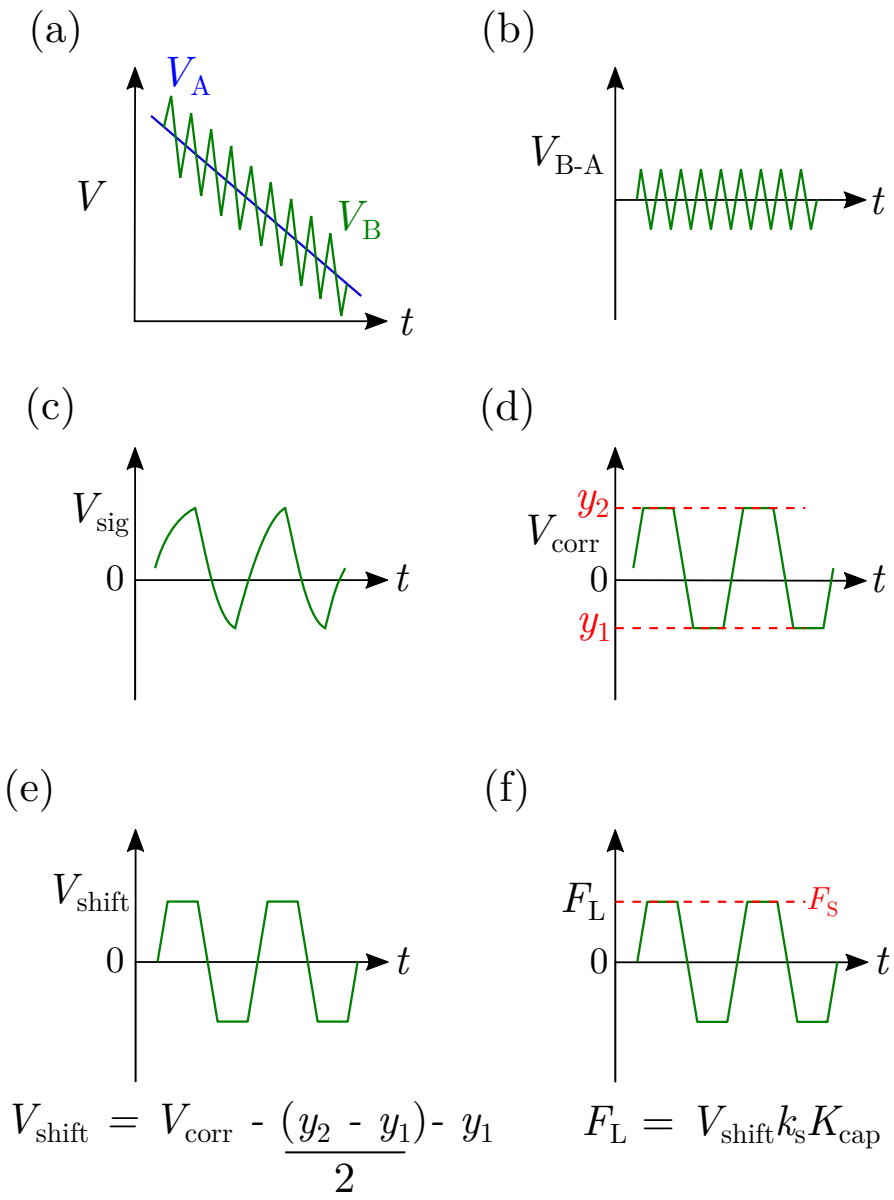


Figure 2.16 (a)-(e) Steps in determining the lateral force-time profile in (f). Voltage-time plots for (a) sectors A (V_A) and B (V_B) of the PZT, (b) applied shearing voltage (V_{B-A}) by removing A from B, (c) raw capacitance signal (V_{sig}), (d) corrected signal (V_{corr}), and (e) shifted signal (V_{shift}) and its calculation. The calculation for determining the lateral force, F_L, from V_{shift}, the spring constant, k_s, and the capacitance amplifier conversion factor, K_{cap}, is given in (f) alongside the resulting lateral force-time profile. The shear force, F_S, is given by the maxima in $|F_L|$.

2.3 Refractive Indices

Although refractive indices are well documented, values for some systems studied in this thesis were not readily available *e.g.* concentrated salt solutions. As the refractive index is necessary for analysing the FECO, an Abbe refractometer

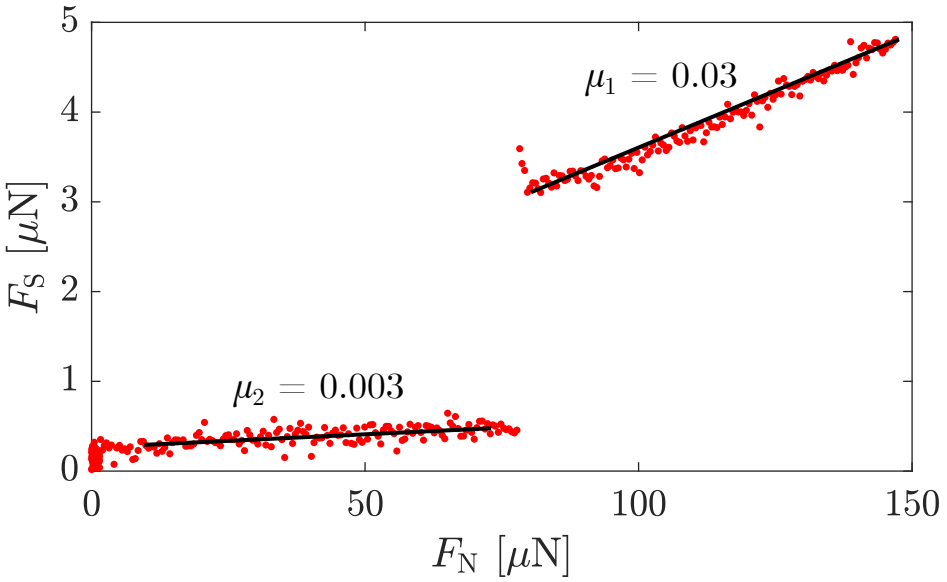


Figure 2.17 Exemplar shear force, F_S, versus normal force, F_N profile (red). Two individual linear regimes (black lines) are observed across the confined film. From the gradient of each regime the corresponding friction coefficient, μ_i, can be determined. Index labels, i, correspond to different observable layers in the normal force-distance profile with lower indexes corresponding to the more confined layers *i.e.* when the surface separation is smaller. At lower normal force, $F_N < 80\ \mu N$, the friction coefficient, $\mu_2 = 0.003$. Whereas, at $F_N > 80\ \mu N$ the coefficient of friction, $\mu_1 = 0.03$. It should be noted that small changes in composition, mica alignment, temperature and contact geometry can influence the calculated friction coefficients by up to a factor of 2.[1]

(Bellingham and Stanley) was used to determine the refractive indices of such systems. A schematic is shown in Figure 2.18.

To measure the refractive index of a liquid sample, a drop of liquid is sandwiched between an illuminating prism and a measurement prism (Abbe double prism). Light from a sodium lamp is passed through the sample-containing double prism. The emerging light then passes through a series of compensating prisms before reaching the eyepiece lens. A control knob allows the user to adjust the position of the measurement prism to locate the light-dark boundary and align it with the microscope crosshairs in the field view. Once this boundary has been aligned, a second eyepiece is used to fine tune the Abbe scale reading using an integral scale and a micrometer drum. The Abbe scale reading, micrometer position and temperature are recorded, and converted into the refractive index

using the Abbe Utility software. Measurements are repeated 10 times to improve the final accuracy.

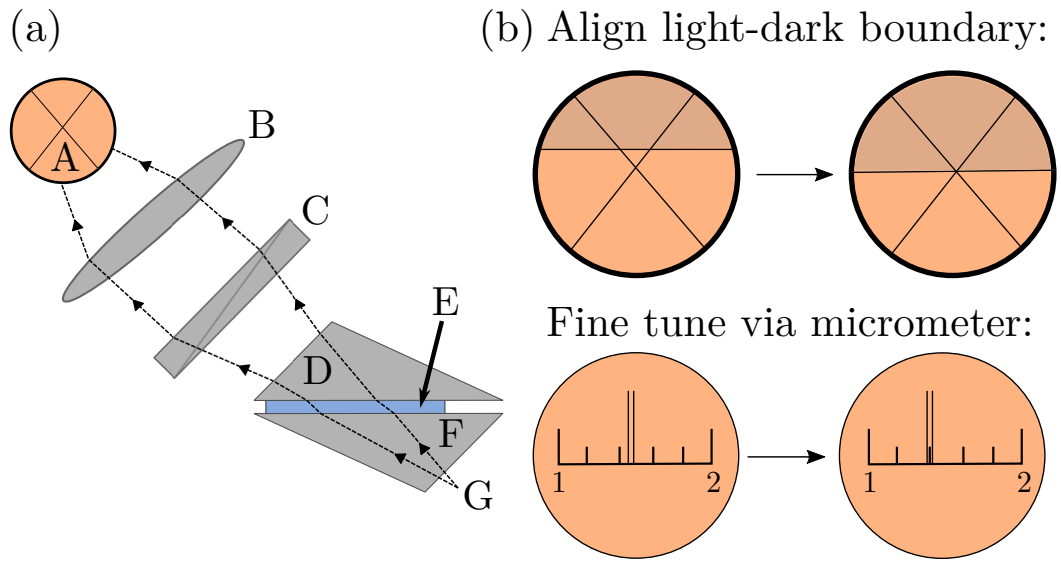


Figure 2.18 Refractometer schematic (a) highlighting the path of the light through the equipment (black dashed lines). Labels correspond to A - field view, B - lens, C - compensating prisms, D - measurement prism, E - sample, F - illuminating prism, G - sodium lamp. (b) Alignment of the light-dark boundary with the microscope crosshairs in the field view (upper), and fine tuning the scale reading via a second eyepiece (lower).

2.4 Differential Scanning Calorimetry

Differential scanning calorimetry (DSC) has been used to study the thermal transitions of a number of bulk fluids. In this section the theory of the technique is outlined and the experimental procedure discussed.

2.4.1 DSC Principles

DSC is a thermal analysis technique that measures the difference in heat flow between sample and reference pans as a function of time and temperature. The reference and sample pans are placed on their respective platforms within the furnace, as per Figure 2.19(a). Typically, the temperature of the furnace is linearly increased or decreased with time. During the temperature ramp, the sample and reference pan temperatures are kept identical. As the reference and sample pans

are identical, if the heat capacity of the sample changes during the ramp, the heat flow to/from the reference pan will need to compensate for the changes to keep the temperatures matched.[90] Therefore, the difference in heat flow between the sample and reference pans will indicate if any thermal transitions have occurred in the sample.

The resulting change in heat flow can be plotted as a function of temperature (a thermogram, see Figure 2.19(b)) to determine the nature of the transition. Thermal transitions will appear as features on the thermogram *e.g.* steps, peaks or troughs. They can be attributed to chemical or physical changes in the sample and are either endothermic (heat absorbed by the sample) or exothermic (heat released by the sample). Endothermic transitions include melting, glass transitions and evaporation, exothermic transitions include crystallisation, curing and oxidation.

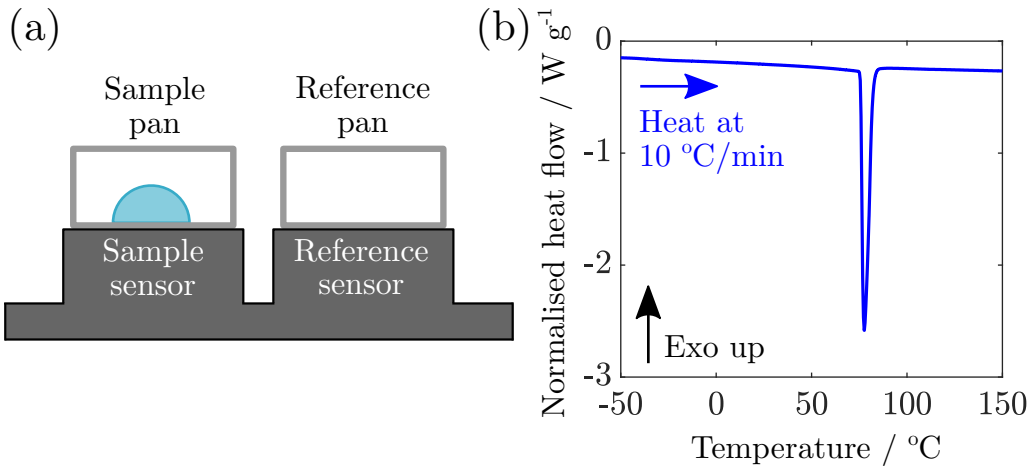


Figure 2.19 (a) Schematic of the sample and reference platforms in the DSC furnace. (b) Exemplar normalised heat flow as a function of temperature plot (thermogram) when heating the sample at 10 °C/min, showing an endothermic transition.

Crystallisation and melting are of particular interest in this work, and the temperature at which these two transitions occur are determined in different ways. Figure 2.20(a) shows an exemplar melting transition on heating the sample. The melt begins at the onset temperature (orange open circle) and is complete at the peak of the transition (pink open circle). As the onset temperature defines the

point at which the material begins to melt, this is taken as the melting point. To determine the onset temperature, the baseline of the thermogram is extrapolated (orange dashed line) and the inflectional tangent of the melting peak taken (orange solid line). The point at which these two lines intersect is taken as the onset temperature.

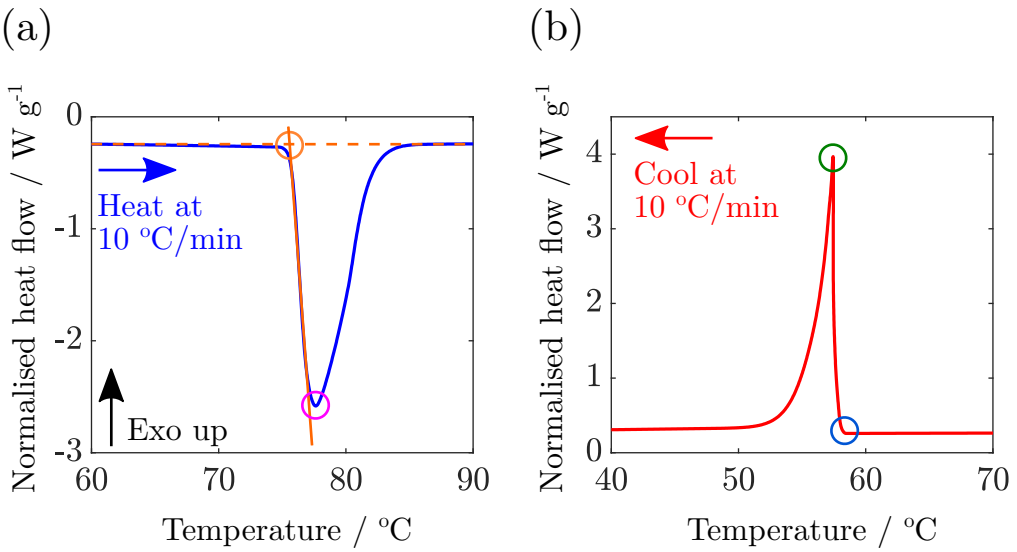


Figure 2.20 Exemplar normalised heat flow as a function of temperature plots (thermograms) when (a) heating and (b) cooling the sample at 10 °C/min. The exothermic direction is the same in both plots. (a) An endothermic melting transition. The onset temperature (orange open circle) occurs at the point at which inflectional tangent of the melting peak (orange solid line) intersects the extrapolated baseline (orange dashed line). The peak temperature corresponds to the fully melted material (pink open circle). (b) An exothermic crystallisation transition. The nucleation temperature occurs at the blue open circle, at which point crystal growth begins and is completed at the peak (green open circle).

Figure 2.20(b) shows an exemplar crystallisation on cooling the sample. As crystallisation is a two-step process involving nucleation and subsequent crystal growth, there are two noticeable features on the thermogram. The open blue circle highlights the temperature at which nucleation occurs. Crystallisation then begins and is complete at the peak temperature highlighted by the open green circle. As the peak temperature defines the point at which the material has fully crystallised, this is taken as the crystallisation point.

2.4.2 Sample Preparation

Individual Components

Ethylene glycol (Sigma-Aldrich, anhydrous, 99.8%) and choline chloride (Sigma-Aldrich, $\geq$ 99%) were used as received. Ethylene glycol was also used directly from the bottle 9 days after the septum was first pierced, and another sample was allowed to equilibrate at room temperature and humidity for at least 24 hours.

Deep Eutectic Solvents

Deep eutectic solvents were prepared at room temperature and pressure. Ethylene glycol (Sigma-Aldrich, anhydrous, 99.8%), choline chloride (Sigma-Aldrich, $\geq$ 99%), glycerol (ITW Reagents, 99.5%), urea (Alfa Aesar, 99%) were used as received.

The following systems were prepared by mixing molar ratios of ChCl, EG, Gly, and/or urea:

- Ternary DESs: 1:1:1 ChCl:EG:Gly and 1:1:1 ChCl:EG:Urea;
- Gly-based DESs: 1:2 ChCl:Gly;
- EG-based DESs: 1:1, 1:2, 1:3, 1:4, 1:5, 1:10, 1:99, 1:999 ChCl:EG.

The resulting mixture was stirred overnight at 60 ^{o}C and subsequently stored at room temperature and pressure until required.

Once the desired sample has been prepared, the pan and lid type are chosen. All samples used a Tzero aluminium pan with a Tzero lid, for solid samples, or Tzero Hermetic lid, for liquid samples (TA Intruments). Between 1 and 20 mg of sample is placed in the pan. A pin hole is made in the lid (to allow volatiles to escape), placed on the pan and crimped using the Tzero press (TA Instruments).

An identical pan and lid are used to produce a reference in the absence of sample.

2.4.3 Experimental Setup

The reference and sample pans are placed in the cell of the DSC250 (TA Instruments), which is purged under nitrogen at a rate of 50 mL/min. By coupling the DSC to the RCS90 cooling accessory (TA Instruments) the cell can be cooled below room temperature to -90 ^{o}C and heated to a maximum of 550 ^{o}C.

Using the TRIOS software (TA Instruments), the experimental method can be designed and subsequently run using the desktop interface. The full method comprises individual segments that control the furnace temperature. For example, a ramp segment will heat or cool the furnace from the current temperature to a set temperature at a desired rate, whereas an isothermal segment will hold the furnace at the current temperature for a set period of time. The method can therefore be tailored according to the system being studied.

There are a few considerations that are made when constructing a method:

1. Thermal History: Although samples may have been prepared in a similar manner, the thermal history of the samples may not necessarily be the same. To compare samples, it is best if the first few segments form a cycle (heat-cool or cool-heat) between the minimum and maximum temperatures of the range to be studied at 10 ^{o}C/min. This allows us to know the exact thermal history of the sample by 'resetting' it. The subsequent cycles, either in the same or different samples, can then be compared more reliably.

2. Maximum Temperature: It is preferable to avoid boiling or decomposing the sample unless it is the final segment of the method. If the sample begins to decompose, the subsequent thermograms will not necessarily be indicative of the original sample but instead will have peaks due to products of the

decomposition. Similarly, if the sample is a mixture that includes water, any water evaporation will change the composition of the mixture resulting in a different thermogram.

3. Heating and Cooling Rates: Thermal transitions can either be kinetic or thermodynamic in origin. Kinetic transitions, like crystallisation, will depend on the rate of cooling. If we cool quickly, a liquid sample may be frustrated in an amorphous-like state and crystallisation may not be observed. On the other hand, cooling at a slower rate will increase the probability of the sample crystallising. The rate of heating and cooling also influences the sensitivity and resolution of the thermal transitions - a faster rate improves sensitivity but reduces resolution, and vice versa.

The full methods are detailed in Chapter 7.

Chapter 3

Control Systems: Ethylene Glycol

Ethylene glycol, pictured in Figure 3.1(a), is a polar solvent with a number of useful applications. For example, ethylene glycol can be used to generate hydrogen-rich fuel gases through aqueous-phase and steam reforming.[91] It can also be used in large-scale nanomaterial synthesis and is commonly found in antifreeze.[91] Of particular interest are applications of ethylene glycol under confinement or near surfaces. Action of ethylene glycol in fuels cells occurs at the surfaces,[92] while it is also found as a lubricant in glass and cement grinding.[91] The polymerised form of EG is called polyethylene glycol (PEG), shown in Figure 3.1(b), and is a common material in many technologies. In COVID-19 mRNA vaccines, lipid nanoparticles need to pass through confined environments to reach biological targets within the body. The nanoparticles are coated in PEG chains which help reduce nanoparticle aggregation.[10,93] This is an example of the very common use of PEG chains as coatings for liposomes and other drug nanoparticles. PEG is also ubiquitous in household and cleaning products as a safe and cheap method to tune liquid properties. When the polymer chain length is reduced to n = 1, a single ethylene glycol unit is recovered.

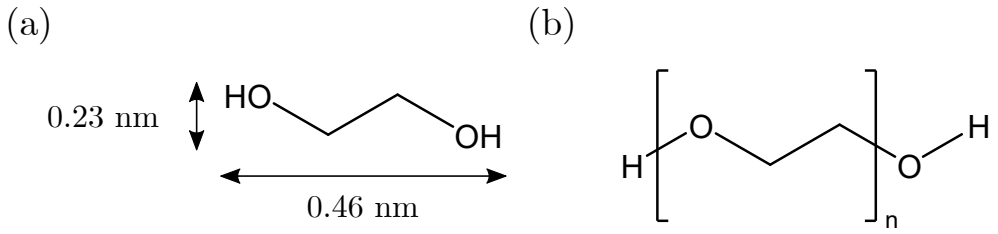


Figure 3.1 (a) Molecular structure and approximate dimensions of ethylene glycol.[65] (b) Polyethylene glycol repeat unit where n is the number of repeating units in the chain. If n = 1, we recover a single ethylene glycol unit.

Previous measurements across confined films of ethylene glycol have been conducted with the surface force balance[48] and atomic force microscopy (AFM).[65] Christenson and Horn[48] observed a short-range oscillatory force with a periodicity of 0.5 nm and a strong double-layer repulsive force at long-range, with a Debye length, $\lambda_D = 40$ nm. They also noted the difficulty in reaching separations < 2 nm due to the high viscosity.[48] 30 years later, Chen *et al.*[65] studied ethylene glycol at a graphite electrode interface with no applied potential using AFM, and observed layers of 0.45 nm. They also observed a thinner innermost layer of 0.2 nm which they attributed to a different orientation of ethylene glycol at the surface.[65] The frictional response of ethylene glycol has been studied with a tribometer yielding friction coefficients between 0.03-0.25, that depend on the surface material and rotation speed.[94] Superlubricity was also observed on addition of sulfuric, hydrochloric, oxalic, and aminosulfonic acids to ethylene glycol in the work of Li *et al.*[94]

With molecular solvents, it is useful to consider their properties in terms of their likeness to two well-established solvents: water and oils. As previously mentioned, ethylene glycol is a polar solvent with a dielectric constant, $\epsilon_r = 41$.[95] It also has two hydroxyl groups present allowing ethylene glycol to form a hydrogen bond network. With regards to these properties, ethylene glycol is more akin to water. One difference is the high viscosity of ethylene glycol, $\eta = 19$ cP (21-22 ^{o}C),[48] which is ≈ 20 times greater than the value of water, hence a more

oil-like property. The density of hydrogen bonds is also lower than in water, and the presence of an ethyl chain in ethylene glycol gives the molecule a degree of conformational freedom.

In this chapter, we investigate the properties of dry and ambient ethylene glycol under confinement. The 'dry' ethylene glycol corresponds to a pure anhydrous sample studied with a phosphorus pentoxide desiccant in the air-tight SFB. Once the dry measurements are complete, the sample is allowed to equilibrate at atmospheric humidity, *in situ* in the SFB, for more than 12 hours, and is termed 'ambient' ethylene glycol. It is assumed that the 'ambient' ethylene glycol has a higher water content. We will consider both normal and lateral forces across the nanofilms. Finally, we will consider whether ethylene glycol behaves more like water or oil under confinement, and any influence of water on the observed properties.

3.1 Normal Forces

Normal force profiles for ethylene glycol under dry and ambient conditions are shown in Figure 3.2. In both instances, the short- and long-range forces appear similar. As discussed in Section 2.2.3, viscous forces can influence the observed normal force profiles. To avoid viscous forces dominating the observed normal force, all reported runs were acquired at velocities, $v < 2$ nm s^{-1}, which has been calculated to give a negligible viscous force for this liquid.

3.1.1 Structural Forces across Confined Ethylene Glycol

Within 5 nm of the closest approach, an oscillatory force is observed. In Figures 3.2(a) and (b), the series of repulsive hard walls followed by a 'jump-in' point to smaller surface separation (due to the spring instability when $\partial F_{\mathrm{N}}(D)/\partial D \geq k_{\mathrm{N}}$) are indicative of a layered structure between the surfaces. The separation be-

tween the hard walls in both dry and ambient ethylene glycol are comparable, 0.38 ± 0.09 nm and 0.39 ± 0.06 nm, respectively, and correspond to the long dimension of an ethylene glycol molecule (Figure 3.1(a)), corroborating with literature measurements.[48,65]

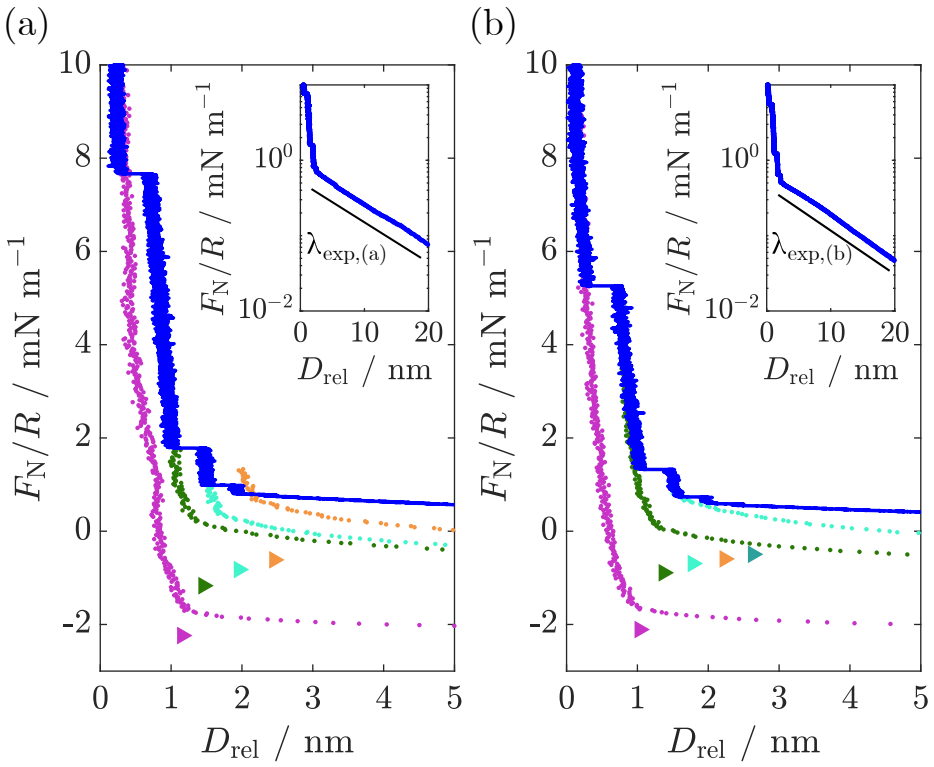


Figure 3.2 Representative normal force, F_N, normalised by the radius of curvature, R, as a function of surface separation relative to the closest approach, D_{rel}, profiles in (a) dry and (b) ambient ethylene glycol. The profile on approach is shown in dark blue. Retractions from each observed layer allow the adhesive minima to be explored. From near-surface layers to the outermost, retractions are shown in the following order: pink, green, cyan, orange, blue-grey. The corresponding minimum adhesive force and jump out position for each layer are indicated by triangular points. In both instances the inset shows a log-linear representation of the normal force on approach. The solid black line indicates the gradient of the long-range exponential decay where $\lambda_{exp,(a)} = 7.9 \pm 0.3$ nm and $\lambda_{exp,(b)} = 7.8 \pm 0.3$ nm.

The magnitude of F_N/R at the jump-in points in dry and ambient ethylene glycol are comparable, with a slight reduction in the magnitude for the ambient sample. As ethylene glycol is hygroscopic, we can attribute this reduction to adsorbed water disrupting and weakening the layered structure when compared to dry ethylene glycol.

While the force profiles in Figure 3.2 show typical behaviour in the ambient samples, we also observed an unusual systematic time-dependent effect whereby the closest separation reached changed with time. This is represented in Figure 3.3. During the course of the measurement across ambient ethylene glycol, the pressure required to reach each layer decreases and as a result deeper layers can be accessed. In the following, we consider possible explanations for this shift.

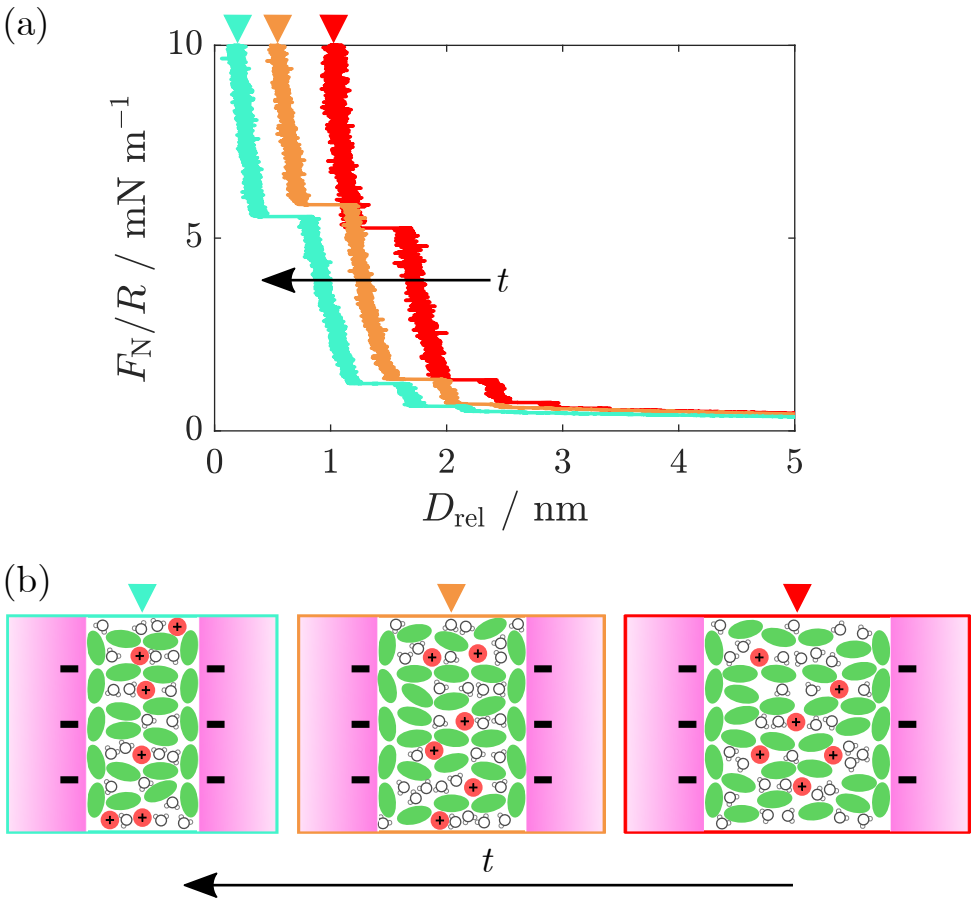


Figure 3.3 (a) Representative normal force, F_N, normalised by the radius of curvature, R, as a function of surface separation relative to the closest approach, D_{rel}, profiles in ambient ethylene glycol as a function of time, t, *i.e.* the distance values for all runs are plotted relative to the position of the innermost layer observed in the final run. The inverted triangles indicate the successive innermost hard walls and the corresponding confined structure schematics are hypothesised in (b). The negatively charged mica surfaces are shown in pink, ethylene glycol molecules in green, water molecules in white and grey, and cations in red.

Water weakens the equilibrium structure allowing deeper layers to be accessed. Over the course of the measurement, the ethylene glycol adsorbs

water. The water acts to disrupt and weaken the EG structure and as a result, a reduced force is required to access deeper layers. This hypothesis could be studied by changing the point at which the interfacial forces are measured. If the whole EG film has been influenced, the distances of closest approach on two different points would be comparable, and the hypothesis would be supported.

Water influences the equilibration dynamics. The liquid film is mechanically compressed and decompressed during the measurement. During the time between compression runs, the system does not equilibrate fully. On subsequent runs, the same layers are accessed at a weaker force and deeper layers can be explored. This implies that the shift in position is imposed and may vary with the time between successive runs.

Even though we observe a shift in the layer positions, dry and ambient ethylene glycol nanofilms remain in the confined region even under high load, corroborating with the non-zero surface separation observed by Christenson and Horn.[48]

3.1.2 DLVO Forces

The insets of Figures 3.2(a) and (b) show the long-range normal force decaying exponentially with surface separation according to $F_N/R \propto \exp(-D_{rel}/\lambda_{exp})$, where λ_{exp} is the experimentally observed decay length. In dry and ambient ethylene glycol, $\lambda_{exp,(a)} = 7.9 \pm 0.3$ nm and $\lambda_{exp,(b)} = 7.8 \pm 0.3$ nm, respectively, indicating minimal influence of humidity on the observed decay length. From Debye-Hückel theory (see Section 1.4), the observed decay length corresponds to a monovalent ion concentration of 0.8 mM. Ions present in the confined region are likely due to the dissolution of potassium ions from the mica surface,[20] impurities in the EG sample, or other dissolved ions from the environment or cleaning procedures. It could be suggested that excess protons from the dissociation of

ethylene glycol contribute to the ionic strength in the confined region, however at room temperature the $pK_a = 15.1$[95] so we expect minimal dissociation.

Using the experimentally observed decay length and an estimated Hamaker constant, A_H, the DLVO force (introduced in Chapter 1) can be fitted as shown in Figure 3.4. The van der Waals contribution,

$$F_{vdW} = -\frac{A_H R}{6D^2}, \tag{3.1}$$

where R is the radius of curvature and D is the surface separation. As the dielectric constant of ethylene glycol is roughly half that of water, the mica-water-mica Hamaker constant, $A_H = 2.2 \times 10^{-20}$ J,[3] is halved to estimate the mica-ethylene glycol-mica Hamaker constant, $A_H = 1.1 \times 10^{-20}$ J.

The electric double-layer (EDL) contribution,

$$F_{elec} = \frac{RZ}{\lambda_D} \exp\left(\frac{-D}{\lambda_D}\right), \tag{3.2}$$

where,

$$Z = 64\pi\epsilon_r\epsilon_0\left(\frac{kT}{ze}\right)^2 \tanh^2\left(\frac{ze\psi_0}{4kT}\right), \tag{3.3}$$

λ_D is the Debye length (here, $\lambda_D = \lambda_{exp}$), ϵ_0 is the vacuum permittivity, k is Boltzmann's constant, T is the temperature, z is the electrolyte valency, e is the elementary charge, and ψ_0 is the surface potential. As ethylene glycol is a neutral molecule, we assume $z = 1$ due to the dissolution of potassium ions from the mica surface. From fitting the EDL force we yield a surface potential, $\psi_0 = 42 \pm 1$ mV.

From Figure 3.4 it is clear that the DLVO force in dry and ambient ethylene glycol is dominated by the EDL contribution at $D_{rel} > 5$ nm, with minimal F_{vdW}.

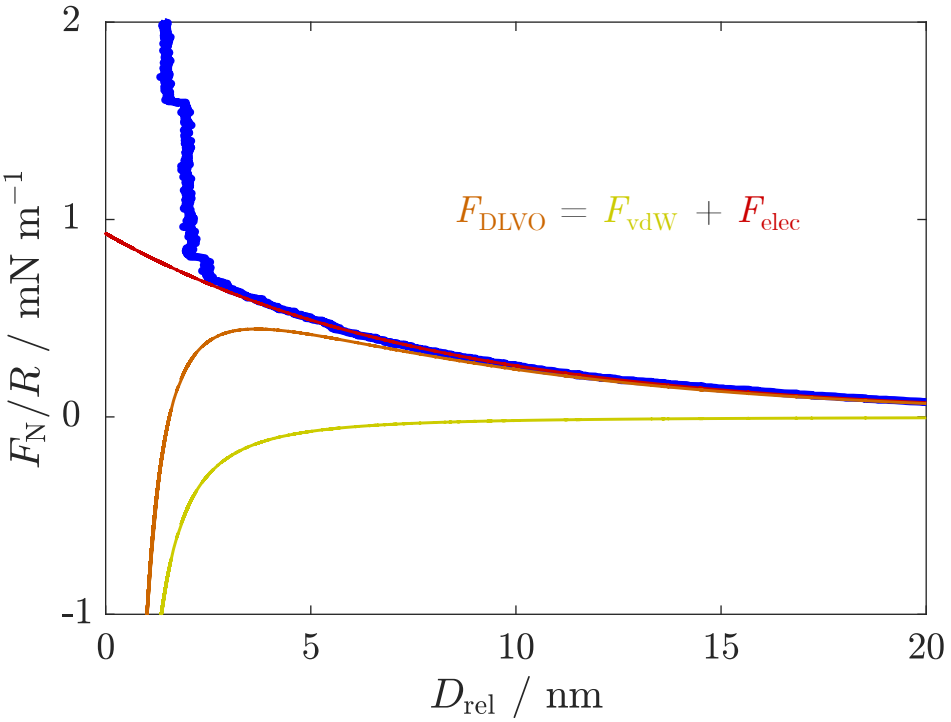


Figure 3.4 Representative normal force, F_N, normalised by the radius of curvature, R, as a function of surface separation relative to the closest approach, D_{rel}, profile in ethylene glycol (blue). The contributions of the electrostatic force (red), F_{elec}, and van der Waals force (yellow), F_{vdW}, to the DLVO force (orange), F_{DLVO}, are shown.

3.1.3 Oscillatory Forces

On retracting the surfaces (Figure 3.2: pink, green, cyan and orange dotted lines), the adhesive minimum for the corresponding layer can be explored. On reaching the force minimum (Figure 3.2: pink, green, cyan, orange, and blue-grey triangles), the surfaces will 'jump out' to large surface separation. The adhesive force minima decrease when retracting from layers further away from the surface. This is expected as the layers are less ordered under a weaker confinement. In the ambient sample (Figure 3.2(b)), there is a small reduction in the magnitude of force at the jump out points that can be attributed to adsorbed water disrupting the layered structure, as per Section 3.1.1.

For each layer, the value of surface separation, D_{min}, and absolute force, $|F_{min}/R|$, at the jump out point can be extracted. These quantities can be used

to fit the observed molecular layering to an oscillatory force, $F_{\text{osc}}(D)$,[9,76,96,97] according to,

$$F_{\text{osc}}(D) = A \exp\left(-\frac{D}{\lambda_{\text{osc}}}\right) \cos\left(\frac{2\pi D}{\xi} + \phi\right), \tag{3.4}$$

where A is an exponential prefactor, λ_{osc} is the decay length of the damped oscillation, ξ is the oscillation periodicity, and ϕ is the phase of the oscillation. The fitting process is shown in Figure 3.5 for dry ethylene glycol, the results of which are quantitatively similar for ambient ethylene glycol.

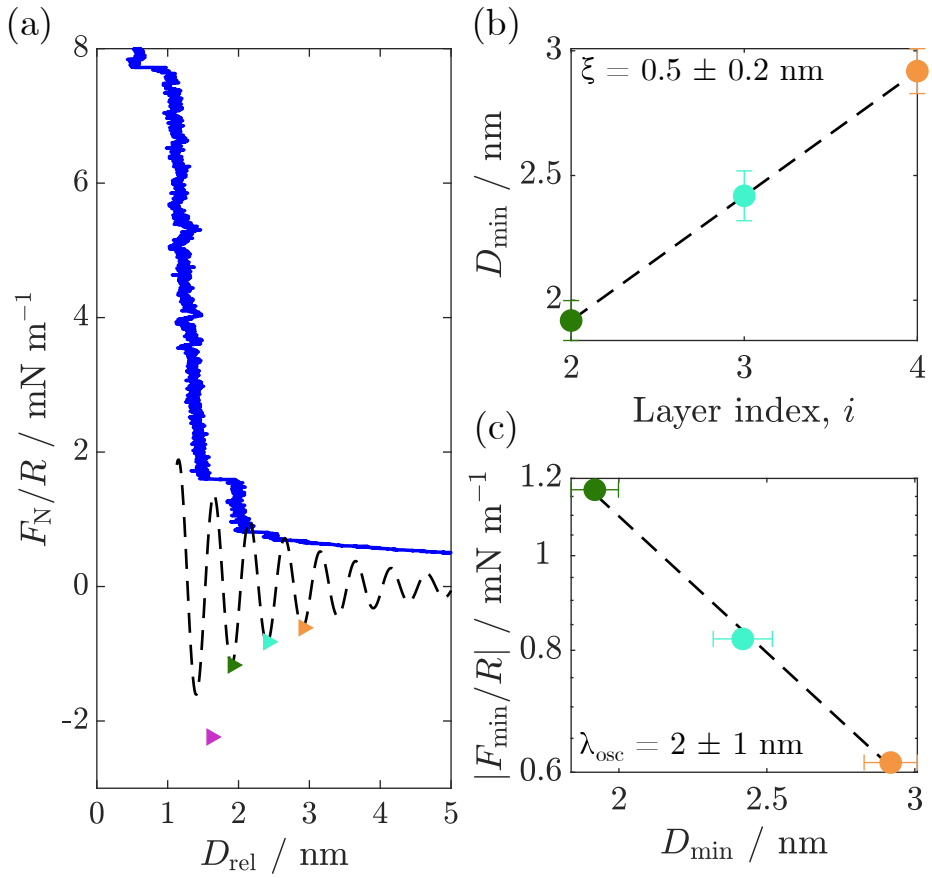


Figure 3.5 (a) Representative normal force, F_{N}, normalised by the radius of curvature, R, as a function of surface separation relative to the closest approach, D_{rel}, profile in ethylene glycol (blue). Adhesive minima for the four observed layers are indicated by the triangular points. The oscillatory force (black dashed line) is fitted using Equation 3.4 and the parameters calculated in (b) and (c). The gradient of the surface separation at the jump out point, D_{min}, as a function of the layer index, i, in (b) yields the oscillation periodicity, $\xi = 0.5 \pm 0.2$ nm. The gradient of the absolute force at the jump out point, $|F_{\text{min}}/R|$, as a function of the surface separation at the jump out point, D_{min}, on a log-linear plot in (c) yields the exponential decay length of the damped oscillation, $\lambda_{\text{osc}} = 2 \pm 1$ nm.

In Figure 3.5(b), $D_{\min}$ is plotted as a function of the layer index, i, where the innermost surface layer is denoted $i = 1$ and successively further out layers are denoted $i = 2, 3, ..., n$, yielding a linear fit where $dD_{\min}/di = \xi = 0.5 \pm 0.2$ nm. In molecular liquids, the correlations observed at the nanoscale are equivalent to the bulk correlations.[4] We therefore expect ξ to be similar to the bulk density-density correlations observed in scattering experiments. Matsugami *et al.*[98] performed large-angle X-ray scattering on pure EG and they did indeed observe correlations at 0.48 nm corresponding to the intermolecular interactions between neighbouring EG molecules, hence corroborating our calculated value of ξ.

We obtain $\lambda_{\text{osc}} = 2 \pm 1$ nm from the gradient of the log-linear representation of $|F_{\min}/R|$ as a function of $D_{\min}$, in Figure 3.5(c). λ_{osc} provides information regarding the decay of the liquid structure with surface separation, with a length on the order of molecular dimensions. The error in λ_{osc} means that we cannot quantitatively conclude the range over which the structure persists. Nonetheless, an exponentially decaying behaviour is observed, that, in combination with the oscillatory density correlations, is akin to the radial distribution function observed in liquids. The resulting damped oscillatory force is shown by the black dashed line in Figure 3.5(a).

3.2 Lateral Forces

We now study dry and ambient ethylene glycol under confinement when a shearing motion is applied across the film.

3.2.1 Quantised Friction across Ethylene Glycol Nanofilms

The frictional response of dry ethylene glycol is shown in Figure 3.6. The shear force, F_{S}, as a function of F_{N}, is shown in Figure 3.6(a). At large separations (low F_{N}), there is a negligible shear force *i.e.* only the imposed lateral motion is observed

with no coupling between the confining surfaces. As the separation decreases (red curve), we observe discontinuities in F_S-F_N that arise from the discontinuities in the surface separation as a function of normal force (as per Section 3.1). In the outermost layer, (i), the shear force is still negligible ($F_S \approx 0$ μN). This is highlighted in Figure 3.6(bi) where the lateral force, F_L, is plotted as a function of time, yielding a featureless noise-like signal. As further molecular layers are squeezed out [(i) to (ii), (ii) to (iii)], we observe a simultaneous increase in the amplitude of the F_L-time oscillations, and in F_S. The signal (Figure 3.6(b)) in the innermost layer (iii) is indicative of a more solid-like confined film, where we observe an initial elastic regime up to a yield point followed by a sharp transition to the plastic regime.[36]

The discrete increase in F_S yields steps in the F_S-F_N profile in Figure 3.6(a). F_S is defined as follows,

$$F_S^i = \mu F_N^i + \alpha^i \left(\frac{A^i F_{adh}^i}{\pi d^i R} \right), \tag{3.5}$$

where i is the layer index, μ is the load-controlled friction coefficient, α is the adhesion-controlled friction coefficient, A is the flat contact area, F_{adh} is the adhesion force between the surfaces, and d is the distance between shearing liquid layers.[32,99] Thus the discontinuities in F_S-F_N arise from the discontinuities in D-F_N, that are attributed to a different number of molecular layers in the confined film. As the number of molecular layers varies, the contribution from the adhesive force between the surfaces changes. This observation of discrete F_S-F_N regimes, corresponding to a different number of molecular layers in the confined film with a given friction coefficient, has been called 'quantised friction'.[32] By measuring the surface separation and shear forces concurrently, any changes in the observed frictional response can be directly attributed to the change in film thickness.

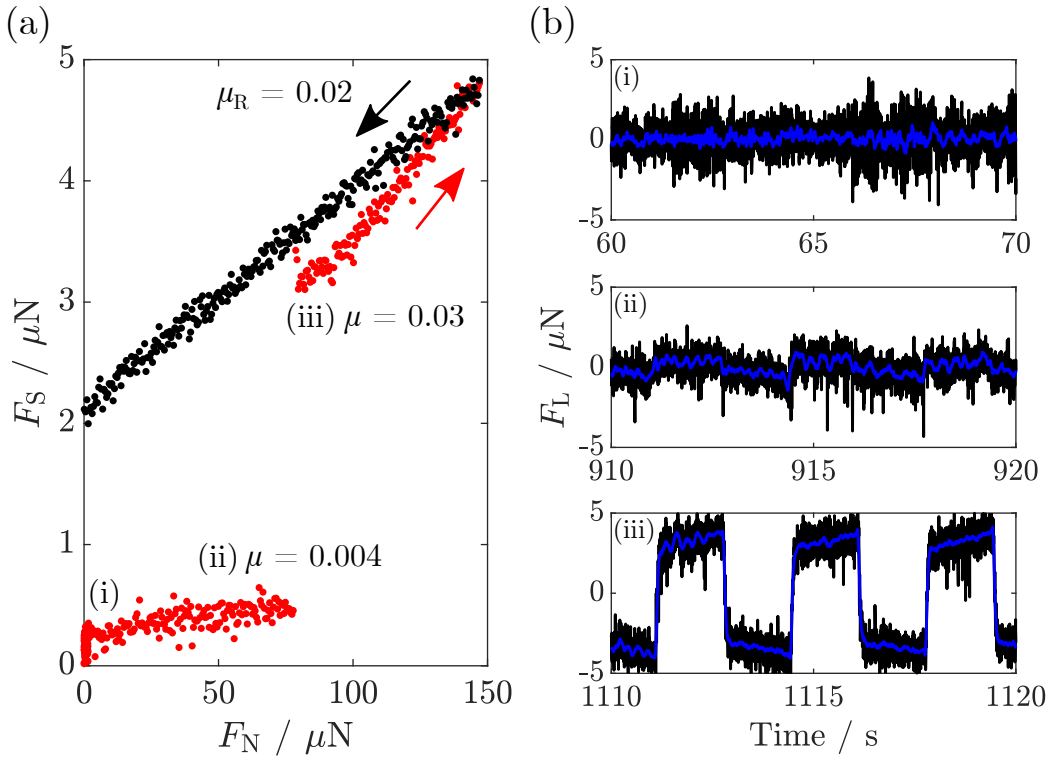


Figure 3.6 Representative (a) shear force, F_S, as a function of the normal force, F_N, across dry ethylene glycol. (b) Lateral friction signals, F_L, as a function of time, with and without a smoothing filter in blue and black, respectively. Three friction regimes are observed in (a) and are indicated by (i), (ii) and (iii). The corresponding lateral friction signals are indicated with the same labels in (b). (a) F_S with increasing F_N is shown in red, the black line indicates F_S with decreasing F_N. Red and black arrows highlight the direction of applied load. No friction coefficient can be extracted for layer (i). The friction coefficient of layer (ii) is $\mu = 0.004$. The friction coefficient of layer (iii) is $\mu = 0.03$ on approach and $\mu_R = 0.02$ on retraction. The frictional response shown is representative of multiple repeat measurements and is qualitatively reproducible. It should be noted that small changes in composition, mica alignment, temperature and contact geometry can influence the calculated friction coefficients by up to a factor of 2.[1]

Within each layer, F_S increases linearly with F_N, and from the gradient in each layer, the corresponding friction coefficient can be extracted. As shown in Figure 3.6(a), $\mu = 0.004$ in layer (ii) and in layer (iii) a steeper gradient is observed corresponding to $\mu = 0.03$. The increase in friction coefficient as molecular layers are squeezed out is likely due to the greater inter- and intra-layer ordering nearer the mica surface, increasing the activation barrier to sliding across the film.[32] It is also possible that the active shear plane changes.[1] These results show that as F_N increases, the superlubricity ($\mu < 0.01$) of dry ethylene glycol films is lost at

$F_N \approx 80$ μN.

The shear force can also be explored under negative applied loads as we separate the surfaces. In Figure 3.6(a), the black curve indicates F_S as the surfaces are separated from layer (iii). We can explore the adhesive minimum of a particular layer by retracting from it whilst applying a lateral motion, similar to the retractions in Section 3.1.3. The lateral motion results in shear-induced liquification whereby we observe a smooth retraction with no 'jump out' from the adhesive minimum, and the magnitude of the adhesive minima are reduced when compared with 'normal' retractions, *i.e.* no lateral motion.[100]

F_S decreases with F_N quasilinearly so we can determine the friction coefficient on retraction, $\mu_R = 0.02$, which is comparable to the μ on increasing load. We can therefore conclude that the friction profile is both quantised and demonstrating multi-valued regions. This phenomenon has been observed previously in ionic liquids[32,36] and occurs as a result of the oscillatory nature of F_N. At constant F_N, we observe layers at multiple values of D_{rel} (Figure 3.5(a), black dashed line). Similarly, at constant F_N, multiple values of F_S are observed. For example, when $F_N = 50$ μN, $\mu = 0.004$ or $\mu = 0.02$, with the relevant value depending on the film thickness, as in Figure 3.6(a).

3.2.2 The Role of Adsorbed Water

Figure 3.7 compares the frictional response across dry and ambient ethylene glycol.

All shear force measurements across dry ethylene glycol were carried out using the piezoelectric tube (PZT) method where both the normal and lateral motion are imposed by the PZT. The PZT method was also used across ambient ethylene glycol with a maximum $F_N \approx 200$ μN, but no quantised friction was observed. Instead, a second method was used where the normal and lateral motion are

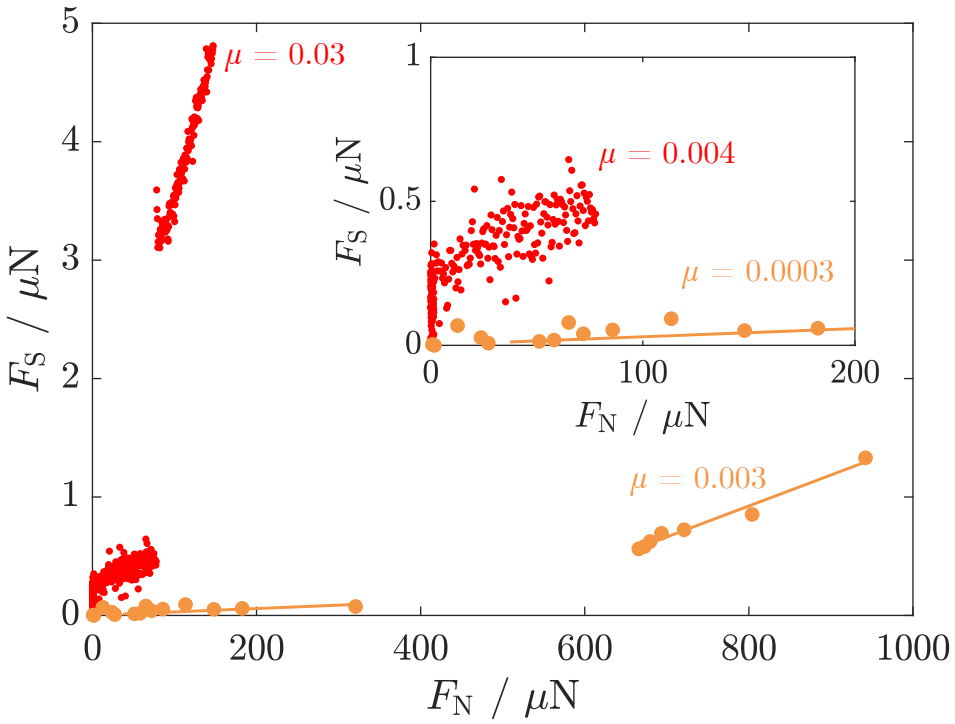


Figure 3.7 Representative shear force, F_S, as a function of the normal force, F_N, across dry (red) and ambient (orange) ethylene glycol. At the highest studied loads, $\mu = 0.03$ and $\mu = 0.003$ in dry and ambient ethylene glycol, respectively. The inset shows F_S over the range $F_N = 0 - 200$ μN. Under lower loads $\mu = 0.004$ and $\mu = 0.0003$ in dry and ambient ethylene glycol, respectively. The frictional response shown is representative of multiple repeat measurements and is qualitatively reproducible. Note: small changes in composition, mica alignment, temperature and contact geometry can influence the calculated friction coefficients by up to a factor of 2.[1]

applied by the motor and PZT, respectively, allowing access to F_S under higher loads, see Figure 3.7.

At higher F_N, another molecular layer is squeezed out and we observe a corresponding increase in the magnitude and gradient of the shear force (indicated by the step in Figure 3.7 at $F_N \approx 650$ μN). Quantised friction is therefore also apparent in ambient ethylene glycol, but with reduced magnitude and superlubric friction coefficients at all applied loads. This change in the friction behaviour can be attributed to water. As discussed in Section 3.1.1, adsorbed water can influence the equilibrium structure and/or the equilibration dynamics of the film. If the in-plane structure is weaker, the activation barrier to sliding reduces, hence

a reduction in F_S and the observed friction coefficients.

3.3 Summary

In this chapter, normal and shear forces across dry and ambient ethylene glycol nanofilms have been studied. Normal force profiles across both systems show a structural force with jump-in points corresponding to the long dimension of ethylene glycol. When fitting the short-range oscillatory force, we again recover the long dimension of ethylene glycol from the oscillation period, $\xi = 0.5 \pm 0.2$ nm. The long-range normal forces are well described by an EDL-dominated DLVO force with $\lambda_{exp} \approx 8$ nm. These features are independent of water adsorption.

Interestingly, humidity influences the positions of the layers at short-range. As deeper layers are accessed during the course of a measurement, we suggest that water may be influencing the equilibration dynamics. The time between successive runs is likely less than the time required by the film to fully equilibrate, allowing us to access non-equilibrium structures: (a) deeper layers and, (b) previously observed layers at a reduced force. We note that even though a shift in layer position is observed, ethylene glycol remains in the confined region under high loads in both dry and ambient samples.

The frictional response of the nanofilms as a function of load were also presented. Quantised friction is apparent in both systems with low friction coefficients. Adsorbed water acts to reduce the magnitude of the shear force, and superlubric friction coefficients are observed in the ambient samples at all applied loads, supporting the idea of weaker layering in the ambient sample. As ethylene glycol remains in the confined region and low friction coefficients are observed, we would expect it to be a suitable boundary lubricant.

Finally, we will consider these properties and whether they are more akin

to water, oil, or neither, under confinement. Firstly, we observe strong and clear ethylene glycol layering where the layers can sustain a normal load without the surfaces attracting into a primary minimum. This behaviour is apparent in non-polar liquids like octamethylcyclotetrasiloxane and cyclohexane,[45] and numerous ionic liquids.[29] Molecular layers in water are not typically observed, indicating that the water film cannot support a normal load. Instead, a strong DLR with $\lambda_D = 145$ nm followed by a van der Waals attraction at ≈ 3 nm is seen.[18,20] Interestingly, a strong DLR is also evident in ethylene glycol. Lastly, we observe quantised friction where the friction coefficient increases as we access deeper layers. Although quantised friction has been observed in oils,[100–102] the friction coefficient remains the same with increasing confinement. Another class of liquids where quantised friction has been observed and the friction coefficient varies with confinement are ionic liquids. The increasing friction coefficient was attributed to the change in composition of the layers with increasing confinement.[32] Ethylene glycol is therefore more similar to ionic liquids in its frictional response. As ethylene glycol is compressed, the molecular layers may not necessarily have the exact same composition of ethylene glycol, water, and other ions, hence the change in friction coefficient. We can therefore conclude that under confinement, the normal forces across ethylene glycol are more similar to oils than to water, but the shear forces are more akin to ionic liquids.

Chapter 4

Control Systems: Glycerol

Glycerol is a major by-product of biodiesel production and has over two thousand different applications in a wide variety of industries, from pharmaceuticals to the food and beverage industry. Glycerol is used as a lubricant in the production of paper, personal care formulations, and the textile industry.[103,104] It can also be used as a starting material in the production of 1,3-propanediol, polyesters, and hydrogen.[105]

In nature, glycerol acts to stabilise biological macromolecules such as protein conformations and the activity of enzymes.[106] It is also used as a cryoprotectant by a range of organisms, allowing them to survive adverse environmental conditions by increasing the osmolarity of bodily fluids and reducing the amount of water available to produce extracellular ice.[107]

Glycerol nanofilms have been studied previously with AFM[65] and through molecular dynamics simulations.[108] At a graphite electrode interface with no applied potential, Chen *et al.*[65] observed layers of ≈ 0.5 nm. The final layer observed before reaching zero surface separation had a thickness of 0.3 nm. They concluded the layer thicknesses they observed were due to different glycerol

orientations, with the final layer corresponding to glycerol lying with its longest axis parallel to the surface (see Figure 4.1).

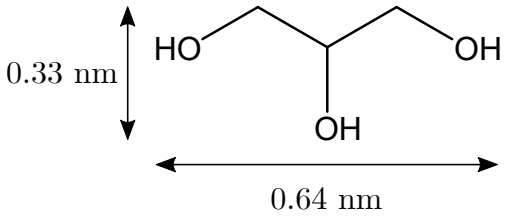


Figure 4.1 Molecular structure and approximate dimensions of glycerol.[65]

The lubrication properties of glycerol have been studied under different conditions.[109–114] A stable friction coefficient of the order, $\mu \approx 0.03$, has been observed across glycerol films between silicon nitride/Inconel 617[114] and steel/steel.[110] Superlubricity across glycerol films has been observed on addition of hydrochloric, sulfuric, lactic, oxalic, citric, and sulfamic acids,[109] and in the presence of diamond-like carbon surface coatings.[111,112]

In this chapter, we treat glycerol as a control system akin to ethylene glycol in Chapter 3. We will briefly consider the polarity, hydrogen bonding ability, and viscosity of glycerol and how they compare with water and oil, before investigating the properties of dry and ambient glycerol under confinement. Dry and ambient samples correspond to the conditions detailed in Chapter 3. It is assumed that the 'ambient' glycerol has a higher water content. Finally, we discuss whether glycerol behaves more like water or oil under confinement, and any influence of water on the observed properties.

Glycerol is a nontoxic, biodegradable, and polar molecule with a dielectric constant, $\epsilon_r = 46.5$.[95] It has three hydroxyl groups per molecule, allowing for the formation of an extensive hydrogen bond network with a high viscosity, $\eta = 1321$ mPa s at 21 ^{o}C.[115] Similar to ethylene glycol, the high dielectric constant and hydrogen bonding ability are similar to water-like properties, but the high viscosity is more oil-like.

4.1 Normal Forces

Normal force profiles for glycerol under dry and ambient conditions are influenced by viscous forces, as reported in Figure 4.2. We begin by considering these effects before discussing the structural forces across glycerol nanofilms (Figure 4.3). In both dry and ambient samples, the short-range forces appear similar and long-range forces are dominated by a viscous contribution.

4.1.1 Viscous Forces

Glycerol is a viscous liquid so we expect a significant viscous or hydrodynamic force to contribute to the overall observed force above certain velocities. In Chapter 2, comparison factors were introduced allowing us to determine approximate velocities at which viscous forces become dominant. Table 4.1 shows approach velocities for each regime when $R = 1$ cm. Approach velocities less than 0.1 nm s^{-1}, as in the low and intermediate regimes, can be difficult to achieve in SFB measurements without thermal drift influencing the linearity of the approach baseline. It is therefore expected that measurements across glycerol nanofilms will often be dominated by viscous forces at large surface separation where the equilibrium forces are small.

Table 4.1 Approach velocities in glycerol corresponding to three force regimes for $R = 1$ cm, discussed in Section 2.2.3. High and low regimes correspond to hydrodynamic and electrostatic forces dominating, respectively. The intermediate regime corresponds to a combination of hydrodynamic and electrostatic forces.

Regime	Velocity / nm s^{-1}
High	2.1
Intermediate	0.025
Low	0.0053

Figure 4.2 highlights the influence of viscous forces on the observed force profiles across glycerol nanofilms. At high velocities, we can fit the observed

distance-time profile (Figure 4.2(a)) to a purely hydrodynamic force,[88,116]

$$F_{\text{hydro}} = -\frac{6\pi\eta R^2 v}{D - b}. \tag{4.1}$$

As we know the viscosity, radius of curvature, and surface separation, we only need to fit the approach velocity, v, and the slip length, b. The fit is shown in orange and $b \approx 3 - 5$ nm. In this system, b is a *negative* slip length, where an immovable layer of molecules within the liquid, of dimension b, sits on the mica surface. This phenomenon is highlighted in Figure 4.2(b). The layer acts to retard the velocity of the neighbouring molecular layers and we subsequently observe a gradient of increasing velocities as we move away from the stopped layer and towards the bulk region.

Viscous forces can be difficult to remove, so accurately interpreting the normal force-separation profiles can be more challenging. As the viscous force is particularly prominent when we are near the surface ($D < \ 20 - 30$ nm), the behaviour in this region is not well-described by a linear approach baseline, and as a result the features of normal force-separation profiles are influenced.

Firstly, the velocity of approach influences the magnitude of the normal force. Figure 4.2(c) shows normal force-separation profiles at $v = 0.4$ nm s^{-1} and 1.5 nm s^{-1} in blue and red, respectively. As the faster approach profile has a larger viscous contribution to the overall force compared with the slower, we observe a greater F_{N}/R at similar D which is attributed to the poorer fit of the linear approach baseline.

The log-linear representation of the blue plot in (c) is shown in Figure 4.2(d). We do not observe a linear decay that would be indicative of a long-range exponentially decaying electrostatic force (*cf.* ethylene glycol). It is likely that, even at lower velocities, deconvolution of any potential long-range exponentially

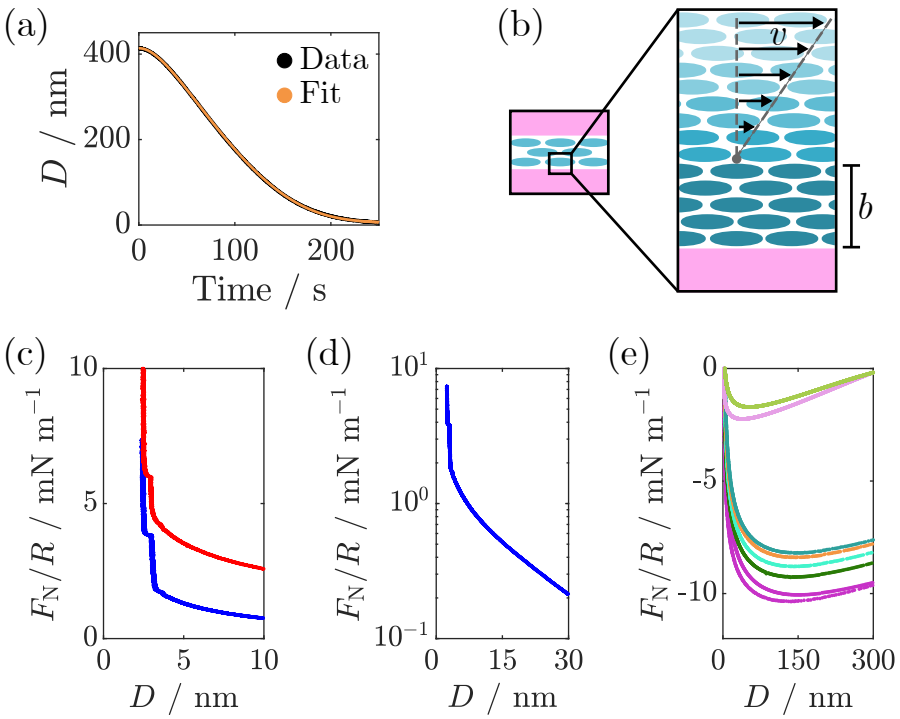


Figure 4.2 The influence of viscous forces across glycerol nanofilms. (a) Representative surface separation, D, as a function of time at high velocity, v, (black) and the fitted D-time profile assuming a purely viscous force (orange) where $v = 4.2$ nm s^{-1} and the negative slip, $b \approx 3 - 5$ nm. (b) Schematic highlighting the stopped layer of molecules corresponding to b (darkest blue) and the velocity gradient away from the stopped layer (lighter blues = greater v). In the case of glycerol, b could correspond to 9-15 molecular layers if they arrange with their long dimension parallel to the surface, or 5-8 molecular layers if perpendicular. The mica surfaces are shown in pink. (c) Velocity of approach has a noticeable influence on the normal force-separation profile. Approach velocities of 0.4 nm s^{-1} and 1.5 nm s^{-1} are shown in blue and red, respectively. (d) Log-linear representation of the blue plot in (c). Even at lower velocities it is difficult to deconvolute any potential long-range electrostatic force from the viscous force. (e) Normal force-separation profiles on retracting from the observed layers. Retractions, from near-surface layers to the outermost, are shown in the following order: pink, green, cyan, orange, blue-grey. The lighter pink and green correspond to retractions from the same layers as the darker pink and green, respectively, but with a lateral motion applied simultaneously.

decaying electrostatic force from the viscous force would be difficult. We would need to approach at much slower velocities (out of the range of the equipment), to successfully reach the low and intermediate regimes (Table 4.1).

Finally, Figure 4.2(e) shows the normal force-separation profiles on retracting from the observed layers. As we do not know if viscous forces contribute to the overall force profile on retracting, it would be erroneous to quantitatively discuss

the magnitude of the adhesive minima and the surface separation at which the jump out point occurs. Moreover, each layer does not necessarily have a distinct minimum. For example, the two dark pink retractions begin in the same layer but different adhesive minima are observed.

As a result of the viscous forces, we may not be able to quantitatively describe all force profile features. However, it will be possible to make observations at small distances, when the change in separation with time is small and so viscous forces becomes negligible.

4.1.2 Structural Forces across Confined Glycerol

Despite the viscous effects mentioned above, we are able to resolve features at small D with some clarity due to the larger equilibrium forces which dominate above viscous effects in this regime. An oscillatory force within 5 nm of zero surface separation is observed in Figure 4.3 indicating a layered structure between the surfaces. The separation between the hard walls in dry and ambient glycerol are comparable, 0.44 ± 0.01 nm and 0.46 ± 0.01 nm, respectively. It should be noted that within the layers there is a measurable compression *i.e.* we remain in a layer with increasing load where D decreases continuously and no discrete jump-in point is observed. The compression is observed as a finite gradient between the jumps. For example, in the inset of Figure 4.3(a), the layer at ≈ 3 nm compresses by $\Delta_C \approx 0.2$ nm, even under low normal load. Compression can be attributed to deformation of the mica surfaces and/or squeezing the molecular layers.[117] As the measurements in Figure 4.3 were completed with thin mica (< 3 μm), the compression observed here can be attributed to the latter. Considering both the jump-in separation, Δ_J, and compression yields a dimension, $\Delta_J + \Delta_C \approx 0.65$ nm, which corresponds with the long dimension of a glycerol molecule (Figure 4.1). The final jump-in point to $D = 0$ nm was measurably thinner, 0.27 ± 0.02 nm, and

is likely due to the glycerol molecules lying flat against the mica surface. These results corroborate the work of Chen *et al.*[65]

At short-range, the positions of the layers relative to $D = 0$ nm remain the same in the dry and ambient samples. Qualitatively, there is a slight decrease in the magnitude of F_N/R in the ambient sample, when compared with the equivalent dry jump-in points. Similar to ethylene glycol, glycerol is hygroscopic and adsorbed water likely weakens the layered structure.

On retracting the surfaces (Figure 4.2(e)), the adhesive force minima decrease when retracting from layers further away from the surface due to a weaker confinement and hence a more disordered structure.

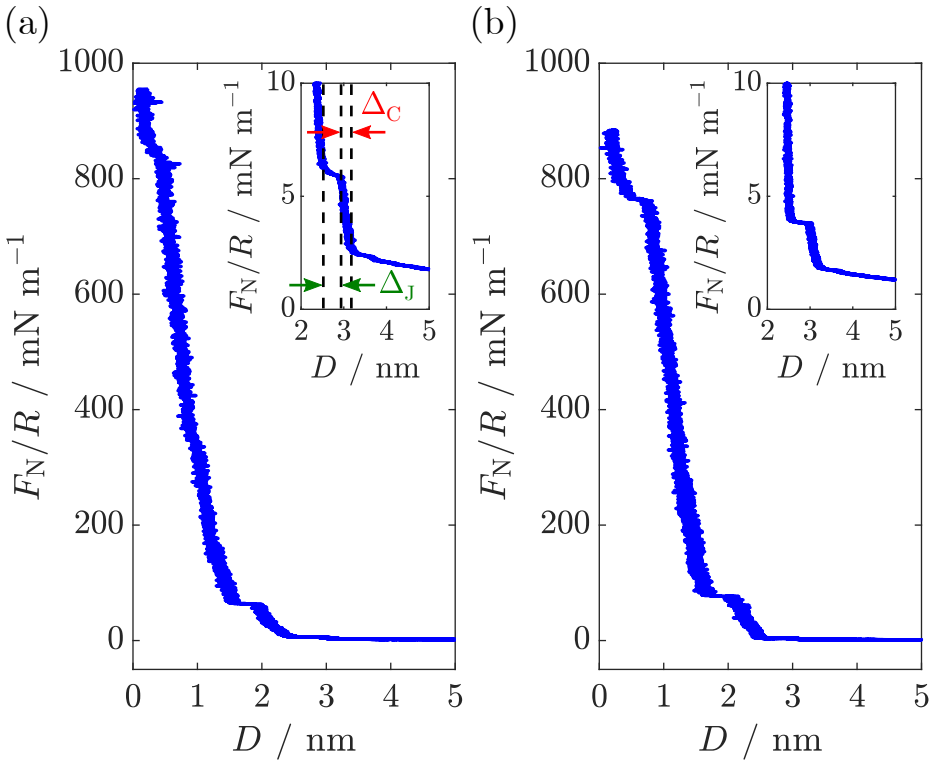


Figure 4.3 Representative normal force, F_N, normalised by the radius of curvature, R, as a function of surface separation, D, profiles in (a) dry and (b) ambient glycerol. In both instances the inset shows the structural forces when $F_N/R < 10$ mN m^{-1}. The inset in (a) shows the jump-in separation, Δ_J, and layer compression, Δ_C, in green and red, respectively. Higher loads are accessed by using a stiffer normal spring.

4.2 Lateral Forces

We now study dry and ambient glycerol under confinement when a shearing motion is applied across the film.

4.2.1 Quantised Friction across Glycerol Nanofilms

The frictional response of dry glycerol is shown in Figure 4.4. The surface separation and shear force as a function of the normal force are shown in the top and bottom plots of Figure 4.4(a), respectively. At large separations, there is a negligible shear force. As the separation decreases (red curves), molecular layers and discrete steps in the F_S-F_N profile are observed. As mentioned in Section 3.2, these steps occur as a result of the oscillatory structural force which gives rise to discontinuities in D-F_N. These are attributed to a different number of molecular layers in the confined film and as this number varies, the contribution from the adhesive force between the surfaces changes. By measuring the surface separation and shear forces concurrently, any changes in the observed frictional response can be directly attributed to the change in film thickness.

Within each layer, F_S increases quasilinearly with F_N and we can determine the friction coefficient from the gradient. In the bottom plot of Figure 4.4(a), $\mu = 0.02$ in layer (i) and $\mu = 0.05$ in layer (ii), which are comparable with literature measurements.[110,114] In layer (i) a small step is apparent in the F_S-F_N profile at ≈ 40 μN without a corresponding change in the layer index in the top plot. This is likely due to a molecular rearrangement within the layer as the load increases, that has a greater adhesive force between the surfaces, supporting the argument that the layer compression may be attributed to squeezing of the molecular layers into a more ordered structure.

Unlike ethylene glycol, the friction coefficients observed in different glycerol

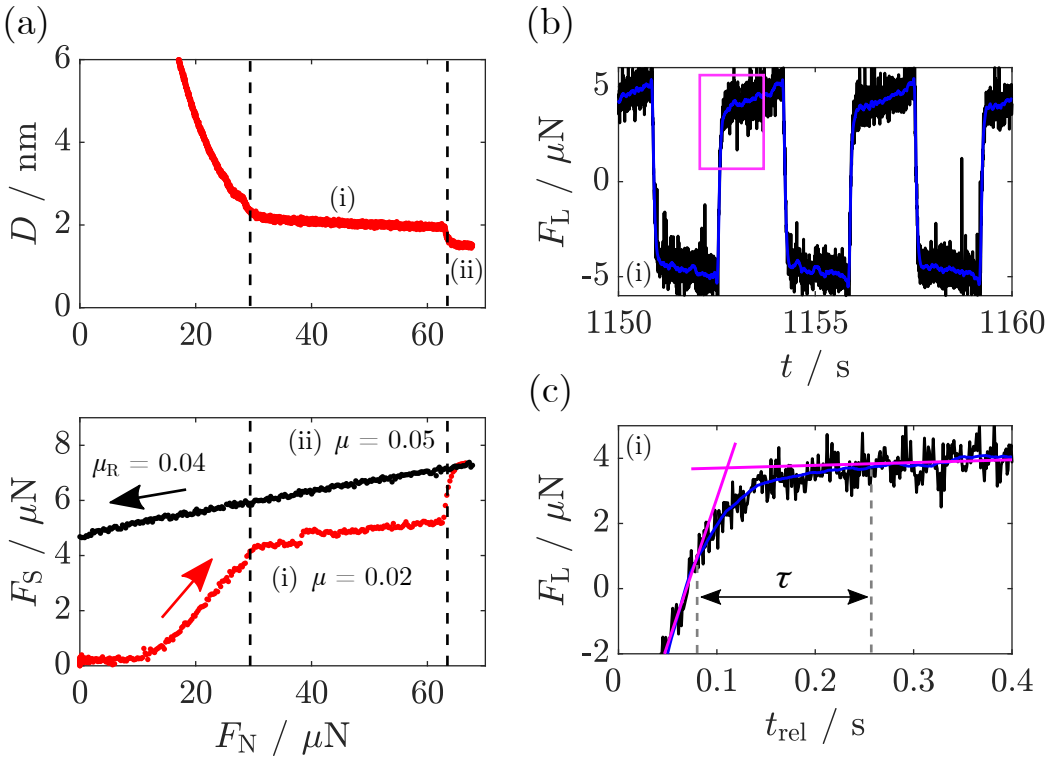


Figure 4.4 Representative (a) surface separation, D, (top plot) and shear force, F_S, (bottom plot) as a function of the normal force, F_N, across dry glycerol. Bottom plot: F_S with increasing F_N is shown in red, the black line indicates F_S with decreasing F_N. Red and black arrows highlight the direction of applied load. The friction coefficient of layer (i) is $\mu = 0.02$. The friction coefficient of layer (ii) is $\mu = 0.05$ on approach and $\mu_R = 0.04$ on retraction. The vertical dashed lines in (a) highlight the simultaneous discrete steps in surface separation and shear force with normal force. (b) Lateral friction signal, F_L, as a function of time in layer (i), with and without a smoothing filter in blue and black, respectively. The signal within the pink box is shown in (c) highlighting the viscous, liquid-like lateral friction signal that relaxes between the elastic and plastic regimes (pink lines) with time, $\tau \approx 0.2$ s. The frictional response shown is representative of multiple repeat measurements and is qualitatively reproducible. Note: small changes in composition, mica alignment, temperature and contact geometry can influence the calculated friction coefficients by up to a factor of 2.[1]

layers are comparable and greater confinement only influences the adhesive contribution to F_S. Shearing across glycerol nanofilms therefore occurs via a similar sliding mechanism regardless of load or film thickness.

The shear force under negative applied loads is shown for layer (ii) in black in the bottom plot of Figure 4.4(a). On retracting the surfaces a friction coefficient, $\mu_R = 0.04$ is observed that is comparable to the μ on increasing load. This phenomenon of quantised friction has been discussed in Section 3.2 and is a

consequence of the oscillatory force which in turn is a consequence of molecular layering. The magnitude of the adhesive minima are reduced when compared to 'normal' retractions as shown by the lighter pink and green profiles in Figure 4.2(e), and we observe a smooth retraction with no measurable 'jump out'.[100]

Figure 4.4(b) shows the lateral force as a function of time, t, in layer (i) during two full shearing cycles. A portion of the signal is highlighted by a pink square and shown in Figure 4.4(c). Here, the lateral force is plotted as a function of a relative time, t_{rel}, to highlight the timescale of relaxation, τ. When transitioning from the elastic to the plastic regime in the lateral force-time profile, a distinct curvature is observed (rather than a discontinuity) with a relaxation time, $\tau \approx 0.2$ s. This timescale is comparable to the relaxation times observed across ionic liquids, and indicates a viscous, liquid-like film.[36,89]

The relaxation time observed in Figure 4.4(c) can be compared with the predicted relaxation timescale expected in a Couette flow.[84,89,102] Couette flow arises when two undeformable planar surfaces move laterally with respect to one another across an incompressible liquid film. If that fluid is a viscous, charge-less, Newtonian liquid, with a no-slip boundary condition, the force opposing the lateral motion is purely viscous.[89] As one of the surfaces in the SFB is attached to a vertical leaf spring, the viscous force can be balanced with the restoring force of the spring. It should be noted that the conditions in our measurements are not fully described by a Couette flow, for example glycerol does observe a slip length, however it provides us with a point of comparison. The relaxation timescale in a Couette flow is given by

$$\tau_{\mathrm{Couette}} \approx \frac{A\eta}{k_{\mathrm{s}} D_{\mathrm{liq}}}, \tag{4.2}$$

where A is the area of the planar surfaces, η is the bulk viscosity, k_{s} is the vertical leaf (or shear) spring constant, and D_{liq} is the liquid film thickness. For a 1 nm film of glycerol ($\eta = 1.321$ Pa s at 21 ^{o}C)[115] between two planar surfaces

($A \approx 523\ \mu m^2$)[89] and $k_s = 388\ N\ m^{-1}$, $\tau_{Couette} \approx 1.8$ ms, roughly two orders of magnitude faster than the observed τ. We can also determine an effective viscosity, $\eta_{eff} \approx 150$ Pa s, from the observed value of τ. The confined liquid film appears to show an effective viscosity two orders of magnitude larger than bulk glycerol. This result has also been reported using SFA measurements across ionic liquids by considering the drainage of the liquid from the confined region during the jump-in transitions.[118]

4.2.2 The Role of Adsorbed Water

Figure 4.5 compares the frictional response across dry and ambient glycerol. The measurements are shown for glycerol nanofilms under higher loads compared to Figure 4.4, but the same conclusions can be made.

Quantised friction is apparent in ambient glycerol with reduced magnitude of F_S. For the same layer in the dry and ambient samples, the friction coefficient decreases slightly but are still of comparable magnitude. For example, the layer starting at $D \approx 2.5$ nm in Figure 4.3 corresponds to the quasilinear regime between $F_S = 250 - 650\ \mu N$ in Figure 4.5, and $\mu = 0.08$ and $\mu = 0.03$ in the dry and ambient samples, respectively. When the $D \approx 1.6$ nm layer is reached in the dry sample (at $F_N > 900\ \mu N$), F_S exceeds the limit of our setup ($F_{S,max} \approx 110\ \mu N$) and we are unable to access the corresponding friction coefficient on approach. However, in the ambient sample, the magnitude of F_S has decreased below the instrumental limit and we can determine $\mu = 0.04$. This leads us to conclude that the sliding mechanism in dry and ambient glycerol does not change, but adsorbed water does weaken the layered structure and hence the adhesive contribution to F_S.

The viscous contribution discussed in Section 4.1.1 is also present in the F_S-F_N profiles, indicated by the large increase in F_S between $F_N = 30\ \mu N$ (Figure 4.5,

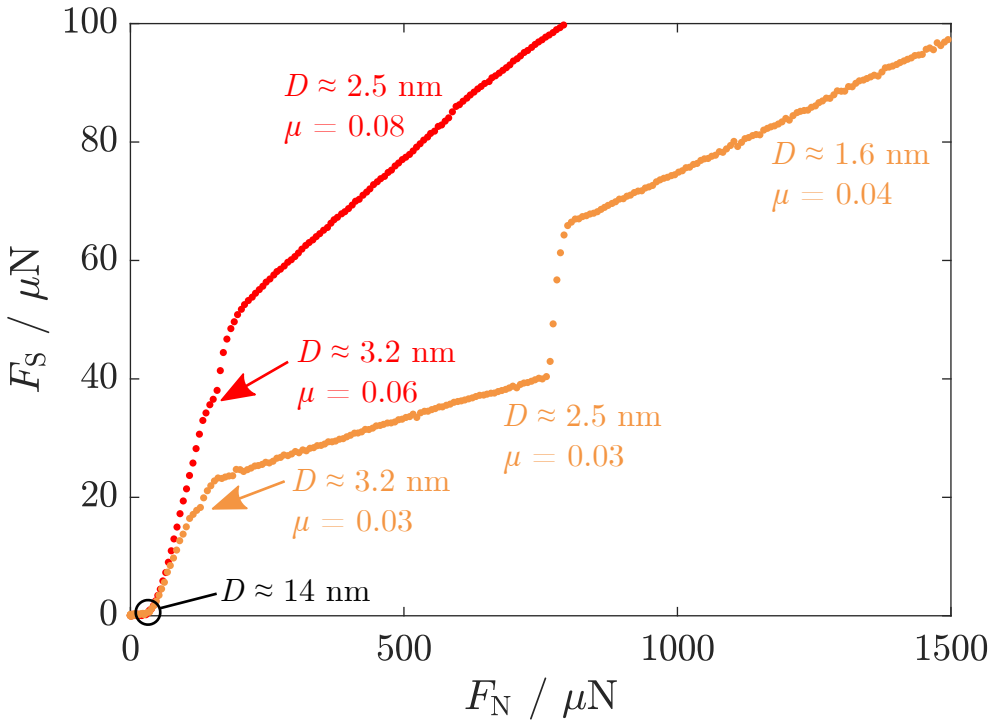


Figure 4.5 Representative shear force, F_S, as a function of the normal force, F_N, across dry (red) and ambient (orange) glycerol. Higher loads are accessed by using a stiffer normal spring. Friction coefficients, μ, are shown for each layer at surface separation, D. The red and orange arrows highlight the outermost layers, and the black circle indicates when F_S begins to increases with load at $F_N \approx 30$ μN. The frictional response shown is representative of multiple repeat measurements and is qualitatively reproducible. Note: small changes in composition, mica alignment, temperature and contact geometry can influence the calculated friction coefficients by up to a factor of 2.[1]

black circle) and the normal force at which we enter the outermost layers (indicated by the red and orange arrows). We suggest this steep variation of F_S with F_N is a result of the continual squeeze out of the viscous film rather than discrete molecular layers, and hence why we do not observe this steep variation in the F_S-F_N profiles of the less viscous ethylene glycol (Section 3.2).

4.3 Summary

In this chapter, normal and shear forces across dry and ambient glycerol nanofilms have been studied. Viscous forces dominate the normal force profiles at all approach velocities studied and fitting the data to an expression for the Reynolds

lubrication force gives $b \approx 3 - 5$ nm. Normal force profiles are influenced by viscous forces in multiple ways:

1. The velocity of approach directly influences the magnitude of F_{N}/R through inadequate linear baseline fitting.

2. We cannot deconvolute any potential exponentially decaying electrostatic force from the viscous contribution.

3. Adhesive minima cannot be described quantitatively.

Nonetheless, short-range structure and dynamics can be analysed. Normal force profiles show a structural force with jump-in points of 0.44 ± 0.01 nm and 0.46 ± 0.01 nm in dry and ambient samples, respectively. In combination with the molecular layer compression, the total observed dimension corresponds to the long dimension of glycerol. The innermost layer is measurably thinner and can be attributed to the glycerol molecules lying flat against the mica. Positions of the molecular layers remain the same throughout. The features discussed above do not depend on adsorbed water content.

The frictional response of the nanofilms as a function of load were also reported. Quantised friction is apparent in both systems with comparable friction coefficients between the layers. The lateral friction signals showed a relaxation time between the elastic and plastic regimes, indicative of a viscous, liquid-like film. Adsorbed water weakens the layered structure, reducing the adhesive contribution to F_{S}. Water does not, however, influence the sliding mechanism, apparent from the comparable friction coefficients in both dry and ambient samples.

Finally, we will consider these properties and whether they are more akin to water, oil, or neither under confinement. Glycerol forms molecular layers under confinement as observed previously in ethylene glycol (see Chapter 3), non-polar

liquids,[45] and ionic liquids.[29] We observe quantised friction where the friction coefficient does not vary as we access deeper layers, similar to that seen in more oil-like systems.[100–102] We can therefore conclude that under confinement, the normal and shear forces across glycerol are more similar to the behaviour of oils.

Chapter 5

Nanostructure of Deep Eutectic Solvents (I)

Deep eutectic solvents (DESs) were first reported in 2001 by Abbott *et al.*[79] and are now commonly recognised as a sub-category of ionic liquids (ILs). ILs are 1 component systems containing 2 constituent ions (cations and anions), whereas DESs are usually formed from a eutectic mixture of a salt and some molecular component,[65] resulting in a 2 component system containing 3 constituents: cations, anions, and molecular solvent. Their name originates from their phase behaviour at the eutectic composition (see Figure 5.1) where the freezing point depression exceeds that predicted by ideal solution theory,[119] making most DESs liquid below $\approx 150\ ^{o}\mathrm{C}$.[81]

At the eutectic composition, the mixture is frustrated from solidifying due to the presence of large, asymmetric ions and/or strong hydrogen bonding between the components. The former is also used to explain the phase behaviour of room-temperature ILs.[120] DESs are most commonly formed from the complexation of a quaternary ammonium salt and some hydrogen bond donor (*e.g.* amides,

polyols, polyacids).[80] At the eutectic composition, the favourable hydrogen bonding interactions formed in the mixed liquid phase are stronger than the interactions in the individual component phases,[121] resulting in a finite negative contribution to the enthalpy of mixing, which depresses the freezing point and widens the liquidus range (see Chapter 7).

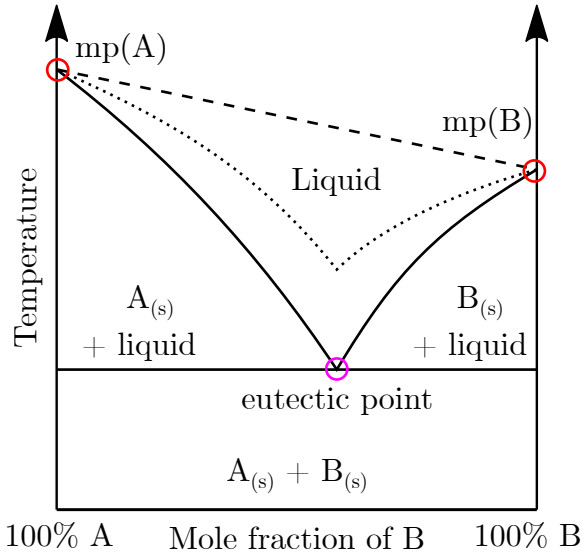


Figure 5.1 Schematic adaptation of a two component solid-liquid phase diagram for a simple ideal eutectic mixture (dotted line) and a deep eutectic solvent (solid line).[80,119] The horizontal solid line corresponds to the solidus. The melting points (mp) of pure A and B are highlighted by red circles and are connected by the black dashed line. The eutectic point is shown by the pink circle.

ILs and DESs have similar physical properties including tunability, high polarity, low vapour pressures, wide liquidus ranges, and thermal stability.[80] Depending on the components used, DESs can also have advantages over ILs including biodegradability, non-toxicity, and ease of manufacture from inexpensive starting materials.[81] In fact, compared to ILs, DESs have been classed as more 'green' solvents that can be used in synthesis,[122] metal processing applications like electrodeposition,[80] and as lubricants.[123–126] Chemical industries including pharmaceuticals, petrochemicals, and bulk chemical production rely on organic solvents that can be harmful and/or environmentally damaging.[77] Green and sustainable chemistry practices have been suggested to address the large-scale

consumption of these solvents, and the corresponding waste production. This includes shifting towards alternative solvents that are more sustainable, and hence the interest in DESs.[82,83]

In the following three chapters, we will discuss the interfacial, confinement and bulk properties of DESs. Here, in Part (I), we will discuss the interfacial properties of the DES formed from choline chloride (ChCl) and ethylene glycol (EG). In Part (II) (Chapter 6), we will discuss the interfacial properties of the DES formed from ChCl and glycerol (Gly). Finally, Chapter 7 will explore the bulk phase behaviour of ChCl:EG mixtures using differential scanning calorimetry, and we will re-examine the concept and definition of a 'deep eutectic solvent'.

This chapter will focus on both on-eutectic and off-eutectic mixtures of ChCl and EG. Molecular structures of the components are shown in Figure 5.2. The on-eutectic composition is defined as a 1:2 molar mixture of ChCl:EG,[123] and off-eutectic by a 1:X molar mixture where X $\neq$ 2. We will firstly study the normal and lateral forces across 1:2 ChCl:EG nanofilms with changing water content. Off-eutectic mixtures of 1:3 and 1:10 ChCl:EG will then be explored, before discussing differences in the on- and off-eutectic behaviours.

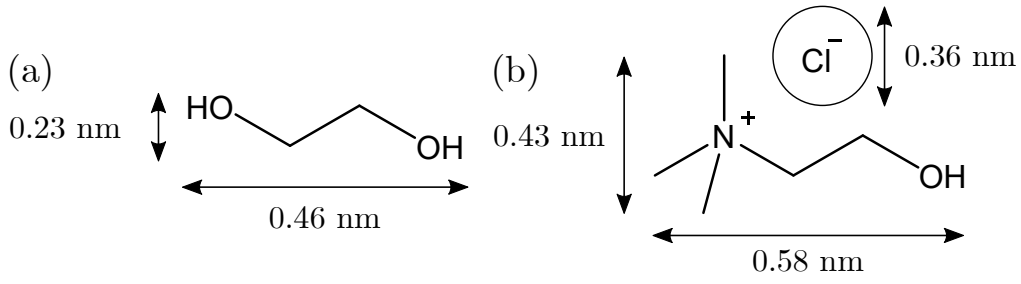


Figure 5.2 Molecular structure and approximate dimensions of (a) ethylene glycol and (b) choline chloride.[65,127]

5.1 1:2 Choline Chloride:Ethylene Glycol

In this section, we will discuss normal and shear forces across 1:2 ChCl:EG. We measure samples that have been prepared in numerous ways and clarify the terminology used in this section below.

Dry. Prepared using anhydrous reagents. The mixture was stirred under a nitrogen atmosphere, and the resulting liquid also stored under nitrogen. The sample was injected between the lenses and studied with a phosphorus pentoxide desiccant in the air-tight SFB. The chamber was also purged with nitrogen. Karl Fischer titration showed a water content $\approx$ 19.7 ppm.

Ambient. The **dry** sample is allowed to equilibrate with the mica surfaces for more than 12 hours in the SFB. The chamber is not open to atmospheric humidity, and hence we assume the chamber is still under a nitrogen atmosphere.

Air-equilibrated. The **dry** sample is allowed to equilibrate at atmospheric humidity for 1 to 24 hours before measuring. Karl Fischer titration showed a water content $\approx$ 3800 ppm.

Wet. Different weight percentages of ultrapure water are added to the DES.

It is assumed that the water content increases as follows: dry, ambient, air-equilibrated, wet.

The measurements, analyses and interpretations reported in this section were completed in partnership with Dr James Hallett, and relates to the published article by Hallett, Hayler, and Perkin.[1] Karl Fischer titration measurements were completed by Andrew Wang (DPhil student in the group of Charles Monroe, Oxford).

5.1.1 Normal Forces

Dry

The normal force profile across dry 1:2 ChCl:EG is shown in Figure 5.3(a). We observe an oscillatory force at $D < 3$ nm, indicative of molecular layering between the surfaces. The separation between the hard walls is uniform with a dimension of 0.45 $\pm$ 0.03 nm. Using dimensional arguments, the steps can be attributed to the larger dimension of the choline ions lying parallel to the mica surface. In ionic liquids the wavelength of the oscillation typically matches the ion-pair dimension, implying that electroneutral pairs of layers are expelled, as per Figure 5.4(a).[29] Whereas, in the present experiments, electroneutral layers do not correspond to the ion-pair dimension and are instead consistent with a single layer containing all three constituents: choline cations, chloride anions, and EG. This 'checkerboard-like' behaviour, shown in Figure 5.4(b), has also been reported in ionic liquids,[34,70,71] and allows electroneutrality to be maintained without templating into separate cation and anion-dominated layers. This corroborates molecular dynamics simulations by Mamme *et al.*,[128] where they observe layers of mixed composition beyond the Stern layer.

The positions of the layers on successive measurements and separate experiments are highly reproducible, but the magnitude of F_{N}/R can vary due to small differences in DES composition and the charge on the mica.

The inset of Figure 5.3(a) shows the long-range normal force decaying exponentially with surface separation with an experimental decay length, $\lambda_{\mathrm{exp,(a)}} = 12 \pm 1$ nm. From Debye-Hückel theory (using $\epsilon_r = 32$),[129] the predicted Debye length, $\lambda_{\mathrm{D}} \approx 0.1$ nm, which is two orders of magnitude shorter than observed. 1:2 ChCl:EG is a concentrated electrolyte (≈ 4.3 M, where M is defined as the moles of solute per volume of solution) and therefore this anomalously long decay

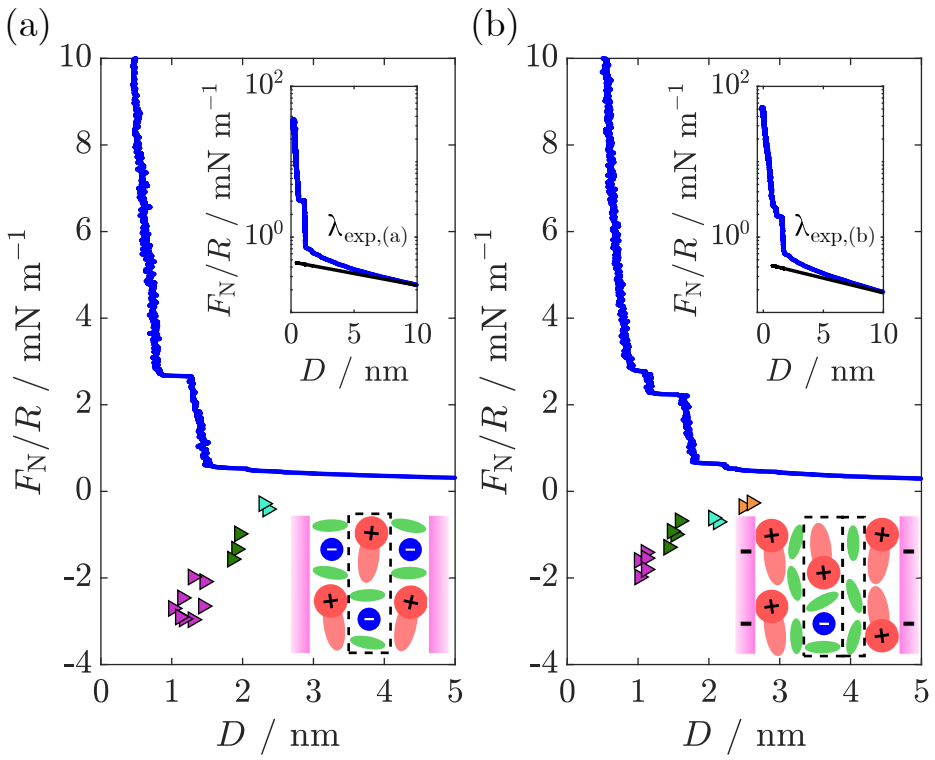


Figure 5.3 Representative normal force, F_N, normalised by the radius of curvature, R, as a function of surface separation, D, profiles in (a) dry and (b) ambient 1:2 ChCl:EG. The profile on approach is shown in dark blue. Retractions from each observed layer allows the adhesive minima to be explored. The adhesive force minima and jump out positions for each layer are indicated by triangular points. From near-surface layers to the outermost, retractions are shown in the following order: pink, green, cyan, orange. In both instances the inset shows a log-linear representation of the normal force on approach. The solid black line indicates the gradient of the long-range exponential decay where $\lambda_{exp,(a)} = 12 \pm 1$ nm and $\lambda_{exp,(b)} = 11 \pm 1$ nm. Proposed confined structure schematics are also shown. The (negatively charged) mica surfaces are shown in pink, ethylene glycol molecules in green, choline cations in red, and chloride anions in blue. The dashed black box indicates the squeeze-out repeat unit giving rise to steps in the force-distance profile.

length can be linked to underscreening-like behaviour reported by Smith *et al.*[27] Underscreening is discussed extensively in Chapter 8.

On retracting the surfaces, the adhesive minimum for the corresponding layer can be explored. On reaching the force minimum (Figure 5.3: pink, green, cyan and orange triangles), the surfaces 'jump out' to large surface separation. The adhesive force minima decrease when retracting from layers further away from the surface. This is expected as the layers are less ordered under a weaker confinement.

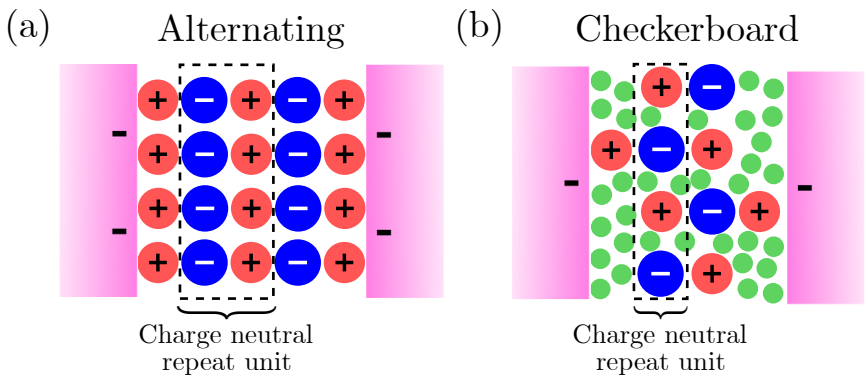


Figure 5.4 Schematics of confined (a) alternating and (b) checkerboard structures. The charge-neutral repeat units are indicated using dashed black boxes. In (a) the repeat unit contains a layer of cations (red) and a layer of anions (blue), and in (b) the repeat unit comprises a single layer containing cations, anions, and solvent (green). The negatively charged mica surfaces are shown in pink.

Ambient

The normal force profile across ambient 1:2 ChCl:EG is shown in Figure 5.3(b). We again observe an oscillatory force at $D < 3$ nm, however the surface structure changes. The dimension of the outermost layers remains at 0.45 nm, but we now observe a thinner 0.23 $\pm$ 0.03 nm layer adjacent to the innermost surface layer. This dimension is comparable to the short dimension of ethylene glycol and we suggest the small layer corresponds to ethylene glycol lying parallel to the mica surface, with the hydroxyl groups pointing towards the bulk reservoir.

The inset of Figure 5.3(b) shows a long-range normal force decaying exponentially with surface separation with an experimental decay length comparable to the dry sample, $\lambda_{\text{exp,(b)}} = 11 \pm 1$ nm.

The final layer observed before reaching $D = 0$ nm has a thickness of ≈ 0.9 nm. When compared with the final observed layer in dry 1:2 ChCl:EG (≈ 0.8 nm), the ambient final layer was consistently larger. Allowing the system to equilibrate therefore influences the observed surface structure.

We propose two different mechanisms for the formation of the EG layer on

equilibration. Firstly, it is known that the mica surface charge equilibrates with ultrapure water in roughly 1 hour through the dissolution of potassium ions.[18] In a concentrated DES environment, potassium ion dissolution may be slower and it would therefore take longer for the mica to equilibrate. Only when the system is held at large surface separation for several hours can the mica equilibrate. As the mica becomes more negatively charged, choline cations will move towards the surface with their positive ammonium heads at the mica surface. The ethylene glycol that previously sat next to the mica surface (Figure 5.3(a)) is then excluded from the innermost layer and forms an adjacent EG-rich layer (Figure 5.3(b)). The second mechanism involves the adsorption of water. It is likely that, although the sample is within a nitrogen-filled chamber in the presence of phosphorus pentoxide dessicant, some atmospheric water will penetrate the chamber and be adsorbed by the hygroscopic DES. Any change in the water content could influence the surface structure by altering the intermolecular interactions in the sample[130] or through enhanced potassium ion dissolution.

To further study the influence of more extensive adsorption of water, a dried sample was allowed to equilibrate at atmospheric humidity before measuring the interfacial forces in the SFB. Karl Fischer titration showed the water content of the air-equilibrated sample to be 3800 ppm (*cf.* water content of dry sample $\approx$ 19.7 ppm).

A representative force profile measured 1 hour after injecting the air-equilibrated liquid is shown in Figure 5.5 (dark blue). We observe layers consistent with the dry samples of 0.45 $\pm$ 0.05 nm but with larger F_N/R, likely due to the enhancement of intermolecular hydrogen bonds or the mica surface charge, as discussed above. When the sample is allowed the equilibrate over 24 hours at large surface separation, the blue-grey curve is observed in Figure 5.5. The two layers that were present in the 1 hour sample are expelled simultaneously with

a dimension of 0.72 $\pm$ 0.05 nm. The magnitude of F_N/R also sits between the values of the individual layers. As the observed dimension now exceeds the largest dimension in the system (choline cation $\approx$ 0.58 nm), single checkerboard-like layers are not feasible and we propose that separated layers of excess cations and excess (anions+EG) are observed. We therefore suggest that after long equilibration times, the mica surface charge in the air-equilibrated sample is large enough to separate the checkerboard-like layers (blue-outlined schematic in Figure 5.5) into cation- and (anion+EG)-dominated layers (grey-outlined schematic in Figure 5.5).

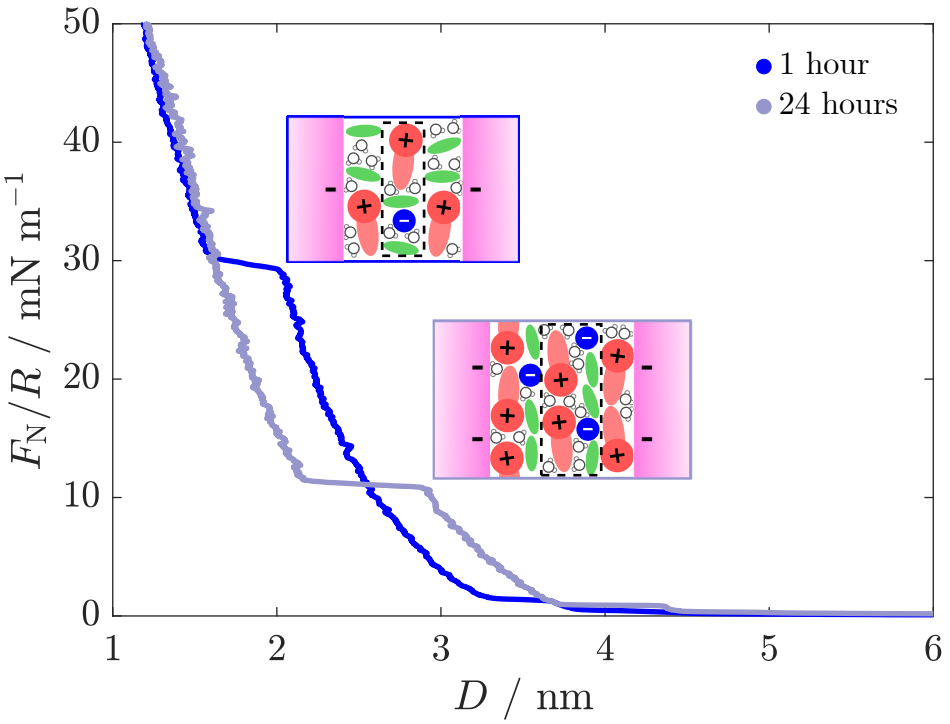


Figure 5.5 Representative normal force, F_N, normalised by the radius of curvature, R, as a function of surface separation, D, profiles in air-equilibrated 1:2 ChCl:EG. The dark blue curve shows the force profile 1 hour after injecting the liquid. The blue-grey curve shows the force profile after a 24 hour equilibration. Proposed confined structure schematics determined using dimensional arguments are also shown. The negatively charged mica surfaces are shown in pink, ethylene glycol molecules in green, choline cations in red, chloride anions in blue, and water molecules in white and grey. The dashed black box indicates the squeeze-out repeat unit giving rise to steps in the force-distance profile.

It should also be noted that in both samples that the layers are highly compressible, evidenced by the change in D with increasing F_N/R between discrete

steps. It is likely the compression is a result of the liquid film reorganising or excluding neutral species from the confined region.

Wet

Figure 5.6 shows the normal force profiles across 1:2 ChCl:EG on addition of (a) 30 wt% and (b) 50 wt% water. Both samples exhibit molecular layering with dimensions exceeding that of a single molecular species that are of comparable size: (a) 0.74 $\pm$ 0.08 nm and (b) 0.80 $\pm$ 0.08 nm. We attribute the larger dimensions to the formation of alternating cation- and (anion+EG)-dominated layers (schematised in Figure 5.6(b)).

The insets of Figures 5.6(a) and (b) show the long-range normal force decaying exponentially with surface separation with $\lambda_{\text{exp,(a)}} = 6 \pm 1$ nm and $\lambda_{\text{exp,(b)}} = 4 \pm 1$ nm. We suggested the presence of underscreening-like behaviour in dry 1:2 ChCl:EG. This apparent decrease in the decay length with decreasing concentration (increasing water content) is also consistent with reports of underscreening, where the decay length is observed to increase with increasing concentration in the concentrated regime.[131]

The final layer observed before reaching $D = 0$ nm, in both samples, has a thickness of 0.5 $\pm$ 0.1 nm which is smaller than those observed in both dry (0.8 nm) and ambient 1:2 ChCl:EG (0.9 nm).

A much larger F_{N}/R is also required to remove the innermost layers of the wet samples compared with the dry. Subsequently, the adhesive minimum is stronger for the innermost layer with $F_{\text{min}}/R = 16 - 20$ mN m^{-1} (pink solid lines in Figure 5.6). This value is comparable to the adhesive minimum previously observed in mica-mica measurements across water where $F_{\text{min}}/R \approx 16$ mN m^{-1}.[18] We therefore propose the final observed jump-in point corresponds to the choline cation Stern layer being expelled, leaving a layer of water in the confined region.

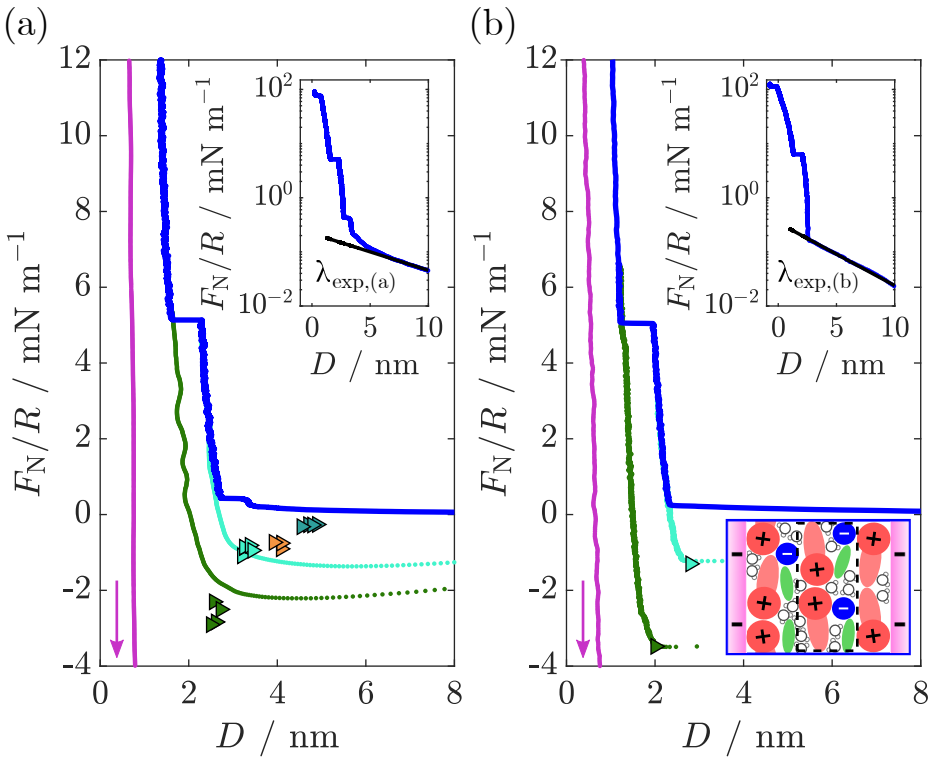


Figure 5.6 Representative normal force, F_N, normalised by the radius of curvature, R, as a function of surface separation, D, profiles in 1:2 ChCl:EG with (a) 30 wt% and (b) 50 wt% water. The profile on approach is shown in dark blue. Retractions from each observed layer allows the adhesive minima to be explored. The adhesive force minima and jump out positions for each layer are indicated by triangular points. From near-surface layers to the outermost, retractions are shown in the following order: pink, green, cyan, orange, blue-grey. The pink arrows indicate deep minima for the innermost layers that cannot be shown on this scale ($F_{min}/R = 16-20$ mN m^{-1}). In both instances the inset shows a log-linear representation of the normal force on approach. Higher loads are accessed by using a stiffer normal spring. The solid black line indicates the gradient of the long-range exponential decay where $\lambda_{exp,(a)} = 6 \pm 1$ nm and $\lambda_{exp,(b)} = 4 \pm 1$ nm. A proposed confined structure schematic determined using dimensional arguments is also shown. The negatively charged mica surfaces are shown in pink, ethylene glycol molecules in green, choline cations in red, chloride anions in blue, and water molecules in white and grey. The dashed black box indicates the squeeze-out repeat unit giving rise to steps in the force-distance profile.

5.1.2 Lateral Forces

We now study dry, ambient and wet 1:2 ChCl:EG with varying load whilst applying a shearing motion across the film.

Dry

The frictional response of dry 1:2 ChCl:EG is shown in Figure 5.7(a). The surface separation and shear force, F_{S}, as a function of F_{N} are shown in the top and bottom plots in Figure 5.7, respectively. At large separations, there is a negligible shear force. As the separation decreases, molecular layers and discrete steps in the F_{S}-F_{N} profile are observed.

As mentioned in Section 3.2, these steps occur as a result of the oscillatory structural force which gives rise to discontinuities in D-F_{N}. These are attributed to a different number of molecular layers in the confined film and as this number varies, the contribution from the adhesive force, F_{adh}, between the surfaces changes,

$$F_{\mathrm{S}}^{i} = \mu F_{\mathrm{N}}^{i} + \alpha^{i}\left(\frac{A^{i}F_{\mathrm{adh}}^{i}}{\pi d^{i} R}\right). \qquad \text{(3.5 revisited)}$$

By measuring the surface separation and shear forces concurrently, any changes in the observed frictional response can be directly attributed to the change in film thickness.

Within each layer F_{S} increases quasilinearly with F_{N}, with a gradient corresponding to the friction coefficient. In dry 1:2 ChCl:EG the observed friction coefficients are superlubric (arbitrarily defined as $\mu < 0.01$) at all measured loads.

Ambient

The change in surface structure across ambient 1:2 ChCl:EG (Figure 5.3) is reflected in the frictional response shown in Figure 5.7(b). In the outermost layer (i), the friction coefficient remains superlubric. However, when entering (ii) the EG layer, the friction coefficient increases by an order of magnitude to $\mu = 0.03$, and for the innermost layer (iii) the friction coefficient increases by another order of magnitude to $\mu = 0.12$.

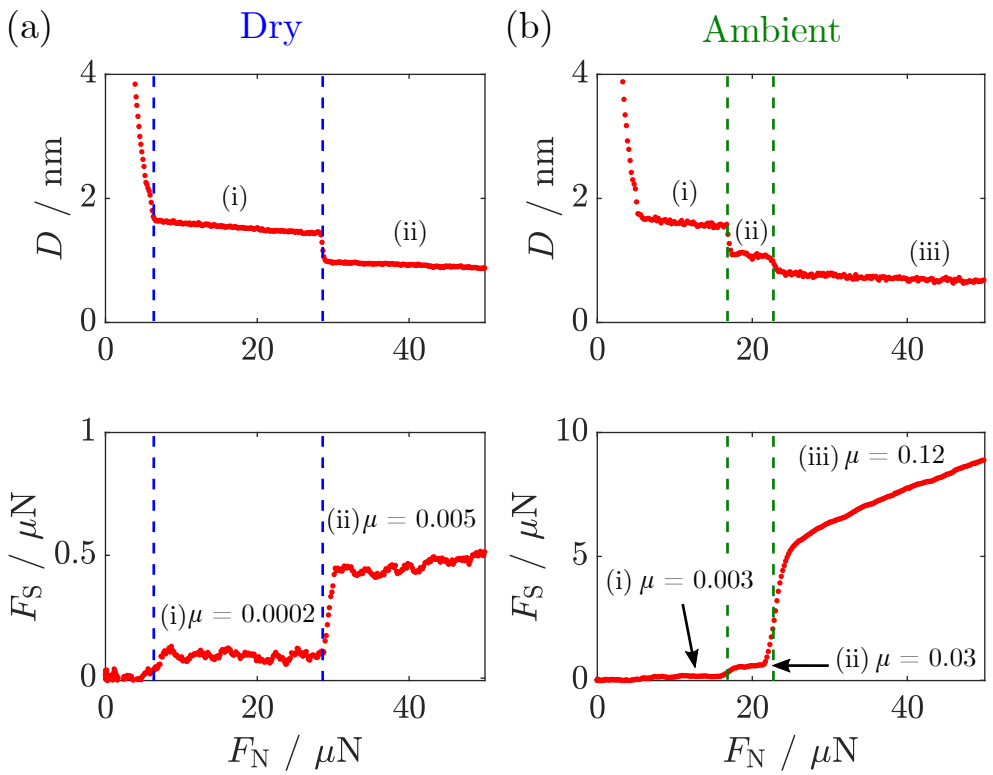


Figure 5.7 Representative surface separation, D, (top plots) and shear force, F_S, (bottom plots) as a function of increasing normal force, F_N, across (a) dry and (b) ambient 1:2 ChCl:EG. The vertical dashed lines highlight the simultaneous discrete steps in surface separation and shear force with normal force. (a) bottom plot: the friction coefficients of layers (i) and (ii) in dry 1:2 ChCl:EG are $\mu = 0.0002$ and $\mu = 0.005$, respectively. (b) bottom plot: the friction coefficients of layers (i), (ii), and (iii) in ambient 1:2 ChCl:EG are $\mu = 0.003$, $\mu = 0.03$, and $\mu = 0.12$, respectively. The frictional response shown is representative of multiple repeat measurements and is qualitatively reproducible. Note: small changes in composition, mica alignment, temperature and contact geometry can influence the calculated friction coefficients by up to a factor of 2.[1]

Wet

Across wet samples of 1:2 ChCl:EG, the change in surface structure is also highlighted in the frictional response shown in Figure 5.8. In both samples, two friction coefficients are observed with increasing load. The friction coefficients of layers (ii) in Figures 5.8(a) and (b) are maintained up to high load. When the innermost layer is accessed at $F_N > 500$ μN (not shown), F_S exceeds the limit of our setup ($F_{S,max} \approx 110$ μN) and we are unable to access the corresponding friction coefficient on approach.

For 30 wt% water (Figure 5.8(a), bottom plot) the friction coefficient in the outermost layer (i) remains superlubric, increasing by 3 orders of magnitude in the penultimate layer (ii). There is also a significant increase in F_S at the (i) to (ii) transition, which is indicative of a more liquid-like layer becoming more solid-like upon confinement.

For 50 wt% water (Figure 5.8(b), bottom plot) the friction coefficients in the (i) outermost and (ii) penultimate layers remain superlubric up to high loads.

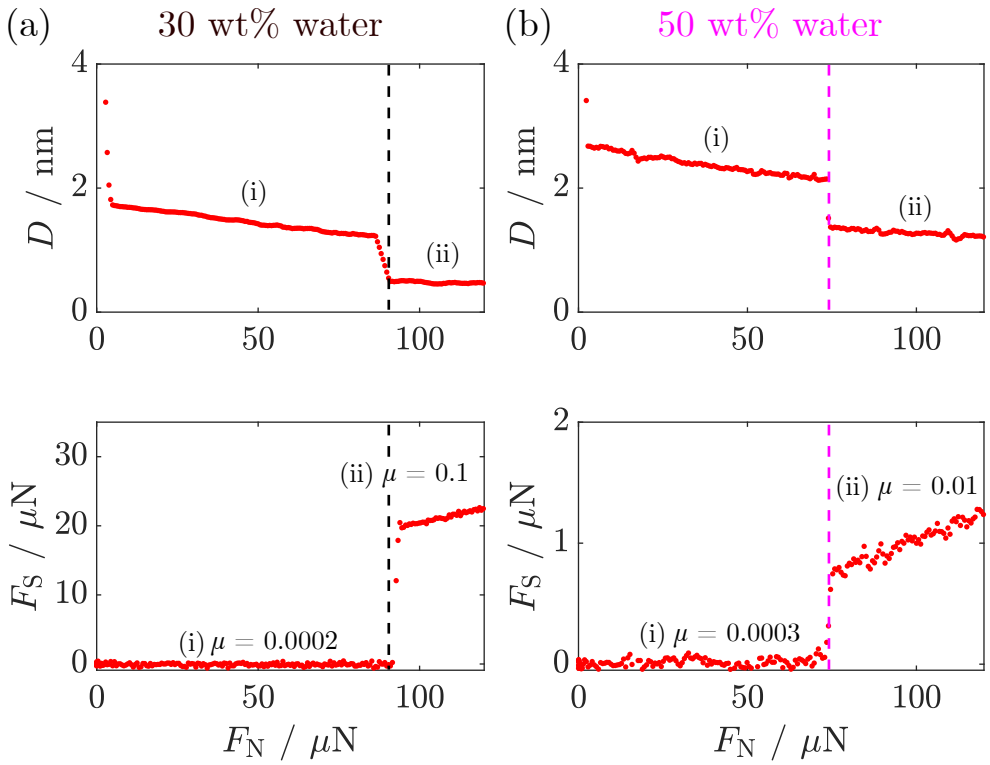


Figure 5.8 Representative surface separation, D, (top plots) and shear force, F_S, (bottom plots) as a function of increasing normal force, F_N, across 1:2 ChCl:EG with (a) 30 wt% and (b) 50 wt% water. The vertical dashed lines highlight the simultaneous discrete steps in surface separation and shear force with normal force. (a) bottom plot: the friction coefficients of layers (i) and (ii) in 30 wt% water 1:2 ChCl:EG are $\mu = 0.0002$ and $\mu = 0.1$, respectively. (b) bottom plot: the friction coefficients of layers (i) and (ii) in 50 wt% water 1:2 ChCl:EG are $\mu = 0.0003$ and $\mu = 0.01$, respectively. The frictional response shown is representative of multiple repeat measurements and is qualitatively reproducible. Note: small changes in composition, mica alignment, temperature and contact geometry can influence the calculated friction coefficients by up to a factor of 2.[1]

5.2 1:3 Choline Chloride:Ethylene Glycol

In this section, we present the normal and lateral forces across off-eutectic 1:3 ChCl:EG samples. For the off-eutectic samples, the 'fresh' samples were prepared at room temperature and pressure, and stirred overnight at 60 ^{o}C at atmospheric pressure. We measure the fresh sample then allow the liquid to equilibrate at atmospheric humidity in the SFB for more than 12 hours, after which time it is termed 'ambient'. It is assumed that the 'ambient' samples have a higher water content.

5.2.1 Normal Forces

The normal force profile across a fresh sample of 1:3 ChCl:EG is shown in Figure 5.9(a). The oscillatory force at $D < 3$ nm is indicative of molecular layering between the surfaces. Two layers are observed with a thickness of 0.50 $\pm$ 0.01 nm. Similar to dry 1:2 ChCl:EG, the layer dimension is determined by the short axis of the choline cation, corresponding to a checkboard-like configuration of cations, anions and EG (see schematic in Figure 5.9(c)).

The positions of the layers remain constant during the course of the measurement, whereas the magnitude of F_{N}/R is observed to decrease with time, as in Figure 5.9(b). This observation is likely a result of the influence of equilibration time, discussed in Section 3.1.1. We propose the force weakens with time as the confined structure is disrupted by either,

- water adsorbed during the course of the measurement, or
- the short time between approach-retraction cycles not allowing the mica to equilibrate fully, reducing the surface charge and leading to less robust layers.

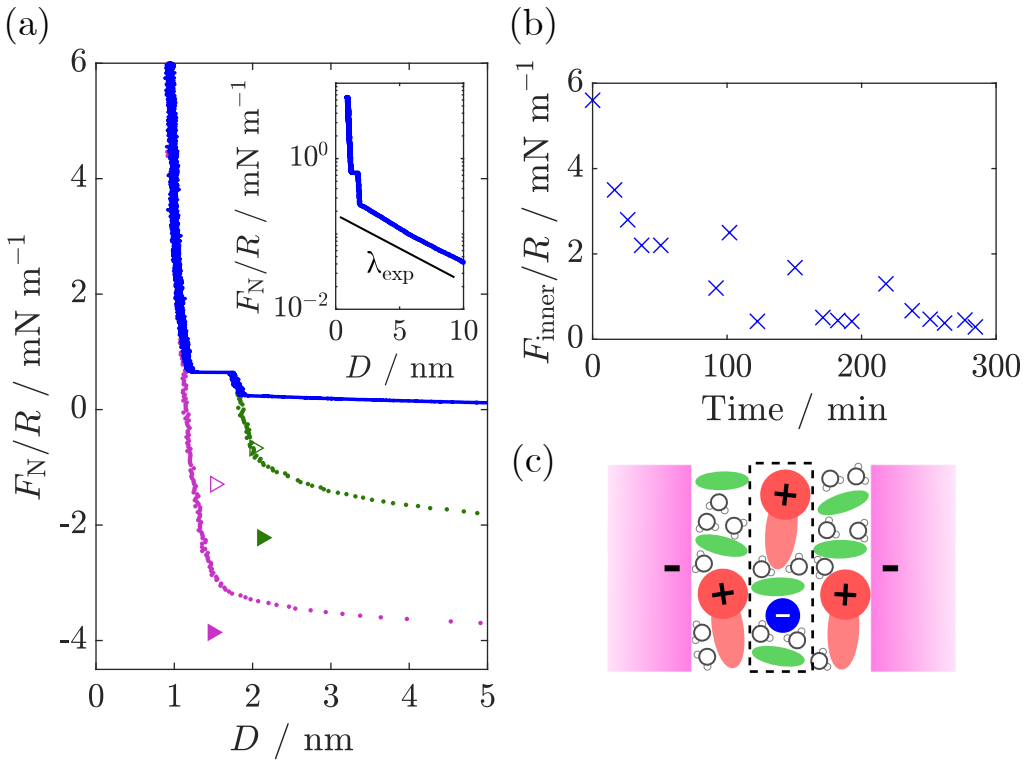


Figure 5.9 (a) Representative normal force, F_N, normalised by the radius of curvature, R, as a function of surface separation, D, profile in fresh 1:3 ChCl:EG. The profile on approach is shown in dark blue. Retractions from each observed layer allows the adhesive minima to be explored. The innermost and outermost layer retractions are shown in pink and green, respectively. The corresponding minimum adhesive force and jump out position for each layer are indicated by full pink and green triangles. The open triangles correspond to the adhesive minima when a lateral motion is applied. The inset shows a log-linear representation of the normal force on approach. The solid black line indicates the gradient of the long-range exponential decay where $\lambda_{exp} = 5.8 \pm 0.4$ nm. (b) Force at which the jump-in point to the innermost layer occurs, F_{inner}/R, as a function of time. (c) Proposed confined structure schematic determined using dimensional arguments. The negatively charged mica surfaces are shown in pink, ethylene glycol molecules in green, choline cations in red, chloride anions in blue, and water molecules in white and grey. The dashed black box indicates the squeeze-out repeat unit giving rise to steps in the force-distance profile.

On retracting the surfaces (Figure 5.9(a)), the magnitude of the adhesive force decreases when retracting from layers further away from the surface. The adhesive force minima are also weaker when a lateral motion is applied during the retraction due to shear-induced liquification.[100]

When the system is left to equilibrate for $>$ 12 hours, the surface structure changes considerably. Figure 5.10(a) shows that an oscillatory force is still observed

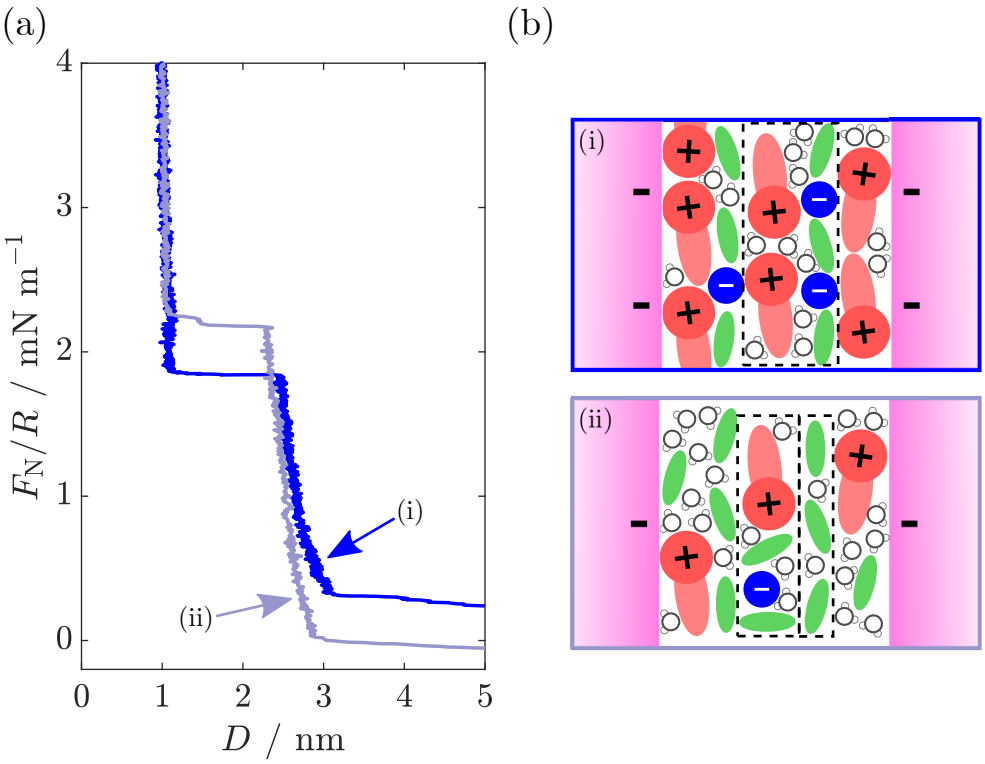


Figure 5.10 (a) Representative normal force, F_N, normalised by the radius of curvature, R, as a function of surface separation, D, profiles in ambient 1:3 ChCl:EG. The dark blue profile is representative of measurements taken in the first 45 minutes, the blue-grey profile is representative of measurements taken after the first 60 minutes. (b) Proposed confined structure schematics for (i) pre-45 minutes and (ii) post-60 minutes, determined using dimensional arguments. The negatively charged mica surfaces are shown in pink, ethylene glycol molecules in green, choline cations in red, chloride anions in blue, and water molecules in white and grey. The dashed black box indicates the squeeze-out repeat unit giving rise to steps in the force-distance profile.

at $D < 5$ nm. The force profiles taken in the first 45 minutes are represented by the dark blue line and show a single large layer of 0.80 $\pm$ 0.02 nm. Similar to the 24-hour equilibrated and wet 1:2 ChCl:EG, the layers are too large to be associated with a single molecular species and we instead propose alternating cation- and (anion+EG)-dominated layers, as schematised in Figure 5.10(bi).

After measuring for approximately 60 minutes (6 approach-retraction cycles), the surface structure changes and we observe the force profile given in blue-grey. The larger layer appears to split into two smaller layers of 0.23 $\pm$ 0.01 nm and 0.53 $\pm$ 0.01 nm, with the smallest layer sitting nearer the surface. These

dimensions are akin to those measured in ambient 1:2 ChCl:EG, where mixed composition layers are observed with a smaller EG layer neighbouring the choline cation Stern layer (see Figure 5.10(bii)).

This observation further supports our proposition that the mica surface equilibration time influences the surface structure. As we leave the system to equilibrate, the mica surface becomes more negatively charged and sufficiently large enough to template the alternating cation- and (anion+EG)-dominated layers observed initially. As the measurements continue, with short time between approach-retraction cycles, the mica cannot equilibrate fully and the surface charge becomes too low to template alternating cation- and anion-dominated layers. However, the charge is still significant enough that a choline cation Stern layer is required next to the surface, excluding an EG layer and returning to the mixed checkerboard-like layers observed in the fresh 1:3 sample (Figure 5.9).

5.2.2 Lateral Forces

The frictional response of fresh 1:3 ChCl:EG is shown in Figure 5.11. At large separations, the shear force is negligible. As the separation decreases, we observe molecular layers and discrete steps in the shear force-normal force profile as a result of the adhesive contribution (see Section 5.1.2).

Shear force increases quasilinearly within layers (i) and (ii), and we can determine superlubric friction coefficients of $\mu = 0.005$ and $\mu = 0.007$ in the outermost and innermost layers, respectively. In contrast to both 1:2 ChCl:EG and pure EG, the observed friction coefficients in 1:3 ChCl:EG layers are similar and greater confinement only influences the adhesive contribution to the shear force. We therefore suggest that shearing across 1:3 ChCl:EG nanofilms occurs via a similar sliding mechanism regardless of load or film thickness.

Quantised friction is evident from the shear force under negative applied loads shown for layer (ii) in black in the bottom plot of Figure 5.11, where multiple shear force values can be assigned to a single normal force. The friction coefficient on retraction from layer (ii), $\mu_R = 0.009$, is also comparable to μ on increasing load.

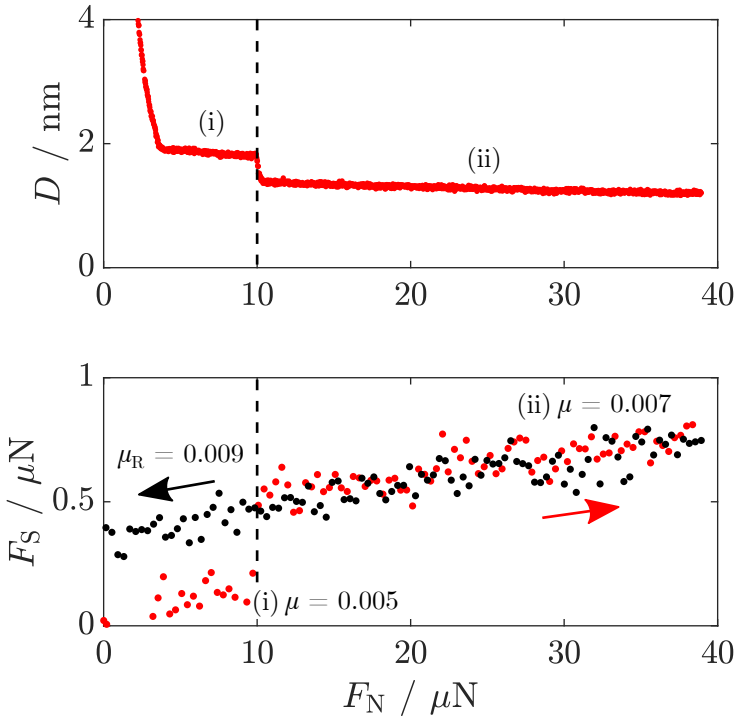


Figure 5.11 Representative surface separation, D, (top plot) and shear force, F_S, (bottom plot) as a function of increasing normal force, F_N, across 1:3 ChCl:EG. Two layers are observed in the top plot and are indicated by (i) and (ii). The corresponding friction regimes are indicated with the same labels in the bottom plot. The vertical dashed lines highlight the simultaneous discrete steps in surface separation and shear force with normal force. Bottom plot: F_S with increasing F_N is shown in red, the black line indicates F_S with decreasing F_N. Red and black arrows highlight the direction of applied load. The friction coefficient of layer (i) is $\mu = 0.005$. The friction coefficient of layer (ii) is $\mu = 0.007$ on approach and $\mu_R = 0.009$ on retraction. The frictional response shown is representative of multiple repeat measurements and is qualitatively reproducible. Note: small changes in composition, mica alignment, temperature and contact geometry can influence the calculated friction coefficients by up to a factor of 2.[1]

5.3 1:10 Choline Chloride:Ethylene Glycol

In this section, we present the normal and lateral forces across the 1:10 off-eutectic composition of ChCl:EG. For the off-eutectic samples, the 'fresh' samples were prepared at room temperature and pressure, and stirred overnight at 60 ^{o}C at atmospheric pressure. We measure the fresh sample then allow the liquid to equilibrate at atmospheric humidity in the SFB for more than 12 hours, after which time it is termed 'ambient'. It is assumed that the 'ambient' samples have a higher water content.

5.3.1 Normal Forces

Figure 5.12 shows the normal force profiles across fresh and ambient 1:10 ChCl:EG. Molecular layering is observed in both systems with comparable layer thicknesses of 0.425 $\pm$ 0.005 nm and 0.39 $\pm$ 0.01 nm in the fresh and ambient samples, respectively. The layer dimensions are comparable to both the short axis of the choline cation and the long axis of an ethylene glycol molecule. We propose two potential structures in Figure 5.12(c): (i) a mixed composition checkerboard-like layer and (ii) a pure EG layer. With a much higher concentration of EG in 1:10 ChCl:EG, we cannot discount the latter structure.

On retracting the surfaces (Figure 5.12(a): pink, green and cyan dotted lines), the magnitude of the adhesive force decreases when retracting from layers further away from the surface. The adhesive force minima are also weaker when a lateral motion is applied during the retraction due to shear-induced liquification.[100]

5.3.2 Lateral Forces

The frictional response of 1:10 ChCl:EG is shown in Figure 5.13. Shear force increases quasilinearly within layers (i) and (ii), and we can determine the friction coefficients as (i) $\mu = 0.0009$ and (ii) $\mu = 0.003$. Similar to 1:3 ChCl:EG, the

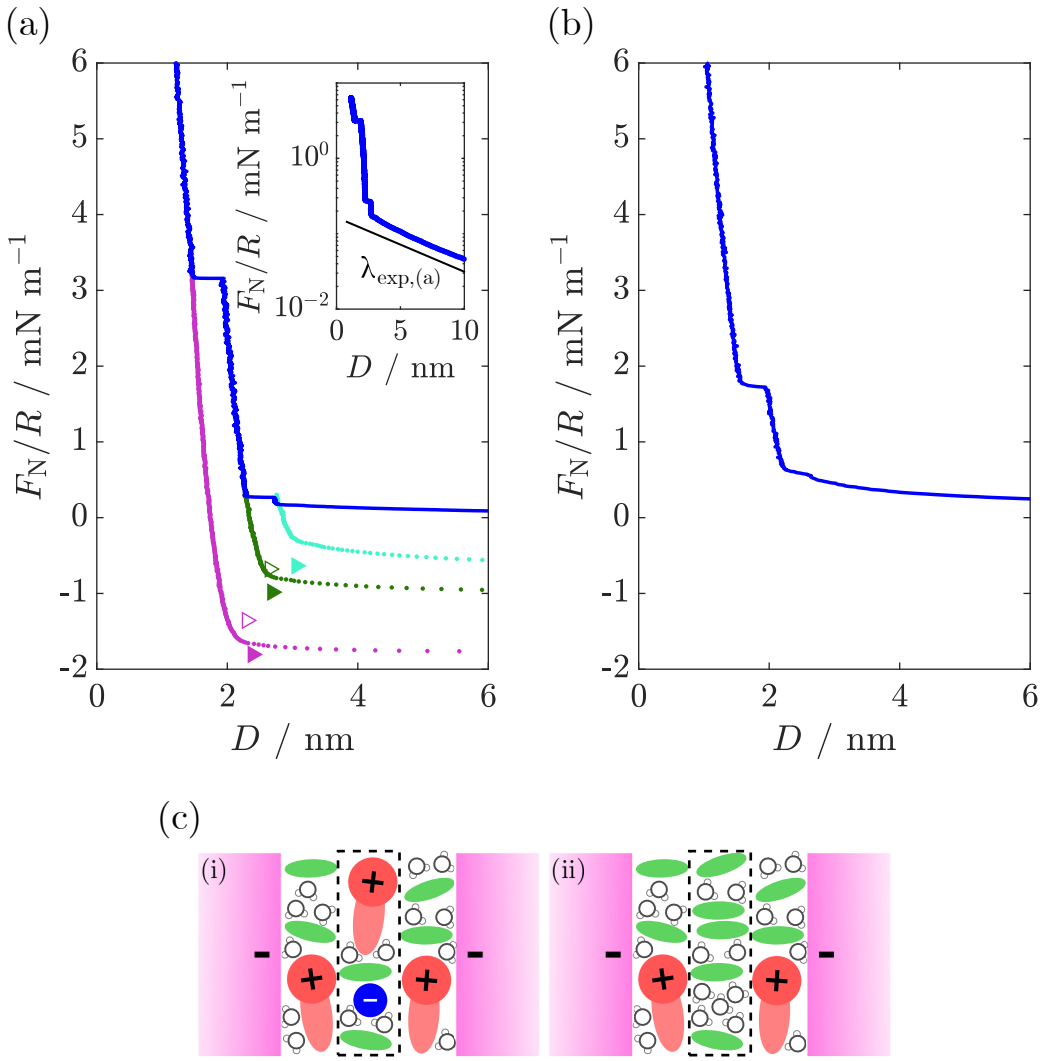


Figure 5.12 Representative normal force, F_N, normalised by the radius of curvature, R, as a function of surface separation, D, profiles in (a) fresh and (b) ambient 1:10 ChCl:EG. (a) The profile on approach is shown in dark blue. Retractions from each observed layer allows the adhesive minima to be explored. From near-surface layers to the outermost, retractions are shown in the following order: pink, green, cyan. The corresponding minimum adhesive force and jump out position for each layer are indicated by full pink, green and cyan triangles. The empty triangles correspond to the adhesive minima when a lateral motion is applied. The inset shows a log-linear representation of the normal force on approach. The solid black line indicates the gradient of the long-range exponential decay where $\lambda_{exp,(a)} = 8.0 \pm 0.3$ nm. (c) Two proposed confined structure schematics (i) and (ii), determined using dimensional arguments. The negatively charged mica surfaces are shown in pink, ethylene glycol molecules in green, choline cations in red, chloride anions in blue, and water molecules in white and grey. The dashed black box indicates the squeeze-out repeat unit giving rise to steps in the force-distance profile.

observed friction coefficients in 1:10 ChCl:EG layers are similar and greater confinement only influences the adhesive contribution to the shear force. We

therefore suggest that shearing across 1:10 ChCl:EG nanofilms also occurs via a similar sliding mechanism regardless of load or film thickness.

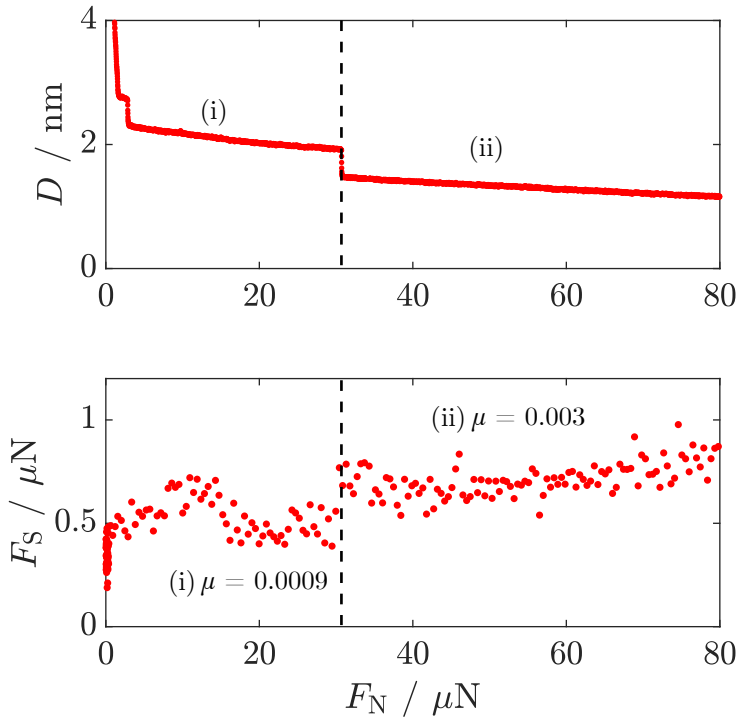


Figure 5.13 Representative surface separation, D, (top plot) and shear force, F_S, (bottom plot) as a function of increasing normal force, F_N, across 1:10 ChCl:EG. Two layers are observed in the top plot and are indicated by (i) and (ii). The corresponding friction regimes are indicated with the same labels in the bottom plot. The vertical dashed lines highlight the simultaneous discrete steps in surface separation and shear force with normal force. Bottom plot: F_S with increasing F_N is shown in red. The friction coefficient of layers (i) and (ii) are $\mu = 0.0009$ and $\mu = 0.003$, respectively. The frictional response shown is representative of multiple repeat measurements and is qualitatively reproducible. Note: small changes in composition, mica alignment, temperature and contact geometry can influence the calculated friction coefficients by up to a factor of 2.[1]

5.4 On- and Off-Eutectic ChCl:EG

In this chapter, normal and lateral forces across on- and off-eutectic mixtures of ChCl:EG have been studied. We will now discuss the observations with regards to the literature, and compare the properties of on- and off-eutectic mixtures under confinement.

5.4.1 Normal Forces

All force profiles exhibited an oscillatory force at short-range indicating the presence of molecular layering. The surface structures in 1:2 ChCl:EG were highly dependent on the water content and the equilibration time. 1:3 ChCl:EG also exhibited an equilibration time dependence. Similarities in the structures were observed with the mixed checkerboard-like layers (see Figure 5.4(b)) potentially being a common structure amongst the studied systems. We note that all suggested 1:2 ChCl:EG structures were also observed in 1:3 ChCl:EG.

Previous measurements across confined 1:2 ChCl:EG nanofilms have been conducted with AFM at graphite[65] and platinum[67] electrodes with varying potential and water content. At graphite between +1 and -0.5 V, the final observed layer ($\approx$ 0.3 nm) can be attributed to the EG molecule. When the potential reaches -1 V, the structure changes and the final step (0.45 nm) can be discerned as a choline cation enriched layer.[65] In contrast, at a platinum electrode, positive potentials yield a layer of thickness 0.45 nm and negative potentials yield a layer of thickness 0.25 nm. On addition of water to 1:2 ChCl:EG at a platinum electrode, the structure at open circuit potential changes dramatically. A single layer of thickness $\approx$ 0.5 nm is observed for the dry case but the addition of 10 wt% water increases the step size to 1 nm and this is maintained up to 50 wt% water. When a positive or negative potential is applied to the wet samples, the layering structure is no longer observed.[67]

Similar structures are observed in both SFB and AFM measurements of dry and ambient 1:2 ChCl:EG. On the other hand, in the wet samples, we clearly observe strong layering between the negatively charged mica surfaces. It should be noted that SFB and AFM can result in different observations, as shown by Cheng *et al.*[132] across ionic liquids, but the larger contact area in SFB measurements is more representative of the electrode-DES interfacial structure.

Long-ranged forces were observed with anomalously long decay lengths in dry, ambient, 30 wt%, and 50 wt% 1:2 ChCl:EG systems, that decreased with added water. This behaviour is consistent with literature reports of underscreening-like behaviour previously observed in ionic liquids.[33,131] In the 1:3 and 1:10 ChCl:EG systems we also observe anomalously long decay lengths. The underscreening phenomenon would lead us to predict that the decay length should decrease with increasing EG content, however this is not the case for 1:2 ($\lambda_{\text{exp}} = 12 \pm 1$ nm), 1:3 ($\lambda_{\text{exp}} = 5.8 \pm 0.4$ nm) and 1:10 ChCl:EG ($\lambda_{\text{exp}} = 8.0 \pm 0.3$ nm). Although Christenson and Horn[48] show the decay length in EG decreases on addition of LiCl, the influence of low concentrations of ChCl in EG should be explored before definitively concluding the presence of underscreening in ChCl and EG mixtures.

5.4.2 Lateral Forces

In 1:2 ChCl:EG, the frictional response strongly depends on the amount of water that is present. In the dry case, we observe superlubric coefficients of friction at all measured loads. This behaviour is also observed for 50 wt% water. In contrast, we observe significantly higher friction coefficients in the ambient and 30 wt% water samples. As we add more water to 1:2 ChCl:EG, an unusual re-entrant superlubric behaviour is observed.

It has been reported that the addition of water to the DES formed by 1:2 ChCl:Urea initially enhances the hydrogen bond network and retains the same structure until ≈ 42 wt% water is added.[130] Beyond this point the DES structure is disrupted and is more akin to a solution containing the DES constituents. We therefore suggest the water in the ambient and 30 wt% samples increases the coefficients of friction by: (a) a change in the surface structure altering the active shear plane, or (b) increasing the resistance to sliding through an enhanced hydrogen bond network. As we reach 50 wt% water, the water is no

longer incorporated into the DES structure and subsequently does not enhance the hydrogen bond network. Instead, we suggest a less well defined structure comprising both water-in-DES and DES-in-water domains. Again, the active shear plane may change, or the DES-in-water regions may enhance the in-plane fluidity, consequently reducing the friction coefficient. This hypothesis supports the weaker magnitude of F_{S} observed in 50 wt% water samples when compared to 30 wt% water samples.

Lubrication across DESs is of interest in the marine industry where it is preferable to have biodegradable lubricants that do not have adverse effects on water systems or contribute to water pollution.[124] The miscibility of 1:2 ChCl:EG with water makes this system ideal for such applications. The lubrication properties of 1:2 ChCl:EG have been studied across steel/steel yielding $\mu = 0.017 - 0.31$.[123–126] On addition of graphene to 1:2 ChCl:EG, the friction coefficient decreases from $\mu = 0.017$ to 0.01.[126] Friction coefficients using steel/aluminium, steel/bronze, and steel/copper surfaces have also been reported where $\mu = 0.15$, 0.58, and 0.59, respectively.

Our observations show much lower friction coefficients in all systems at the lowest loads ($F_{\mathrm{N}} < 20 - 90$ μN), and also at higher loads in dry 1:2 ChCl:EG (see Figures 5.7 and 5.8). In the ambient, 30 wt%, and 50 wt% water samples the friction coefficients at higher loads ($F_{\mathrm{N}} > 20 - 90$ μN) are comparable with the literature range observed across steel/steel. The discrepancy between the low load and dry 1:2 ChCl:EG work, and the literature is likely due to differences in DES composition, surface composition, temperature and setup geometry.[1]

It has also been suggested that the eutectic composition of ChCl:EG gives rise to optimal friction.[124] We can test this hypothesis by comparing the frictional response across pure EG, dry 1:2, 1:3, and 1:10 ChCl EG. Figure 5.14 compares F_{S}-F_{N} profiles across these systems. At $F_{\mathrm{N}} < 80$ μN (Figure 5.14 inset), the

friction coefficients across dry 1:2, 1:3, 1:10 and dry EG are comparable and superlubric. We can therefore conclude the proportion of ChCl in the ChCl:EG mixture does not influence the overall lubrication properties, and the similarity to pure EG may indicate behaviour dominated by shearing of EG domains. As dry 1:2, 1:3 and 1:10 are comparable, and higher friction coefficients are observed in ambient 1:2, the suggestion that trace water in 1:2 ChCl:EG influences the active shear plane or enhances the hydrogen bonding is supported. It is clear from Figure 5.14 that ambient EG has superior lubricating properties.

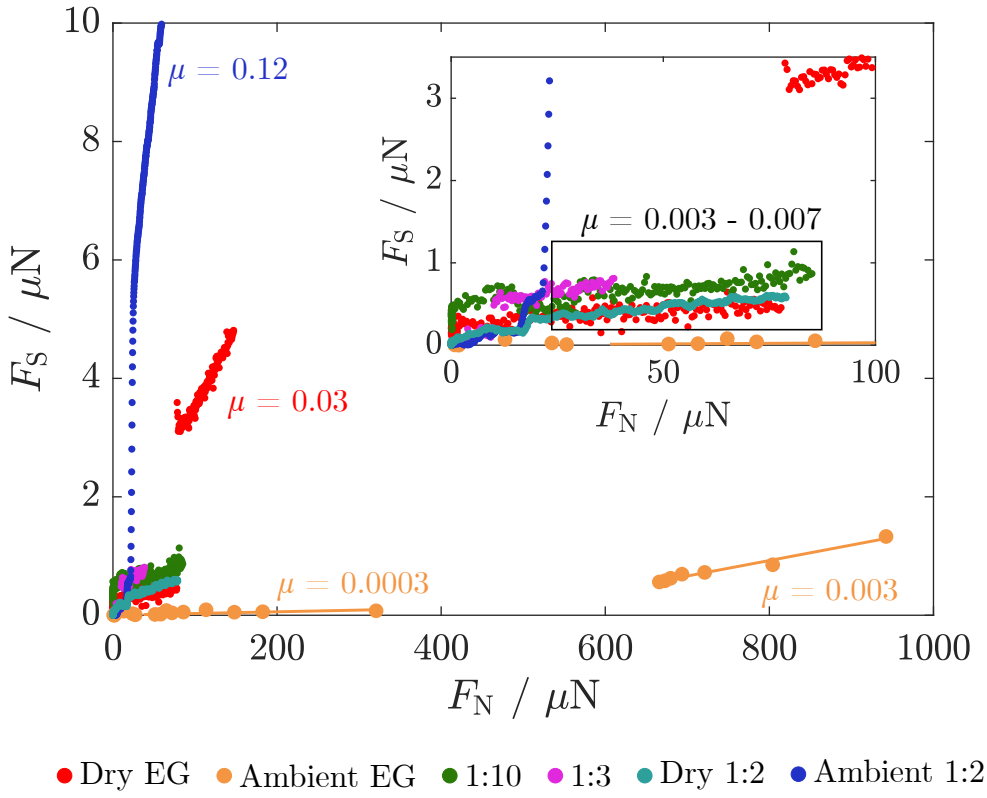


Figure 5.14 Representative shear force, F_S, as a function of the normal force, F_N, across dry (red) and ambient (orange) ethylene glycol, 1:10 ChCl:EG (green), 1:3 ChCl:EG (pink), dry 1:2 ChCl:EG (blue-grey), and ambient 1:2 ChCl:EG (blue). The friction coefficients at high load and high F_S are shown in the main figure: innermost layer of ambient 1:2 ChCl:EG, $\mu = 0.12$; innermost layer of dry EG, $\mu = 0.03$; friction in ambient EG, $\mu = 0.0003$ and $\mu = 0.003$. The inset shows F_S over the range $F_N = 0 - 100$ μN. In this range dry EG, 1:10 ChCl:EG, 1:3 ChCl:EG, and dry 1:2 ChCl:EG show friction coefficients of comparable magnitude between $\mu = 0.003 - 0.007$. Note: small changes in composition, mica alignment, temperature and contact geometry can influence the calculated friction coefficients by up to a factor of 2.[1]

In Figure 5.15, the F_S-F_N profiles are shown for dry and ambient EG, dry and 50 wt% water 1:2 ChCl:EG, and 1:3 ChCl:EG. The results for 30 wt% water are not shown for clarity but to recall $\mu = 0.0002$ when $F_N < 90$ μN, and $\mu = 0.1$ between $F_N = 90 - 450$ μN and $F_S > 20$ μN (Figure 5.8). At higher loads, as per Figure 5.15(a), we see that μ is lowest in ambient EG. Figure 5.15(b) shows F_S-F_N profiles when $F_N < 120$ μN and we notice superlubric behaviour in all systems. Very low friction coefficients are observed across 30 wt% and 50 wt% water 1:2 ChCl:EG when $F_N < 70$ μN, and ambient EG at all loads studied.

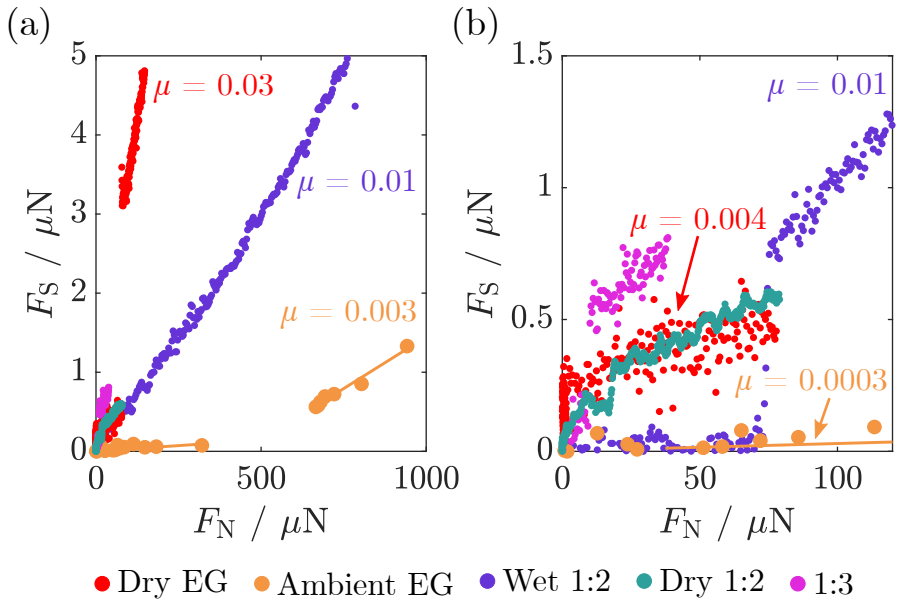


Figure 5.15 Representative shear force, F_S, as a function of the normal force, F_N, across dry (red) and ambient (orange) ethylene glycol, 50 wt% water 1:2 ChCl:EG (purple), dry 1:2 ChCl:EG (blue-grey), 1:3 ChCl:EG (pink). (a) and (b) show the profiles on different scales: $F_N = 0 - 1000$ μN and $F_N < 120$ μN, respectively. Note: small changes in composition, mica alignment, temperature and contact geometry can influence the calculated friction coefficients by up to a factor of 2.[1]

Figures 5.14 and 5.15 highlight the frictional behaviour across on- and off-eutectic ChCl:EG DESs. It is clear that the on-eutectic composition does not give rise to optimal friction, and that ambient EG has far superior lubricating properties compared with dry EG and the studied ChCl:EG DESs. Although the ChCl:EG DESs do not outperform pure EG, they are advantageous in applications that rely on electrolytic lubricants *e.g.* electrotunable friction.[133]

Chapter 6

Nanostructure of Deep Eutectic Solvents (II)

This chapter will focus on the eutectic mixture of 1:2 choline chloride (ChCl) and glycerol (Gly).[134] Molecular structures of the components are shown in Figure 6.1.

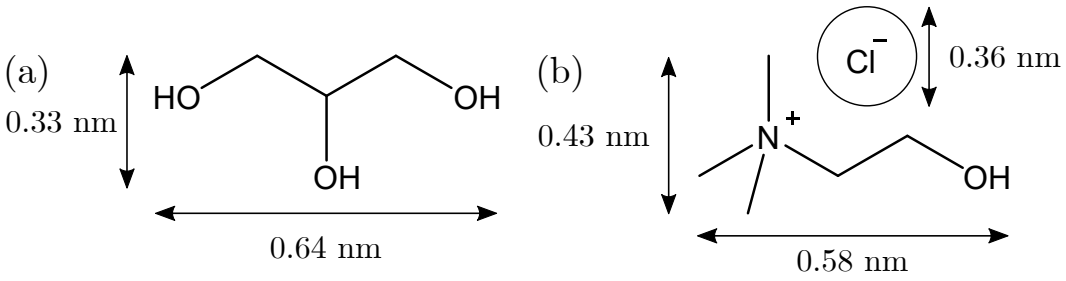


Figure 6.1 Molecular structure and approximate dimensions of (a) glycerol and (b) choline chloride.[65,127]

Similar to 1:2 ChCl:EG, structural forces and lubrication properties of 1:2 ChCl:Gly have been studied previously.[65,67,124,125,135] Measurements across confined 1:2 ChCl:Gly have been made using AFM at both platinum[67] and graphite[65] electrodes. The innermost step was attributed to glycerol in the case of platinum at negative potentials ($\approx$ 0.3 nm) and graphite at potentials of +1 to -0.5 V ($\approx$ 0.4 nm). Choline enriched layers ($\approx$ 0.45 nm) were observed at positive potentials,

including open circuit potential (OCP), at platinum and at graphite at -1 V. When comparing 1:2 ChCl:Gly and 1:2 ChCl:EG at a platinum electrode, it was noted that a larger number of layers was observed in the presence of glycerol suggesting a difference in the hydrogen bond structure.[67] Addition of water to 1:2 ChCl:Gly (at OCP) enhanced the layering structure up to 30 wt% water. The near-surface layer was still attributed to a choline-enriched structure, however layers further out were substantially larger ($\approx$ 0.9 nm) suggesting that associations between the DES components are stronger in the presence of water. On the application of a potential across the 30 wt% water sample, the layering structure was disrupted and a number of weaker, thinner layers ($\approx$ 0.3 nm at OCP -0.25 V) were observed.[67]

1:2 ChCl:Gly is also water-miscible and a suitable candidate for biodegradable lubricants in the marine industry and as industrial gear oils. Coefficients of friction have been reported across steel/aluminium, $\mu = 0.55$, steel/bronze, $\mu = 0.4$, steel/copper, $\mu = 0.45$, and steel/steel, $\mu = 0.35$.[124,125]

In this chapter we will study the normal and lateral forces across dry and ambient 1:2 ChCl:Gly nanofilms, before considering the influence of added water on the observed normal forces. We will discuss our results with regards to the observations made in the pure solvent, 1:2 ChCl:EG, and the literature measurements throughout.

6.1 Normal Forces

Glycerol has substantial viscosity, so we begin with a discussion of the influence of viscous forces on normal force measurements, highlighted in Figure 6.2. Normal force-distance profiles across dry and ambient 1:2 ChCl:Gly are shown in Figure 6.3. We measure samples that have been prepared in two different ways and clarify the terminology used in this section below.

Dry. Prepared using anhydrous reagents. The mixture was stirred under a nitrogen atmosphere, and the resulting liquid also stored under nitrogen. The sample was injected between the lenses and studied with a phosphorus pentoxide desiccant in the air-tight SFB.

Ambient. The **dry** sample is allowed to equilibrate with the mica surfaces for more than 12 hours in the SFB. The chamber is open to atmospheric humidity.

Wet. Different weight percentages of ultrapure water are added to the DES.

It is assumed that the water content increases as follows: dry, ambient, wet.

6.1.1 Viscous Forces

Dry 1:2 ChCl:Gly is a viscous liquid with viscosity $\eta = 376$ mPa s at 20 ^{o}C.[81] Using the comparison factors in Chapter 2, we can estimate the velocity at which viscous forces dominate the total measured force, as in Table 6.1. As we cannot easily approach at velocities less than 0.1 nm s^{-1}, it is expected our results across dry 1:2 ChCl:Gly will often be dominated by viscous forces in particular at large surface separation where the equilibrium forces are small.

Table 6.1 Approach velocities in 1:2 ChCl:Gly corresponding to three force regimes for $R = 1$ cm. High and low regimes correspond to hydrodynamic and electrostatic forces dominating, respectively. The intermediate regime corresponds to a combination of hydrodynamic and electrostatic forces.

Regime	Velocity / nm s^{-1}
High	7.3
Intermediate	0.087
Low	0.019

Figure 6.2 highlights the influence of viscous forces across 1:2 ChCl:Gly nanofilms. At high velocity, we can fit the observed distance-time profile (Fig-

ure 6.2(a)) to a purely hydrodynamic force,

$$F_{\text{hydro}} = -\frac{6\pi\eta R^2 v}{D-b}. \qquad \text{(4.1 revisited)}$$

The fit is shown in orange and the negative slip length, $b \approx 1.2 - 1.6$ nm. Figure 6.2(b) shows a representative force profile on a log-linear scale. We do not observe a linear decay and instead the decay appears to be curved due to the dominant viscous forces that cannot be avoided. Finally, Figure 6.2(c) shows the normal force-separation profiles on retracting from the observed layers. As we do not know if viscous forces contribute to the overall force profile on retracting, it would be erroneous to quantitatively discuss the magnitude of the adhesive minima. It is also difficult to define the surface separation at which the jump out point occurs. As a result of the viscous forces, we may not be able to quantitatively describe all force profile features. However, it will be possible to make observations at small distances, when the change in separation with time is small and so viscous forces becomes negligible.

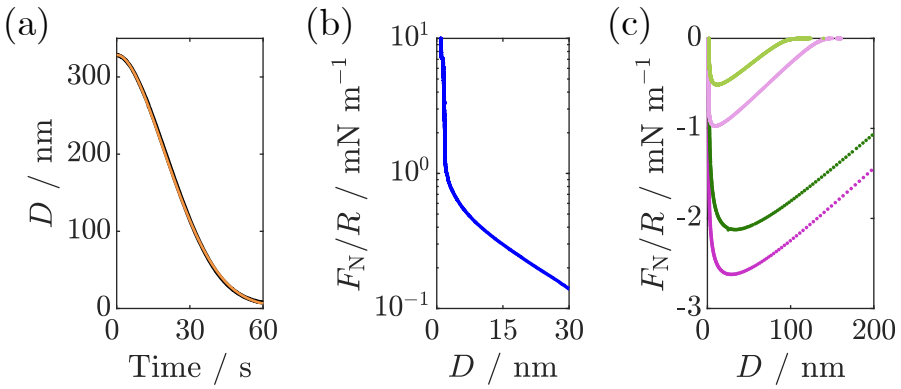


Figure 6.2 The influence of viscous forces across 1:2 ChCl:Gly nanofilms. (a) Representative surface separation, D, as a function of time at high velocity, v, (black) and the fitted D-time profile assuming a purely viscous force (orange) where $v = 22.4$ nm s^{-1} and the negative slip, $b \approx 1.2 - 1.6$ nm. (b) Log-linear representation of a representative normal force-surface separation profile in 1:2 ChCl:Gly. Even at lower velocities it is difficult to deconvolute any potential long-range electrostatic force from the viscous force. (c) Normal force-separation profiles on retracting from the observed layers. Retractions, from the innermost and outermost layers are shown in pink and green, respectively. The lighter pink and green correspond to retractions from the same layers as the darker pink and green, respectively, but with a lateral motion applied simultaneously.

6.1.2 Structural Forces

Despite the viscous effects mentioned above, we are able to resolve features at small D with some clarity due to the larger equilibrium forces which dominate above viscous effects in this regime. The force profiles in Figure 6.3 show oscillatory forces indicative of a layering structure between the surfaces in both dry and ambient 1:2 ChCl:Gly samples.

The force profiles show two steps, one with a weaker amplitude at $F_{\mathrm{N}}/R < 1$ mN m^{-1} and one with a larger amplitude at $F_{\mathrm{N}}/R \approx 5 - 7$ mN m^{-1}. The two steps are separated by a region of continuous squeeze-out. The step dimensions are $\Delta_{\mathrm{J}} = 0.33 \pm 0.02$ nm and 0.49 ± 0.01 nm in the dry and ambient samples, respectively, whilst the squeeze-out extends over $\Delta_{\mathrm{C}} \approx 1$ nm. From the change in step dimension with exposure to atmospheric humidity, it is clear that a structural change has occurred. In dry 1:2 ChCl:Gly, the layer thickness corresponds well with the short dimension of the glycerol molecule in Figure 6.1(a). When the system is exposed to atmospheric humidity and a long equilibration time, the dimension increases and is large enough to be accounted for by the choline cation.

Neutron diffraction measurements and simulations of 1:2 ChCl:Gly by Turner and Holbrey [136] indicated the network of Gly-Gly hydrogen bonds present in pure Gly is retained in 1:2 ChCl:Gly. We therefore suggest that the steps (Δ_{J}) observed in the dry sample are predominantly due to glycerol molecules. Similar to the equilibration dynamics discussed in Chapter 5, the concentrated DES environment may increase the time for potassium ion dissolution, hence increasing the mica surface charge equilibration time. This effect may be amplified further by the high viscosity which will reduce molecular mobility.

After an extended equilibration period at large distance and exposure to atmospheric humidity, the mica surface charge equilibrates (becoming more neg-

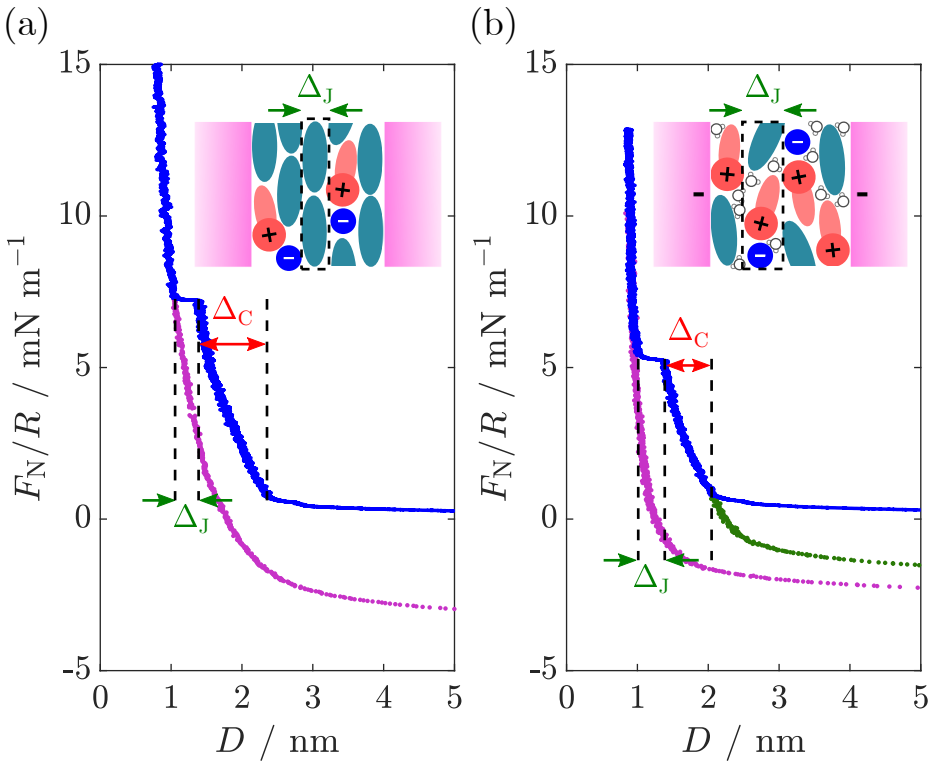


Figure 6.3 Representative normal force, F_N, normalised by the radius of curvature, R, as a function of surface separation, D, profiles in (a) dry and (b) ambient 1:2 ChCl:Gly. The jump-in separation, Δ_J, and layer compression, Δ_C, are shown in green and red, respectively. The innermost and outermost layer retractions are shown in pink and green, respectively. Proposed confined structure schematics determined using dimensional arguments are shown. The (negatively charged) mica surfaces are shown in pink, glycerol molecules in blue-grey, choline cations in red, chloride anions in blue, and water molecules in white and grey. The dashed black box indicates the squeeze-out repeat unit giving rise to steps in the force-distance profile.

atively charged) and the structure changes from glycerol-dominated layers to a mixed composition checkerboard-like structure as shown in Figures 6.3(a) and (b), respectively. This structural transition is observed at a graphite electrode when a more negative potential is applied which mimics the mica surface charge behaviour suggested here.[65]

In both Figures 6.3(a) and (b), the point of closest approach was at $D = 1$ nm, which is comparable to the fitted negative slip length (Section 6.1.1). We propose that the point of closest approach observed corresponds to the thickness of an immovable solid-like layer of molecules at the surface that cannot be squeezed out

over the normal loads applied here. In Chapter 4, the final observed layer in pure glycerol (before reaching mica-mica contact) also sat at $D \approx 1$ nm, and was only removed at higher loads, $F_N/R \approx 800$ mN m^{-1}.

At the jump-in point to the innermost layer, the magnitude of F_N/R is less in the ambient sample compared with the dry. Both glycerol and choline chloride are hygroscopic so adsorbed water could weaken the layering structure, but this does not corroborate the observations by Hammond *et al.*[67] where increased water content strengthened the interfacial structure. The proposed change in layering structure could result in confined layers that are weaker than those that are dominated by Gly, as the Gly-Gly hydrogen bond network is disrupted.

As mentioned in Section 6.1.1, we should only qualitatively discuss the adhesive minima. On retracting the surfaces, the adhesive force minima decrease when retracting from layers further away from the surface due to a weaker confinement. It is also apparent that the adhesive minimum of the innermost layer is weaker in the ambient sample. This further supports the proposed change to a weaker structure.

6.2 Lateral Forces

We now study dry and ambient 1:2 ChCl:Gly under confinement when a shearing motion is applied across the film.

The frictional response of dry 1:2 ChCl:Gly is shown in Figure 6.4. At large separation, there is a negligible shear force. As the separation decreases in the top plot of Figure 6.4(a), two molecular layers are observed and simultaneous discrete steps in the F_S-F_N profile are measured in bottom plot. The discrete steps arise from the discontinuities in D-F_N, that are attributed to a different number of molecular layers in the confined film (see Section 3.2). As the number of molecular

layers varies, the contribution from the adhesive force between the surfaces changes. Measuring the surface separation and shear forces concurrently means that any changes in the observed frictional response can be directly attributed to the change in film thickness.

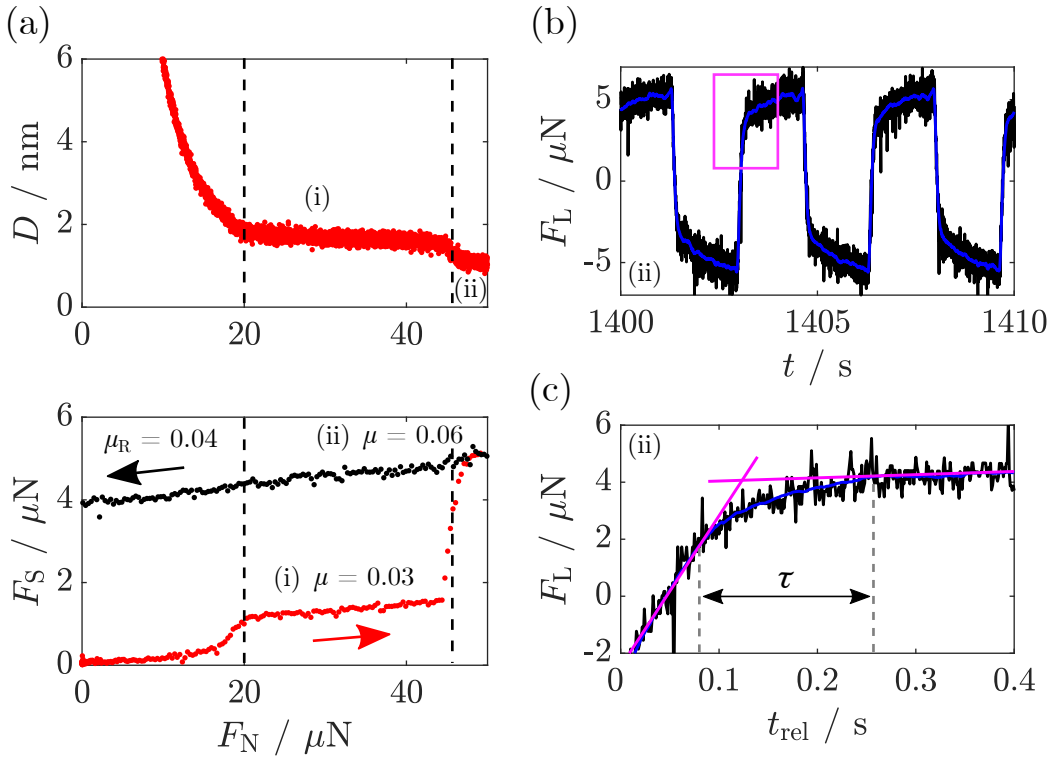


Figure 6.4 Representative (a) surface separation, D, (top plot) and shear force, F_S, (bottom plot) as a function of the normal force, F_N, across dry 1:2 ChCl:Gly. Bottom plot: F_S with increasing F_N is shown in red, the black line indicates F_S with decreasing F_N. Red and black arrows highlight the direction of applied load. The friction coefficient of layer (i) is $\mu = 0.03$. The friction coefficient of layer (ii) is $\mu = 0.06$ on approach and $\mu_R = 0.04$ on retraction. The vertical dashed lines in (a) highlight the simultaneous discrete steps in surface separation and shear force with normal force. (b) Lateral friction signal, F_L, as a function of time in layer (ii), with and without a smoothing filter in blue and black, respectively. The signal within the pink box is shown in (c) highlighting the viscous, liquid-like lateral friction signal that relaxes between the elastic and plastic regimes (pink lines) with time, $\tau \approx 0.2$ s. The frictional response shown is representative of multiple repeat measurements and is qualitatively reproducible. Note: small changes in composition, mica alignment, temperature and contact geometry can influence the calculated friction coefficients by up to a factor of 2.[1]

The gradient of the linear regions in the bottom plot of Figure 6.4(a) corresponding to layers (i) and (ii), yield friction coefficients of $\mu = 0.03$ and $\mu = 0.06$, respectively. It should also be noted that the friction coefficients in different

molecular layers are comparable and greater confinement only influences the adhesive contribution to the shear force.

Under negative applied loads, the friction coefficient on retraction is found to be $\mu_{\mathrm{R}} = 0.04$, as in the bottom plot of Figure 6.4(a). The friction coefficient on retraction is comparable to that on approach, and this quantised friction behaviour is a result of molecular layering (discussed in Section 3.2). The adhesive minima are weaker when a shearing motion is applied simultaneously to the normal motion due to shear-induced liquification (see Figure 6.2).[100]

The lateral force trace during three back-and-forth shearing cycles in layer (ii) is plotted in Figure 6.4(b). The portion of the signal highlighted by the pink square is shown in Figure 6.4(c), and is instead plotted as a function of relative time to highlight the timescale of relaxation, τ. A distinct curvature is observed when transitioning from the elastic to the plastic regime in the lateral force-time profile with a relaxation time, $\tau \approx 0.2$ s. This relaxation behaviour is typical of a viscous, liquid-like film.[36,89]

The relaxation time observed in Figure 6.4(c) can be compared with the predicted relaxation timescale expected in a Couette flow (as per Section 4.2.1).[84,89,102] Couette flow arises when two undeformable planar surfaces move laterally with respect to one another across an incompressible liquid film, where the fluid is a viscous, charge-less, Newtonian liquid, with a no-slip boundary condition.[89] The force opposing the lateral motion is purely viscous, and this can be balanced with the restoring force of the vertical leaf spring in the SFB. It should be noted that the conditions in our measurements are not fully described by a Couette flow, for example 1:2 ChCl:Gly does observe a slip length, however it provides us with a point of comparison. The relaxation timescale in a Couette flow is given by

$$\tau_{\mathrm{Couette}} \approx \frac{A\eta}{k_{\mathrm{s}} D_{\mathrm{liq}}}. \qquad \text{(4.2 revisited)}$$

For a $D_{\text{liq}} = 1$ nm film of 1:2 ChCl:Gly ($\eta = 376$ mPa s at 20 ^{o}C)[81] between two planar surfaces ($A \approx 523$ μm^2)[89] and $k_{\text{s}} = 470$ N m^{-1}, $\tau_{\text{Couette}} \approx 0.4$ ms, roughly three orders of magnitude faster than the observed τ. We can also determine an effective viscosity, $\eta_{\text{eff}} \approx 480$ Pa s, from the observed value of τ. The confined liquid film appears to show an effective viscosity three orders of magnitude larger than bulk 1:2 ChCl:Gly. A similar observation has been reported using SFA measurements across ionic liquids by considering the drainage of the liquid from the confined region during the jump-in transitions.[118] In the work of Han and Espinosa-Marzal,[118] an effective viscosity two orders of magnitude larger than the bulk viscosity was reported in the confined film.

Figure 6.5 compares the frictional response across dry (red) and ambient (orange) 1:2 ChCl:Gly. Quantised friction is still apparent for the ambient sample with reduced F_{S} for the innermost layer. This supports the proposed ambient structure being weaker than the dry, and hence reducing the adhesive contribution to F_{S}. For the same layer in the dry and ambient samples, the friction coefficients are of comparable magnitude. For example, the innermost layers of the dry and ambient samples have $\mu = 0.06$ and $\mu = 0.05$, respectively. This leads us to conclude that the sliding mechanism in the dry and ambient samples does not change with equilibration time or atmospheric humidity.

Our results across dry and ambient 1:2 ChCl:Gly nanofilms show friction coefficients an order of magnitude lower than the literature values mentioned earlier ($\mu = 0.35 - 0.55$).[124,125] This could potentially be a result of a different DES composition, surface composition, temperature, and setup geometry.[1] We could also be exploring a different lubrication regime.[137] The observed coefficients do, however, corroborate well with the friction coefficients observed across pure glycerol (see Chapter 4). We suggest that the frictional behaviour is dominated by shearing of Gly domains, akin to the EG domains dominating the behaviour in

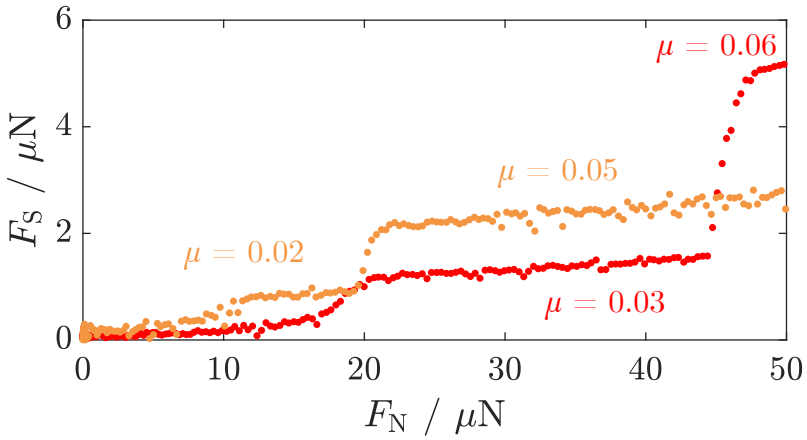


Figure 6.5 Representative shear force, F_S, as a function of the normal force, F_N, across dry (red) and ambient (orange) 1:2 ChCl:Gly. The frictional response shown is representative of multiple repeat measurements and is qualitatively reproducible. Note: small changes in composition, mica alignment, temperature and contact geometry can influence the calculated friction coefficients by up to a factor of 2.[1]

ChCl:EG DESs, and therefore conclude the molecular component is important in determining the lubrication properties of the DESs studied.

6.3 The Influence of Added Water

Figure 6.6 shows the normal force profiles across 1:2 ChCl:Gly on addition of (a) 10 wt% and (b) 30 wt% water.

On addition of 10 wt% water, the layering dimension of 0.42 ± 0.01 nm is comparable to that observed in ambient 1:2 ChCl:Gly, suggesting a mixed checkerboard-like structure as schematised in Figure 6.3(b). We also observe that the innermost layer sits ≈ 0.3 nm from mica-mica contact which can be interpreted as a single mixed checkerboard-like layer between the confining surfaces.

The structure changes when 30 wt% water is added and we now observe a smaller innermost layer of $\Delta_J = 0.22 \pm 0.02$ nm and an outer layer of $\Delta_J = 0.33 \pm 0.01$ nm.

Our results at 10 wt% water corroborate the observation of a near-surface

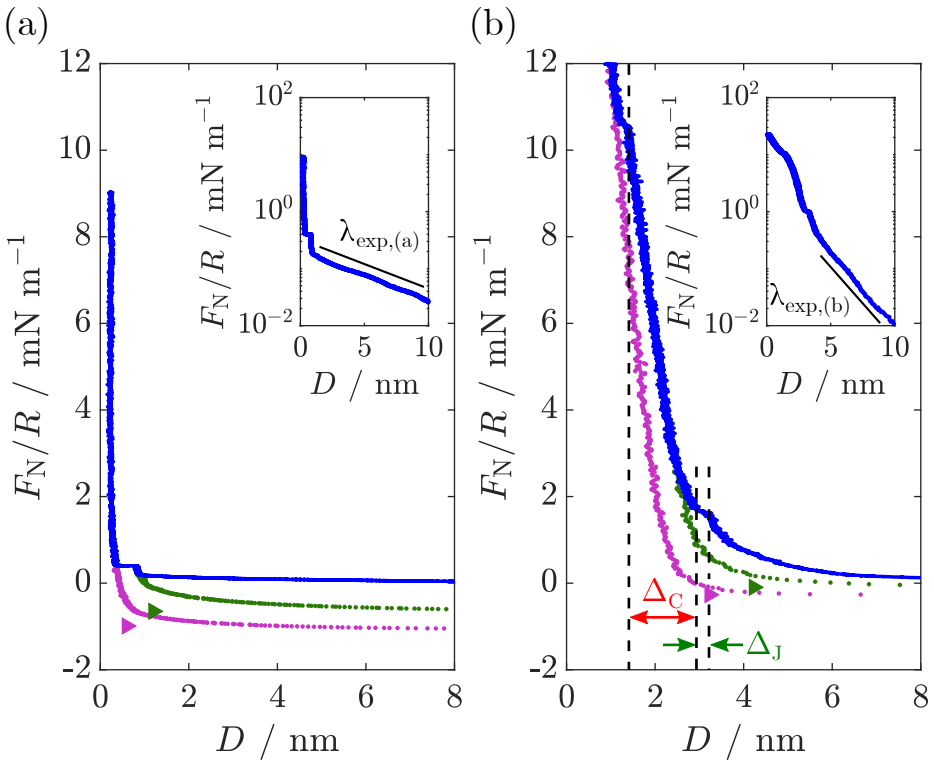


Figure 6.6 Representative normal force, F_N, normalised by the radius of curvature, R, as a function of surface separation, D, profiles in 1:2 ChCl:Gly with (a) 10 wt% and (b) 30 wt% water. The profile on approach is shown in dark blue. The jump-in separation, Δ_J, and layer compression, Δ_C, are shown in green and red, respectively. Retractions from each observed layer allows the adhesive minima to be explored. The adhesive force minima and jump out positions for each layer are indicated by triangular points. The innermost and outermost layer retractions are shown in pink and green, respectively. In both instances the inset shows a log-linear representation of the normal force on approach. The solid black line indicates the gradient of the long-range exponential decay where $\lambda_{exp,(a)} = 6.6 \pm 0.5$ nm and $\lambda_{exp,(b)} = 1.65 \pm 0.08$ nm.

choline-dominated layer by Hammond *et al.*[67] We do not, however, observe layers further out of a larger dimension ≈ 0.9 nm as seen in both 10 wt% and 30 wt% water by Hammond *et al.*[67]

In the work of Hammond *et al.*,[67] at OCP -0.25 V, a number of weak layers ≈ 0.3 nm thick were observed atop a soft repulsive force in the 30 wt% water sample but no interpretation was provided. We also observe a soft repulsion with large regions of compression, evidenced by the change in D with increasing load whilst remaining in the same layer, and comparable jumps inward. As the compression occurs at low loads, we do not believe surface deformation is the

source. It was noted by Hammond *et al.*[67] that the interfacial structure increases up to 30 wt% water for 1:2 ChCl:Gly, after which point the structure is less well defined. As 30 wt% water seems to be the 'tipping' point between a water-in-DES and DES-in-water system, we propose the extensive compression ($\Delta_C \approx 1.4$ nm) is a result of continuous expulsion of a disordered (*i.e.* no molecular layering) liquid phase. It is possible that nanoscale phase separation occurs at this point, leading to water-in-DES and DES-in-water domains, with the latter being less well structured and more akin to a salt solution. In this system, it is difficult to visualise and rationalise the source of the observed steps amongst the regions of compression. As the small layers were reproducible, we do not consider them to be artefacts. The dimensions observed are on the order of both water[23] and glycerol molecules, but we would require further information, either through measurements (*e.g.* scattering experiments) or simulations, to reach a definite conclusion.

Qualitatively, there is a reduction in the push-through force to the innermost layer when comparing the ambient and 10 wt% water 1:2 ChCl:Gly samples as water weakens the interfacial structure. Hammond *et al.*[67] also observe a slight reduction in the innermost push-through force at 10 wt% water versus 0 wt% water at OCP. As we propose a significantly different structure in 30 wt% water 1:2 ChCl:Gly, it would be inappropriate to compare the push-through forces observed in this system with ambient and 10 wt% water 1:2 ChCl:Gly samples.

In both Figures 6.6(a) and (b) the insets show the log-linear representation of the normal force profiles. Addition of 10 wt% water reduces the viscosity to $\eta \approx 91.4$ mPa s at 21 ^{o}C,[138] allowing us to access velocities in the intermediate regime and isolate long-range electrostatic forces (see Table 6.2). The long-range normal force appears to decay exponentially with surface separation with $\lambda_{\mathrm{exp,(a)}} = 6.6 \pm 0.5$ nm and $\lambda_{\mathrm{exp,(b)}} = 1.65 \pm 0.08$ nm. From Debye-Hückel theory (using $\epsilon_r \approx 22$),[129,139] the predicted Debye lengths in the 10 wt% and

30 wt% water samples are $\lambda_D \approx 0.09$ nm and 0.1 nm, respectively. It is clear from the results in Figure 6.6, that the experimental decay lengths exceed the predicted Debye lengths. We also observe an apparent decrease in the decay length with increasing water content which is consistent with literature reports of underscreening-like behaviour in concentrated electrolytes.[33,131] Underscreening is discussed in more detail in Chapter 8.

Table 6.2 Approach velocities in 1:2 ChCl:Gly with 10 wt% water corresponding to three force regimes for $R = 1$ cm. High and low regimes correspond to hydrodynamic and electrostatic forces dominating, respectively. The intermediate regime corresponds to a combination of hydrodynamic and electrostatic forces.

Regime	Velocity / nm s^{-1}
High	30
Intermediate	0.36
Low	0.076

On retracting the surfaces, the adhesive force minima are progressively weaker when comparing dry, ambient, 10 wt% water, and 30 wt% water samples. This supports the observations of weaker interfacial structure when adding 10 wt% water, and the presence of weak disordered domains when adding 30 wt% water. The similarity of the adhesive minima in the 30 wt% water sample could also support the idea of disordered structures that are not influenced by the extent of confinement.

6.4 Summary

In this chapter, normal and shear forces across dry and ambient 1:2 ChCl:Gly nanofilms have been studied. We have also explored the influence of added water on the observed normal forces.

Viscous forces dominate the dry and ambient normal force profiles at all velocities and fitting the data to an expression for the Reynolds lubrication force

gives a negative slip length, $b \approx 1.2 - 1.6$ nm. The calculated b corroborates well with the observed point of closest approach in both dry and ambient normal force profiles.

Structural forces with $\Delta_J = 0.33 \pm 0.02$ nm and 0.49 ± 0.01 nm were observed in the dry and ambient samples, respectively. We propose the former are a result of glycerol-glycerol networks retained in the DES and that, upon equilibration and exposure to atmospheric humidity, the structure changes from glycerol-dominated layers to a mixed composition checkerboard-like structure (see Figure 6.3(b)). The transition to a weaker structure, potentially due to the disruption of the Gly-Gly hydrogen bond network, is supported by the observation of both jump-in points and adhesive minima that are weaker.

On the addition of 10 wt% water to 1:2 ChCl:Gly, a similar layering structure to the ambient sample of 0.42 ± 0.01 nm is observed. The innermost layer sits approximately 0.3 nm from mica-mica contact suggesting a single mixed composition checkerboard-like layer confined between the surfaces. When 30 wt% water is added, a structural change is observed that can be rationalised by noting that 30 wt% water is the approximate 'tipping point' between a water-in-DES and DES-in-water system. We suggest the large compressive regions are a result of continuous expulsion of a disordered liquid phase, with small layers that are comparable to the dimensions of water and/or glycerol molecules.

Long-ranged forces were observed in the 10 wt% and 30 wt% water samples that decayed with anomalously long lengthscales. We also observe a decrease in the decay length with increasing dilution, consistent with literature reports of underscreening-like behaviour observed in 1:2 ChCl:EG (see Chapter 5) and ionic liquids.[33,131]

The frictional response of the nanofilms as a function of load were also

reported for dry and ambient 1:2 ChCl:Gly. Quantised friction is apparent in both systems with comparable friction coefficients between layers. From the lateral friction signal we observe a relaxation between the elastic and plastic regimes on a timescale indicative of viscous liquid-like behaviour. After equilibration at atmospheric humidity, the coefficients of friction are comparable to the dry sample but F_S is reduced, supporting the proposed weaker structure in the ambient sample. As the friction coefficients are comparable between the two samples, we conclude that the sliding mechanism does not change with equilibration time or atmospheric humidity. The observed friction behaviour in 1:2 ChCl:Gly is similar to the behaviour observed in pure glycerol.

With regards to the lubrication properties of DESs, we can conclude from the results presented here and in Chapter 5 that the behaviour is dominated by shearing domains of molecular solvent (EG or Gly), evidenced by the similarity between the DES and pure solvent lubrication properties.

Chapter 7

Differential Scanning Calorimetry

This chapter will focus on the bulk phase behaviour of the two component mixture of choline chloride (ChCl) and ethylene glycol (EG). We will begin by discussing solution theories, the literature measurements and our motivation for studying the phase behaviour of ChCl:EG. There will also be a discussion of a few DSC observations made during the course of obtaining the measurements. Finally, we study the phase behaviour of ChCl:EG, construct a phase diagram, and discuss its relevance and implications.

7.1 Background and Motivation

7.1.1 Ideal Solution Theory

Ideal solution theory was briefly mentioned in Chapter 5 with regards to the definition of a deep eutectic solvent as per Figure 7.1. Here, we explore ideal solution theory further, following the line of Atkins and de Paula.[140]

The chemical potential, μ_i, of component i in an ideal solution can be determined from the chemical potential of the pure component, μ_i^*, the molar gas

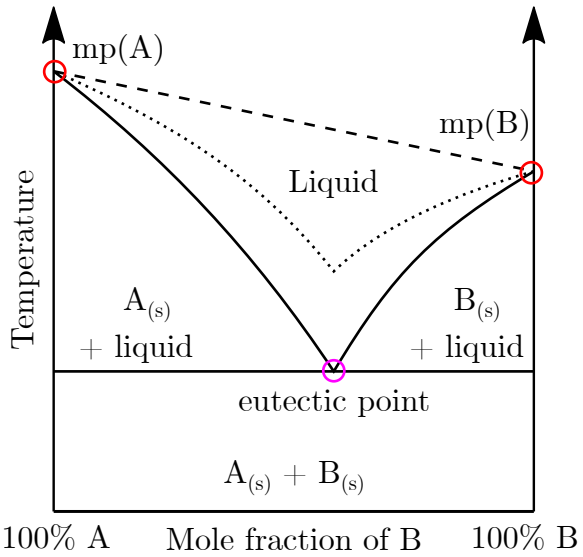


Figure 7.1 Figure 5.1 revisited. Schematic adaptation of a two component solid-liquid phase diagram for a simple ideal eutectic mixture (dotted line) and a deep eutectic solvent (solid line).[80,119] The horizontal solid line corresponds to the solidus. The melting points of pure A and B are highlighted by red circles and are connected by the dashed line. The eutectic point is shown by the pink circle.

constant, R, the temperature, T, and the mole fraction, x_i, of component i,

$$\mu_i = \mu_i^* + RT \ln x_i. \tag{7.1}$$

The mole fraction can be calculated from the number of moles, n_i, of component i and the total number of moles of all the components in the system, n_{tot}. It can also be determined from the number of molecules, N_i, of component i and the total number of molecules of all the components in the system, N_{tot},

$$x_i = \frac{n_i}{n_{\text{tot}}} = \frac{N_i}{N_{\text{tot}}}. \tag{7.2}$$

Equation 7.1 is derived below.

When mixing two components, 1 and 2, the Gibbs free energy of the final mixture, G^{mixed}, can be defined as,

$$G^{\text{mixed}} = G^{\text{unmixed}} + \Delta_{\text{mix}} G, \tag{7.3}$$

where G^{unmixed} is the initial total Gibbs free energy of the pure (unmixed) components and $\Delta_{\text{mix}}G$ is the Gibbs free energy of mixing. $\Delta_{\text{mix}}G$ is related to the enthalpy, $\Delta_{\text{mix}}H$, and entropy of mixing, $\Delta_{\text{mix}}S$, by,

$$\Delta_{\text{mix}}G = \Delta_{\text{mix}}H - T\Delta_{\text{mix}}S. \tag{7.4}$$

A mixture behaves ideally if the average energy of the 1-2 interactions in the mixture are the same as the 1-1 and 2-2 interactions in the pure liquids. As the energies are the same in the individual components and the mixture, $\Delta_{\text{mix}}H = 0$.

We can determine $\Delta_{\text{mix}}S$ from,

$$\Delta_{\text{mix}}S = S^{\text{mixed}} - S^{\text{unmixed}}, \tag{7.5}$$

and the Boltzmann formula,

$$S = k_{\text{B}} \ln \Omega, \tag{7.6}$$

where k_{B} is the Boltzmann constant and Ω is the number of microstates (different molecular arrangements with the same total energy).

Let us consider a lattice of pure 1 with N_1 lattice sites and N_1 molecules of 1. As the molecules of 1 are identical, there is only one possible arrangement of the molecules on the lattice, and $\Omega_1 = 1$. The same rationale holds for any pure component. The entropy of the unmixed state is therefore given by the sum of pure component entropies, S_1 and S_2,

$$S^{\text{unmixed}} = S_1 + S_2 = k_{\text{B}}(\ln \Omega_1 + \ln \Omega_2) = k_{\text{B}} \ln \Omega_1\Omega_2 = 0. \tag{7.7}$$

When N_1 molecules of 1 and N_2 molecules of 2 are mixed, we have $N = N_1 + N_2$

lattice sites. The number of microstates is then given by

$$\Omega = \frac{N!}{N_1!N_2!}, \tag{7.8}$$

where $N!$ is the number of possible arrangements across N lattice sites, and $N_1!N_2!$ is the number of permutations of each type of molecule on the lattice. The entropy of the mixed state is therefore

$$S^{\text{mixed}} = k_{\text{B}} \ln \frac{N!}{N_1!N_2!}. \tag{7.9}$$

and the ideal entropy of mixing is given by

$$\Delta_{\text{mix}}S = k_{\text{B}} \ln \frac{N!}{N_1!N_2!} - 0 = k_{\text{B}} \ln \frac{N!}{N_1!N_2!}. \tag{7.10}$$

Equation 7.10 can be rewritten using Stirling's approximation as

$$\Delta_{\text{mix}}S = -k_{\text{B}}\left(N_1 \ln \frac{N_1}{N} + N_2 \ln \frac{N_2}{N}\right), \tag{7.11}$$

and subsequently written in terms of the number of moles, $n_{1/2}$, and mole fraction, $x_{1/2}$, of the components,

$$\Delta_{\text{mix}}S = -R(n_1 \ln x_1 + n_2 \ln x_2), \tag{7.12}$$

where $n_i = N_i/N_{\text{A}}$, and N_{A} is the Avogadro constant.

Combining Equations 7.4, 7.12, and $\Delta_{\text{mix}}H = 0$ gives the Gibbs free energy of mixing as

$$\Delta_{\text{mix}}G = \Delta_{\text{mix}}H - T\Delta_{\text{mix}}S = RT(n_1 \ln x_1 + n_2 \ln x_2), \tag{7.13}$$

and therefore the Gibbs free energy of the final ideal mixture from Equation 7.3 is

$$G^{\text{mixed}} = G^{\text{unmixed}} + RT(n_1 \ln x_1 + n_2 \ln x_2). \tag{7.14}$$

As the chemical potential of component 1, μ_1, is related to the Gibbs free energy, G, by the following:

$$\mu_1 = \left(\frac{\partial G}{\partial n_1}\right)_{n_2,T,p}, \tag{7.15}$$

we can differentiate Equation 7.14 with respect to n_1 at constant n_2, T, and pressure, p. This yields the chemical potential of component 1 in an ideal mixture,

$$\mu_1 = \mu_1^* + RT \ln x_1, \tag{7.16}$$

as per Equation 7.1 where $i = 1$. Equation 7.15 can also be differentiated with respect to n_2 at constant n_1, T, and p to obtain the chemical potential of component 2.

7.1.2 Regular Solutions

Ideal solution theory is valid when the solute and solvent molecules are similar.

In regular solutions the interactions between 1-1, 2-2, and 1-2 are not identical and $\Delta_{\text{mix}}H \neq 0$. However, the entropy of mixing is treated ideally (*i.e.* random mixing) where $\Delta_{\text{mix}}S$ is given by Equation 7.12.

We can determine $\Delta_{\text{mix}}H$ from,

$$\Delta_{\text{mix}}H = H^{\text{mixed}} - H^{\text{unmixed}}. \tag{7.17}$$

If we again consider a lattice model of molecules 1 and 2, we can assume the

volume does not change upon mixing ($\Delta V = 0$) and hence the enthalpy can be directly related to the internal energy, U,

$$\Delta H = \Delta U + p\Delta V = \Delta U + 0 = \Delta U. \tag{7.18}$$

It is also assumed that molecules only interact with their nearest neighbours in the lattice model.

In pure 1 with N_1 molecules, each molecule of 1 will be surrounded by z nearest neighbours. As the lattice contains pure 1 molecules, we only need to consider 1-1 interactions with interaction energy, w_{11}. The enthalpy of pure 1 is therefore,

$$H_1 = \frac{1}{2} z N_1 w_{11}, \tag{7.19}$$

where the factor of a half avoids double-counting the interactions. The same rationale holds for any pure component, and we can therefore write H^{unmixed} as,

$$H^{\text{unmixed}} = \frac{1}{2} z (N_1 w_{11} + N_2 w_{22}), \tag{7.20}$$

where N_2 is the number of 2 molecules and w_{22} is the 2-2 interaction energy. Equation 7.20 can be rewritten in terms of the mole fraction, $x_{1/2}$, of the components giving,

$$H^{\text{unmixed}} = \frac{1}{2} z (N_1 + N_2)(w_{11} x_1 + w_{22} x_2). \tag{7.21}$$

When 1 and 2 are mixed, we must now consider four possible scenarios. What is the chance that: 1's neighbour is 1, 1's neighbour is 2, 2's neighbour is 1, and 2's neighbour is 2? If we consider the first scenario, we know that the enthalpy of pure 1 is given by Equation 7.19. The enthalpy of 1 in the mixture will therefore need to account for the mole fraction of 1 in the mixture, and hence Equation 7.19

becomes

$$H_{11} = \frac{1}{2} z N_1 w_{11} x_1. \tag{7.22}$$

It follows that the enthalpies of the remaining scenarios are determined in the same manner,

$$H_{12} = \frac{1}{2} z N_1 w_{12} x_2, \tag{7.23}$$

$$H_{21} = \frac{1}{2} z N_2 w_{21} x_1, \tag{7.24}$$

$$H_{22} = \frac{1}{2} z N_2 w_{22} x_2, \tag{7.25}$$

where $w_{12} = w_{21}$ is the 1-2 interaction energy.

The enthalpy of the resulting final mixture is therefore

$$H^{\text{mixed}} = \frac{1}{2} z (N_1 w_{11} x_1 + N_1 w_{12} x_2 + N_2 w_{21} x_1 + N_2 w_{22} x_2), \tag{7.26}$$

which can be written as

$$H^{\text{mixed}} = \frac{1}{2} z (N_1 + N_2)(w_{11} x_1^2 + w_{22} x_2^2 + 2 w_{12} x_1 x_2). \tag{7.27}$$

The enthalpy of mixing (Equation 7.17) can then be written as

$$\begin{aligned} \Delta_{\text{mix}} H = & \frac{1}{2} z (N_1 + N_2)(w_{11} x_1^2 + w_{22} x_2^2 + 2 w_{12} x_1 x_2) \\ & - \frac{1}{2} z (N_1 + N_2)(w_{11} x_1 + w_{22} x_2), \end{aligned} \tag{7.28}$$

which is equivalent to

$$\begin{aligned} \Delta_{\text{mix}} H &= (n_1 + n_2) x_1 x_2 z N_{\text{A}} \left[w_{12} - \left(\frac{w_{11} + w_{22}}{2} \right) \right] \\ &= (n_1 + n_2) x_1 x_2 w, \end{aligned} \tag{7.29}$$

where w is the interaction parameter defined as

$$w = zN_{\mathrm{A}}\left[w_{12} - \left(\frac{w_{11} + w_{22}}{2}\right)\right]. \tag{7.30}$$

Combining Equations 7.4, 7.12, and 7.29 gives the Gibbs free energy of mixing as

$$\begin{aligned}\Delta_{\mathrm{mix}}G &= \Delta_{\mathrm{mix}}H - T\Delta_{\mathrm{mix}}S \\ &= (n_1 + n_2)x_1x_2w + RT(n_1 \ln x_1 + n_2 \ln x_2),\end{aligned} \tag{7.31}$$

and therefore the Gibbs free energy of the final regular mixture from Equation 7.3 is

$$G^{\mathrm{mixed}} = G^{\mathrm{unmixed}} + (n_1 + n_2)x_1x_2w + RT(n_1 \ln x_1 + n_2 \ln x_2). \tag{7.32}$$

Differentiating Equation 7.32 with respect to n_1 at constant n_2, T, and p, therefore gives the chemical potential of component 1 in the regular solution as,

$$\mu_1 = \left(\frac{\partial G}{\partial n_1}\right)_{n_2,T,p} = \mu_1^* + RT \ln x_1 + wx_2^2. \tag{7.33}$$

Equation 7.33 can also be differentiated with respect to n_2 at constant n_1, T, and p to obtain the chemical potential of component 2 in a regular solution.

Both ideal and regular solution theories have been used to quantitatively describe the liquidus range of DESs.[141]

7.1.3 Depression of Freezing Point

When a solute is added to a solvent, both the freezing and boiling points change relative to the pure solvent, as in Figure 7.2. This is due to an increased number of microstates (different molecular arrangements with the same total energy) available in the solution when compared with the pure liquid. As the number of microstates is related to the entropy of the system, an additional entropic contribution is

present on the addition of solute. If the solution is more entropically favourable than the pure solvent, and because $(\partial G/\partial T)_p = -S$, the Gibbs free energy, and chemical potential of the solution is reduced relative to the pure liquid, widening the liquidus range.

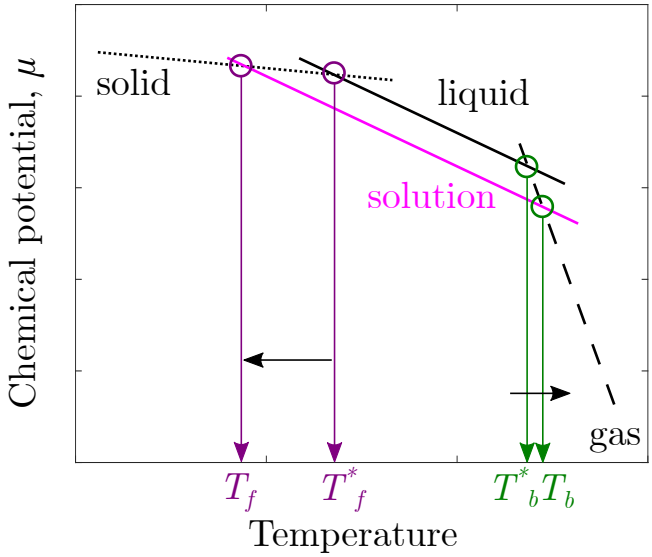


Figure 7.2 Schematic adaptation of the chemical potential, μ, as a function of temperature across solid (black dotted line), liquid (black solid line), and gaseous (black dashed line) solvent.[140] When a solute is added the resulting solution has the chemical potential given by the pink solid line. Relative to the pure liquid, the purple open circles and arrows highlight the depression (black leftwards arrow) in freezing point from T^*_f to T_f, the green open circles and arrows highlight the elevation (black rightwards arrow) in boiling point from T^*_b to T_b. The pure solvent freezing and boiling points are indicated by T^*.

If the ideal mixture comprises solvent A and solute B, at the freezing point, the chemical potential of A in the solid, $\mu^*_{\mathrm{A}}(\mathrm{s})$, and solution phase (Equation 7.1) must be equal,

$$\mu^*_{\mathrm{A}}(\mathrm{s}) = \mu^*_{\mathrm{A}}(\mathrm{l}) + RT \ln x_{\mathrm{A}}. \tag{7.34}$$

By rearranging this equation into the form,

$$\ln x_{\mathrm{A}} = \frac{\mu^*_{\mathrm{A}}(\mathrm{s}) - \mu^*_{\mathrm{A}}(\mathrm{l})}{RT} = \frac{-\Delta_{\mathrm{fus}}G}{RT}, \tag{7.35}$$

we obtain the mole fraction of A as a function of the Gibbs energy of fusion,

$\Delta_{\text{fus}}G$.

As the Gibbs free energy is typically calculated from other thermodynamic quantities, we should express Equation 7.35 as a function of a measurable quantity like the enthalpy of fusion, $\Delta_{\text{fus}}H$. Taking the derivative of Equation 7.35 with respect to T and using the Gibbs-Helmholtz equation,

$$\left(\frac{\partial(G/T)}{\partial T}\right)_p = \frac{-H}{T^2}, \tag{7.36}$$

yields

$$\frac{\mathrm{d}\ln x_{\text{A}}}{\mathrm{d}T} = \frac{\Delta_{\text{fus}}H}{RT^2}. \tag{7.37}$$

We can then integrate Equation 7.37 over the mole fractions $x_{\text{A}} = 1$ to x_{A} ($\ln x_{\text{A}} = 0$ to $\ln x_{\text{A}}$), and the freezing points of pure A, T^*, and the mixture, T,

$$\int_0^{\ln x_{\text{A}}} \mathrm{d}\ln x_{\text{A}} = \int_{T^*}^{T} \frac{\Delta_{\text{fus}}H}{RT^2}\mathrm{d}T, \tag{7.38}$$

$$\ln x_{\text{A}} = \ln(1 - x_{\text{B}}) = \frac{\Delta_{\text{fus}}H}{R}\left(\frac{1}{T^*} - \frac{1}{T}\right). \tag{7.39}$$

Rearranging this equation into

$$T = \frac{T^*\Delta_{\text{fus}}H}{\Delta_{\text{fus}}H - RT^*\ln x_{\text{A}}}, \tag{7.40}$$

allows us to plot T as a function of x_{A} using literature or measured values of $\Delta_{\text{fus}}H$ and T^*, and we can therefore predict how the amount of solute influences the observed freezing point. Figure 7.3 shows the ideal solution liquidus lines for ethylene glycol and choline chloride in cyan and red, respectively.

A similar argument can be made for the elevation of boiling point.

7.1.4 Kinetic Considerations

Thermodynamically, the freezing point (liquid to solid) and the melting point (solid to liquid), T_m, are equivalent. However, the freezing (or crystallisation) point is highly influenced by kinetics and is not always equivalent to the melting point.

Two types of crystallisation exist. Typically, during cooling, a system will crystallise from an amorphous liquid to a more organised solid structure. Crystallisation can also occur during heating, where an amorphous solid transitions to a crystalline solid, and is referred to as cold-crystallisation.

Crystallisation is a two-step process where nucleation centres must occur before crystal growth can begin. If the system has a high purity, it is more difficult for nucleation to occur as less defects and impurities are present to act as nucleation centres. The system is kinetically stable in the absence of nucleation centres and can be cooled far below its melting temperature, remaining in a supercooled liquid-like state.

The crystallisation temperature also depends on the rate of cooling. If a liquid is cooled quickly, the system has less time to organise itself into a highly ordered structure and less perfect crystals are formed. Lower crystallisation temperatures are observed when forming less perfect crystals. Conversely, a slow cooling rate allows this rearrangement to occur over a longer timescale forming more perfect thermodynamic crystals with a higher crystallisation point.

7.1.5 Literature Measurements

Shahbaz *et al.*[142] measured the melting points of four molar ratios of ChCl:EG using DSC (Figure 7.3, black full circles). The compositions studied were 1:1.75, 1:2, 1:2.25, and 1:2.5 ChCl:EG. From this narrow range, a freezing point-EG mole

fraction plot was produced and they suggest a eutectic point at a temperature, $T_f = -66$ °C, and an EG mole fraction, x_{EG}, of 0.667 *i.e.* 1:2 ChCl:EG. It should be noted that no thermograms are presented in this manuscript.

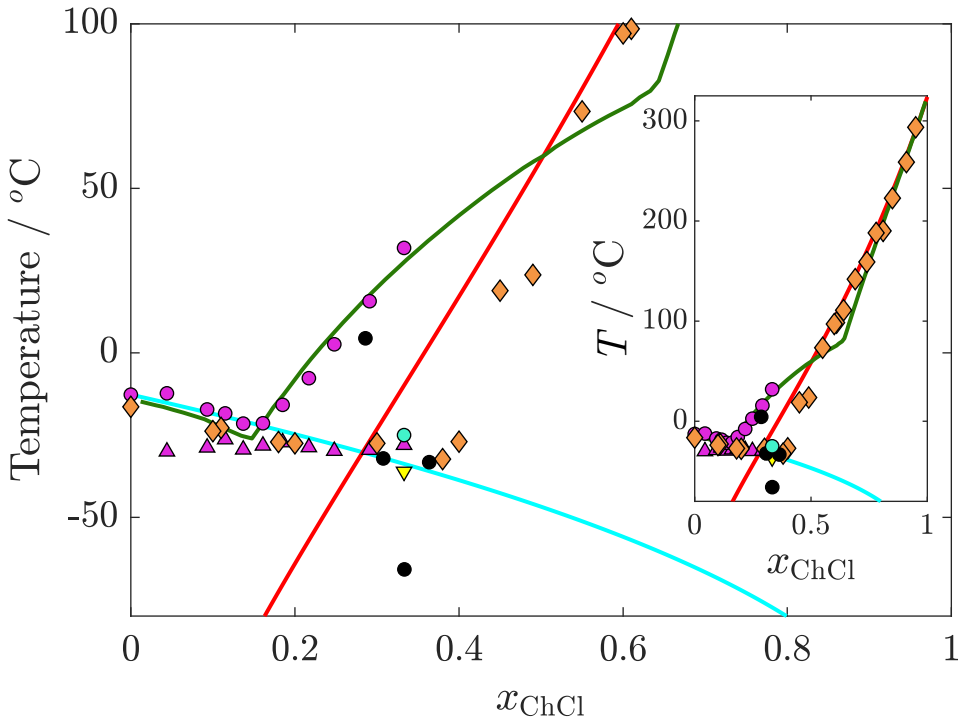


Figure 7.3 Literature temperature-composition (mole fraction of ChCl, x_{ChCl}) phase diagram for the ChCl:EG system. Ibrahim *et al.*[143] - yellow triangle; Crespo *et al.*[144] - green solid line; Agieienko and Buchner[145] - magenta triangles and circles highlight the solidus and liquidus lines, respectively; Silva *et al.*[83] - orange diamonds; Shahbaz *et al.*[142] - black circles; Jani *et al.*[146] - cyan circle. Ideal solution liquidus lines calculated using Equation 7.40 for ethylene glycol (cyan solid line) and choline chloride (red solid line). For ethylene glycol, $\Delta_{\mathrm{fus}}H = 9960$ J mol^{-1} and $T^* = -12.69$ °C.[95] For choline chloride, $\Delta_{\mathrm{fus}}H = 4300 \pm 600$ J mol^{-1} and $T^* = 324 \pm 7$ °C.[147]

Since this work, the eutectic temperature of 1:2 ChCl:EG has regularly been cited as -66 °C.[65,81,124,148–151] In the last few years, other eutectic temperatures have been observed for the ChCl:EG system. Ibrahim *et al.*[143] suggest $T_f = -36$ °C but show no thermograms of the transition (Figure 7.3, yellow triangle). Silva *et al.*[83] observe a solidus line at roughly -32 °C at $x_{\mathrm{EG}} = 0.62$ (Figure 7.3, orange diamonds), with no deviation from ideality *i.e.* ideal solution theory is applicable. Using statistical associating fluid theory (SAFT)-type equations, Crespo *et al.*[144] model the solid-liquid equilibrium behaviour of ChCl:EG yielding a eutectic point

at $x_{\mathrm{EG}} > 0.8$ and $T_f \approx -33$ ^{o}C (Figure 7.3, green solid line). A less negative eutectic temperature of $T_f \approx -29$ ^{o}C was also observed recently by Agieienko and Buchner[145] at $x_{\mathrm{EG}} \approx 0.83$ (Figure 7.3, magenta circles and triangles). This recent work presents thermograms highlighting the melting transition. They conclude that 1:2 ChCl:EG is not the eutectic composition, and the depression of the freezing point at $x_{\mathrm{EG}} \approx 0.83$ (1:4.85 ChCl:EG) is not significant enough to class the eutectic mixture as a DES.[145]

Other studies have focused on the high temperature transitions in 1:2 ChCl:EG and found an EG-associated transition at 168 ^{o}C and ChCl decomposition at roughly 303 ^{o}C.[152] Also, the influence of water on DESs have been studied.[146,153] Phase diagrams of the ChCl:EG (1:2 and 1:3) and water mixtures were presented by Jani *et al.*[146] In dry 1:2 ChCl:EG a single exothermic peak is observed at -25 ^{o}C (Figure 7.3, cyan circle), but otherwise no crystallisation is observed between 0-30 wt% water. Beyond 30 wt% water, the phase behaviour changes. For 40 and 50 wt% water, crystallisation is observed on cooling, and during heating a broad melting transition is seen between -96 and -31 ^{o}C. At faster cooling rates ($\approx$ 60 ^{o}C/min), crystallisation can be avoided in the 40 and 50 wt% water samples. At the highest water contents between 60 and 87 wt%, crystallisation is always observed and melting occurs between -49 and -3 ^{o}C, increasing with increasing water content.[146]

As the eutectic point of ChCl:EG is still under debate, we present our contribution in Section 7.3.

7.2 DSC Observations

In this section, we discuss some observations made during the course of obtaining DSC measurements.

7.2.1 Featureless Thermograms

Figure 7.4 shows exemplar thermograms when heating three DES systems: 1:1:1 ChCl:EG:glycerol (Gly), 1:2 ChCl:Gly, and 1:1:1 ChCl:EG:Urea. Over the temperature ranges studied, no transitions were observed.

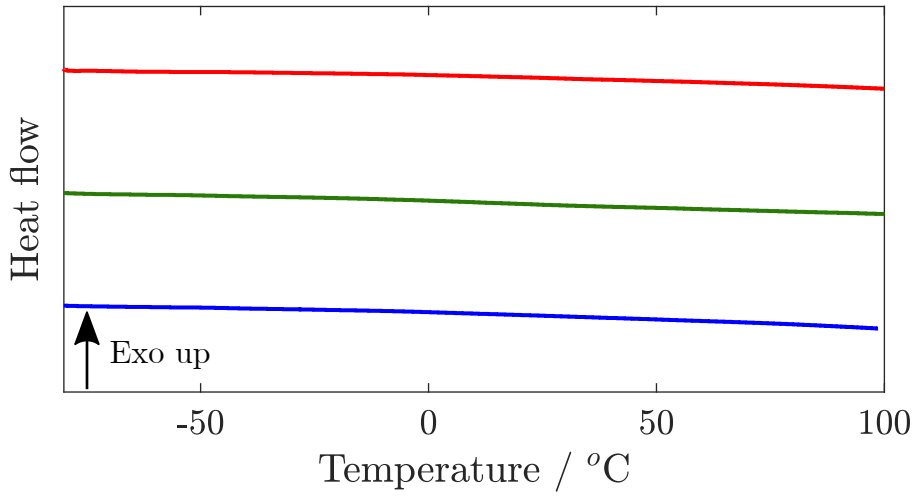


Figure 7.4 Heating DSC scans (offset vertically for clarity) for 1:1:1 ChCl:EG:Gly (blue), 1:2 ChCl:Gly (green), and 1:1:1 ChCl:EG:Urea (red). All samples were heated at 10 ^{o}C/min. The arrow indicates the direction of exothermic (exo) transitions.

Similar observations were made by Morrison *et al.*[154] for the 1:1 ChCl:malonic acid system where no thermal events were observed on heating, except for a shift in the baseline. They attributed this behaviour to a glassy material undergoing a glass transition. This behaviour was verified using hot-stage microscopy, showing that the glassy material liquefies between -84 and -60 ^{o}C.[154] It was noted that the resulting DES is very viscous (η = 721 mPa s at 25 ^{o}C)[80] and that this may contribute to the lack of features.

In Table 7.1, the viscosities are given for 1:2 ChCl:(EG/Gly/Urea) mixtures. It is likely the viscosities of the systems studied here also contribute to the lack of features. Although the viscosities of the 1:1:1 mixtures are not available, we can estimate a viscosity between that of 1:2 ChCl:EG and 1:2 ChCl:(Gly/Urea). If the system to be studied is viscous, it is more likely to remain amorphous on

the timescale of the measurement due to the reduced molecular mobility of the species, disfavouring nucleation and subsequent crystal growth.

Table 7.1 Viscosities of 1:2 choline chloride:X DESs at 25 ^{o}C.[155]

X	Viscosity / mPa s
Ethylene glycol	37
Glycerol	259
Urea	750

We conclude that the featureless thermograms observed in Figure 7.4 are either a result of no thermodynamic transitions over the temperature range studied, or the thermal events are kinetically arrested as a result of the high viscosity of the system. It may be that extremely long hold times at cool temperatures could reveal phase transitions in these materials.[145]

7.2.2 The Influence of Water

Small quantities of water can influence the observed thermograms. Figure 7.5(a) shows thermograms for three EG samples. In blue, we study a pure anhydrous EG sample taken directly from a new bottle. We then study a sample from the same septum-sealed bottle 9 days later, shown in green. Finally, we remove a sample from the bottle and allow it to equilibrate for over 24 hours at room temperature and humidity, shown in red.

As more water is absorbed by EG, the melting peak at approximately -13 ^{o}C shifts to lower temperatures, as expected (see Section 7.1.3). We also observe a small melting peak at approximately -65 ^{o}C in the samples that have absorbed water. Our results corroborate the work of Cordray *et al.*,[156] where the solid-liquid phase diagram for ethylene glycol and water showed a metastable phase at -63.5 ^{o}C and $x_{\mathrm{EG}} \approx 0.64$, and a decrease in the melting point on addition of small amounts of water.

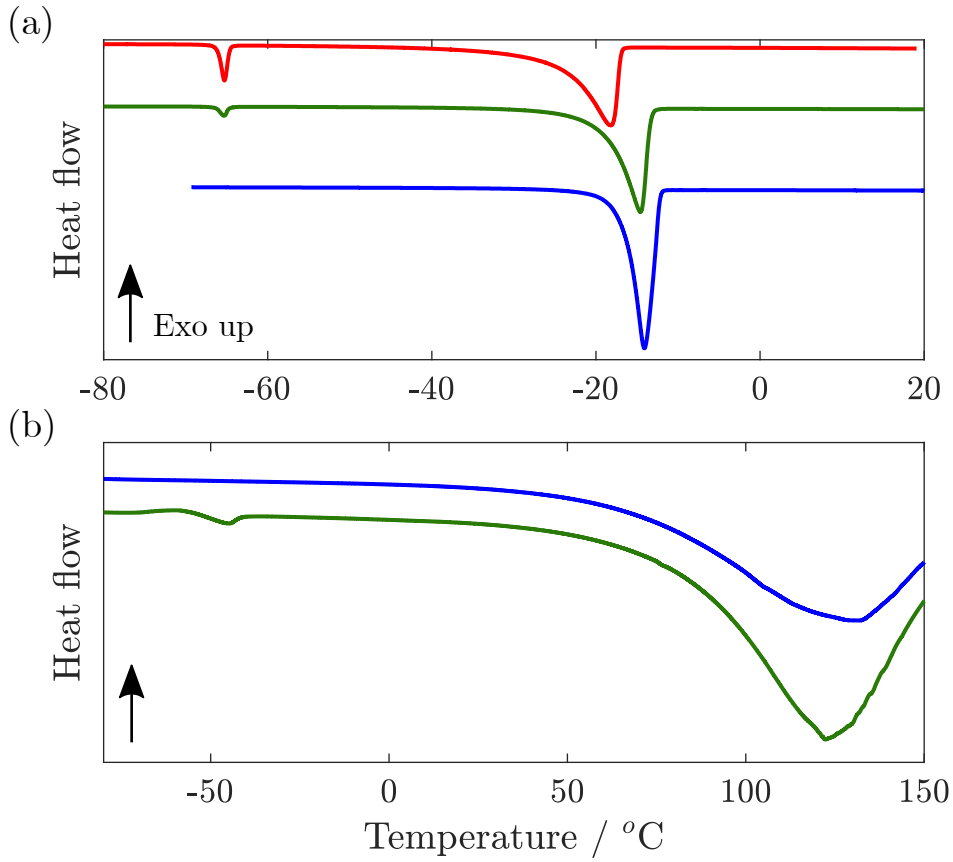


Figure 7.5 Heating DSC scans (offset vertically for clarity) highlighting the influence of water on (a) pure ethylene glycol and (b) 1:2 ChCl:EG and water mixtures. The arrows indicate the direction of exothermic (exo) transitions. (a) Three ethylene glycol samples were heated at 1 °C/min: directly from the bottle, first time the septum was pierced (blue); directly from the bottle, 9 days after the septum was pierced (green); 24 hour equilibrated, room temperature and humidity (red). (b) Two 1:2 ChCl:EG and water mixtures were heated at 10 °C/min: 30 wt% water (blue) and 50 wt% water (green).

The peak at −65 °C can be attributed to water present in the EG, as we do not observe it in the anhydrous sample. By integrating the area underneath each peak, we can compare the peak intensities to gauge how dry the EG sample is. For example, as the anhydrous EG sample does not exhibit a low-temperature melt, the melt 1 (−65 °C): melt 2 (−13 °C) ratio is 0% : 100%. These ratios are 2.3% : 97.7% and 6.7% : 93.3% in the 9 days after and equilibrated samples, respectively. This method of comparison would be particularly useful in the laboratory environment if the user wanted to determine how dry an unknown EG sample was (or another chemical with a water-specific thermal event), or if a

drying process has been successful.

With larger quantities of water, we must be careful when deciding the maximum temperature ($T_{\max}$) of the ramp. Figure 7.5(b) shows thermograms for 1:2 ChCl:EG with 30 wt% (blue) and 50 wt% water (green). In both samples, we observe a broad endotherm with a peak around 120 ^{o}C as water evaporates. However, the onset of this boiling event, and subsequent loss of water, starts as low as 20 ^{o}C. By driving both systems beyond the boiling point of water, the samples are dried to an unknown extent. Therefore, for the scans shown in Figure 7.5(b) we can only attribute the thermal events below the boiling point onset to the 30 wt% and 50 wt% water samples. Beyond this point, we are no longer studying these compositions and determining the exact water content is not possible *in situ*.

7.2.3 Thermal History

Figure 7.6 shows heating scans from -90 ^{o}C to different $T_{\max}$ values for samples of wet 1:10 ChCl:EG. In Figure 7.6(a), the first heating ramp to 0 ^{o}C shows no thermal events (blue). The sample is then cooled to -90 ^{o}C and the following heating ramp is shown in green. No thermal events are observed at $T < 0$ ^{o}C, however above 0 ^{o}C we observe the start of an endothermic transition due to water evaporation. We then prepare a new sample pan (*i.e.* not the sample used in (a)), and increase $T_{\max}$ to 150 ^{o}C. The first run in Figure 7.6(b) shows the broad endothermic peak due to water evaporation, with no thermal events before this point. On the following heating ramp, we observe a series of exothermic and endothermic transitions below 0 ^{o}C, that appear to overlap. When $T_{\max}$ is increased to 200 ^{o}C as in Figure 7.6(c), during the first heating ramp we evaporate off the water but also begin to boil the EG at approximately 200 ^{o}C. In the following heating ramp we observe a series of small exothermic peaks followed by

an endothermic peak below 0 ^{o}C, and a single endotherm at approximately 77 ^{o}C. At $T_{max} = 250$ ^{o}C, the water and EG are boiled off completely in the first ramp (Figure 7.6(d)), resulting in a subsequent ramp that has a single endotherm at 77 ^{o}C due to a choline chloride solid-solid transition.[157,158]

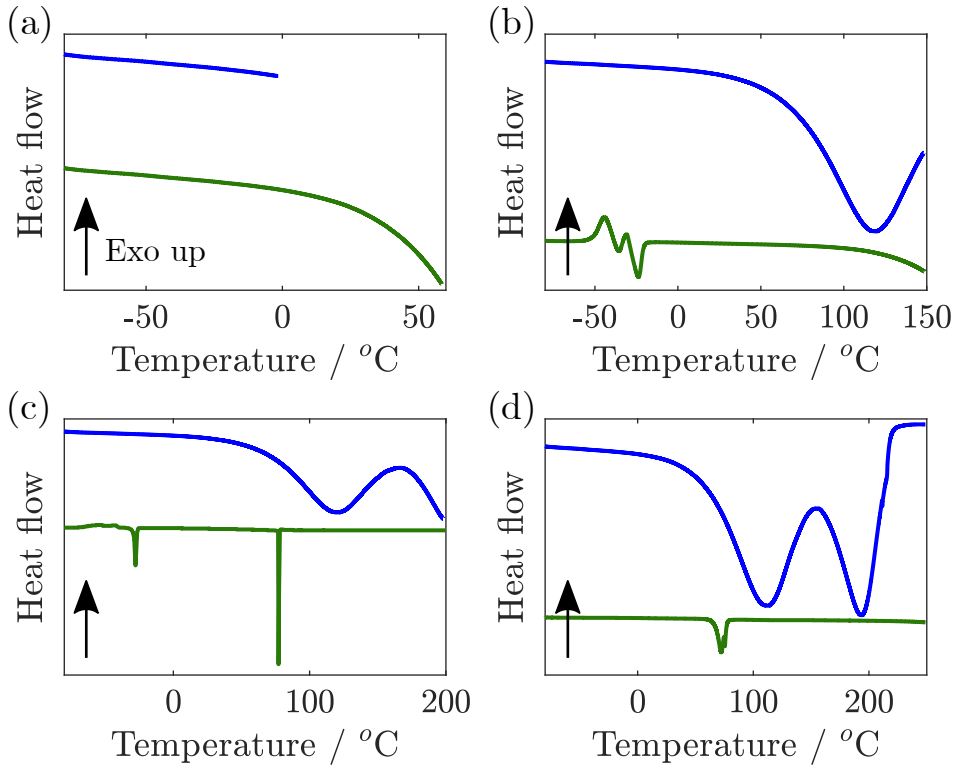


Figure 7.6 Heating DSC scans (offset vertically for clarity) highlighting the influence of thermal history on 1:10 ChCl:EG samples. The arrows indicate the direction of exothermic (exo) transitions. All heating ramps start at -90 ^{o}C. (a) First heating ramp at 10 ^{o}C/min to 0 ^{o}C (blue) and subsequent heating ramp at 10 ^{o}C/min to 60 ^{o}C (green). (b) First heating ramp at 10 ^{o}C/min to 150 ^{o}C (blue) and subsequent heating ramp at 10 ^{o}C/min to 150 ^{o}C (green). (c) First heating ramp at 10 ^{o}C/min to 200 ^{o}C (blue) and subsequent heating ramp at 1 ^{o}C/min to 200 ^{o}C (green). (d) First heating ramp at 10 ^{o}C/min to 250 ^{o}C (blue) and subsequent heating ramp at 10 ^{o}C/min to 250 ^{o}C (green).

These results highlight the importance of knowing the thermal history of the sample, as previous heating-cooling cycles can influence the observed thermograms quite dramatically. For example, if a liquid sample has been cooled below its freezing point quickly, a melting peak may not be observed in the subsequent heating cycle. Although thermodynamically the sample should crystallise below its melting point, quench cooling can kinetically inhibit crystallisation forming a

more glassy liquid, and hence no subsequent melting transition.

A similar thermal history dependence was also observed when studying dry and ambient 1:2 ChCl:EG.

7.3 Choline Chloride:Ethylene Glycol

In this section, we attempt to construct the ChCl:EG temperature-composition phase diagram using the thermal events observed in a series of thermograms.

With regards to the observations made in Section 7.2, we should firstly highlight the preparation methods as this gives an idea of the exposure to water. We should also consider the previous heating-cooling cycles. 'Resetting' the thermal history of the samples allows us to discuss the observed thermal events relative to the now known thermal history.

Pure EG (anhydrous) and ChCl samples were used as received. All ChCl:EG samples were prepared and stored at room temperature and pressure. We studied DESs with the following ChCl:EG molar ratios: 1:1, 1:2, 1:3, 1:4, 1:5, 1:10, 1:99, 1:999. The thermograms in Figure 7.7 are from the heating ramp immediately after the heating-cooling cycle that defines the thermal history. The thermal history of each sample is as follows.

- Pure EG: heat from -70 ^{o}C to 50 ^{o}C at 10 ^{o}C/min, hold at 50 ^{o}C for 5 minutes, cool from 50 ^{o}C to -70 ^{o}C at 10 ^{o}C/min, hold at -70 ^{o}C for 5 minutes.
- Pure ChCl: heat from 0 ^{o}C to 200 ^{o}C at 10 ^{o}C/min, hold at 200 ^{o}C for 5 minutes, cool from 200 ^{o}C to 0 ^{o}C at 10 ^{o}C/min, hold at 0 ^{o}C for 5 minutes.
- 1:1, 1:2, 1:3, 1:4, 1:5, 1:10 ChCl:EG: heat from -90 ^{o}C to 200 ^{o}C at 10 ^{o}C/min,

hold at 200 ^{o}C for 5 minutes, cool from 200 ^{o}C to -90 ^{o}C at 10 ^{o}C/min, hold at -90 ^{o}C for 5 minutes.

- 1:99 ChCl:EG: heat from -90 ^{o}C to 100 ^{o}C at 10 ^{o}C/min, hold at 100 ^{o}C for 5 minutes, cool from 100 ^{o}C to -90 ^{o}C at 10 ^{o}C/min, hold at -90 ^{o}C for 5 minutes.

- 1:999 ChCl:EG: heat from -90 ^{o}C to 50 ^{o}C at 1 ^{o}C/min, hold at 50 ^{o}C for 5 minutes, cool from 50 ^{o}C to -90 ^{o}C at 1 ^{o}C/min, hold at -90 ^{o}C for 5 minutes.

Although faster heating rates increases the magnitude (sensitivity) of the observed thermal events, the resolution is compromised. To construct a phase diagram, it is important that the resolution is maximised to obtain more accurate peak and onset temperatures, hence a slower heating rate should be used. However, a disadvantage of a slower heating rate is the increase in experiment time *e.g.* heating from 0 ^{o}C to 100 ^{o}C at 2 ^{o}C/min and 0.5 ^{o}C/min takes 50 minutes and 200 minutes (3.3 hours), respectively. The thermograms in Figure 7.7 were all heated at 1 ^{o}C/min to obtain reproducible peak and onset temperatures over reasonable experiment times.

Three thermal transitions in Figure 7.7 were used to construct the phase diagram in Figure 7.8. Firstly, the leftmost exothermic peak observed at approximately -65 ^{o}C in the 1:1, 1:2, 1:3, 1:4, 1:5, 1:10 and 1:99 ChCl:EG samples (Figure 7.7(a)). We attribute this peak to the cold-crystallisation (c-c) of the sample. The second peak of interest is the endotherm observed between -30 and -10 ^{o}C. In pure EG, this corresponds to the melting point of EG. On addition of ChCl, this peak shifts to lower temperatures before converging at approximately -28 ^{o}C, which we attribute to the melting of the DES. Finally, the rightmost endotherm observed at 77 ^{o}C in pure ChCl, 1:1, 1:2, 1:3, 1:4, 1:5 and 1:10 mixtures (Fig-

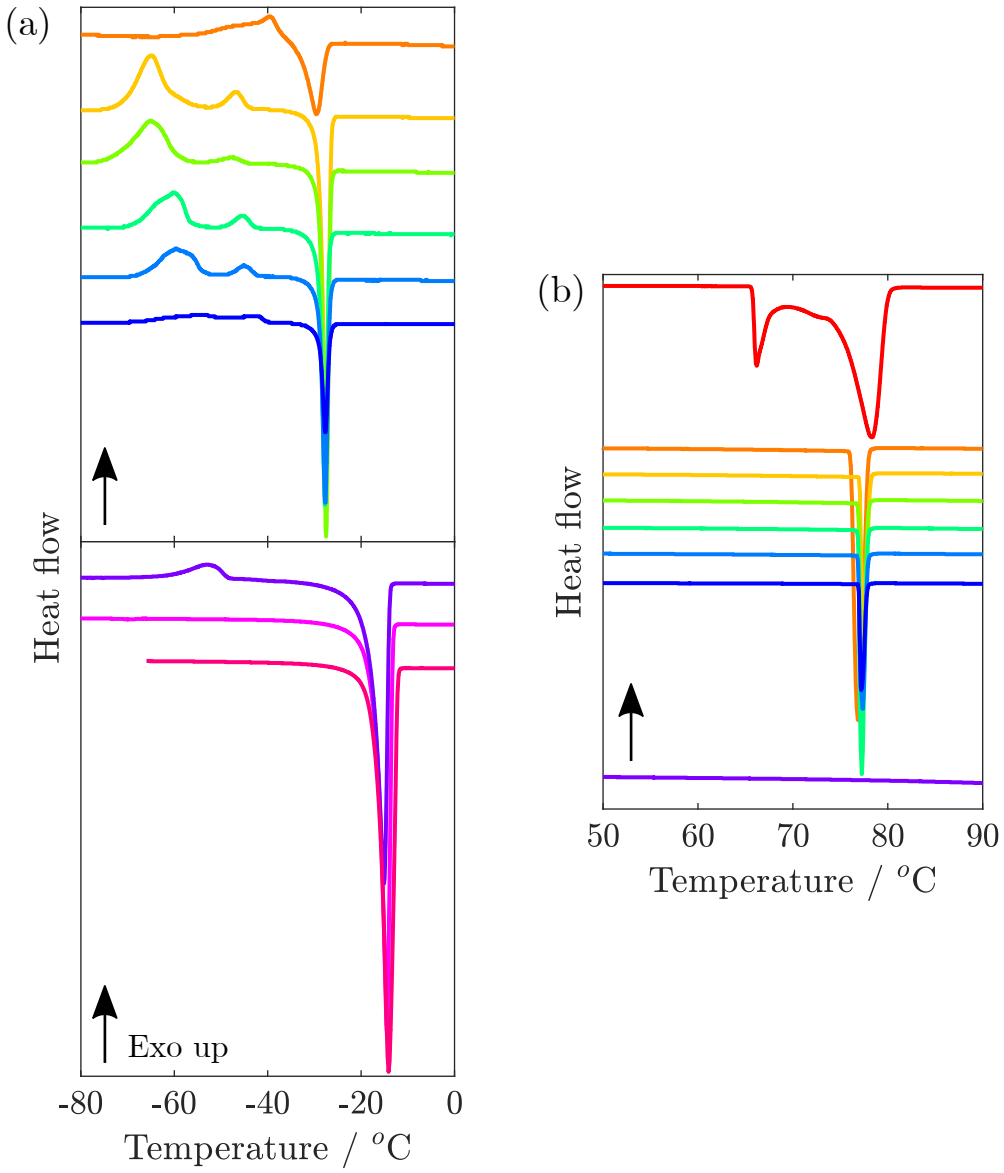


Figure 7.7 Heating DSC scans (offset vertically for clarity) for ChCl and EG mixtures at different compositions (a) below 0 ^{o}C and (b) above 50 ^{o}C. No thermal events were observed between 0 ^{o}C and 50 ^{o}C. All samples were heated at 1 ^{o}C/min. The arrows indicate the direction of exothermic (exo) transitions. In both plots, scans from top to bottom show increasing EG content: dry ChCl (red), 1:1 ChCl:EG (orange), 1:2 ChCl:EG (yellow), 1:3 ChCl:EG (bright green), 1:4 ChCl:EG (turquoise), 1:5 ChCl:EG (blue), 1:10 ChCl:EG (dark blue), 1:99 ChCl:EG (purple), 1:999 ChCl:EG (magenta), dry EG (raspberry).

ure 7.7(b)), corresponding to the solid-solid transition[157] (s-s trs) observed when the crystal structure of ChCl changes from orthorhombic (α-ChCl) to face-centred cubic (β-ChCl).[158]

To produce the phase diagram in Figure 7.8, we have taken the peak tem-

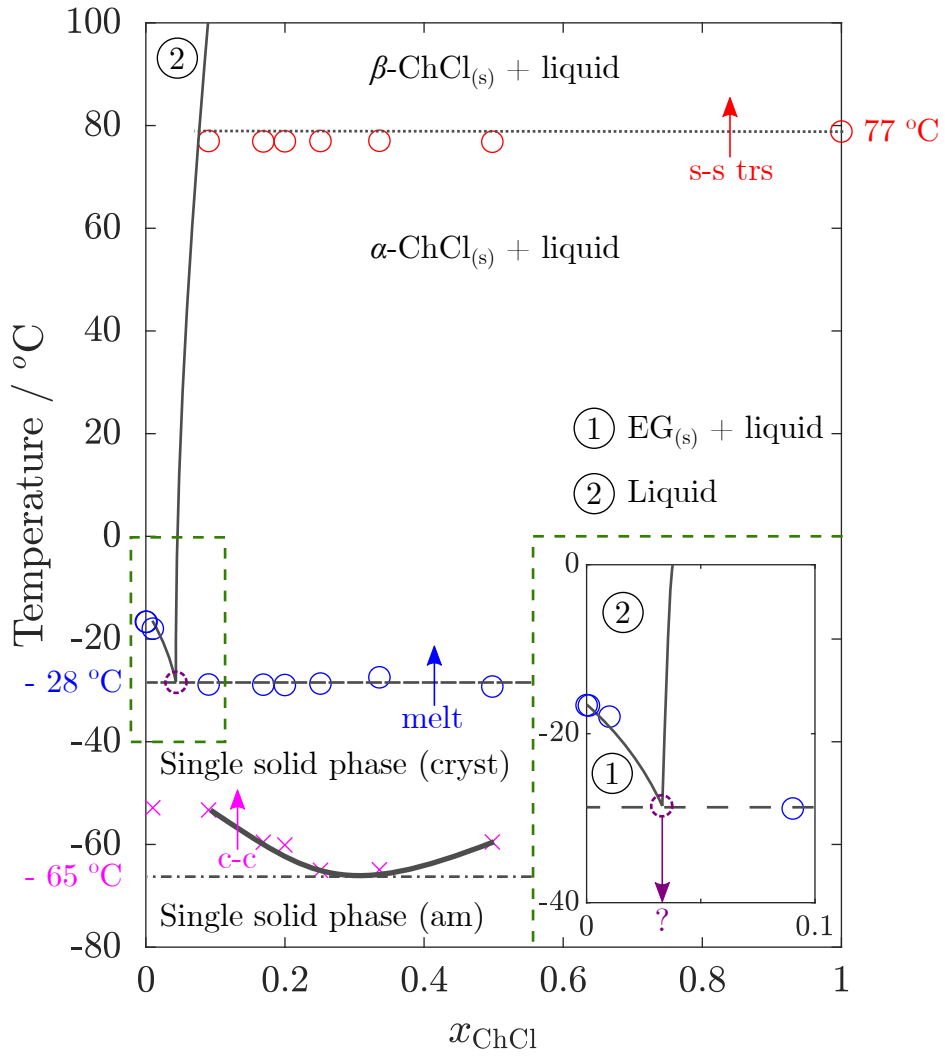


Figure 7.8 Empirical temperature-composition (mole fraction of ChCl, x_{ChCl}) phase diagram for the ChCl:EG system. The thermal events observed in Figure 7.7 are plotted: cold-crystallisation (c-c, pink), melt (blue), solid-solid transition (s-s trs, red). Onset and peak temperatures are plotted as open circles and crosses, respectively. The region within the green dashed box is shown in the inset where $x_{\mathrm{ChCl}} < 0.1$ (the axes labels are omitted for clarity). All lines are empirical and drawn 'by eye' *i.e.* solution theory/mathematical fitting has not been used. We observe six different regions: amorphous (am) single solid phase (below dot-dashed line); crystalline (cryst) single solid phase (between dot-dashed and dashed lines); solid α-ChCl + liquid two phase region (between dashed and dotted lines); solid β-ChCl + liquid two phase region (above dotted line); solid EG + liquid two phase region (indicated by ①); single liquid phase (indicated by ②). The predicted eutectic point is highlighted by the purple dashed open circle.

peratures of the c-c transitions, and the onset temperatures of the melts and s-s transitions (see Chapter 2). At the lowest temperatures studied, we observe a c-c

that appears to act in a eutectic manner with a minimum at -65 ^{o}C. As the temperature is increased, a melting transition occurs. When $x_{\mathrm{ChCl}} > 0.09$ the melting point is -28 $\pm$ 1 ^{o}C. In this work, we do not study the range $0.01 < x_{\mathrm{ChCl}} < 0.09$ but when $x_{\mathrm{ChCl}} < 0.01$, the observed melting point increases and is more comparable to that of pure EG.[156] For $x_{\mathrm{ChCl}} > 0.09$, we also observe a s-s transition at 77 ^{o}C, characteristic of the change from α to β-ChCl.[157] Using these three transitions, we hypothesise a liquidus line given by the thin solid black line in Figure 7.8 and a eutectic point highlighted by the purple dashed open circle. Above the proposed liquidus line we suggest a single liquid phase. Between the solidus (-28 ^{o}C) and liquidus lines, we suggest two two-phase regions. To the left of the eutectic composition, a region of solid EG + liquid, and to the right, a solid α-ChCl + liquid region.

7.4 Summary

In this chapter, we have discussed the observations made during DSC acquisition. We have also explored the phase behaviour of ChCl:EG mixtures using DSC.

Featureless thermograms can occur if the system has no thermodynamic transitions over the range of temperatures studied. If the system has a high viscosity, predicted thermodynamic transitions may be kinetically arrested due to the reduced molecular mobility.

DSC is a useful tool for gauging how dry a sample is if a water-specific thermal event is observed in the system. For example, here we studied the influence of atmospheric humidity on EG and observed a clear increase in the water-associated peak with increased exposure to water. DSC would be particularly useful in determining the success of drying processes, *e.g.* using a Schlenk line to dry a liquid, both qualitatively and quantitatively, without the need for specialised

equipment like Karl Fischer titrators.

The maximum temperature and thermal history are both important considerations to make before performing DSC. If water is present in large quantities, the boiling onset can occur at much lower temperatures than expected thermodynamically. To maintain the water content, $T_{\max}$ must be chosen with care. Knowing the thermal history of the sample is important as the observed thermograms depend on previous heating and cooling processes. We have observed a thermal history dependence in both 1:2 and 1:10 ChCl:EG systems, and suggest that an initial scan should always be taken. This scan acts to 'reset' the thermal history of the sample, where the thermal events can be interpreted relative to the known history.

Interestingly, a ChCl:EG phase diagram emerges akin to the works of Shahbaz *et al.*,[142] Agieienko and Buchner,[145] and Gilmore *et al.*,[159] see Figure 7.9. The bulk phase behaviour of ChCl:EG mixtures does not show a eutectic melt at -66 ^{o}C and a 1:2 ChCl:EG composition as reported by Shahbaz *et al.*[142] Instead we observe a cold-crystallisation at this temperature that behaves in a eutectic manner, and suggest a eutectic composition at far lower x_{ChCl}. The eutectic melt we observe supports the work of Agieienko and Buchner[145] where a solidus line is observed at -29 ^{o}C. Our eutectic composition is found at lower x_{ChCl} compared to Agieienko and Buchner,[145] but our results are comparatively less complete, and we would need to probe the liquidus line further to confirm its behaviour. The work of Agieienko and Buchner[145] studies the thermal transitions below $T_{\max} \approx 50$ ^{o}C. As our measurements probe higher temperatures, we also observe the ChCl solid-solid transition when x_{ChCl} is greater than the eutectic composition, also observed by Gilmore *et al.*[159] in the ChCl:Urea phase diagram for $x_{\mathrm{ChCl}} = 0.45 - 0.90$. Constructing the ChCl:EG phase diagram from DSC measurements was not trivial and involved considering both thermodynamic and kinetic transitions. To improve the accuracy of our phase diagram, we suggest the

use of a second technique in conjunction with DSC. For example, Gilmore *et al.*[159] found that DSC was unsuitable in identifying the ChCl:Urea phase transition points and instead used polarised optical microscopy.

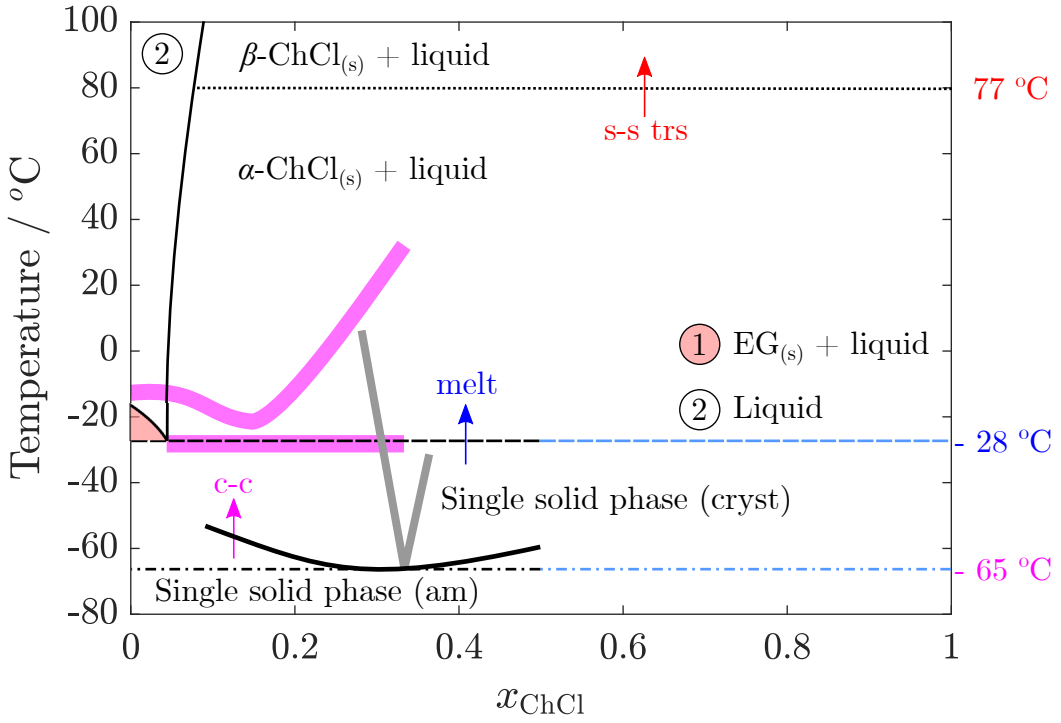


Figure 7.9 Empirical temperature-composition (mole fraction of ChCl, x_{ChCl}) phase diagram for the ChCl:EG system. The thermal events observed are: cold-crystallisation (c-c, pink arrow, thick solid black line), melt (blue arrow, dashed black line), solid-solid transition (s-s trs, red arrow, dotted black line). All black lines are inferred from the data measured and presented in this chapter *i.e.* from Figure 7.8. Individual data points are now removed for clarity. We observe six different regions: amorphous (am) single solid phase (below dot-dashed line); crystalline (cryst) single solid phase (between c-c solid line and dashed line); solid α-ChCl + liquid two phase region (between dashed and dotted lines); solid β-ChCl + liquid two phase region (above dotted line); solid EG + liquid two phase region (indicated by the red shaded area and ①); single liquid phase (indicated by ②). No thermal transitions were observed in the blue dashed and dot-dashed lined regions. The works of Agieienko and Buchner[145] and Shahbaz *et al.*[142] are shown by the pink and grey shaded areas, respectively.

In on- and off-eutectic mixtures, thermal events and likely other properties and applications, are strongly influenced by both thermodynamics and kinetics. Our results highlight that the freezing and melting points of a system are not necessarily the same, and the terms should not be used interchangeably. We also suggest that a clearer definition of a DES is required that addresses both kinetics

and thermodynamics, as freezing (or crystallisation) can be controlled kinetically but interpreted thermodynamically *i.e.* $T_f = T_m$.

Chapter 8

Underscreening in Concentrated Electrolytes

An *electrolyte* is a condensed medium containing mobile charge carriers that allows the passage of current.[3] They are ubiquitous and we encounter them in a myriad of fields, from energy storage including devices like supercapacitors, to human biology where electrolytes are found in our blood plasma.

The theory and behaviour of dilute electrolytes is well established by Debye-Hückel (DH) theory.[74] In contrast, concentrated electrolytes cannot be described by DH theory as the assumptions on which the theory is derived, break down *e.g.* point charges and negligible correlation effects.

Recent experiments are challenging our understanding of the interactions observed in concentrated electrolytes. Here, we add some further experimental insights.

8.1 Theory of Electrolytes

8.1.1 Dilute Electrolytes: Debye-Hückel Theory

Our understanding of dilute electrolytes is well established as Debye-Hückel (DH) theory is valid.[3,74–76] Here we discuss DH theory with respect to a solid-liquid interface where the geometry gives rise to a 1D decay *i.e.* as a function of surface separation only. This geometry is akin to the pseudo-1D geometry found in the surface force balance setup.

For two charged surfaces interacting across a dilute electrolyte, DH theory predicts a monotonic decrease in the electrostatic potential, $\psi(D)$, as a function of the surface separation, D,

$$\psi(D) \approx \psi_0 \exp(-\kappa D), \tag{8.1}$$

where ψ_0 is the surface potential and κ is the inverse of the Debye (screening) length, λ_D. This characteristic decay length is given by

$$\kappa^{-1} = \lambda_\mathrm{D} = \sqrt{\frac{\epsilon_r \epsilon_0 k_\mathrm{B} T}{\sum_i n_{\infty i} e^2 z_i^2}}, \tag{8.2}$$

where ϵ_r is the dielectric constant of the medium, ϵ_0 is the vacuum permittivity, k_B is the Boltzmann constant, T is the temperature, $n_{\infty i}$ is the bulk number density of ion i, e is the elementary charge and z_i is the valency of ion i. In a dilute electrolyte containing 2 constituent ions (cations and anions) in a 1:1 ratio with ion density $n_\infty = n_{\infty -} = n_{\infty +}$, $\sum_i n_{\infty i} e^2 z_i^2 = 2 n_\infty e^2 z^2$, and Equation 8.2 can be written simply as

$$\kappa_{1:1}^{-1} = \sqrt{\frac{\epsilon_r \epsilon_0 k_\mathrm{B} T}{2 n_\infty e^2 z^2}} \propto \frac{1}{\sqrt{n_\infty}}. \tag{8.3}$$

Deriving DH theory

A number of assumptions are made when deriving DH theory:

- ions are point charges (*i.e.* neglect ion size),
- the solvent is a continuous medium with a fixed dielectric constant (*i.e.* the solvent molecules are not treated as particles),
- there are no ion correlations, no specific-ion effects, and the ions only experience an average potential from all other ions (*i.e.* mean field approximation),
- the electrolyte is symmetric (*i.e.* $A^{z+}B^{z-}$, not $A^{y+}B^{z-}$ where $y \neq z$).

We arrive at Equation 8.1 by first considering the Boltzmann distribution of ions in the system,

$$n_{\pm}(D) = n_{\infty} \exp\left(\frac{\mp ze\psi(D)}{k_{\mathrm{B}}T}\right), \tag{8.4}$$

where $n_{\pm}(D)$ is the number density of cations (+) and anions (-) at D, and n_{∞} is the bulk number density. We can write the subsequent total charge density, $\rho(D)$, as

$$\rho(D) = \rho_{+}(D) + \rho_{-}(D) = zen_{\infty}\left[\exp\left(\frac{-ze\psi(D)}{k_{\mathrm{B}}T}\right) - \exp\left(\frac{ze\psi(D)}{k_{\mathrm{B}}T}\right)\right], \tag{8.5}$$

where $\rho_{\pm}(D)$ is the charge density of cations/anions (note: from herein we drop (D) for clarity). To solve this equation, we require Poisson's law which links ρ and ψ using the Laplace-operator, ∇^2, by

$$\nabla^2\psi = \frac{\mathrm{d}^2\psi}{\mathrm{d}D^2} = \frac{-\rho}{\epsilon_0\epsilon_r}. \tag{8.6}$$

Substituting ρ by the definition given in Equation 8.5 yields the Poisson-Boltzmann

(PB) equation,

$$\frac{\mathrm{d}^2\psi}{\mathrm{d}D^2} = \frac{-zen_\infty}{\epsilon_0\epsilon_r}\left[\exp\left(\frac{-ze\psi}{k_\mathrm{B}T}\right) - \exp\left(\frac{ze\psi}{k_\mathrm{B}T}\right)\right]. \tag{8.7}$$

To solve this second order differential equation, two boundary conditions are required. Firstly, as the surface separation tends to infinity, the potential should tend towards zero ($\psi \to 0$ as $D \to \infty$). The second condition is that electroneutrality must be maintained across the system, $\int_0^\infty(\rho_+ + \rho_-)\mathrm{d}D + \sigma = 0$, where σ is the surface charge density. Equation 8.7 can then be solved exactly to give,

$$\psi(D) = \frac{2k_\mathrm{B}T}{ze}\ln\left[\frac{1+\tanh(ze\psi_0/4k_\mathrm{B}T)e^{-\kappa D}}{1-\tanh(ze\psi_0/4k_\mathrm{B}T)e^{-\kappa D}}\right]. \tag{8.8}$$

In the dilute regime, the potential is assumed to be weak such that $ze\psi_0 << k_\mathrm{B}T$ and we can assume that $e^x \approx 1 + x$ (Taylor series up to first order). Equation 8.7 can then be linearised,

$$\frac{\mathrm{d}^2\psi}{\mathrm{d}D^2} = \frac{-zen_\infty}{\epsilon_0\epsilon_r}\left(1 - \frac{ze\psi}{k_\mathrm{B}T} - 1 - \frac{ze\psi}{k_\mathrm{B}T}\right) = \frac{2z^2e^2n_\infty}{\epsilon_0\epsilon_r k_\mathrm{B}T}\psi = \kappa_{1:1}^2\psi, \tag{8.9}$$

and solved analytically to yield

$$\psi(D) \approx \psi_0\exp(-\kappa D). \tag{8.1 revisited}$$

As the concentration increases, λ_D is expected to decrease according to DH theory (solid lines in Figure 8.1). At high ion concentrations, the Debye length will be comparable to, and then smaller than the molecular dimensions of the electrolyte. DH theory is not expected to hold at such high concentrations where the finite size of the ions becomes relevant. Key assumptions fail including ions behaving as point charges, negligible ion correlation effects, and a continuous

solvent.

8.1.2 Recent Observations in Concentrated Electrolytes

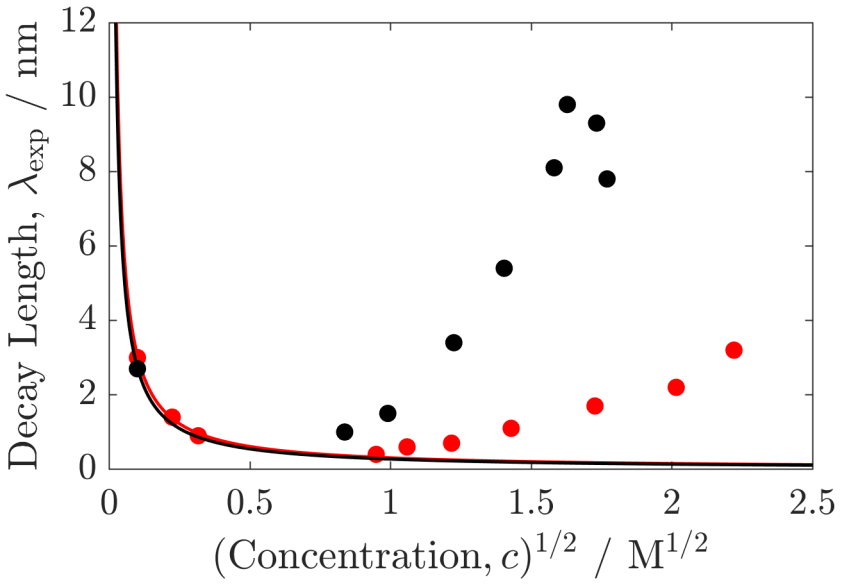


Figure 8.1 Measured decay length, λ_{exp}, as a function of the square root of concentration, c, for aqueous sodium chloride solutions (red circles) and the ionic liquid 1-butyl-1-methylpyrrolidinium bis(trifluoromethylsulfonyl)imide in propylene carbonate (black circles). DH theory predicts that the Debye length will decrease with concentration according to the red and black solid lines for dielectric constants $\epsilon_r = 80.1$ and $\epsilon_r = 64$, respectively. Adapted from Smith *et al.*[27]

Long-range forces across concentrated electrolytes were first observed experimentally by Gebbie *et al.*[33] in an ionic liquid. The long-range forces appeared to decay monotonically (contradicting the predicted damped oscillatory behaviour in Section 8.1.3), and with a decay length much greater than that predicted by DH theory (as per Figure 8.1).[27]

Anomalously long-range decay lengths have been observed in a number of concentrated electrolytes including pure ionic liquids,[27,34] ionic liquid-solvent mixtures,[96] aqueous monovalent salts,[26,27] deep eutectic solvents,[1] water-in-salt electrolytes,[50] and colloidal systems.[160] The influence of temperature has also been explored in aprotic[161] and protic[64] ionic liquids. Finally, long-range decay lengths have been observed using independent techniques, namely surface force balance

measurements,[35] colloid probe atomic force microscopy (AFM),[64] fluorescence microscopy,[162] and colloidal and thin film studies.[160]

In the concentrated regime, the screening length is observed experimentally to increase with increasing ion concentration in contradiction to the DH prediction. This phenomenon, where long-ranged forces are observed across concentrated electrolytes under confinement, was termed *underscreening* to recognise that the field from the surface is screened less effectively than in the DH prediction, and decays with an anomalously long screening length, λ_S.[96] Empirically, it appeared that λ_S scales according to the following relationship at high ion concentration,

$$\lambda_S \propto l_B c a^3, \tag{8.10}$$

where c is the ion concentration, a is the ion-pair diameter and

$$l_B = \frac{(ez_i)^2}{4\pi\epsilon_0\epsilon_r k_B T} \tag{8.11}$$

is the Bjerrum length.[131] Equation 8.10 can also be written as,

$$\left(\frac{\lambda_S}{\lambda_D}\right) = A + \left(\frac{a}{\lambda_D}\right)^{\alpha}, \tag{8.12}$$

where $\alpha = 3$, and A is a constant.[131]

The physical origin of underscreening is yet to be understood but a number of hypotheses have been presented. This includes ionic liquids behaving as dilute electrolytes due to the aggregation of cation-anion pairs that reduces the free ion concentration;[33,163,164] analogies to n-doped semiconductors;[120] and that concentrated electrolytes behave like an ionic crystal with Schottky defects, where the observed screening length can be attributed to the number of defects.[96,131]

8.1.3 Theory of Concentrated Electrolytes

Although an interest in the behaviour of concentrated electrolytes has peaked recently, the theory behind their behaviour dates back to the 1930s. A decade after the seminal work of Debye and Hückel,[74] John Kirkwood developed a method for the treatment of liquids from the standpoint of classical statistical mechanics.[165] In a later paper, a general theory based on this statistical treatment would be formulated and applied to concentrated electrolytes.[166] Through detailed mathematical arguments, the solution of the liquid radial distribution function (rdf), $g(r)$, which takes into account both the cation and anion sizes is determined as $g(r) = \phi(r)/r$, where

$$\phi(r) = \sum_{n=1}^{\infty} A_n \exp(-z_n r), \tag{8.13}$$

r is the ion-ion separation, A_n is a pre-exponential factor, and $z_n = \alpha_n + i\beta_n$ are sets of roots from $n = 1$ to ∞, of the transcendental equation,

$$z^2 - \kappa^2 \cosh(za) = 0. \tag{8.14}$$

Here, κ is as described by DH theory and a is the ion radius.

The real and imaginary contributions to the roots determines the behaviour of the ion correlations. In dilute electrolytes, the roots are real (*i.e.* $\beta_n = 0$) and their contribution to the exponential term in Equation 8.13 results in a rapid decay with increasing r, as per DH theory. As the concentration increases, there is a crossover from charge-based monotonic decay to a charge-based exponentially damped oscillatory decay at $a/\lambda_D \approx \sqrt{2}$,[167] known as the Kirkwood transition. At this point the real roots merge into a repeated root. In more concentrated solutions, the roots are complex (*i.e.* $\alpha_n,\ \beta_n \neq 0$) which imparts an oscillatory

form to the solution, resulting in a rdf that is characteristic of a liquid *i.e.* a liquid of ions rather than a gas of ions.

The idea of sets of multiple roots governing the decay behaviour of electrolytes is still an ongoing discussion amongst the community. Recent works of Adar *et al.*[168] and Kjellander[97] build upon the foundations of Kirkwood,[166] and show that in concentrated electrolytes the charge correlations cannot be parameterised by a single screening length like DH theory. In fact, multiple terms or 'modes' are required with each term having a different amplitude governing their dominance (see Figure 8.2).

When considering pair correlation functions, a further transition was observed by Fisher and Widom.[169] At every temperature there is an associated transition at a given pressure, known as the Fisher-Widom line, corresponding to the crossover from a monotonic to an oscillatory decay that is determined by the packing density rather than the charge density. The Fisher-Widom transition applies to all fluids, including electrolytes, and so must be considered alongside the charge (Kirkwood-type) correlations.

Important progress was made in the 1990s when Attard,[167] and de Carvalho and Evans[170] explored correlation functions, using the primitive model and different approximations: hypernetted chain closure and mean spherical approximation, respectively. The results yielded the same three decay regimes with increasing concentration (shown in Figure 8.3): electrostatic monotonic exponential (low concentration, Figure 8.3(a)), electrostatic damped oscillatory (intermediate concentration, Figure 8.3(b)), density damped oscillatory (high concentration, Figure 8.3(c)). Ennis *et al.*[171] also observed these regimes with the Dressed Ion Theory (DIT).[172,173] Molecular dynamics simulations by Keblinski *et al.*[174] on gaseous and molten sodium chloride corroborated the theoretical arguments of Attard,[167] de Carvalho and Evans,[170] and Ennis *et al.*[171]

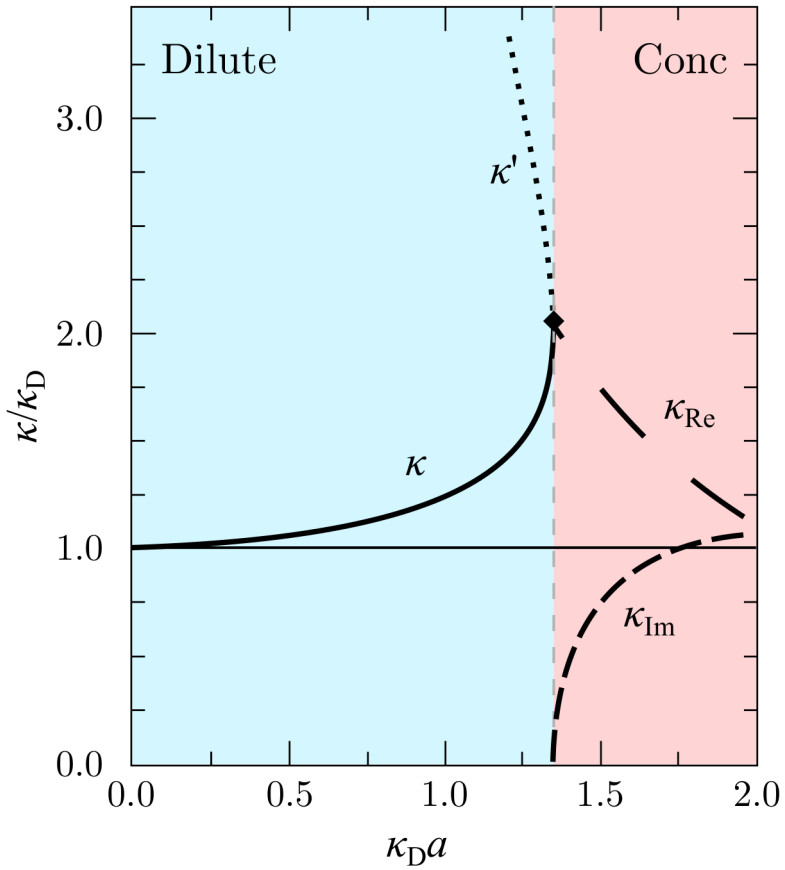


Figure 8.2 Adapted from Kjellander.[97] Screening parameter, κ, normalised by the Debye parameter, κ_D, as a function of $\kappa_D a$, where a is the ionic diameter and $\kappa_D a \propto \sqrt{c}$. The electrolyte in this instance is an aqueous solution of a 1:1 electrolyte at room temperature. At low concentrations (blue region), there are two screening parameters, κ (solid line) and κ' (dotted line), and the decay length is dominated by the 'smallest' mode, κ^{-1}. As the concentration increases and we approach the Kirkwood transition (black diamond), the parameters merge. Beyond the Kirkwood transition and into the concentrated (conc) regime (red region), the two screening parameters are complex conjugates such that $\kappa = \kappa_{Re} + i\kappa_{Im}$ and $\kappa' = \kappa_{Re} - i\kappa_{Im}$, where κ_{Re} and κ_{Im} are shown by the long-dashed and short-dashed lines, respectively.

Based on these theoretical and computational predictions, it appears perhaps not so surprising that multiple decay regimes are observed experimentally in concentrated electrolytes (*e.g.* long-range exponential, short-range oscillatory). However, the experimentally observed decay modes have not yet been quantitatively connected with the modes observed theoretically.

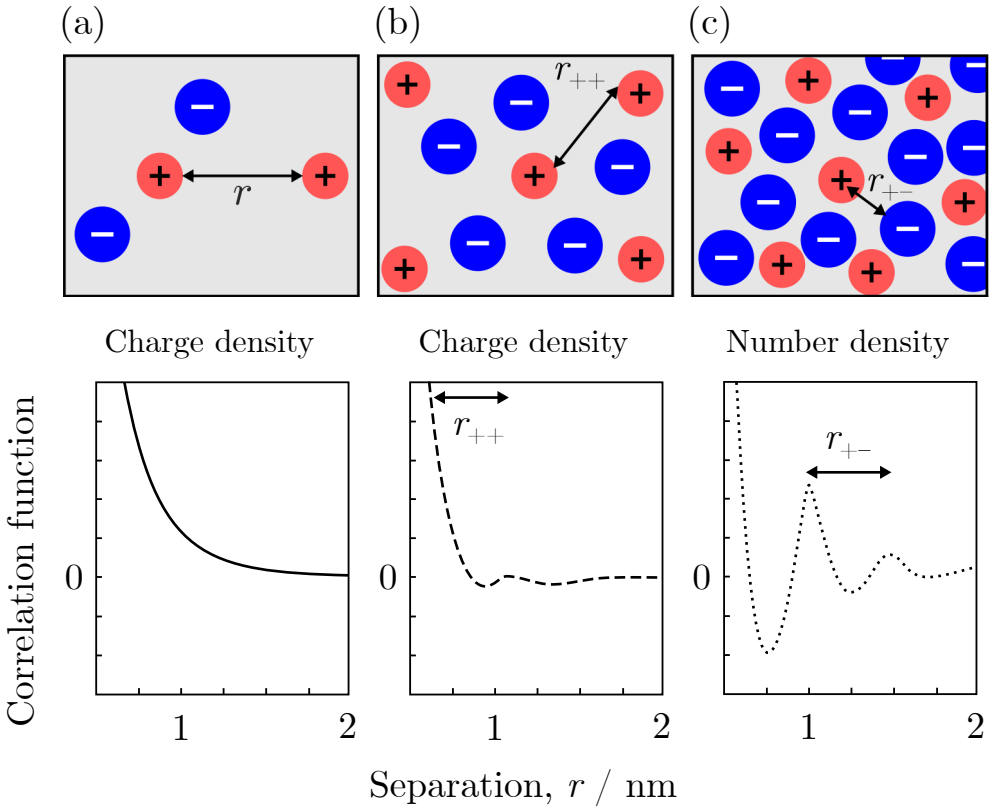


Figure 8.3 Electrolyte schematics and representative correlation functions at (a) low, (b) intermediate, and (c) high monovalent ion concentrations. (a) Correlations in charge density decay as a monotonic exponential function. (b) Correlations in charge density decay as a damped oscillatory function. The oscillatory wavelength is approximately equal to the distance between shells of the same charge density, r_{++} (c) Correlations in number density decay as a damped oscillatory function. The oscillatory wavelength is approximately equal to the cation-anion distance, r_{+-}.[167,170]

More recent theoretical and computational studies have had varying success in quantifying the experimental observations. Some have not been able to explain the presence of a long-range monotonic force.[59,175–177] Others have qualitatively reproduced the crossover from dilute to concentrated electrolyte behaviour, but with smaller decay lengths and a scaling exponent $\alpha < 3$.[168,178–182] Long-range monotonic behaviour, as per experiments, has been theoretically rationalised using DIT by considering multiple decay terms, where the leading decay mode can exhibit long-range monotonic behaviour.[97,183–185] However, the quantitative agreement with experiments is not yet possible as some parameters of the theory are not yet obtainable.

Alternative theoretical approaches based on mesoscopic theory[186] and dispersive plasmons[187] have claimed to be successful in deriving the experimentally observed scaling law.

8.1.4 Perspective

To date, underscreening has predominately been observed using the surface force balance.[35] Three other independent techniques have measured underscreening but, it should be noted that these are stand-alone measurements.[64,160,162] A recent study across aqueous alkali metal halides using colloidal probe AFM did not indicate any long-range electrostatic forces.[59] In order to question further whether the observed 'underscreening' is indeed a bulk fluid property as originally supposed, more independent techniques and measurements are required.

The majority of recent theoretical studies[168,178–180] are able to qualitatively reproduce the crossover from dilute to concentrated electrolyte behaviour, *i.e.* a transition from decreasing $\kappa^{-1}(=\lambda)$ with increasing ion concentration in the DH regime to increasing κ^{-1} with increasing concentration in the concentrated regime. However, the high concentration regime is characterised by oscillations that are not observed experimentally. This resembles the earlier works discussed in Section 8.1.3. By replotting key figures presented by Attard,[167] and de Carvalho and Evans,[170] as in Figure 8.4, the scaling behaviour of the electrostatic damped oscillatory regime with increasing concentration can be determined as $\alpha \approx 1.5$. This approximate α value corroborates with the more recent theoretical studies. As the experimentally observed decays appear to behave monotonically, comparing them to the scaling behaviour of the oscillatory regime is not appropriate, and likely contributes to the discrepancy between the experimental and theoretical values. Note that $\lambda/\lambda_{\mathrm{D}}$ is plotted on the y-axis of Figure 8.4, which is equivalent to $\kappa_{\mathrm{D}}/\kappa$ and is therefore the inverse of $\kappa/\kappa_{\mathrm{D}}$ plotted on the y-axis of Figure 8.2.

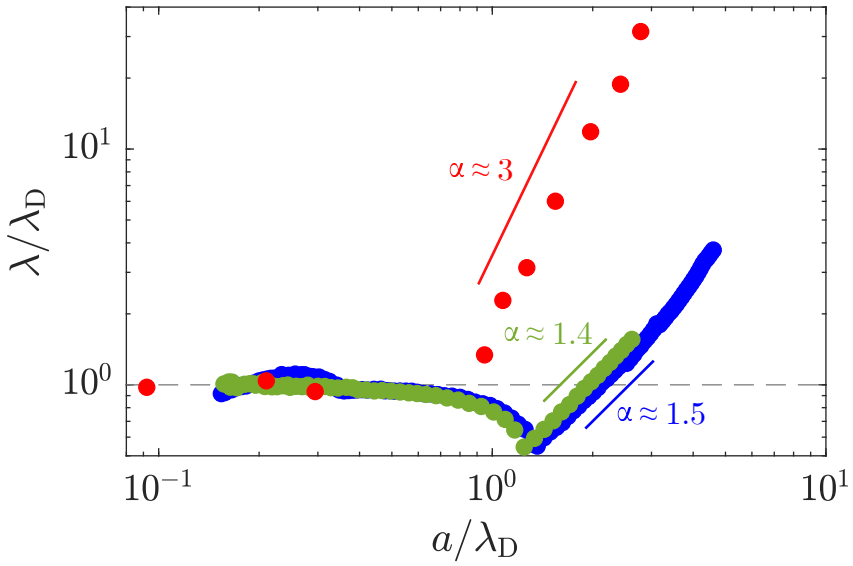


Figure 8.4 Decay length (experimental or theoretical) normalised by the corresponding Debye length, λ/λ_D, as a function of the mean ion diameter normalised by the Debye length, a/λ_D. Red circles correspond to the experimental work of Smith *et al.*[27] Blue and green circles correspond to the theoretical work of Attard,[167] and de Carvalho and Evans,[170] respectively. The solid lines indicate the gradient when $\lambda > \lambda_D$, which is equal to the scaling exponent, α. The dashed grey line indicates $\lambda = \lambda_D$.

We cannot, however, rule out the possibility that the experimental decay does have an oscillatory contribution. For example, the observed decay could be an oscillatory function with an infinitely large wavelength, or a non-dominant oscillatory component exists but cannot be observed due to the more prominent monotonic mode.

The experimentally observed scaling law (Equation 8.12) was proposed by Lee *et al.*[131] Motivated by the works of Kirkwood[165,166] and Keblinski *et al.*,[174] the dimensionless quantities λ_S/λ_D and a/λ_D were adopted. Unfortunately, the definitions of a and ϵ_r are not trivial.[184] The former will be discussed in further detail in Section 8.3.

8.2 Measurements with Concentrated Aqueous Monovalent Salts

Underscreening has been observed in different simple salt-in-water solutions including NaCl,[27] LiCl and CsCl.[26] In this section, we present further evidence of underscreening in aqueous solutions of the simple salts $LiNO_3$ and $NaNO_3$.

Figure 8.5 shows the log-linear representation of the normalised force profiles across (a) 4.56 m $LiNO_3$ and (b) 6.20 m and 7.52 m $NaNO_3$, where m is defined as the moles of solute per kilogram of solvent. At $D > 2$ nm, the long-range forces decay monotonically with experimental decay lengths, λ_{exp}, that exceed those predicted by DH theory (Table 8.1). The experimental decay length in aqueous $NaNO_3$ is also observed to increase with increasing concentration. Both observations are consistent with literature reports of underscreening-like behaviour.[33,131] Molecular layering is observed at $D < 2$ nm in both $LiNO_3$ and $NaNO_3$, with comparable jump-in dimensions of 0.31 $\pm$ 0.01 nm and 0.27 $\pm$ 0.01 nm, respectively.

Table 8.1 Calculated Debye lengths from DH theory, λ_D, and experimentally observed decay lengths, λ_{exp}, for aqueous solutions of $LiNO_3$ and $NaNO_3$ at high concentrations. Concentrations are given in molal, m, and also by the number of water molecules per salt unit.

Solution	λ_D / nm	λ_{exp} / nm	Salt:Water
4.56 m $LiNO_3$	0.14	0.97 $\pm$ 0.07	1:12
6.20 m $NaNO_3$	0.12	1.7 $\pm$ 0.1	1:9
7.52 m $NaNO_3$	0.11	2.1 $\pm$ 0.1	1:7

At these concentrations, we observe two regimes: a long-range monotonic decay mode and a short-range oscillatory mode, with different decay lengths. The molecular layering dimensions in both $LiNO_3$ and $NaNO_3$ correspond approximately to the diameter of water layers previously reported as 0.25-0.35 nm.[23,26] Statistically, these 'oscillations' could correspond to the water-water or ion-water-

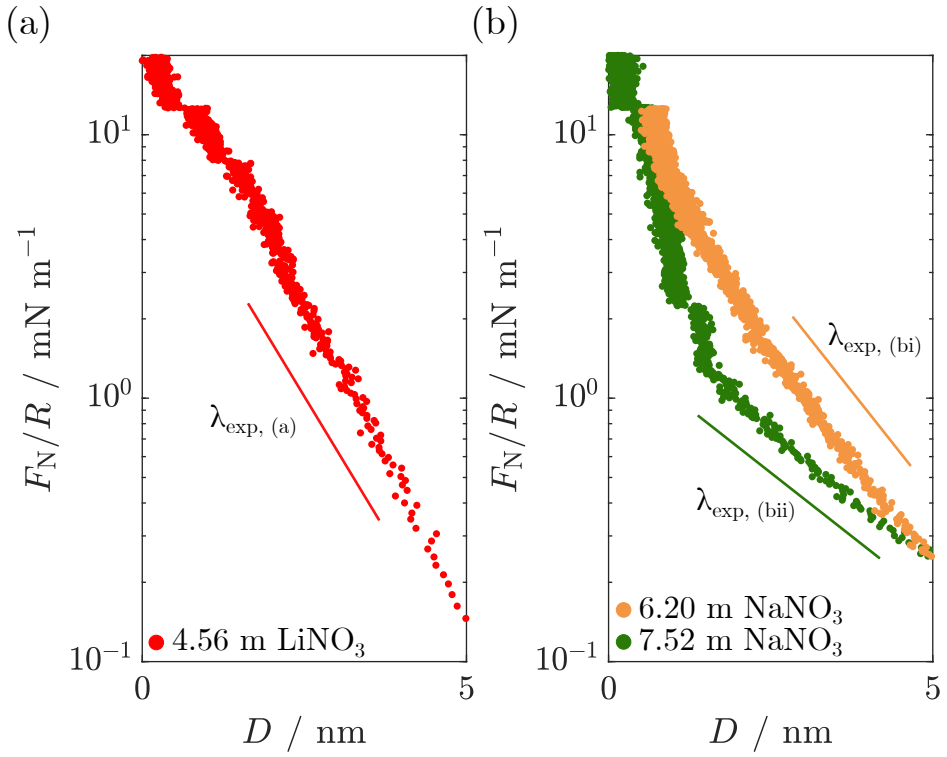


Figure 8.5 Log-linear representation of the normal force, F_N, normalised by the radius of curvature, R, as a function of surface separation, D, profiles across aqueous solutions of (a) 4.56 m $LiNO_3$ and (b) 6.20 m (orange) and 7.52 m (green) $NaNO_3$. The solid lines indicate the gradient of the long-range exponential decay where the experimental decay lengths are $\lambda_{exp,(a)} = 0.97 \pm 0.07$ nm, $\lambda_{exp,(bi)} = 1.7 \pm 0.1$ nm, and $\lambda_{exp,(bii)} = 2.1 \pm 0.1$ nm.

ion correlations. It is also possible to think of these jumps more pictorially, for example that we are squeezing out a single electroneutral layer of mixed cations, anions and water in such a way that water is the last component to be expelled from the confined region. Although the observed molecular layering dimensions are larger than the cation ionic diameters, and smaller than the bare anion diameter and the hydrated ion diameters given in Table 8.2, we cannot assume the layers correspond to water molecules only.

Table 8.2 Ionic and hydrated radii for ions relevant to this work.[127]

Ion	Ionic radius / nm	Hydrated radius / nm
Li^+	0.06	0.38
Na^+	0.10	0.36
NO_3^-	0.26	0.34

8.3 Ion Diameter Considerations

In this section we will revisit the scaling law that has been proposed and discuss the definition of the parameter a:

$$\left(\frac{\lambda_{\mathrm{S}}}{\lambda_{\mathrm{D}}}\right) = A + \left(\frac{a}{\lambda_{\mathrm{D}}}\right)^{\alpha}. \qquad \text{(8.12 revisited)}$$

For ionic liquids, the parameter a was defined as the mean ion diameter estimated from the cube root of the molecular volume, V_m, halved,[27,131]

$$\langle a \rangle \approx \sqrt[3]{\frac{V_m}{2}} \qquad (8.15)$$

where

$$V_m = \frac{M}{\rho N_{\mathrm{A}}}, \qquad (8.16)$$

M is the molar mass, ρ is the density, and N_{A} is Avogadro's constant. The calculated values corroborate experimental X-ray scattering measurements.[27,188] For aqueous salt solutions, the definition of the mean ion diameter is less clear as the ions can be treated as 'bare' or hydrated.

Figure 8.6 highlights three different definitions of a in aqueous monovalent salt solutions. Figure 8.6(a) shows the mean ion diameter, a_1, calculated from the sum of the bare (or unhydrated) ionic radii of the cation, r^+, and anion, r^-,

$$a_1 = r^+ + r^-. \qquad (8.17)$$

When considering the association of hydrated ions, there are three possibilities. Firstly, the hydrated ions may be 'solvent-separated' where the solvation shells do not overlap as in Figure 8.6(b). In this case the mean ion diameter, a_2, is

calculated from the sum of the hydrated radii of the cation, r^{+}_{hyd}, and anion, r^{-}_{hyd},

$$a_2 = r^{+}_{\mathrm{hyd}} + r^{-}_{\mathrm{hyd}}. \tag{8.18}$$

Here, we do not assume $r^{\pm}_{\mathrm{hyd}} = r^{\pm} + d_{\mathrm{H_2O}}$, where $d_{\mathrm{H_2O}}$ is the diameter of a water molecule, and instead use literature values of hydrated radii.[189]

If the solvation shells of the hydrated ions partially overlap, or 'solvent-share', as per Figure 8.6(c), we assume that the width of the overlapping region corresponds to $d_{\mathrm{H_2O}}$. The mean ion diameter, a_3, can then be calculated from the sum of the bare ionic radii of the cation and anion, plus $d_{\mathrm{H_2O}}$,

$$a_3 = r^{+} + r^{-} + d_{\mathrm{H_2O}}. \tag{8.19}$$

The final possibility involves the hydrated ions fully overlapping such that the ions are in contact with one another. As this is similar to Figure 8.6(a), we do not consider it as a unique definition.

Using the literature values of experimental decay lengths in aqueous solutions of NaCl,[27] LiCl and CsCl,[26] and the values determined in Section 8.2 for $LiNO_3$ and $NaNO_3$, we can determine whether the definition of a influences the observed features.

We can rewrite Equation 8.12 as

$$\left(\frac{\lambda_{\mathrm{S}}}{\lambda_{\mathrm{D}}}\right) = A + \left(\frac{a_i}{\lambda_{\mathrm{D}}}\right)^{\alpha} = A + \left(\frac{a^* b_i}{\lambda_{\mathrm{D}}}\right)^{\alpha}, \tag{8.20}$$

where we assume the relevant mean ion diameter, a_i, as per Figure 8.6, can be defined relative to a bare ion diameter, a^*, with $a_i = a^* b_i$. b_i is a multiplicative factor that accounts for the deviation of a_i from a^*. Taking the natural logarithm

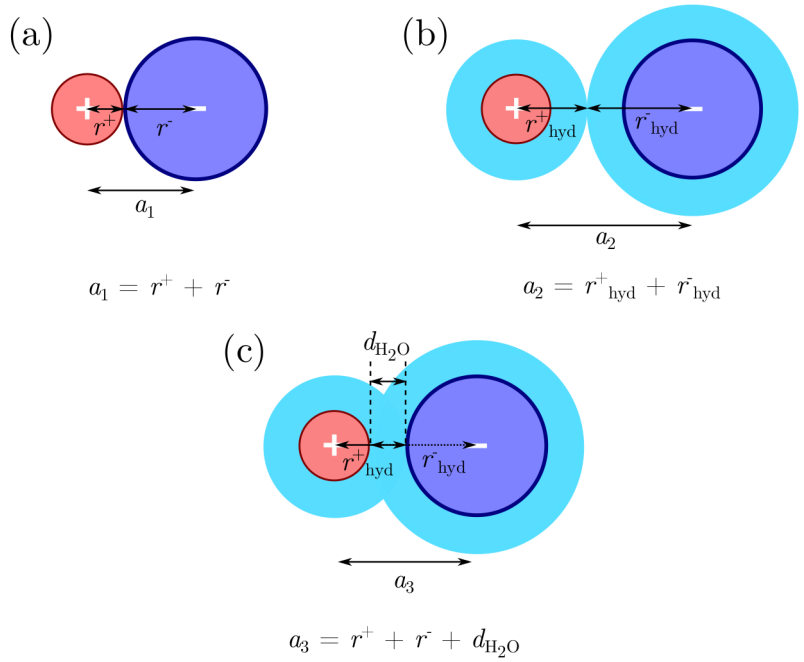


Figure 8.6 Schematics defining the mean ion diameter, a. (a) 'Bare' (or unhydrated) mean ion diameter, a_1, calculated from the sum of the ionic radii of the cation, r^+, and anion, r^-. (b) 'Solvent-separated' mean ion diameter, a_2, calculated from the sum of the hydrated radii of the cation, r^+_{hyd}, and anion, r^-_{hyd}. (c) 'Solvent-shared' mean ion diameter, a_3, calculated from the sum of the bare ionic radii of the cation and anion, plus $d_{\mathrm{H_2O}}$.

of Equation 8.20 yields,

$$\ln\left(\frac{\lambda_{\mathrm{S}}}{\lambda_{\mathrm{D}}}\right) = \ln A + \alpha \ln b_i + \alpha \ln\left(\frac{a^*}{\lambda_{\mathrm{D}}}\right) = C + \alpha \ln\left(\frac{a^*}{\lambda_{\mathrm{D}}}\right), \tag{8.21}$$

where $C = \ln A + \alpha \ln b_i$. Thus we see that deviations in a_i from a^* alters the constant, C, but not the concentration-dependent term $\alpha \ln(a^*/\lambda_{\mathrm{D}})$. We therefore expect an influence on the transition point to underscreening *i.e.* the point at which the experimental decay length begins to increase with increasing concentration ($\lambda_{\mathrm{S}} > \lambda_{\mathrm{D}}$).

Figure 8.7 shows three plots of $\lambda_{\mathrm{exp}}/\lambda_{\mathrm{D}}$ as a function of a_i/λ_{D} for each definition given in Figure 8.6. Here, we use the term λ_{exp} in place of λ_{S}. From

this series of plots we show that α is indeed independent of the definition of a_i. We also observe a variation in the transition point to underscreening, K_i, with the definition of a_i. Figures 8.7(a) and (b) highlight the two 'extremes' of the definition of a_i: when the cation and anion are (a) closest to and (b) furthest away from one another. We see that the values of K_1 and K_2 do not deviate drastically from the predicted Kirkwood transition at $a/\lambda_D \approx \sqrt{2}$.[167] However, the solvent-shared definition gives rise to $K_3 = 1.5 \pm 0.5$, which is closer to the predicted Kirkwood transition. We therefore suggest that the transition point to underscreening could coincide with the Kirkwood transition if the appropriate definition of a_i is resolved.

As the scaling exponent does not depend on the definition of a, we can now present an updated version of λ_{exp}/λ_D as a function of a/λ_D, first plotted by Smith *et al.*[27] Figure 8.8 includes the concentrated aqueous monovalent salts studied both here and in the literature as well as the other concentrated systems that have exhibited underscreening (including 1:2 ChCl:EG studied in Chapter 5). In Figure 8.8(a), we assume for aqueous solutions of NaCl, LiCl, $LiNO_3$, $NaNO_3$, and CsCl, that $a_i = a_1$ (as per Equation 8.17), whereas in Figure 8.8(b) we assume that $a_i = a_3$ (as per Equation 8.19). The data does not necessarily collapse onto a single curve as proposed by the scaling law (Equation 8.10),[131] but depends on how a_i is defined for each system.

There are still outstanding questions with regards to the proposed scaling law and the definitions of the parameters it depends on, namely the concentration. In Figure 8.7, we have used the bulk concentration defined as the number of salt units per volume of solution, with solution densities estimated from the literature.[190–192] However, the experimental decay length is measured under extreme confinement and one should question whether the local and bulk densities (concentrations) are the same, and if they remain constant with increasing confinement. As the

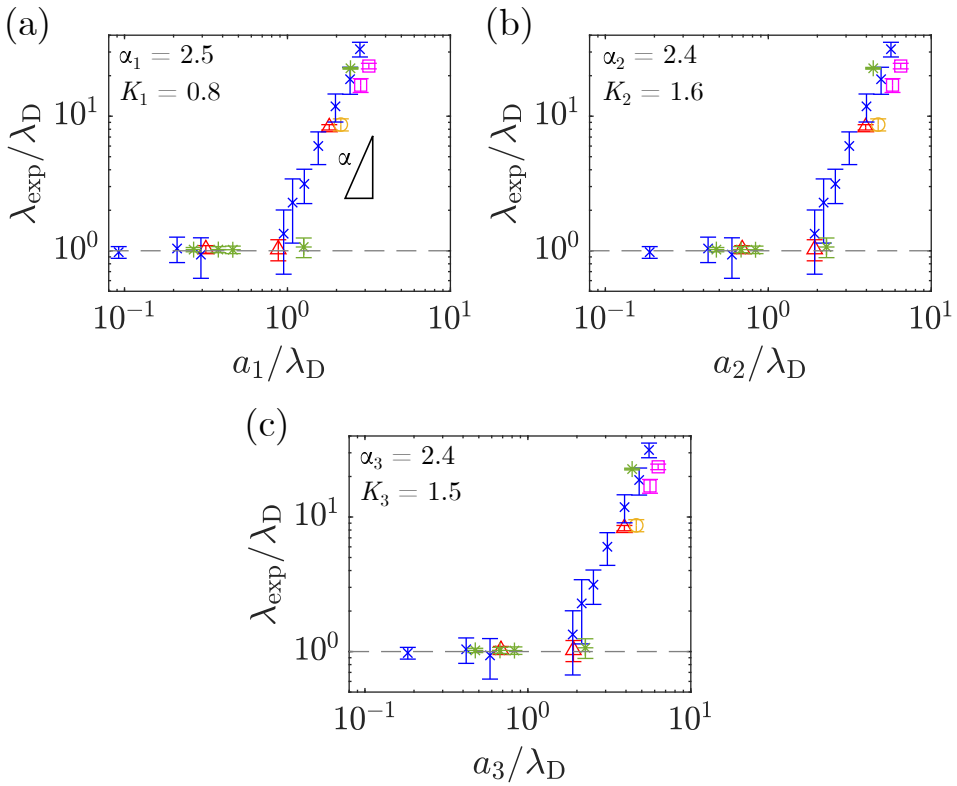


Figure 8.7 Experimental decay length normalised by the corresponding Debye length, λ_{exp}/λ_D, as a function of the mean ion diameter normalised by the Debye length, a_i/λ_D, for different definitions of a_i given in Figure 8.6. Blue crosses correspond to $NaCl_{(aq)}$,[27] red triangles to $LiCl_{(aq)}$,[26] green asterisks to $CsCl_{(aq)}$,[26] pink squares to $NaNO_{3(aq)}$ (this work), yellow circle to $LiNO_{3(aq)}$ (this work). The dashed grey line indicates $\lambda_{exp} = \lambda_D$. (a) The 'bare' mean ion diameter, a_1, yields $\alpha_1 = 2.5 \pm 0.4$ and intersects $\lambda_{exp} = \lambda_D$ when $a_1/\lambda_D = K_1 = 0.8 \pm 0.1$. (b) The 'solvent-separated' mean ion diameter, a_2, yields $\alpha_2 = 2.4 \pm 0.6$ intersecting the dashed grey line at $a_2/\lambda_D = K_2 = 1.6 \pm 0.5$. (c) The 'solvent-shared' mean ion diameter, a_3, yields $\alpha_3 = 2.4 \pm 0.6$ intersecting the dashed grey line at $a_3/\lambda_D = K_3 = 1.5 \pm 0.5$.

dielectric constant depends on the concentration, the same question may be asked as to whether the local and bulk dielectric constants are the same, as this would alter the values of the Debye and Bjerrum lengths. We have also assumed that a does not vary with concentration, which is counterintuitive as one would expect a different number of water molecules in the solvation shells of extremely dilute and highly concentrated electrolytes.

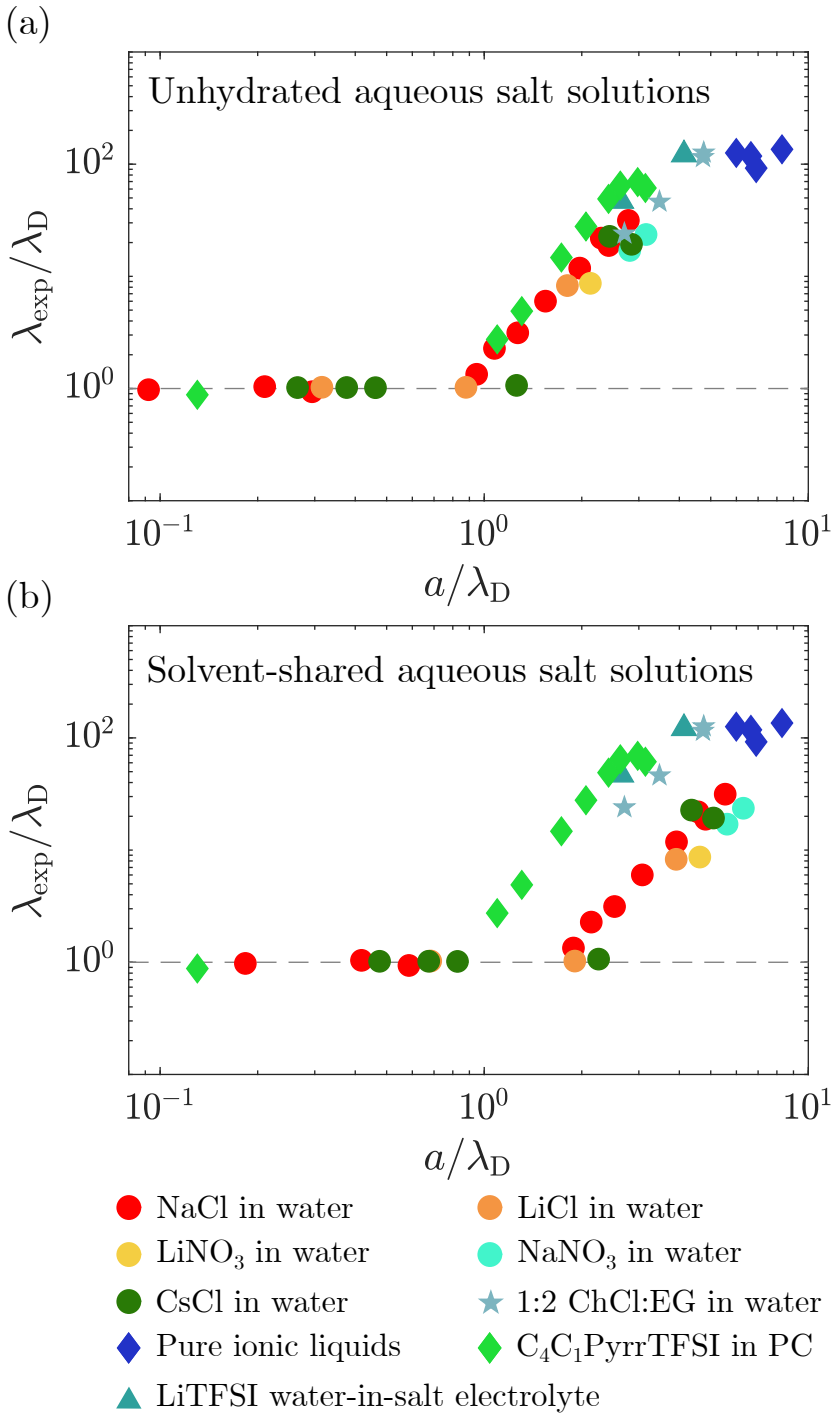


Figure 8.8 Experimental decay length normalised by the corresponding Debye length, λ_{exp}/λ_D, as a function of the mean ion diameter normalised by the Debye length, a/λ_D. Two definitions of a_i are used for aqueous solutions of NaCl, LiCl, $LiNO_3$, $NaNO_3$, and CsCl: (a) unhydrated a_1 and (b) solvent-shared a_3. Red circles correspond to $NaCl_{(aq)}$,[27] orange circles to $LiCl_{(aq)}$,[26] yellow circles to $LiNO_{3(aq)}$ (this work), cyan circles to $NaNO_{3(aq)}$ (this work), green circles to $CsCl_{(aq)}$,[26] blue-grey stars to 1:2 molar ratio choline chloride (ChCl) to ethylene glycol (EG) in water (this work),[1] blue diamonds to pure ionic liquids,[27] green diamonds to C_4C_1Pyrr TFSI ionic liquid in propylene carbonate (PC),[27] and blue-grey triangles to LiTFSI water-in-salt electrolyte.[50] The dashed grey line indicates $\lambda_{exp} = \lambda_D$.

8.4 Confinement Geometry

As discussed in Section 8.1, underscreening seems to be a general phenomenon observed in concentrated electrolytes, with the majority of the measurements carried out using the SFB.[1,27,34,50,96,161] Underscreening has also been observed in ethylammonium nitrate using colloidal probe AFM,[64] however, attempts to reproduce SFB measurements in concentrated aqueous salt solutions have so far been unsuccessful.[59]

There are a number of experimental variables that may explain the origin of the long-range forces observed in SFB measurements including hydrodynamic forces in viscous systems, surface potential, and the geometry of the confinement. Hydrodynamic forces can be accounted for and approach speeds can be controlled, as described by Lhermerout and Perkin,[88] such that underscreening is still observed in more viscous systems. By controlling surface potential it can be explored whether confinement between mica surfaces induces underscreening, and it has been shown that the surface potential does not influence the observed screening behaviour.[193] Finally, when studying the influence of confinement geometry, it was initially concluded that underscreening was present and the experimental decay length did not depend on the geometry.[161] Since this work, the influence of confinement geometry has not been extensively studied and thus this section looks at the influence of confinement geometry on the experimental decay lengths in more detail.

8.4.1 Hydrodynamic Forces

In order to study the effect of geometry on the equilibrium forces, it is important to ensure that small changes to hydrodynamic (non-equilibrium) forces do not influence the results. In the work of Lhermerout and Perkin,[88] measurements of interfacial forces in 1-ethyl-3-methylimidazolium bis(trifluoromethylsulfonyl)imide,

C_2C_1Im TFSI, were made using a surface force balance. Three orders of magnitude of approach velocity, $v = \dot{D}$, were explored to aid in disentangling the viscous and electrostatic contributions to the overall surface force, $F(t)$,

$$F(t) = -\frac{6\pi\eta R^2 \dot{D}}{D - b} + 2\pi RA \exp(-D/\lambda_{\text{exp}}). \tag{8.22}$$

The viscous contribution is described by the first term on the right-hand side and depends on the viscosity, η, the radius of curvature of the lenses, R, and the negative slip length, b (shown in Figure 4.2(b)). The electrostatic interaction is modelled by an exponential function that has an amplitude of $2\pi RA$ and decays with λ_{exp}.

At high velocities, it is expected the viscous force will dominate and the overall interfacial force can be modelled using the viscous term alone *i.e.* $A = 0$. This allows one to fit the negative slip length.

At low velocities, any electrostatic repulsion will not be captured by the purely viscous term and one must consider the electrostatic term, yielding both A and λ_{exp}.

At intermediate velocities, both viscous and electrostatic forces contribute to the total force. Surprisingly, it is also shown that by ignoring the viscous contribution at intermediate velocities (by fitting a linear baseline after the initial start-up curvature), the fitted experimental decay length and amplitude values are consistent with those fitted at lower velocities.

If viscous forces are present, the magnitude of the force will increase with increasing velocity. As long as the velocity is within and below the intermediate regime velocities, the change in magnitude of the force should not influence λ_{exp}. An indication that viscous forces are dominating can be observed when plotting

λ_{exp} as a function of approach speed as in Figure 8.9. When electrostatic forces are dominating, λ_{exp} should not be influenced by approach speed (the 'equilibrium' region to the left of the red line in Figure 8.9). However, when crossing over to viscous dominated forces, λ_{exp} can be seen to increase with velocity (the 'non-equilibrium' region to the right of the red line in Figure 8.9).

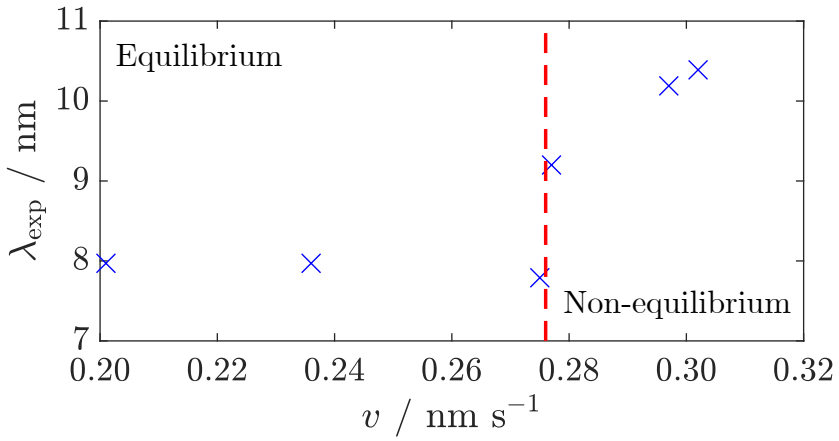


Figure 8.9 Experimental decay length, λ_{exp}, as a function of approach speed across dry C_2C_1Im TFSI at $T \approx 24$ °C, $R = 3.5 \pm 0.3$ cm. As the velocity is increased from 0.201 to 0.275 nm s^{-1}, λ_{exp} does not change significantly (the 'equilibrium' region). Beyond 0.276 nm s^{-1} however, λ_{exp} is observed to increase with increasing velocity (the 'non-equilibrium' region). To the right of the red line viscous forces need to be accounted for.

8.4.2 Comparison Factors

The regimes studied in the work of Lhermerout and Perkin [88] can be compared with other systems. By using the velocity, radius of curvature ($R = 0.885$ cm), and viscosity ($\eta = 37$ mPa s at 25 °C) values, a regime comparison factor, C_{reg}, can be calculated that is proportional to the hydrodynamic force, F_{hydro},

$$C_{reg} = \eta v R^2 \propto F_{hydro}. \tag{8.23}$$

Using the values in Table 8.3, a velocity in any system can be estimated for

each regime,

$$v = \frac{C_{\text{reg}}}{\eta R^2}, \tag{8.24}$$

so long as the viscosity and radius of curvature are known.

Table 8.3 Comparison factors for high, low and intermediate velocity regimes for C_2C_1Im TFSI ($\eta = 37$ mPa s at 25 ^{o}C) and $R = 0.885$ cm.

Regime	Velocity / nm s^{-1}	$C_{\text{reg}} \times 10^6$ / Pa nm m^2
High	95	275
Intermediate	1.1	3.27
Low	0.24	0.696

8.4.3 Using C_{reg} values

In the current work, the ionic liquid C_2C_1Im TFSI ($\eta = 38.1$ mPa s at 21 ^{o}C)[194] has been studied under different confinement geometries. Using the comparison factors in Table 8.3 and Equation 8.24, appropriate approach velocities can be calculated for different radii of curvature (Table 8.4). For example, to observe a purely viscous force across $R = 0.49$ cm lenses, the approach velocity should exceed 301 nm s^{-1}.

Table 8.4 Approach velocities in C_2C_1Im TFSI corresponding to three force regimes for sets of equal radii, R, hemicylindrical lenses. High and low regimes correspond to hydrodynamic and electrostatic forces dominating, respectively. The intermediate regime corresponds to a combination of hydrodynamic and electrostatic forces where the electrostatic force can be isolated.

Regime	Velocity / nm s^{-1}		
	$R = 0.49$ cm	$R = 0.92$ cm	$R = 3.5$ cm
High	301	85.4	6.04
Intermediate	3.58	1.02	0.0718
Low	0.761	0.216	0.0153

The viscosity of C_2C_1Im TFSI makes these measurements more accessible compared to other more viscous ionic liquids. For electrostatic forces to dominate, the approach velocities will need to be slow. If a more viscous ionic liquid is used, the approach velocities would need to be slower. When approaching slowly, the

system is more susceptible to the influence of thermal drift, making it difficult to approach at $v < 0.1$ nm s^{-1} without the linearity of the approach baseline being influenced.

For example, the ionic liquid 1-butyl-1-methylpyrrolidinium bis(trifluoromethylsulfonyl)imide, C_4C_1Pyrr TFSI, has a viscosity, $\eta = 94$ mPa s at 21 ^{o}C.[195] If the measurements were carried out with lenses of the same radii of curvature as in Table 8.4, the corresponding velocities for each regime would be those given in Table 8.5. To observe a dominant electrostatic force (low regime) in C_4C_1Pyrr TFSI using $R = 0.92$ cm lenses, approach velocities less than 0.0873 nm s^{-1} should be used, whereas in C_2C_1Im TFSI velocities less than 0.216 nm s^{-1} can be used - a substantially higher velocity. It is clear that using a system with a lower viscosity broadens the range of velocities that can be used.

Table 8.5 Approach velocities in C_4C_1Pyrr TFSI corresponding to three force regimes for sets of equal radii, R, hemicylindrical lenses. High and low regimes correspond to hydrodynamic and electrostatic forces dominating, respectively. The intermediate regime corresponds to a combination of hydrodynamic and electrostatic forces where the electrostatic force can be isolated.

Regime	Velocity / nm s^{-1}		
	$R = 0.49$ cm	$R = 0.92$ cm	$R = 3.5$ cm
High	122	34.6	2.39
Intermediate	1.45	0.411	0.0284
Low	0.308	0.0873	0.00603

8.4.4 C_2C_1Im TFSI

Literature decay length values for C_2C_1Im TFSI vary depending on temperature[161] and relative humidity.[34] In the following measurements the lower limit of the approach baseline ($\approx 3\lambda$) has been calculated using the value, $\lambda_{exp} = 8.0$ nm[88] (see Section 2.2.4).

Figure 8.10 shows normalised force-distance profiles across dry C_2C_1Im TFSI using different R, and the experimental decay lengths are summarised in Table 8.6.

This work shows an apparent increase in λ_{exp} with increasing R, with λ_{exp} values that exceed the predicted Debye length by 2 orders of magnitude ($\lambda_D \approx 0.06$ nm). The structural forces also become less well defined with increasing R as a result of more extensive surface deformations (glue and/or mica) which limit the applied pressures.[161]

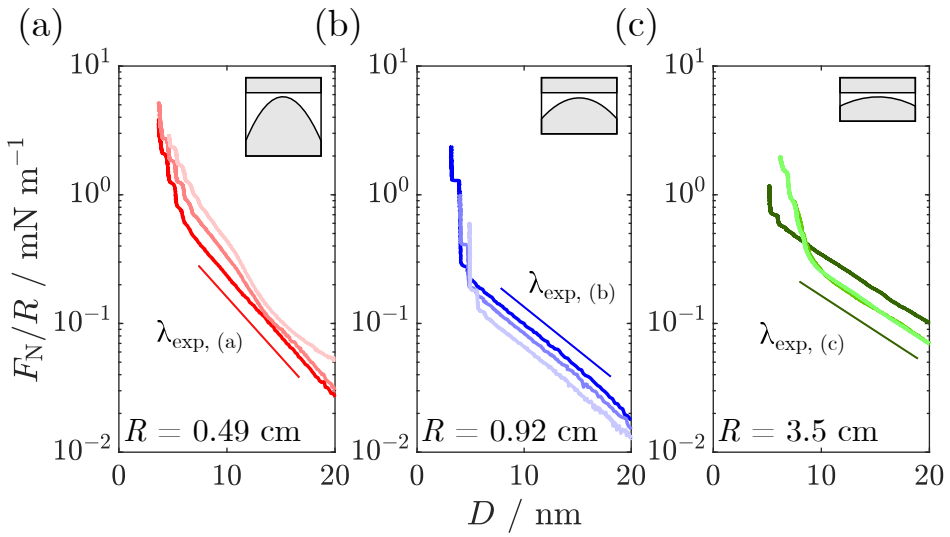


Figure 8.10 Representative normalised force-distance profiles across dry C_2C_1Im TFSI at $T \approx 24$ °C. (a) $R = 0.49 \pm 0.05$ cm, at approach velocities between 0.636-1.56 nm s^{-1}. All profiles have been fitted relative to a fixed baseline set between 30 and 70 nm. The experimental decay length, $\lambda_{exp,(a)} = 4.1 \pm 0.2$ nm. (b) $R = 0.92 \pm 0.09$ cm, at approach velocities between 0.414-1.80 nm s^{-1}. All profiles have been fitted relative to a fixed baseline set between 25 and 40 nm. The experimental decay length, $\lambda_{exp,(b)} = 6.6 \pm 0.1$ nm. (c) $R = 3.5 \pm 0.3$ cm, at approach velocities between 0.201-0.275 nm s^{-1}. The force profiles correspond to those in Figure 8.9 that occur to the left of the red dashed line. All profiles have been fitted relative to a fixed baseline set between 30 and 70 nm. The experimental decay length, $\lambda_{exp,(c)} = 7.9 \pm 0.1$ nm. The insets highlight the confinement geometry.

Table 8.6 Summary of the experimental decay lengths, λ_{exp}, across dry C_2C_1Im TFSI films confined between sets of equal radii of curvature, R, hemicylindrical lenses, observed in Figure 8.10.

Radius of curvature / cm	λ_{exp} / nm
0.49	4.1 ± 0.2
0.92	6.6 ± 0.1
3.5	7.9 ± 0.1

The dependence of λ_{exp} on R is plotted in Figure 8.11. A potential trend is highlighted by the grey dashed line where λ_{exp} tends towards zero as the

confining surfaces become more sharp. As AFM measurements typically use tips with nanometre-scale R, it could be rationalised that underscreening cannot be observed with such sharp tips and hence is absent in AFM literature measurements. However, this observation and conclusion is tentative at this stage due to several factors.

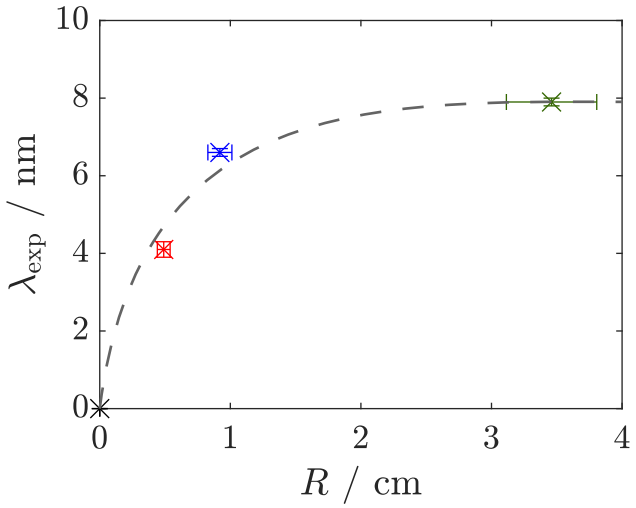


Figure 8.11 Experimental decay length, λ_{exp}, as a function of radius of curvature, R. Red, blue, and green crosses and their associated errors are taken directly from Figure 8.10 and Table 8.6. The grey dashed line acts as a guide to highlight a potential trend with the black cross indicating the point $(R, \lambda_{exp}) = (0, 0)$.

Firstly, the observation contrasts with Gebbie *et al.*[161] where comparable decay lengths using both 1- and 4- to 5-cm-radius surfaces were observed. We also do not expect there to be a trend with R by the Derjaguin approximation. Although the validity of the Derjaguin approximation for sphere-sphere electrostatic interactions has been considered,[196] it is unlikely we are observing a failure of the approximation.

Secondly, the surface deformations discussed with regards to the structural force could be influencing the observed λ_{exp} in this work. Here, we assume R is independent of the applied force. However, as the radius of curvature increases so does the tendency for deformation. If the surfaces deform and R increases during the course of a measurement, the force will not behave as expected for

zero deformation and could be mistaken for a long-range monotonic decay.

More extensive studies using a variety of electrolytes are required to understand the influence of confinement geometry on underscreening. We must also consider if surface deformations are present in this work using an appropriate contact mechanics model *e.g.* JKR, Hertz, DMT.[117,197]

8.5 Summary

In this chapter, we have discussed the literature with regards to the theory of electrolytes. For dilute electrolytes, Debye-Hückel theory is valid but as the concentration increases we observe a change in the electrostatic behaviour from monotonic to oscillatory decay (Kirkwood transition). The Kirkwood transition was successfully reproduced using different models, approximations and simulations before the turn of the century. We have also presented the observations made in concentrated electrolytes over the past decade, which appear qualitatively similar to the theory. The underscreening phenomenon has been observed using independent techniques and seems to be general to many concentrated systems, with an apparent relationship between the observed screening length and mean ion diameter. More recent theoretical studies have attempted to quantify this apparent scaling law, with varying success. It is clear that further independent measurements of underscreening are required.

We report new underscreening-like behaviour in concentrated aqueous lithium and sodium nitrate solutions with experimental decay lengths that exceed predicted Debye lengths, and an increase in the experimental decay length with increasing sodium nitrate concentration. Molecular layering is also observed in both nitrate salts with a dimension coinciding with the diameter of water.

The definition of the mean ion diameter in aqueous monovalent salt solutions

is discussed, and does not influence the scaling exponent but it does alter the transition point to underscreening. To further understand the scaling law, the definition of bulk and local concentrations should be considered which may impact the dielectric constants. It should also be determined whether, and if so how, a varies with concentration.

Finally, we report that underscreening is present regardless of confinement geometry. Hydrodynamic forces are discussed and considered before reporting a confinement geometry dependence of decay length in concentrated electrolytes. However, this is not expected and could be due to surface deformations. More extensive work is required to understand the influence of confinement geometry including contact mechanics calculations and studies involving other electrolytes.

Chapter 9

Conclusions and Outlook

The work in this thesis explores the bulk and interfacial properties across electrolyte films. Of particular interest are deep eutectic solvents (DESs), a concentrated eutectic mixture of (typically) a salt and some molecular component. As chemical industries shift towards more sustainable chemistry practices, the large-scale consumption of harmful organic solvents must be addressed.[77] Depending on the components, DESs can be used as a 'greener' solvent alternative in synthesis,[122] metal processing applications like electrodeposition,[80] and as lubricants.[123–126] The main body of this thesis explores the behaviour of two DESs: choline chloride:ethylene glycol (ChCl:EG) and ChCl:glycerol (Gly), and the corresponding pure molecular fluids using the surface force balance (SFB). Using a differential scanning calorimeter (DSC), the bulk phase behaviour of the ChCl:EG DES is also measured.

A key conclusion from this work is that the eutectic point of ChCl:EG does not coincide with the point reported by Shahbaz *et al.*[142] at -66 ^{o}C and a molar ratio of 1:2 ChCl:EG. Instead, the eutectic melt observed in Chapter 7 corroborates the recent work of Agieienko and Buchner,[145] and is observed at a

far lower ChCl composition. Probing the thermal events of ChCl:EG mixtures using DSC highlights the importance of considering thermodynamic and kinetic transitions separately. In fact, a cold-crystallisation that behaves in a eutectic manner around -66 ^{o}C and a molar ratio of 1:2 ChCl:EG, is observed here. However, crystallisation is a kinetic phenomenon whereas the melting point is thermodynamic, and it is not necessarily correct to assume that the freezing and melting points are equal. Within the DES community, a clearer definition of a 'deep eutectic solvent' is required that does not only depend on kinetic thermal behaviour *i.e.* a depression in the *freezing point*. Instead, both the thermodynamic and kinetic behaviour should be considered to produce a less ambiguous definition.

It has been speculated that the 'on-eutectic' ChCl:EG gives rise to optimal friction.[124] As the studies under confinement were completed prior to the bulk phase measurements, the 'on-eutectic' composition was taken as 1:2 ChCl:EG.[142] In Chapter 5, the frictional response of both 'on-eutectic' and 'off-eutectic' ChCl:EG mixtures were studied. It was shown that 1:2 ChCl:EG does not give rise to optimal friction and that the overall lubrication properties at $F_{\mathrm{N}} < 80$ μN were not influenced by the proportion of ChCl. In light of the conclusion made above and the fact that optimal lubrication properties are not seen in 1:2 ChCl:EG, one can conclude that 1:2 ChCl:EG is not particularly remarkable.

To test the hypothesis of optimal friction at the eutectic composition, bulk phase behaviour in the ChCl:EG mixtures would need to be studied extensively at $x_{\mathrm{ChCl}} < 0.1$ to confirm the 'real' eutectic composition. The phase behaviour could also be explored using another independent technique such as polarised optical microscopy, akin to the measurements by Gilmore *et al.*[159] Once the eutectic composition has been found, the nanoscale frictional response could be measured using the SFB to determine if the eutectic composition does indeed have optimal friction properties.

The lubrication properties of the ChCl:EG and ChCl:Gly DESs explored in Chapters 5 and 6, revealed behaviour dominated by shearing domains of molecular solvent. As pure ethylene glycol and glycerol were studied in Chapters 3 and 4, respectively, a direct comparison could be made between the frictional response in the DES and in the pure solvent. 'Quantised' friction was observed in all systems. In dry EG and dry 1:2 ChCl:EG, the coefficients of friction in the individual friction-load regimes were observed to increase with increasing confinement. On the other hand, in dry Gly and dry 1:2 ChCl:Gly, the friction coefficients remained the same regardless of load or film thickness. In both instances, the dry DESs did not outperform the dry molecular solvents over the loads studied. We therefore conclude that the molecular solvent is important in determining the lubrication properties of these DESs, and that mixing ChCl with EG/Gly does not improve the lubrication properties of the pure solvents. Nonetheless, salt-based DESs are electrolytes and are therefore more suitable for applications that rely on electrolytic lubricants *e.g.* electrotunable friction.[133]

In this work, the normal loads are limited to the micronewton-scale. This work could be extended to measure how both the molecular solvents and the 'real' eutectic composition of ChCl:EG behave under greater loads and at the macroscale. Nanoscale friction under greater loads could be accessed using a stiffer normal spring in the SFB. Using a tribometer would allow friction at the macroscale to be studied with varying load. For ethylene glycol and glycerol, macroscale friction coefficients have been obtained,[94,110,114] but it would be interesting to determine whether the DESs can sustain higher normal loads and if the friction coefficient remains comparable to the pure molecular solvent.

Over the past 5 years, there has been a growing interest in DESs as potential battery electrolytes.[198–201] A future direction of this work would involve studying the behaviour of DESs at electrified surfaces, mimicking the electrode-electrolyte

interface. By using an alternative SFB setup, for example the mica-gold asymmetric system[202] or triple gold setup,[13] surface potential could be controlled. The interfacial structure could then be probed with varying surface potential similar to the atomic force microscopy (AFM) studies of Chen *et al.*[65] and Hammond *et al.*[67] The electrochemical behaviour of the DESs could also be studied at the nanoscale via cyclic-voltammetry, chronoamperometry, and chronocoulometry methods. These studies would reveal information regarding the behaviour of DESs at the electrode interface, and whether they are suitable for technological applications.

In Chapter 8, the focus shifts to considering concentrated electrolytes more generally and the phenomenon of underscreening. In this thesis we expand the range of concentrated electrolytes in which this phenomenon is observed including mixtures of 1:2 ChCl:EG and water, and concentrated aqueous nitrate solutions of sodium and lithium. The scaling exponent, α, proposed by Lee *et al.*[131] is shown not to depend on the definition of the mean ion diameter, and hence this cannot account for the discrepancy between the experimentally and theoretically observed scaling exponents. However, the definition of the mean ion diameter does influence the transition point to underscreening which may coincide with the Kirkwood transition if the appropriate definition of a_i is resolved. Finally, underscreening is shown to be present regardless of confinement geometry.

Further phenomenological and experimental work is required to discern the origin of underscreening, and to understand the differences between theoretical and experimental results. At the nanoscale, the concentration will not necessarily coincide with the bulk value. It may therefore be important to consider the local ion concentrations which in turn influence the local dielectric constants, and hence the proposed scaling law. Furthermore, as the concentration changes, one may expect a to vary as the number of solvent (water) molecules changes in the

solvation shells of the ions. Exploring a larger range of geometries and electrolyte systems will allow the influence of confinement geometry to be quantified more completely. Through further measurements and contact mechanics calculations it may also be realised that the apparent confinement geometry dependence is indeed a result of surface deformation. With regards to underscreening in general, one outstanding discrepancy is the differing observations in SFB and AFM. To address this, the SFB could be modified to study the interfacial forces across electrolytes using silicon surfaces, a material commonly used in AFM.[59] However, compared to atomically smooth mica surfaces, the surface roughness of a silicon surface could compromise the SFB measurement. A method of fabrication would need to be developed that produced smooth silica surfaces, potentially by invoking a template stripping method.[13,14]

References

1. J. E. Hallett, H. J. Hayler and S. Perkin, *Phys. Chem. Chem. Phys.*, 2020, **22**, 20253–20264.

2. Unsplash, https://unsplash.com/, (accessed May 20, 2022).

3. J. Israelachvili, *Intermolecular and Surface Forces*, Elsevier, Waltham, MA, 2011.

4. R. Evans, J. R. Henderson, D. C. Hoyle, A. O. Parry and Z. A. Sabeur, *Mol. Phys.*, 1993, **80**, 155–775.

5. D. Tabor and R. H. S. Winterton, *Nature*, 1968, **219**, 1120–1121.

6. J. N. Israelachvili and D. Tabor, *Proc. R. Soc. Lond. A*, 1972, **331**, 19–38.

7. J. N. Israelachvili and G. E. Adams, *Nature*, 1976, **262**, 774–776.

8. J. Israelachvili, Y. Min, M. Akbulut, A. Alig, G. Carver, W. Greene, K. Kristiansen, E. Meyer, N. Pesika, K. Rosenberg and H. Zeng, *Reports Prog. Phys.*, 2010, **73**, 036601.

9. M. Ludwig and R. von Klitzing, *Curr. Opin. Colloid Interface Sci.*, 2020, **47**, 137–152.

10. W. Lin and J. Klein, *Appl. Phys. Rev.*, 2021, **8**, 031316.

11. H.-Y. Ren, M. Mizukami and K. Kurihara, *Rev. Sci. Instrum.*, 2017, **88**, 095108.

12. L. Chai and J. Klein, *Langmuir*, 2007, **23**, 7777–7783.

13. C. D. van Engers, M. Balabajew, A. Southam and S. Perkin, *Rev. Sci. Instrum.*, 2018, **89**, 123901.

14. J. Britton, N. E. Cousens, S. W. Coles, C. D. van Engers, V. Babenko, A. T. Murdock, A. Koós, S. Perkin and N. Grobert, *Langmuir*, 2014, **30**, 11485–11492.

15. C. D. van Engers, N. E. Cousens, V. Babenko, J. Britton, B. Zappone, N. Grobert and S. Perkin, *Nano Lett.*, 2017, **17**, 3815–3821.

16. J. N. Israelachvili and R. M. Pashley, *J. Colloid Interface Sci.*, 1984, **98**, 500–514.

17. J. Klein, U. Raviv, S. Perkin, N. Kampf, L. Chai and S. Giasson, *J. Phys. Condens. Matter*, 2004, **16**, S5437–S5448.

18. U. Raviv, P. Laurat and J. Klein, *J. Chem. Phys.*, 2002, **116**, 5167–5172.

19. J. N. Israelachvili and G. E. Adams, *J. Chem. Soc. Faraday Trans. 1*, 1978, **74**, 975–1001.

20. R. M. Pashley, *J. Colloid Interface Sci.*, 1981, **80**, 153–162.

21. R. M. Pashley, *J. Colloid Interface Sci.*, 1981, **83**, 531–546.

22. R. M. Pashley, *Adv. Colloid Interface Sci.*, 1982, **16**, 57–62.

23. J. N. Israelachvili and R. M. Pashley, *Nature*, 1983, **306**, 249–250.

24. R. M. Pashley and J. N. Israelachvili, *J. Colloid Interface Sci.*, 1984, **101**, 511–523.

25. R. M. Pashley and J. N. Israelachvili, *J. Colloid Interface Sci.*, 1984, **97**, 446–455.

26. T. Baimpos, B. R. Shrestha, S. Raman and M. Valtiner, *Langmuir*, 2014, **30**, 4322–4332.

27. A. M. Smith, A. A. Lee and S. Perkin, *J. Phys. Chem. Lett.*, 2016, **7**, 2157–2163.

28. S. Perkin, T. Albrecht and J. Klein, *Phys. Chem. Chem. Phys.*, 2010, **12**, 1243–1247.

29. S. Perkin, *Phys. Chem. Chem. Phys.*, 2012, **14**, 5052–5062.

30. A. M. Smith, K. R. Lovelock and S. Perkin, *Faraday Discuss.*, 2013, **167**, 279–292.

31. A. M. Smith, K. R. Lovelock, N. N. Gosvami, P. Licence, A. Dolan, T. Welton and S. Perkin, *J. Phys. Chem. Lett.*, 2013, **4**, 378–382.

32. A. M. Smith, K. R. Lovelock, N. N. Gosvami, T. Welton and S. Perkin, *Phys. Chem. Chem. Phys.*, 2013, **15**, 15317–15320.

33. M. A. Gebbie, M. Valtiner, X. Banquy, E. T. Fox, W. A. Henderson and J. N. Israelachvili, *Proc. Natl. Acad. Sci.*, 2013, **110**, 9674–9679.

34. R. M. Espinosa-Marzal, A. Arcifa, A. Rossi and N. D. Spencer, *J. Phys. Chem. Lett.*, 2014, **5**, 179–184.

35. M. A. Gebbie, A. M. Smith, H. A. Dobbs, A. A. Lee, G. G. Warr, X. Banquy, M. Valtiner, M. W. Rutland, J. N. Israelachvili, S. Perkin and R. Atkin, *Chem. Commun.*, 2017, **53**, 1214–1224.

36. C. S. Perez-Martinez and S. Perkin, *Langmuir*, 2019, **35**, 15444–15450.

37. H.-W. Cheng and M. Valtiner, *Curr. Opin. Colloid Interface Sci.*, 2020, **47**, 126–136.

38. O. Tairy, N. Kampf, M. J. Driver, S. P. Armes and J. Klein, *Macromolecules*, 2015, **48**, 140–151.

39. S. H. Idziak, C. R. Safinya, R. S. Hill, K. E. Kraiser, M. Ruths, H. E. Warriner, S. Steinberg, K. S. Liang and J. N. Israelachvili, *Science*, 1994, **264**, 1915–1918.

40. S. H. Idziak, I. Koltover, K. S. Liang, J. N. Israelachvili and C. R. Safinya, *Int. J. Thermophys.*, 1995, **16**, 299–307.

41. Y. Golan, A. Martin-Herranz, Y. Li, C. R. Safinya and J. Israelachvili, *Phys. Rev. Lett.*, 2001, **86**, 1263–1266.

42. Y. Golan, M. Seitz, C. Luo, A. Martin-Herranz, M. Yasa, Y. Li, C. R. Safinya and J. Israelachvili, *Rev. Sci. Instrum.*, 2002, **73**, 2486–2488.

43. R. M. Pashley and J. N. Israelachvili, *Colloids and Surfaces*, 1981, **2**, 169–187.

44. R. G. Horn and J. N. Israelachvili, *Chem. Phys. Lett.*, 1980, **71**, 192–194.

45. R. G. Horn and J. N. Israelachvili, *J. Chem. Phys.*, 1981, **75**, 1400–1411.

46. H. K. Christenson, *J. Chem. Phys.*, 1983, **78**, 6906–6913.

47. H. K. Christenson, *J. Chem. Soc. Faraday Trans. 1*, 1984, **80**, 1933–1946.

48. H. K. Christenson and R. G. Horn, *J. Colloid Interface Sci.*, 1985, **103**, 50–55.

49. Q. Lu, J. Wang, A. Faghihnejad, H. Zeng and Y. Liu, *Soft Matter*, 2011, **7**, 9366–9379.

50. T. S. Groves, C. S. Perez-Martinez, R. Lhermerout and S. Perkin, *J. Phys. Chem. Lett.*, 2021, **12**, 1702–1707.

51. H. Weiss, H. W. Cheng, J. Mars, H. Li, C. Merola, F. U. Renner, V. Honkimäki, M. Valtiner and M. Mezger, *Langmuir*, 2019, **35**, 16679–16692.

52. H. Kawai, H. Sakuma, M. Mizukami, T. Abe, Y. Fukao, H. Tajima and K. Kurihara, *Rev. Sci. Instrum.*, 2008, **79**, 043701.

53. B. Derjaguin, *Kolloid-Zeitschrift*, 1934, **69**, 155–164.

54. G. Binnig, C. F. Quate and C. Gerber, *Phys. Rev. Lett.*, 1986, **56**, 930–933.

55. W. A. Ducker, T. J. Senden and R. M. Pashley, *Nature*, 1991, **353**, 239–241.

56. S. Rentsch, R. Pericet-Camara, G. Papastavrou and M. Borkovec, *Phys. Chem. Chem. Phys.*, 2006, **8**, 2531–2538.

57. V. Valmacco, M. Elzbieciak-Wodka, D. Herman, G. Trefalt, P. Maroni and M. Borkovec, *J. Colloid Interface Sci.*, 2016, **472**, 108–115.

58. A. M. Smith, P. Maroni, G. Trefalt and M. Borkovec, *J. Phys. Chem. B*, 2019, **123**, 1733–1740.

59. S. Kumar, P. Cats, M. B. Alotaibi, S. C. Ayirala, A. A. Yousef, R. van Roij, I. Siretanu and F. Mugele, *J. Colloid Interface Sci.*, 2022, **622**, 819–827.

60. R. Hayes, S. Z. El Abedin and R. Atkin, *J. Phys. Chem. B*, 2009, **113**, 7049–7052.

61. O. Werzer, E. D. Cranston, G. G. Warr, R. Atkin and M. W. Rutland, *Phys. Chem. Chem. Phys.*, 2012, **14**, 5147–5152.

62. J. Sweeney, G. B. Webber, M. W. Rutland and R. Atkin, *Phys. Chem. Chem. Phys.*, 2014, **16**, 16651–16658.

63. H.-W. Cheng, P. Stock, B. Moeremans, T. Baimpos, X. Banquy, F. U. Renner and M. Valtiner, *Adv. Mater. Interfaces*, 2015, **2**, 1500159.

64. N. Hjalmarsson, R. Atkin and M. W. Rutland, *Chem. Commun.*, 2017, **53**, 647–650.

65. Z. Chen, B. McLean, M. Ludwig, R. Stefanovic, G. G. Warr, G. B. Webber, A. J. Page and R. Atkin, *J. Phys. Chem. C*, 2016, **120**, 2225–2233.

66. Z. Chen, M. Ludwig, G. G. Warr and R. Atkin, *J. Colloid Interface Sci.*, 2017, **494**, 373–379.

67. O. S. Hammond, H. Li, C. Westermann, A. Y. M. Al-Murshedi, F. Endres, A. P. Abbott, G. G. Warr, K. J. Edler and R. Atkin, *Nanoscale Horizons*, 2019, **4**, 158–168.

68. B. Derjaguin and L. Landau, *Prog. Surf. Sci.*, 1993, **43**, 30–59.

69. E. J. W. Verwey and J. T. G. Overbeek, *Theory of the stability of lyophobic colloids*, Elsevier, Amsterdam, 1948.

70. M. Mezger, H. Schröder, H. Reichert, S. Schramm, J. S. Okasinski, S. Schöder, V. Honkimäki, M. Deutsch, B. M. Ocko, J. Ralston, M. Rohwerder, M. Stratmann and H. Dosch, *Science*, 2008, **322**, 424–428.

71. T. Cremer, M. Stark, A. Deyko, H.-P. Steinrück and F. Maier, *Langmuir*, 2011, **27**, 3662–3671.

72. M. Mezger, S. Schramm, H. Schröder, H. Reichert, M. Deutsch, E. J. De Souza, J. S. Okasinski, B. M. Ocko, V. Honkimäki and H. Dosch, *J. Chem. Phys.*, 2009, **131**, 094701.

73. H. Zhou, M. Rouha, G. Feng, S. S. Lee, H. Docherty, P. Fenter, P. T. Cummings, P. F. Fulvio, S. Dai, J. McDonough, V. Presser and Y. Gogotsi, *ACS Nano*, 2012, **6**, 9818–9827.

74. P. Debye and E. Huckel, *Phys. Zeitschrift*, 1923, **24**, 185–206. Translated by Michael J. Braus, 2019.

75. H. S. Frank and P. T. Thompson, *J. Chem. Phys.*, 1959, **31**, 1086–1095.

76. R. Kjellander, *Statistical Mechanics of Liquids and Solutions: Intermolecular Forces, Structure and Surface Interactions Volume I*, CRC Press, Boca Raton, FL, 2020.

77. C. J. Clarke, W. C. Tu, O. Levers, A. Bröhl and J. P. Hallett, *Chem. Rev.*, 2018, **118**, 747–800.

78. S. K. Singh and A. W. Savoy, *J. Mol. Liq.*, 2020, **297**, 112038.

79. A. P. Abbott, G. Capper, D. L. Davies, H. L. Munro, R. K. Rasheed and V. Tambyrajah, *Chem. Commun.*, 2001, **1**, 2010–2011.

80. E. L. Smith, A. P. Abbott and K. S. Ryder, *Chem. Rev.*, 2014, **114**, 11060–11082.

81. Q. Zhang, K. D. O. Vigier, S. Royer and F. Jérôme, *Chem. Soc. Rev.*, 2012, **41**, 7108–7146.

82. A. Paiva, R. Craveiro, I. Aroso, M. Martins, R. L. Reis and A. R. C. Duarte, *ACS Sustain. Chem. Eng.*, 2014, **2**, 1063–1071.

83. L. P. Silva, M. A. Martins, J. H. Conceição, S. P. Pinho and J. A. Coutinho, *ACS Sustain. Chem. Eng.*, 2020, **8**, 15317–15326.

84. J. Klein and E. Kumacheva, *J. Chem. Phys.*, 1998, **108**, 6996–7009.

85. J. N. Israelachvili, N. A. Alcantar, N. Maeda, T. E. Mates and M. Ruths, *Langmuir*, 2004, **20**, 3616–3622.

86. J. N. Israelachvili, *J. Colloid Interface Sci.*, 1973, **44**, 259–272.

87. A. M. Smith, A. A. Lee and S. Perkin, *Phys. Rev. Lett.*, 2017, **118**, 096002.

88. R. Lhermerout and S. Perkin, *Phys. Rev. Fluids*, 2018, **3**, 014201.

89. R. Lhermerout and S. Perkin, *Phys. Chem. Chem. Phys.*, 2020, **22**, 455–466.

90. P. Gill, T. T. Moghadam and B. Ranjbar, *J. Biomol. Tech.*, 2010, **21**, 167.

91. H. Yue, Y. Zhao, X. Ma and J. Gong, *Chem. Soc. Rev.*, 2012, **41**, 4218–4244.

92. L. An, T. S. Zhao, S. Y. Shen, Q. X. Wu and R. Chen, *Int. J. Hydrogen Energy*, 2010, **35**, 4329–4335.

93. P. Bigini, M. Gobbi, M. Bonati, A. Clavenna, M. Zucchetti, S. Garattini and G. Pasut, *Nat. Nanotechnol.*, 2021, **16**, 1169–1171.

94. J. Li, C. Zhang, M. Deng and J. Luo, *Sci. Rep.*, 2014, **4**, 7226.

95. D. R. Lide, *CRC Handbook of Chemistry and Physics*, CRC Press, Boca Raton, FL, 84th edn, 2003.

96. A. A. Lee, C. S. Perez-Martinez, A. M. Smith and S. Perkin, *Faraday Discuss.*, 2017, **199**, 239–259.

97. R. Kjellander, *Soft Matter*, 2019, **15**, 5866–5895.

98. M. Matsugami, T. Takamuku, T. Otomo and T. Yamaguchi, *J. Phys. Chem. B*, 2006, **110**, 12372–12379.

99. J. N. Israelachvili, Y. L. Chen and H. Yoshizawa, *J. Adhes. Sci. Technol.*, 1994, **8**, 1231–1249.

100. E. Kumacheva and J. Klein, *J. Chem. Phys.*, 1998, **108**, 7010–7022.

101. J. N. Israelachvili, P. M. McGuiggan and A. M. Homola, *Science*, 1988, **240**, 189–191.

102. M. L. Gee, P. M. McGuiggan, J. N. Israelachvili and A. M. Homola, *J. Chem. Phys.*, 1990, **93**, 1895–1906.

103. A. Singhabhandhu and T. Tezuka, *Energy*, 2010, **35**, 2493–2504.

104. The Soap and Detergent Association (SDA) Glycerine: an overview, https://www.cleaninginstitute.org/sites/default/files/research-pdfs/Glycerine_-_an_overview.pdf, (accessed May 6, 2022).

105. H. W. Tan, A. R. Abdul Aziz and M. K. Aroua, *Renew. Sustain. Energy Rev.*, 2013, **27**, 118–127.

106. K. Gekko and S. N. Timasheff, *Biochemistry*, 1981, **20**, 4667–4676.

107. J. J. Towey, A. K. Soper and L. Dougan, *Phys. Chem. Chem. Phys.*, 2011, **13**, 9397–9406.

108. W. Zhu, C. Zhang, Y.-d. Zhu, R. An, X.-h. Lu, Y.-j. Shi and S.-y. Jiang, *J. Mol. Liq.*, 2019, **291**, 111238.

109. J. Li, C. Zhang, L. Ma, Y. Liu and J. Luo, *Langmuir*, 2013, **29**, 271–275.

110. W. Habchi, C. Matta, L. Joly-Pottuz, M. I. De Barros, J. M. Martin and P. Vergne, *Tribol. Lett.*, 2011, **42**, 351–358.

111. Y. Long, M. I. D. B. Bouchet, T. Lubrecht, T. Onodera and J. M. Martin, *Sci. Rep.*, 2019, **9**, 6286.

112. M. Björling and Y. Shi, *Tribol. Lett.*, 2019, **67**, 23.

113. A. A. Kuzharov, B. S. Luk'yanov and A. S. Kuzharov, *J. Frict. Wear*, 2016, **37**, 337–345.

114. A. M. Tortora and D. Halenahally Veeregowda, *Adv. Tribol.*, 2016, **2016**, 1–6.

115. A. G. Ferreira, A. P. Egas, I. M. Fonseca, A. C. Costa, D. C. Abreu and L. Q. Lobo, *J. Chem. Thermodyn.*, 2017, **113**, 162–182.

116. D. Y. Chan and R. G. Horn, *J. Chem. Phys.*, 1985, **83**, 5311–5324.

117. R. Lhermerout, *Lubricants*, 2021, **9**, 69.

118. M. Han and R. M. Espinosa-Marzal, *J. Phys. Chem. C*, 2018, **122**, 21344–21355.

119. M. A. Martins, S. P. Pinho and J. A. Coutinho, *J. Solution Chem.*, 2019, **48**, 962–982.

120. M. V. Fedorov and A. A. Kornyshev, *Chem. Rev.*, 2014, **114**, 2978–3036.

121. O. S. Hammond, D. T. Bowron and K. J. Edler, *Green Chem.*, 2016, **18**, 2736–2744.

122. E. R. Cooper, C. D. Andrews, P. S. Wheatley, P. B. Webb, P. Wormald and R. E. Morris, *Nature*, 2004, **430**, 1012–1016.

123. S. D. Lawes, S. V. Hainsworth, P. Blake, K. S. Ryder and A. P. Abbott, *Tribol. Lett.*, 2010, **37**, 103–110.

124. A. P. Abbott, E. I. Ahmed, R. C. Harris and K. S. Ryder, *Green Chem.*, 2014, **16**, 4156–4161.

125. E. I. Ahmed, A. P. Abbott and K. S. Ryder, *Lubrication studies of some type III deep eutectic solvents (DESs)*, AIP Conf. Proc., 2017, vol. 1888, p. 020006.

126. I. Garcia, S. Guerra, J. de Damborenea and A. Conde, *Lubricants*, 2019, **7**, 37.

127. E. R. Nightingale, *J. Phys. Chem.*, 1959, **63**, 1381–1387.

128. M. H. Mamme, S. L. Moors, H. Terryn, J. Deconinck, J. Ustarroz and F. De Proft, *J. Phys. Chem. Lett.*, 2018, **9**, 6296–6304.

129. A. Pandey, R. Rai, M. Pal and S. Pandey, *Phys. Chem. Chem. Phys.*, 2014, **16**, 1559–1568.

130. O. S. Hammond, D. T. Bowron and K. J. Edler, *Angew. Chemie Int. Ed.*, 2017, **56**, 9782–9785.

131. A. A. Lee, C. S. Perez-Martinez, A. M. Smith and S. Perkin, *Phys. Rev. Lett.*, 2017, **119**, 026002.

132. H.-W. Cheng, J.-N. Dienemann, P. Stock, C. Merola, Y.-J. Chen and M. Valtiner, *Sci. Rep.*, 2016, **6**, 30058.

133. F. Bresme, A. A. Kornyshev, S. Perkin and M. Urbakh, *Nature Materials*, 2022, **21**, 848–858.

134. A. P. Abbott, R. C. Harris, K. S. Ryder, C. D'Agostino, L. F. Gladden and M. D. Mantle, *Green Chem.*, 2011, **13**, 82–90.

135. A. Elbourne, N. Meftahi, T. L. Greaves, C. F. McConville, G. Bryant, S. J. Bryant and A. J. Christofferson, *J. Colloid Interface Sci.*, 2021, **591**, 38–51.

136. A. H. Turner and J. D. Holbrey, *Phys. Chem. Chem. Phys.*, 2019, **21**, 21782–21789.

137. L. Burstein, *Tribology for Engineers*, Elsevier, 2011, pp. 65–120.

138. A. Yadav, S. Trivedi, R. Rai and S. Pandey, *Fluid Phase Equilib.*, 2014, **367**, 135–142.

139. D. J. Bergman, *Physics Reports*, 1978, **43**, 377–407.

140. P. Atkins and J. de Paula, *Physical Chemistry*, Oxford University Press, Great Britain, 2006.

141. L. J. Kollau, M. Vis, A. van den Bruinhorst, A. C. C. Esteves and R. Tuinier, *Chem. Commun.*, 2018, **54**, 13351–13354.

142. K. Shahbaz, F. S. Mjalli, M. Hashim and I. M. ALNashef, *J. Appl. Sci.*, 2010, **10**, 3349–3354.

143. R. K. Ibrahim, M. Hayyan, M. A. AlSaadi, S. Ibrahim, A. Hayyan and M. A. Hashim, *J. Mol. Liq.*, 2019, **276**, 794–800.

144. E. A. Crespo, L. P. Silva, J. O. Lloret, P. J. Carvalho, L. F. Vega, F. Llovell and J. A. Coutinho, *Phys. Chem. Chem. Phys.*, 2019, **21**, 15046–15061.

145. V. Agieienko and R. Buchner, *Phys. Chem. Chem. Phys.*, 2022, **24**, 5265–5268.

146. A. Jani, T. Sohier and D. Morineau, *J. Mol. Liq.*, 2020, **304**, 112701.

147. L. Fernandez, L. P. Silva, M. A. Martins, O. Ferreira, J. Ortega, S. P. Pinho and J. A. Coutinho, *Fluid Phase Equilib.*, 2017, **448**, 9–14.

148. K. Shahbaz, S. Baroutian, F. S. Mjalli, M. A. Hashim and I. M. AlNashef, *Thermochim. Acta*, 2012, **527**, 59–66.

149. K. Shahbaz, F. S. Mjalli, M. A. Hashim and I. M. AlNashef, *Fluid Phase Equilib.*, 2012, **319**, 48–54.

150. F. S. Bagh, K. Shahbaz, F. S. Mjalli, I. M. AlNashef and M. A. Hashim, *Fluid Phase Equilib.*, 2013, **356**, 30–37.

151. S. J. Bryant, A. J. Christofferson, T. L. Greaves, C. F. McConville, G. Bryant and A. Elbourne, *J. Colloid Interface Sci.*, 2022, **608**, 2430–2454.

152. Q. Abbas and L. Binder, *ECS Trans.*, 2019, **33**, 49–59.

153. X. Meng, K. Ballerat-Busserolles, P. Husson and J. M. Andanson, *New J. Chem.*, 2016, **40**, 4492–4499.

154. H. G. Morrison, C. C. Sun and S. Neervannan, *Int. J. Pharm.*, 2009, **378**, 136–139.

155. C. D'Agostino, R. C. Harris, A. P. Abbott, L. F. Gladden and M. D. Mantle, *Phys. Chem. Chem. Phys.*, 2011, **13**, 21383–21391.

156. D. R. Cordray, L. R. Kaplan, P. M. Woyciesjes and T. F. Kozak, *Fluid Phase Equilib.*, 1996, **117**, 146–152.

157. I. M. Aroso, A. Paiva, R. L. Reis and A. R. C. Duarte, *J. Mol. Liq.*, 2017, **241**, 654–661.

158. R. L. Collin, *J. Am. Chem. Soc.*, 1957, **79**, 6086–6086.

159. M. Gilmore, M. Swadzba-Kwasny and J. D. Holbrey, *J. Chem. Eng. Data*, 2019, **64**, 5248–5255.

160. H. Yuan, W. Deng, X. Zhu, G. Liu and V. S. J. Craig, *Langmuir*, 2022, **38**, 6164–6173.

161. M. A. Gebbie, H. A. Dobbs, M. Valtiner and J. N. Israelachvili, *Proc. Natl. Acad. Sci.*, 2015, **112**, 7432–7437.

162. P. Gaddam and W. Ducker, *Langmuir*, 2019, **35**, 5719–5727.

163. Z. A. H. Goodwin and A. A. Kornyshev, *Electrochem. Commun.*, 2017, **82**, 129–133.

164. J. Huang, *J. Phys. Chem. C*, 2018, **122**, 3428–3433.

165. J. G. Kirkwood, *J. Chem. Phys.*, 1934, **2**, 767–781.

166. J. G. Kirkwood, *Chem. Rev.*, 1936, **19**, 275–307.

167. P. Attard, *Phys. Rev. E*, 1993, **48**, 3604–3621.

168. R. M. Adar, S. A. Safran, H. Diamant and D. Andelman, *Phys. Rev. E*, 2019, **100**, 042615.

169. M. E. Fisher and B. Widom, *J. Chem. Phys.*, 1969, **50**, 3756–3772.

170. R. J. F. L. de Carvalho and R. Evans, *Mol. Phys.*, 1994, **83**, 619–654.

171. J. Ennis, R. Kjellander and D. J. Mitchell, *J. Chem. Phys.*, 1995, **102**, 975–991.

172. R. Kjellander and D. J. Mitchell, *Chem. Phys. Lett.*, 1992, **200**, 76–82.

173. R. Kjellander and D. J. Mitchell, *J. Chem. Phys.*, 1994, **101**, 603–626.

174. P. Keblinski, J. Eggebrecht, D. Wolf and S. R. Phillpot, *J. Chem. Phys.*, 2000, **113**, 282–291.

175. F. Coupette, A. A. Lee and A. Härtel, *Phys. Rev. Lett.*, 2018, **121**, 075501.

176. A. A. Lee, J.-P. Hansen, O. Bernard and B. Rotenberg, *Mol. Phys.*, 2018, **116**, 3147–3153.

177. G. Feng, M. Chen, S. Bi, Z. A. H. Goodwin, E. B. Postnikov, N. Brilliantov, M. Urbakh and A. A. Kornyshev, *Phys. Rev. X*, 2019, **9**, 021024.

178. B. Rotenberg, O. Bernard and J.-P. Hansen, *J. Phys. Condens. Matter*, 2018, **30**, 054005.

179. N. Anousheh, F. J. Solis and V. Jadhao, *AIP Adv.*, 2020, **10**, 125312.

180. S. W. Coles, C. Park, R. Nikam, M. Kanduc, J. Dzubiella and B. Rotenberg, *J. Phys. Chem. B*, 2020, **2020**, 1778–1786.

181. K. Ma, C. Lian, C. E. Woodward and B. Qin, *Chem. Phys. Lett.*, 2020, **739**, 137001.

182. P. Cats, R. Evans, A. Härtel and R. van Roij, *J. Chem. Phys.*, 2021, **154**, 124504.

183. R. Kjellander, *J. Chem. Phys.*, 2016, **145**, 124503.

184. R. Kjellander, *J. Chem. Phys.*, 2018, **148**, 193701.

185. R. Kjellander, *Phys. Chem. Chem. Phys.*, 2020, **22**, 23952–23985.

186. A. Ciach and O. Patsahan, *J. Phys. Condens. Matter*, 2021, **33**, 37LT01.

187. M. Apostol, *Chem. Phys.*, 2022, **558**, 111514.

188. C. S. Santos, N. S. Murthy, G. A. Baker and E. W. Castner, *J. Chem. Phys.*, 2011, **134**, 121101.

189. J. Mähler and I. Persson, *Inorg. Chem.*, 2012, **51**, 425–438.

190. A. N. Campbell, G. H. Debus and E. M. Kartzmark, *Can. J. Chem.*, 1955, **33**, 1508–1514.

191. C. Luo, Q. Su and W. Mi, *J. Chem. Eng. Data*, 2013, **58**, 625–633.

192. W. M. Haynes, *CRC Handbook of Chemistry and Physics*, CRC Press, Boca Raton, FL, 95th edn, 2014.

193. A. Southam, *PhD thesis*, University of Oxford, 2022.

194. R. G. Seoane, S. Corderí, E. Gómez, N. Calvar, E. J. González, E. A. Macedo and Á. Domínguez, *Ind. Eng. Chem. Res.*, 2012, **51**, 2492–2504.

195. Y. Deng, P. Husson, A. M. Delort, P. Besse-Hoggan, M. Sancelme and M. F. Costa Gomes, *J. Chem. Eng. Data*, 2011, **56**, 4194–4202.

196. S. Zhou, *Colloid Polym. Sci.*, 2019, **297**, 623–631.

197. R. G. Horn, J. N. Israelachvili and F. Pribac, *J. Colloid Interface Sci.*, 1987, **115**, 480–492.

198. C. Zhang, Y. Ding, L. Zhang, X. Wang, Y. Zhao, X. Zhang and G. Yu, *Angew. Chemie Int. Ed.*, 2017, **56**, 7454–7459.

199. W. Chu, X. Zhang, J. Wang, S. Zhao, S. Liu and H. Yu, *Energy Storage Mater.*, 2019, **22**, 418–423.

200. J. Zhao, J. Zhang, W. Yang, B. Chen, Z. Zhao, H. Qiu, S. Dong, X. Zhou, G. Cui and L. Chen, *Nano Energy*, 2019, **57**, 625–634.

201. Q. Xu, L. Y. Qin, Y. N. Ji, P. K. Leung, H. N. Su, F. Qiao, W. W. Yang, A. A. Shah and H. M. Li, *Electrochim. Acta*, 2019, **293**, 426–431.

202. R. Tivony, D. B. Yaakov, G. Silbert and J. Klein, *Langmuir*, 2015, **31**, 12845–12849.